A LOW COST GAS PHASE ANALYSIS SYSTEM FOR THE DIAGNOSIS OF BACTERIAL INFECTION

by

Samuel Oghenekevwe Agbroko

A thesis presented for the degree of
Doctor of Philosophy

School of Engineering
University of Warwick
United Kingdom
May 20, 2019

Contents

Acknowledgements

I would like to express gratefulness to God for the gift of life and the granting me the strength to complete this work.

Special thanks to my supervisor Prof. James Covington for his guidance during this project. His support during tough times helped me complete this project. I would also like to thank Frank Courtney, Ian Griffith and Gavin Downs for their technical support. Thanks to my colleagues, Dr. Siavash Esfahani and Wangi Pandan Sari for their support in the lab.

My unreserved gratitude goes to my parents Godset and Christiana Oteri for their love and support during this work. I am immensely grateful that they also covered my tuition and maintenance cost, words cannot express my appreciation. The love and support of my siblings - Akpevwe, Tega, Oke and Brorhie were a constant source of happiness, thank you all for always being there for me.

Declaration

This thesis is submitted to the University of Warwick in support of the application for the degree of Doctor of Philosophy. It has not been submitted in part, or in whole, for a degree or other qualification at any other University. Parts of this thesis are published by the author in peer-reviewed research papers listed. Apart from commonly understood and accepted ideas, or where reference is made to the work of others, the work described in this thesis is carried out by the author in School of Engineering of the University of Warwick except in the cases below:

- Gas Sensor Calibration Rig (Chapter 3) was designed in collaboration with Dr. Siavash Esfahani.
- LabVIEW software for Gas Sensor Calibration Rig (Chapter 3) was designed by Prof. James Covington.

Samuel Oghenekevwe Agbroko

2015-2019

List of Published Work

- **Samuel O. Agbroko** and James Covington. A novel, low-cost, portable PID sensor for detection of VOC. *Multidisciplinary Digital Publishing Institute Proceedings* volume 1, page 482,2017.

- James A. Covington, **Samuel Agbroko**, and Akira Tiele. A simple, portable, computer-controlled odour generator. *Olfaction and Electronic Nose (ISOEN), 2017 ISOCS/IEEE International Symposium* page 13. IEEE, 2017.

- James A Covington, **Samuel O Agbroko**, Akira Tiele. Development of a portable, multichannel olfactory display transducer. *IEEE Sensors Journal*, 18(12):49694974, 2018.

- **Samuel O. Agbroko** and James Covington. A novel, low-cost, portable pid sensor for the detection of volatile organic compounds. *Sensors and Actuators B: Chemical*, 275:10-15, 2018.

- Emily Stark, James Covington, **Samuel Agbroko**, Chenjing Peng, and Elan Barenholtz. Deep learning investigation of mass spectrometry analysis from melanoma samples. *Olfaction and Electronic Nose (ISOEN), 2019 ISOCS/IEEE International Symposium* 2019 (Accepted).

Abstract

Drug resistance is becoming a major concern in both the western world and in developing countries. The over use of common anti-bacterial drugs has resulted in a plethora of multi-drug resistant diseases and an ever reducing number of effective treatments – and is now of major concern to the UK government. One of the major reasons behind this is the difficulty in identifying bacterial infections from viral infections, especially in primary care where patients have an expectation of receiving medication. For most viral conditions, there is no effective treatment and the body fights off the disease, thus prescribing anti-bacterial drugs simply results in the proliferation of drugs within the community – increasing the rate of drug resistance. Increasing drug resistance contributed to the rise of superbugs (drug resistant bacteria) which are expected to kill an about 10 million people a year worldwide by the year 2050 and could result to an economic loss of £63 trillion. Increasing drug resistance contributed to the rise of superbugs (drug resistant bacteria) which are expected to kill an about 10 million people a year worldwide by the year 2050 and could result to an economic loss of £63 trillion. Therefore, there is a strong medical and economic need to develop tools that can diagnose bacterial diseases from viral infections, focused towards primary care.

One means of achieving this is through the detection of gas-phase biomarkers

of disease. It is well known that the metabolic activity of bacteria is significantly different from its host. Many studies have shown that it is possible to detect a bacterial infection, identify the strain and its current life-cycle stage simply by measuring bacterial metabolic emissions. In addition, the human body's response to a bacterial infection is significantly different from a viral infection the human body's response to a bacterial infection is significantly different from a viral infection, allowing human stress markers to also be used for differentiating these conditions. Thus, there is evidence that these bio-markers exist and could be detected.

However, a major limiting factor inhibiting the wide-spread deployment of this concept is the unit cost of the analytical instrumentation required for gas analysis. Currently, the main preferred methods are GCMS (gas chromatography/mass spectrometry), TOF-MS (time of flight – MS) and SIFT-MS (selective ion flow tube – MS). Though excellent at undertaking this role, the typical unit cost of these instruments is in excess of £100k, making them out of reach of current GP budgets. Therefore, what is required is a low-cost, portable instrument that can detect bacterial infections from viral infections and be applicable to primary care.

List of Abbreviations

AC	Alternating Current
ACC	Activated Carbon Cloth
ADT	Aspirator Drift Tube
AFE	Analogue Front End
auc	Area Under Curve
CD	Corona Discharge
CD-IMS	Corona Discharge Ion Mobility Spectrometry
CM	Confusion Matrix
DAC	Digital to Analog Converter
DC	Direct Current
DTIMS	Drift Time Ion Mobility Spectrometer
EMI	Electromagnetic Interference
FAIMS	Field Asymmetric Ion Mobility Spectrometry
GATT	Generic Attributes Profile
GC	Gas Chromatograpy
GC-IMS	Gas Chromatography Ion Mobility Spectrometry
GC-MS	Gas Chromatography Mass Spectrometry
GUI	Graphical User Interface
HC	Hierarchical clustering
IBD	Inflammatory Bowel Disease

IE	Ionisation Energy
IMS	Ion Mobility Spectrometry
KNN	K-nearest neighbour
KMC	k-means clustering
LC	Liquid Chromatography
LDA	Linear Discriminant Analysis
LOD	Limit of Detection
LR	Logistic Regression
MFC	Mass Flow Controller
MFM	Mass Flow Meter
MOS	Metal Oxide Sensor
MCC	Multi Capillary Column
MS	Mass Spectrometry
MSL	Micro Stereo Lithography
NB	Naive Bayes
NI-DAQ	National Instrument Data Acquisition board
OEM	Original Equipment Manufacturer
PC	Pre-concentrator
PCA	Principal Component Analysis
ppb	parts per billion
ppm	parts per million
PID	Photoionization Detector
PWM	Pulse Width Modulation
R-F	Random Forest
RF	Radio Frequency
RFI	Radio Frequency Interference

SIFT-MS Selected Ion Flow Tube Mass Spectroscopy

SVM Support Vector Machine

TD Thermal Desorber

TIMS Trapped Ion Mobility Spectrometer

TWDT Traveling Wave Drift Tubes

UART Universal Asynchronous Receiver/Transmitter

UV Ultraviolet

UWP Universal Windows Platform

VOC Volatile Organic Compound

List of Symbols

C	Concentration
C_{vp}	Vapour concentration
d	Distance
E	Electric field
F	Flow rate
hv	Photon energy
K	Mobility coefficient
K_0	Reduced mobility coefficient
m	Mass
M	Molecule
M_w	Molecular weight
N	Neutral density
P	Pressure
P_{vp}	Vapour pressure
q_d	Permeation rate
t	Temperature (degree celsius)
T	Temperature (kelvin)
t_d	Drift time
V	Voltage
v_d	Drift velocity

List of Figures

List of Tables

Chapter 1

Introduction - Smell in diagnostic medicine

Before the advent of sophisticated diagnostic instruments physicians diagnosed diseases based on their senses [1, 2]. It was not uncommon for physicians to touch, taste or smell their patients' wastes in an attempt to identify their ailments. The use of smell in diagnosis grew traction because it was understood that certain diseases resulted in the production of Volatile Organic Compound (VOC)s with characteristic smells. Greek physician Hippocrates (460 -370 BC) poured human sputum over hot coal to release distinct smells indicative of tuberculosis infection [3]. There has been other reports in literature of physicians diagnosing diseases using smell. For example, Poulton *et al.* reported that nursing sisters at the East Birmingham Hospital were able to diagnosis rotavirus gastroenteritis by smelling stools of patients before culture results were available. The nurses classified 69% of stools correctly for 23 babies [4].

The method of diagnosing diseases by smelling patients' waste has several advan-

tages when compared with conventional diagnostic methods. Conventional bacterial diagnostic methods can be expensive, time consuming, and sometimes requiring several days for cell culture. The delay associated with cultures has a negative effect on patients' therapy [2, 3]. For example, in the case of sepsis patients' for example, delays in administering antibiotic has been reported to increase mortality by 10 to 15% [5]. Physicians aim to administer antibiotics after bacterial infection is confirmed to curb the rise in drug resistant bacterial strains which has resulted in about 700,000 deaths a year and could cost about £63tn per year[6]. Consequently, physicians wait for a positive prognosis before giving antibacterial medication. With each hour delay in confirming bacterial infection, the risk of progression to septic shock for sepsis patients increases by 8% [7]

Diagnosis based on detection of VOCs enables a rapid, non-invasive method of identifying pathogens. VOCs have been described as organic compounds with boiling points from about 50°C to about 260°C, therefore they have relatively high vapour pressure at room temperature [8, 9]. This includes sulfides, ketones, alcohols, isocyanates, aldehydes, and hydrocarbons, which are vapours at ambient temperatures [10]. VOCs are produced in living organisms as a result of normal metabolic function. These compounds are released in saliva, blood, urine, faeces and sweat. Pathogens in the human body have distinct metabolism hence produce characteristic VOC profiles [11, 12]. Therefore the presence of these pathogens can be diagnosed by detecting their VOC profile in human waste[13].

VOCs from breath, saliva, skin, blood, urine and faeces samples have been analysed to diagnose diseases such as tuberculosis, lung cancer, schizophrenia, diabetes, inflammatory bowel disease and infections [10, 13–22]. The ease of obtaining waste samples from humans along with the rapid nature of gas based diagnostic methods

has led to increased research in VOC based analytic tools. Currently, Gas Chromatography Mass Spectrometry (GC-MS) systems [10, 14–17] Ion Mobility Spectrometry (IMS) systems [16, 19, 20, 22, 23], and electronic noses [16, 21, 23, 24] are some of the major instruments used in analysis of gas samples for diagnosing diseases. Photoionization Detector (PID) technology has also been used in diagnosis [25].

Mass Spectrometry (MS) is often stated as the gold standard for VOC analysis because of its high sensitivity, accuracy, reproducibility and overall robustness. However, wide adoption of this technology is limited by several factors including cost of purchase, complexity of operation and long analysis time [26, 27]. Its size and weight reduce their portability and restrict their use to mostly laboratory analysis. Similar factors also limits wide adoption of IMS, although IMSs are slightly smaller and cheaper than MSs. The cost and size of this equipment limits their use in point of care in hospital wards and GP surgeries, especially in developing countries [23]. PIDs and electronic nose instruments are smaller in size and more portable in comparison.PIDs are significantly cheaper than the other technologies mentioned. However, both electronic nose and PID technologies do not offer information on the identity of VOCs under test as they are sensitive to a wide range of compounds hence have poor selectivity [21, 28]. A major advantage in using PID sensors is the speed of analysis with some commercial PIDs offering analysis times within a second [29]. Therefore, what is needed is a diagnostic tool that offers similar sensitivity and accuracy of the MS systems at a lower price point. Such a tool will enable faster diagnosis of bacteria by eliminating the need for time consuming culture method, improve therapy for patients and help curb the rise of drug-resistant bacterial strains.

1.1 Research aims

The goal of this project is to develop a prototype point of care tool that has the potential to be developed into a future commercial product for bacterial detection. The biological medium selected is urine. To achieve this goal, a low-cost novel VOC detector has been designed. The design approach merges merits of commercial IMS systems and PID sensors. Unlike these commercial PID devices, the detector developed in this study provides compositional information on the compound being tested. With the design approach taken, the instrument could be made available to consumers at a lower cost than IMS systems with a market potential to sit somewhere between the lower end PID and higher end MS and IMS systems. Peripheral Pre-concentrator (PC) and Gas Chromatograpy (GC) systems were also developed to boost the sensitivity and specificity of the detector. An end user software was designed to enable non-technical personnel to use the instrument for diagnosis. Several chemical analysis were carried out on the components to benchmark the instruments performance in VOC analysis. Initial diagnostic tests were also carried out using urine and some key biomarkers for bacterial infections. Finally, statistical methods applied in the area of gas based diagnostic medicine were also investigated. This was done to develop an understanding of statistical approaches which were best suited for this instrument.

1.2 Thesis structure

This section presents a brief overview of the thesis.

Chapter 2 PID and IMS Technologies

Since the work done in this project hinges on PID and IMS technologies, this chapter discusses the theories, principle of operation, and development of PID and IMS technologies. It presents some commercially existing designs and their applications. It also discusses some of the merits and disadvantages of these technologies.

Chapter 3 Development of a Gas Sensor Calibration Rig

This chapter discusses the development of a gas sensor calibration test rig which was designed with the aim of producing a repeatable test environment for calibrating gas sensors. The test rig provides gas mixtures at defined flow rates, pressure, temperature and humidity.

Chapter 4 Design of a Pre-concentrator and Gas Chromatograph

PCs and GCs help to improve concentration, sensitivity accuracy and selectivity of gas analytical systems. Therefore, PCs and GCs were designed to improve the overall performance of this diagnostic instrument. The development of a PC and GC will be presented in this chapter.

Chapter 2.2 Design and development of a VOC Ionisation Detector

The design of a novel VOC sensor that combines the advantages of PID and IMS sensors is described in this chapter. The chapter also discusses VOC detection tests that were carried out to demonstrate the sensor's performance.

Chapter 6 System Assembly and Software

In this chapter, the assembly of the PC, GC and VOC detector components into a prototype diagnostic analytical instrument will be presented. This chapter will also cover the software designed to manage various aspects of the instrument including power supply, pneumatics, data management.

Chapter 7 Biomedical Tests and Results

Preliminary tests were carried out using urine and key biomarkers for bacterial infections. This chapter presents findings from these tests. It also presents statistical tools that aids users in diagnostic tests using this instrument.

The results of all of the tested technologies are compared in the concluding chapter. The qualities and limitations of the instrument are explored and recommendations are presented for further work.

1.3 References

[1] Jeremy K Nicholson and John C Lindon. Systems biology: metabonomics. *Nature*, 455(7216):1054, 2008.

[2] Lieuwe DJ Bos, Peter J Sterk, and Marcus J Schultz. Volatile metabolites of pathogens: a systematic review. *PLoS pathogens*, 9(5):e1003311, 2013.

[3] Elizabeth Hong-Geller and Samantha Adikari. Volatile organic compound and metabolite signatures as pathogen identifiers and biomarkers of infectious disease. In *Biosensing Technologies for the Detection of Pathogens-A Prospective Way for Rapid Analysis*. InTech, 2018.

[4] J Poulton and MJ Tarlow. Diagnosis of rotavirus gastroenteritis by smell. *Archives of disease in childhood*, 62(8):851–852, 1987.

[5] Bristol B Whiles, Amanda S Deis, and Steven Q Simpson. Increased time to initial antimicrobial administration is associated with progression to septic shock in severe sepsis patients. *Critical care medicine*, 45:623–629, April 2017.

[6] http://www.bbc.co.uk/news/health-30416844, November, 2018.

[7] Arthur P. Wheeler and Gordon R. Bernard. Treating patients with severe sepsis. *New England Journal of Medicine*, 340(3):207–214, 1999. PMID: 9895401.

[8] Peder Wolkoff and Gunnar D Nielsen. Organic compounds in indoor air—their relevance for perceived indoor air quality? *Atmospheric Environment*, 35(26):4407–4417, 2001.

[9] Nigel B Goodman, Anne Steinemann, Amanda J Wheeler, Phillip J Paevere, Min Cheng, and Stephen K Brown. Volatile organic compounds within indoor environments in australia. *Building and Environment*, 122:116–125, 2017.

[10] Mohammed Ashrafi, Matt Bates, Mohamed Baguneid, Teresa Alonso-Rasgado, Riina Rautemaa-Richardson, and Ardeshir Bayat. Volatile organic compound detection as a potential means of diagnosing cutaneous wound infections. *Wound Repair and Regeneration*, 25(4):574–590, 2017.

[11] K Liddell. Smell as a diagnostic marker. *Postgraduate medical journal*, 52(605):136–138, 1976.

[12] Stefan Schulz and Jeroen S Dickschat. Bacterial volatiles: the smell of small organisms. *Natural product reports*, 24:814–842, August 2007.

[13] Shneh Sethi, Ranjan Nanda, and Trinad Chakraborty. Clinical application of volatile organic compound analysis for detecting infectious diseases. *Clinical microbiology reviews*, 26(3):462–475, 2013.

[14] Michael Phillips, Victoria Basa-Dalay, Graham Bothamley, Renee N Cataneo, Phung Kim Lam, Maria Piedad R Natividad, Peter Schmitt, and James Wai. Breath biomarkers of active pulmonary tuberculosis. *Tuberculosis*, 90(2):145–151, 2010.

[15] Jiemin Zhou, Zi-Ao Huang, Ujendra Kumar, and David DY Chen. Review of recent developments in determining volatile organic compounds in exhaled breath as biomarkers for lung cancer diagnosis. *Analytica chimica acta*, 996:1–9, 2017.

[16] David Beale, Oliver Jones, Avinash Karpe, Saravanan Dayalan, Ding Oh, Konstantinos Kouremenos, Warish Ahmed, and Enzo Palombo. A review of analytical techniques and their application in disease diagnosis in breathomics and salivaomics research. *International journal of molecular sciences*, 18(1):24, 2016.

[17] Brian M Ross, Sandeep Shah, and Malcolm Peet. Increased breath ethane and pentane concentrations in currently unmedicated patients with schizophrenia. *Open Journal of Psychiatry*, 1(01):1, 2011.

[18] Wolfram Miekisch, Jochen K Schubert, Dierk A Vagts, and Klaus Geiger. Analysis of volatile disease markers in blood. *Clinical chemistry*, 47(6):1053–1060, 2001.

[19] Nora van Gaal, Rozanne Lakenman, James Covington, Richard Savage, Evelien de Groot, Marije Bomers, Marc Benninga, Chris Mulder, Nanne de Boer, and

Tim de Meij. Faecal volatile organic compounds analysis using field asymmetric ion mobility spectrometry: non-invasive diagnostics in paediatric inflammatory bowel disease. *Journal of breath research*, 12(1):016006, 2017.

[20] Riikka J Niemi, Antti N Roine, Emmi Eräviita, Pekka S Kumpulainen, Johanna U Mäenpää, and Niku Oksala. Faims analysis of urine gaseous headspace is capable of differentiating ovarian cancer. *Gynecologic oncology*, 151(3):519–524, 2018.

[21] Laura Capelli, Gianluigi Taverna, Alessia Bellini, Lidia Eusebio, Niccolò Buffi, Massimo Lazzeri, Giorgio Guazzoni, Giorgio Bozzini, Mauro Seveso, Alberto Mandressi, et al. Application and uses of electronic noses for clinical diagnosis on urine samples: A review. *Sensors*, 16(10):1708, 2016.

[22] Agnieszka Ulanowska, Magdalena Ligor, Anton Amann, and Bogus^{3}aw Buszewski. Determination of volatile organic compounds in exhaled breath by ion mobility spectrometry. *Chemia Analityczna*, 53(6):953–965, 2008.

[23] Jorge Pereira, Priscilla Porto-Figueira, Carina Cavaco, Khushman Taunk, Srikanth Rapole, Rahul Dhakne, Hampapathalu Nagarajaram, and José Câmara. Breath analysis as a potential and non-invasive frontier in disease diagnosis: an overview. *Metabolites*, 5(1):3–55, 2015.

[24] Alphus D Wilson and Manuela Baietto. Advances in electronic-nose technologies developed for biomedical applications. *Sensors (Basel, Switzerland)*, 11:1105–1176, 2011.

[25] Hideo Ueda and Mitsuo Hiromoto. Device and method for expiratory air examination, June 20 1995. US Patent 5,425,374.

[26] Samuel O Agbroko and James Covington. A novel, low-cost, portable pid sensor for the detection of volatile organic compounds. *Sensors and Actuators B: Chemical*, 275:10–15, 2018.

[27] M Ariel Geer Wallace and Joachim D Pleil. Evolution of clinical and environmental health applications of exhaled breath research: review of methods and instrumentation for gas-phase, condensate, and aerosols. *Analytica chimica acta*, 2018.

[28] K. Yan and D. Zhang. Sensor evaluation in a breath analysis system. In *2014 International Conference on Medical Biometrics*, pages 35–40, 2014.

[29] http://www.hnu.com/pdf/portableanalyzertechnology_specs514.pdf, November, 2018.

Chapter 2

PID and IMS Technologies

2.1 Introduction

In Chapter 1, it was explained that the aim of this initiative is to develop a gas analytic instrument based on the Photoionization Detector (PID) and Ion Mobility Spectrometry (IMS) technology for the diagnosis of bacterial infection. To embark on such work, a review of these technologies is required. This chapter discusses the theories, principle of operation, and the development of PID and IMS technologies that has been undertaken. It presents some commercially existing designs and their applications. It also discusses some of the merits and disadvantages of these technologies.

2.2 PID

2.2.1 Theory

Literature on current design and development of PIDs is scarce. There is tough competition amongst manufacturers, therefore major design components are carefully guarded secrets in the sensor industry. However, general information on its working principles have been released by some PID manufacturers and they will be covered in this section.

The PID is a sensor for detecting compounds using photoionization. A PID functions by ionising molecules using high-energy photons in the Ultraviolet (UV) range [1] and detecting the charge given off when these molecules become neutral. The timescale of this process is in the order of femtosenconds to milliseconds [2] resulting in the increased use of PIDs for instantaneous analysis. The operation of commercial PIDs can be divided into three steps:

- supply of gas phase analytes
- ionisation
- detection

In PID devices, ionisation is achieved using high-energy photons from an UV light source (Figure 2.1). The light source or bulb houses a discharge gas that releases energy when excited. This energy ionises Volatile Organic Compound (VOC) molecules which are later detected by anode and cathode electrodes.

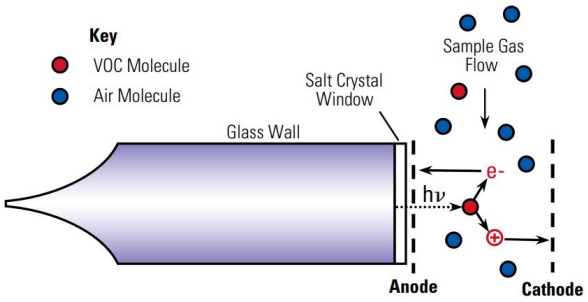

Figure 2.1: General schematic of a PID sensor [3].

Properties such as wavelength and ionisation energy of the bulb are affected by the nature of discharge gas selected, pressure within the bulb accelerating voltage, e.t.c [4]. Figure 2.2 shows the intensity and spectrum of light from bulbs with xenon, krypton and argon gas. When excited, a krypton bulb will emit 116.9 ηm and 123.9 ηm an equivalent of 10 eV and 10.6 eV [5].

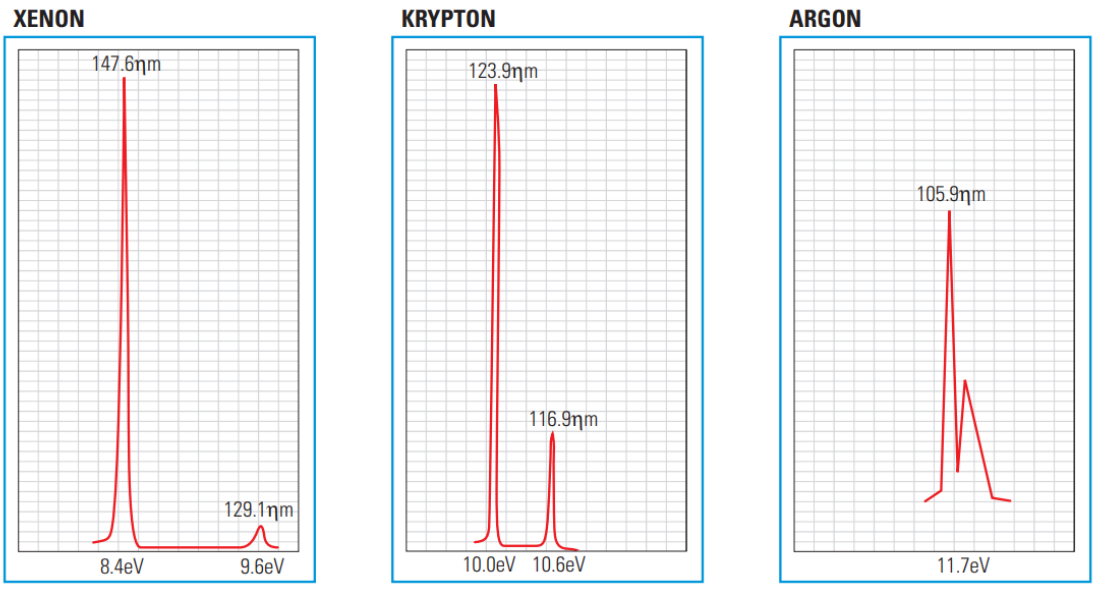

Figure 2.2: The wavelengths emitted by xenon, krypton and argon UV bulbs [5].

Common fill gasses used in photoionization bulbs and their ionisation energies

(IE) are shown in Table 2.1 [2].

Table 2.1: Ionisation energy of common UV lamps.

Fill gas	**Nominal eV**
Argon	11.7 - 11.8
Krypton	10.6
Hydrogen	10.2
Krypton	9.5
Oxygen	9.5
Xenon	8.44

The choice of bulb used in ionisation is essential to the performance of a PID device. The PID is only able to ionise molecules with ionisation energies below the ionisation energy of the UV bulb used. A comparison of fill gas and ionisation energies of compounds is shown in Table 2.2. From Table 2.2, a PID device with a Krypton UV bulb will not be suitable for detection of choloroform. Hence ionisation bulbs are selected to match the gas application.

Table 2.2: Ionisation energy of common VOCs and UV lamps.

UV Lamp	**Compound**	**IE (eV)**
	Oxygen	12.07
	Acetonitrile	12.20
	Nitrogen	15.58
	Water	12.62
Argon: 11.7	Acetic acid	10.65
	Methanol	10.84
	Chloroform	11.47
Krypton: 10.6	Isopropanol	10.17
	Ammonia	10.07
	Hexane	10.13
	Heptane	9.93
	Acetone	9.7
	Toluene	8.83
	Propanol	10.02
	Ethanol	10.48
	Isobutylene	9.22
	2-Pentanone	9.381
	2-Hexanone	9.35
Xenon: 8.4	Benzyl radical	7.2
	Acridine	7.8
	Anisole	8.2
	Napththalene	8.14

In photoionisation, molecules are ionised by absorbing the energy released from a photodischarge source. The ionisation reaction mechanism leading to the formation of photoions is given by Equation 2.1 [6].

$$hv + M \rightarrow M^{+} + e^{-} \tag{2.1}$$

Photons (hv) from the photodischarge source are absorbed by a molecule of the analyte (M). When hv is greater than the ionisation energy (IE) of the molecule, an electron is released leading to the formation of a cation.

In the detection step, an electric field is supplied to drive the cations to an electrode. The resulting current is measured and it is an indication of the quantity of M^+ present, hence, providing information on the concentration of the analytes. Inherent in this process are two advantages of PIDs. One advantage is that some level of selectivity can be achieved due to the difference in hv and IE of the analytes. Depending on the choice of UV lamp used for ionisation, detection could be targeted at compounds below the ionisation potential of the UV lamp. However, the system will still detect all molecules below the ionisation potential and so specificity is limited. This advantage enables analysis in air since the components of air have higher IE than most UV lamps. A second advantage in using PID sensors is their ability to function in ambient pressure requiring less auxiliary equipment to operate. This facilitates portability of PID sensors and makes them suitable for testing in a range of environments and has resulted in their increased use for *in situ* analysis. While these advantages are desirable, application of PIDs sensors in analysis requiring compositional information is limited because PIDs sensors only provides a concentration value of the sample being tested.

2.2.2 Commercial PID devices

PID is a compact high-performance device with response time in the order of seconds [7] and sensitivity down to 0.5 parts per billion (ppb). Some commercially available PID sensors are listed in Table 2.3.

Table 2.3: Selected commercial PID devices

Distributor	**Product**	**Range (ppm)**
AdvancedSense DirectSens IAQ	Graywolf	LOD < 5ppm [8]
Alphasense	PID-AH2	0.001 - 50 [9]
Alphasense	PID-A12	0.050 - 6000 [10]
Dräger	Multi-PID 2	0 - 20000 [11]
Dräger	PID HC	N/A [12]
HNU	Portable Analysers	0 - 3000 [13]
Ion Science	MiniPID 2	0 - 6000 [14]
Ion Science	Club	0.001 - 5000 [15]
Ion Science	Tiger	0 - 20000 [16]
Mocon	piD-TECH	0.00005 - 10000 [17]
RAE Systems	MiniRAE 3000	0 - 15000 [18]
RAE Systems	ppbRAE 3000	0.001 - 10000 [19]

Commercial PIDs sensors could be placed in two manufacturing categories, namely Original Equipment Manufacturer (OEM) and consumer devices.

OEM PID devices

This category of PID devices are designed to be integrated as components in another analytical equipment. Most commercial designs are similar to the OEM PID sensor from Mocon one shown in Figure 2.3. This compact design houses the detection circuit, electrodes and UV ionisation source in a 20 $\times$ 17 mm package.

Figure 2.3: An OEM piD-TECH PID sensor by Mocon Inc.

The electronics are manufactured on a flexible PCB that wraps around the bulb. An insulating material is used to shield the circuit from external Electromagnetic Interference (EMI) or Radio Frequency Interference (RFI). This is represented in the section view in Figure 2.4. Molecules to be analysed travels through the filter into the chamber. This filter protects the sensor from particles and dirt and allowing only gas samples to go through. The molecules are ionised in the chamber by the photons entering the chamber form the UV bulb below. Electrodes are used to partition the chamber area and create and electric field. Current generated at the electrodes is measured and processed by electronics housed on a flexible PCB. A voltage signal corresponding to the gas concentration is produced from one of the signal connectors at the bottom of the sensor.

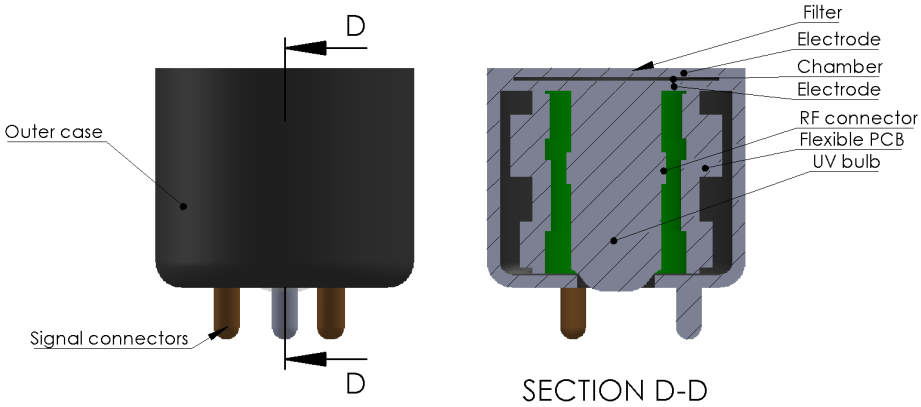

Figure 2.4: An OEM piD-TECH PID sensor by Mocon Inc.

There are usually 3 connector pins at the bottom sensor. They are used for power supply, return and concentration signal. OEM PID sensors available currently sold by several manufacturers including Mocon, Alphasense, Ion Science. They cost approximately $500.

Consumer PID

These PID devices are designed to be used without the need for support equipments like power supplies. This category of PID devices usually add several peripherals such as screens, pumps and batteries to the PID sensor. These peripherals enhance the performance of the sensor. For example, the addition of a pump improves sample flow through the device increasing the sample size and concentration output.

Figure 2.5 shows an example of a PID device targetted at the end user. It includes a pump and a battery with up to 24 hours run time. It also includes a USB port to for easy download of measurement data. The Tiger VOC detector is enclosed in a portable package 340 $\times$ 90 $\times$ 60 mm package. It only weights 0.72

kg making it suitable for hand held *in situ* applications [20]. Some end user PID devices are available from HNU, Ion Science and RAE Systems.

Figure 2.5: The Tiger VOC Detector by Ion Science [21].

2.2.3 PID applications

PID sensors were previously used mainly for the detection of effluents from Gas Chromatograpy (GC) columns [22]. In one of the early designs, Driscoll (1977) in collaboration with HNU reported mounting a PID sensor on the end of a GC [23]. Driscoll design also incorporated a Flame Ionisation Detector (FID) for comparison and several compounds including toulene, benzene, acetone, ethlene and ethonol were analysed. It was observed that the 10.2 eV PID detector offered a 30 fold improvement in sensitivity. Driscoll recommended that the PID should be considered a sensitive detector "in it's own right". In the 1980's, the PID continued to be used as a detector for GC systems. Freedman reported using the PID sensor designed by Driscoll in the analysis of hydrocarbons from oil vapour in carbon dioxide. Freedman

reported responses for concentrations as low as 2 ppb.

With improvement in design technology, PID sensors became more compact in size and portable handheld designs became commercially available. The application of PID sensors began to shift from GC detectors to stand alone VOC detectors given the rapid analysis offered by PIDs [24]. This shift was also fuelled by the fact that Mass Spectrometry (MS) and IMS systems were becoming more available and performed better as detectors for GC effluents.

One of the early commercially available stand alone PID instrument was the EE 300-100 portable PID Solvent Detector by ELE Internation in Herfortshire, England. This design featured a 10.2 eV UV ionisation source. The instrument was used by Hobbs *et al.* in 1994 to analyse odours from pig and chicken wastes. Hobbs *et al.* reported responses for VOCs, NH_3 and H_2S.

Currently, stand alone PID sensors are used to detect VOC in various industries. Provectus Remediation LTD, an environmental remediation company reported using the Tiger PID to indicate VOC concentrations in contaminated ground during their environmental investigations, trials and treatment. They have also applied the instrument in the area of safety, using it to check occupational exposure on very contaminated sites [25]. Also in the area of safety and personnel protection, Southampton's National Oceanography Centre (NOC) reported using two Cub PID devices from Ion Science to reduce employees' risk of exposure to chemicals. The PIDs used provides quick response to the presence of hazardous VOCs.[26].

2.3 Ion Mobility Spectrometry (IMS)

2.3.1 Theory

IMS is a term used to refer to methods, instrumentation and principles for characterising substances through a stream of supporting gas in an electric field [6]. This includes flow, gas compositions, pressure, modes and strength of electric fields and methods of ion formation. Over the years, several types of IMS technologies have been developed. For traditional IMS, swarm of ions are injected into a pathway called the drift tube, and the time taken to travel accross the tube is measured. The velocity of drift v_d is obtained from the time t_d taken to transverse the tube with a distance d cm (Equation 2.2).

$$v_d = \frac{d}{t_d} \tag{2.2}$$

The length of the drift tube has varied over the years and tubes down to 4 cm have been designed. The environment in the drift tube is ambient pressure with an electric field E which is given by Equation 2.3.

$$E = \frac{V}{d} \tag{2.3}$$

The drift velocity v_d in 2.2 is normalised to the electric field E to produce the mobility coefficient K (Equation 2.4). The value of k and hence the drift velocities are different for different ion species [27].

$$K = \frac{v_d}{E} \tag{2.4}$$

The drift velocity is affected by temperature T and pressure p inside the drift tube, hence the mobility coefficient is usually normalised to 273 K and 760 torr. This produces the reduced mobility coefficient K_0:

$$K_0 = K * \left(\frac{273}{T}\right)\left(\frac{P}{760}\right) \tag{2.5}$$

Operation of an IMS system, begins with the formation of ions from molecules in a sample by the reaction between the molecules and already existing charge (Figure 2.6(a)). This charges are referred to as reagent or reactant ions. The reaction between the reactant ions and sample ions produces product ions which are injected down the drift region (Figure 2.6(b)) through the ion gate. The product ions travel through the drift region up to the end of the drift tube where they come in a contact with the detector, which is usually a Faraday plate. On collision with the Faraday plate, ions lose their charge and become neutral inducing a current flow at the plate. This current is measured and plotted against time to give the mobility spectrum (Figure 2.6(c)). A stream of gas referred to as buffer gas or drift gas constantly flows through the drift tube in opposite direction to the ion stream. This gas helps to maintain a constant purified atmosphere for collisions within the drift tube.

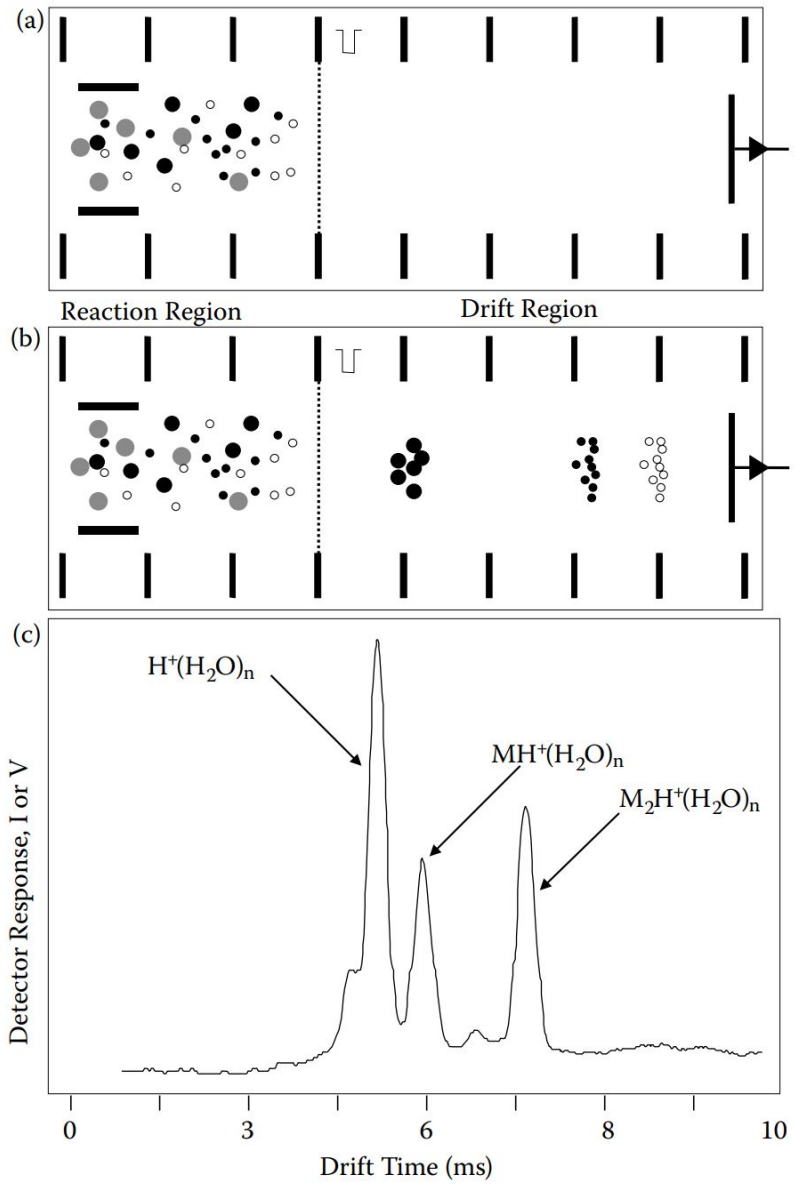

Figure 2.6: Illustration of IMS showing (a) ion formation (b) ion drift and (c) ion mobility spectrum [6].

Over the years, various IMS designs have been developed including Drift Time Ion Mobility Spectrometer (DTIMS), Traveling Wave Drift Tubes (TWDT), Trapped Ion Mobility Spectrometer (TIMS), Aspirator Drift Tube (ADT) and Field Asymmetric Ion Mobility Spectrometry (FAIMS). Before discussing these technologies,

the next section covers some ionisation techniques that have been implemented across the various IMS technologies.

2.3.2 IMS ionisation techniques

Ion formation is a major component of IMS systems. Ionisation in IMSs usually occurs at ambient pressure. The commonly deployed ionisation methods for IMS instruments are radioactive, corona discharge, and photoionisation and an overview of these is given in this section.

Radioactive ionisation

Radioactive sources are preferred in IMSs because they provide reliable stable operation without the need for external power supply and have been used in many IMS instruments [28–33]. ^{63}Ni is the preferred source for radioactive ionisation in IMSs[29]. In use, a thin layer of 10 mCi ^{63}Ni is coated onto a metal strip [34]. The ionisation process begins with the emission of high energy beta particles from the radioactive source. This process is shown in Equation 2.6.

$$^{63}_{28}\mathrm{Ni} \longrightarrow \beta^- + ^{63}_{29}\mathrm{Cu} \tag{2.6}$$

The beta particles collide with nitrogen in the atmosphere in air to produce $N_2{}^+$ as shown in Equation 2.7.

$$\mathrm{N_2} + \beta^- \longrightarrow \mathrm{N_2}^+ + \beta' + \mathrm{e}^- \tag{2.7}$$

Positive ions are formed after this reaction is followed by further reactions leading

to the ionisation of samples [34, 35]. In a purified air, the reaction process terminates in the formation of $H^+(H_2O)_n$ proton clusters as shown in Equation 2.8 - 2.13.

$$N_2 + e^- \longrightarrow {N_2}^+ + 2\,e^- \tag{2.8}$$

$${N_2}^+ + {N_2}^+ \longrightarrow {N_4}^+ + N_2 \tag{2.9}$$

$${N_4}^+ + H_2O \longrightarrow 2\,N_2 + {H_2O}^+ \tag{2.10}$$

$${H_2O}^+ + H_2O \longrightarrow H^+H_3O + OH \tag{2.11}$$

$${H_3O}^+ + H_2O + N_2 \longrightarrow H^+(H_2O)_2 + N_2 \tag{2.12}$$

$$H^+(H_2O)_2 + H_2O + N_2 \longrightarrow H^+(H_2O)_3 + N_2 \tag{2.13}$$

The $H^+(H_2O)_n$ reactant ions react with neutral sample molecules M, yielding a product ion and a protonated monomer:

$$H^+(H_2O)_n + M \longleftrightarrow MH^+(H_2O^*)_n \longleftrightarrow MH^+(H_2O)_{n-x} + xH_2O \tag{2.14}$$

Negative polarity product ions are also formed. This is as a result of the association of the sample molecule M and negative reactant ion $O_2^-(H_2O)_n$:

$$O_2^-(H_2O)_n + M \longleftrightarrow MO{-}_2(H_2O^*)_n \longleftrightarrow MO_2^-(H_2O)_{n-x} + xH_2O \tag{2.15}$$

Other radioactive isotopes have also been used as ionisation sources in IMS instruments including ^{241}Am [36], similar to those in household smoke detectors and beta-emitting tritium sources [37, 38].

Corona Discharge (CD) ionisation

CD has been utilised as ion source for IMS systems with some works reporting a 10^6 times increase in the number of electrons produced when compared with ^{63}Ni[39–41]. In CD ionisation IMS (Corona Discharge Ion Mobility Spectrometry (CD-IMS)), a sharp needle or thin wire is placed close to metal plate and a potential difference of 1 - 3 kV is applied between the needle and the plate. Electric discharges develop in the gap between the needle tip and the plate and the ions formed in this gap are similar to those formed using a ^{63}Ni ionisation source.

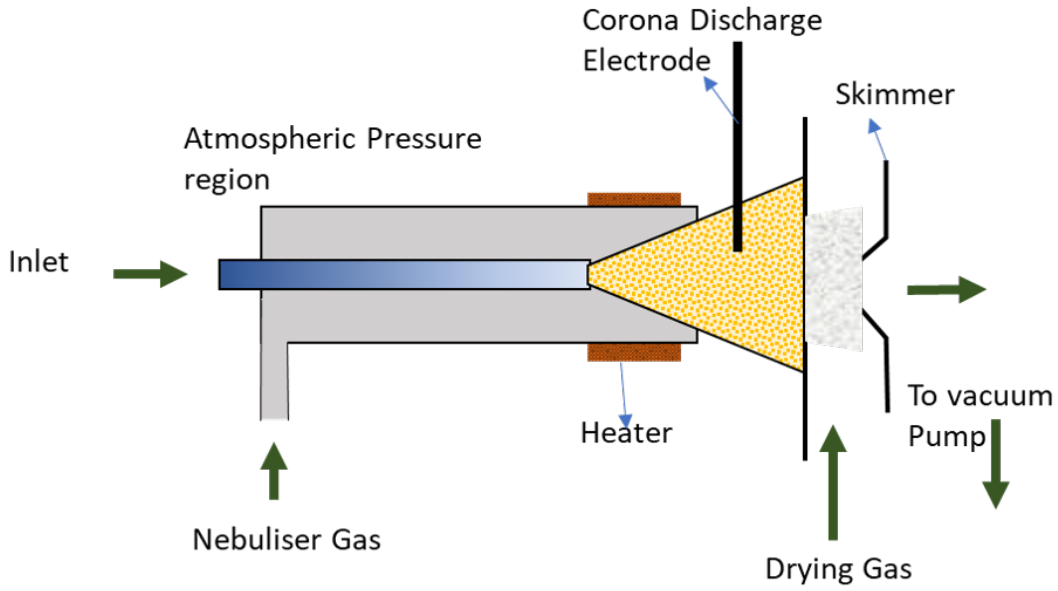

Figure 2.7: Corona discharge ionisation in IMS.

The gap is usually between 2 to 8 mm. As there is no radioactive source, CD ion sources have been deemed valuable. However, the need for an external power source is a major drawback in the implementation of CD ionisation.

Photoionisation

As discussed in Section 2.2, the photoionisation process involves ionising molecules using high energy photons released from a photodischarge source. The ionisation reaction mechanism leading to the formation of photoions is given by Equation 2.16 [6, 31].

$$hv + M \rightarrow M^+ + e^- \tag{2.16}$$

Photons (hv) from the photodischarge source are absorbed by a molecule of the analyte (M) leading to the formation of an excited molecule (M^*). When hv is greater than the ionisation energy (IE) of the molecule, the molecule releases an electron leading to the formation of a cation.

The cation travels to the detector where it loses the charge to become a neutral molecule. The current generated as a result is measured at the detector. Gesellschaft fur analytische Sensorsysteme (Dortmund, Germany) manufactures several IMS instruments using photoionisation [42].

2.3.3 IMS drift tubes designs

DTIMS

DTIMS is the one of the first IMS concepts developed. Here, ions travel in a drift tube through opposing neutral gas in the presence of an electric field [43]. Voltages from ±1 to 10 kV are required to generate electric fields [44] in DTIMS and this has been considered a drawback to implementing this technology. Ionised samples in a carrier gas are introduced into a drift tube with a uniform electric field. Stacked metal rings in a tubular geometry [6] are used generate the electric field in the drift

tube. The rings could also be separated by alternative insulating rings. Each ring in the stack is connected to a node in a series of resistors. This provides a gradient of electric field within the drift tube when a voltage is applied across the resistors.

A counter flow of neutral gas flows from the detection region towards the ionisation region preventing the build-up of impurities in the drift tube. The counter or drift gas flow also decelerates the ion swarm based on their size and shape resulting in a separation of ions based on these characteristics [45]. An electronic ion gate or shutter between the ionisation region and the drift tube is used to pulse ions into the drift tube and a predetermined interval. The gate is usually fabricated from thin parallel wires. An electric field at the gate is used to pass or block ions from entering the drift tube. The ions travel through the tube at a constant velocity which is proportional to the electric field and interaction with the neutral gas.

The drift tube terminates at the detector or Faraday plate. After colliding with the detector, ions in the stream lose their charge and current is generated due to the flow of electrons. The current is measured and plotted against the drift time for a packet of ion to obtain the DTIMS spectra. In some designs, optional guard ring is added between the metal rings and the detector to capacitively decouple the detector from the approaching ions.

Some DTIMS designs over the years have improved these basic concepts to enhance performance. For example Balm and Hill [46] showed that it was possible to improve the speed of response by using a unidirectional flow in the drift tube. Their DTIMS design comprised of a 7.5 cm drift tube operated at 140°C with an electric field gradient of 215 V/cm. The electric field gradient was obtained using a 3000 V supply applied to a repeller plate at the detector. The voltage was dropped across the tube using a series of 1 MΩ resistors which are connected to the rings. This

was also one of the first designs to feature a microprocessor [6]. An ^{63}Ni radioactive source was used but the design could be reconfigured to use a photoionisation source. In use, ions are generated when gaseous samples enters the vicinity of the ^{63}Ni radioactive source as already explained. The ions formed are stopped from entering the drift tube by a 900 V/cm field applied at the entrance gate (Figure 2.8). This electric field is removed for 0.2 ms thus opening the gate and allowing ions to travel down the drift tube. The ions migrate down the drift tube at different mobilities arriving at the exit gate at different times depending on their mobilities. If the exit gate is opened, the ions continue to the detector. If the exit gate is closed, detection does occurs. The opening and closing of entrance and exit gates are controlled at intervals to produce and ion mobility spectrum.

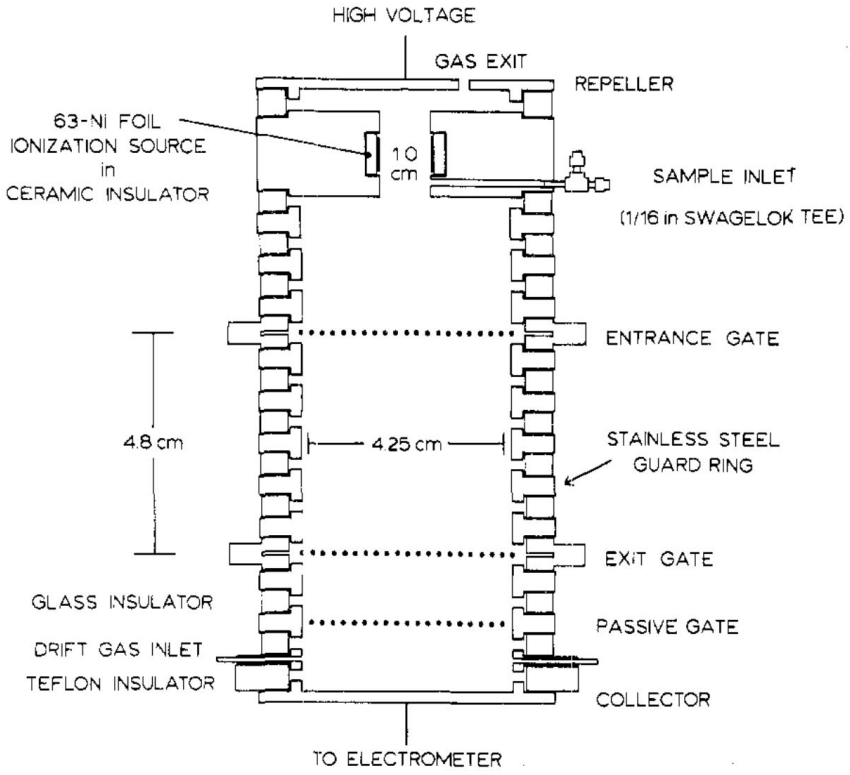

Figure 2.8: Illustration of unidirectional DTIMS by Balm and Hill [46].

In the late 1980s, Graseby Dynamics showed that the resolving power of DTIMS could be improved by increasing the length of the drift tube [6]. Their drift tube consisted of copper bands as drift rings and measured 50 cm in length with a diameter of 1 cm. The resolving power of the drift tube was over 150 in air at ambient pressure. In another work, Davis *et al* improved resolving power by increasing pressure and temperature within the drift tube [47]. A resolving power of 100 was achieved using 10.7 cm drift tube operated at 2.3 atm.

The IONSCAN 400B was one of the first bench top DTIMS commercial designs. It was targeted at explosive/narcotic analyses and had a resolving power of 20. The drift tube was 10 cm long and housed several rings referred to as focussing rings (Figure 2.9) [6, 48] . The gating grid served as an ion shutter, pulsing packets of ions into the drift tube. Clusters of ions with similar mobilities drift through the focusing ring until they arrive at the collector. The ions lose charge and generate a current at the collector. A plot of the drift time and measured current is used to produce the mobility spectrum.

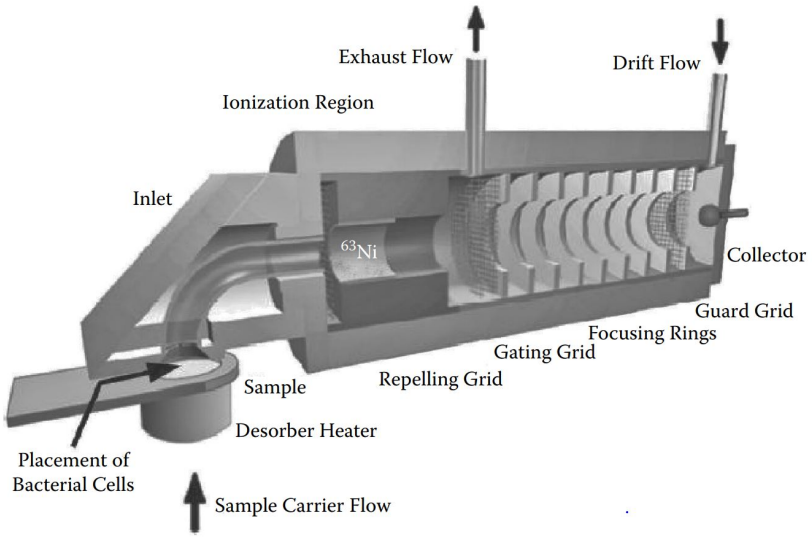

Figure 2.9: Cross section of inlet and drift tube from a Barringer IONSCAN 400B drift tube IMS [6].

Current commercial devices using DTIMS technology includes RAID-M 100 from Bruker [49], GC-IMS-ODOR from G.A.S. Gesellschaft für Analytische Sensorsysteme mbH [50], Quantum Sniffer QS-H150 from Implant Sciences [51],GDA-FR from Airsense Analytics [52], E5000 Series Trace Detectors from Scintrex [53].

TWDT

In TWDT, ions a propelled through a drift tube with a repeating series of symmetric waves which propagates through the tube [54]. Separation in the drift tube is achieved by altering the magnitude and speed of the waveform. TWDT does not require a counter drift gas however, ions entering the drift types are pulsed analogous to the DTIMS. This technology is employed in the Synapt G2-Si High Definition Mass Spectrometry from Waters [55]. The SYNAPT G2-Si High Definition Mass Spectrometry by Waters Corporation is a commercial TWDT IMS instrument cou-

pled with a MS [56, 57].

The rings in a TWDT drift tube are connected to opposite phase of a Radio Frequency (RF) field [54]. A voltage pulse is superimposed on one or a couple rings resulting in ion motion. The pulse is moved to the neighbouring ring(s) and is relaxed on the previous ring(s). This is propagated down the drift tube at a rate of 300 to 1300 m/s [6]. This process is repeated as stream of ions travel form through the drift tube. Separation of ion packets by their mobilities occur in drift tube due to the velocity and amplitude of the wave and gas pressure in the drift tube.

Trapped ion mobility spectrometer (TIMS)

In TIMS, ions are separated in a drift tube with increasing electric field. Ions travelling through the drift tube are trapped in a region where the electric field is compensated for by the gas drift force. The ions are separated based on their size-to-charge ratio and packets of ions are released to the detector by varying the electric field [58, 59]. Commercial instruments using this drift tube technology includes the Itemiser DX from Morpho [60] and Kaye Validator by GE Sensing (Billerica, MA) [61].

ADT

The ADT is one of the simplest concepts of IMS drift tubes. In this design, the ionised gas sample flows through a series of opposing plates with constant electric field (Figure 2.10). Ions are collected at the plates based on their mobility [62]. Smaller ions with high mobility are easily deflected on fall on the front set of plates. Larger ions with less mobility will be deflected less and are collected primarily by

end electrodes.

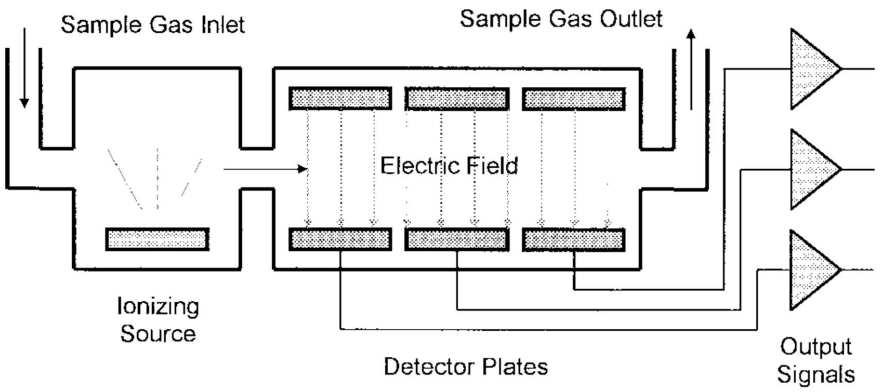

Figure 2.10: An ADT IMS drift tube [62].

A major advantage in the ADT designs is the simplicity of the drift tube and electronics required. This allows ADT to be implemented in handheld designs. However this simplicity is at the expense of resolving power. Zimmerman *et al* reported on the design of miniature IMS unit using an ADT [63]. In their design, a ^{65}Ni radioactive source was used for ionisation of gas samples and the test was carried out at room temperature. The electric field was swept from -94 V to 94 V in 30 steps and a resolving power of 5.5 was obtained.

The Chempro 100i by Environics OY is a handheld IMS instrument utilising an ADT.The battery powered unit in Figure 2.11 measures 230 $\times$ 101 $\times$ 57 mm in size and weighs approximately 880 g [64].

Figure 2.11: The Chempro 100i using aADT IMS drift tube [65].

Field Asymmetric Ion Mobility Spectrometry (FAIMS)

From Equation 2.4, the drift velocity v_d is normalised to the electric field E to produce the mobility coefficient K. At constant density N, the dependence of mobility coefficient K on the electric field can be simplified in Equation 2.17 [6, 27, 54] under strong field conditions.

$$K\left(\frac{E}{N}\right) = K_0\left(1 + \alpha\left(\frac{E}{N}\right)\right) \tag{2.17}$$

Therefore in FAIMS, mobility of the ions is not fixed but undergoes changes depending on the electric field. The dependence of the ion mobility K to the ratio of electric field strength E and the neural density N is accounted for by the function

α. In this approach, ions are transported through continuous conducting surfaces by a carrier gas. The conducting surface could be parallel plates [27] or concentric cylinders [66]. Various gap sizes between the conducting surfaces have been reported ranging from 27 μm to 2 mm [66, 67, 67, 68]. An asymmetric wave with an amplitude of 20000 V/cm or greater is applied to the plates or cylinders and the ions in the stream moves with the electric field using the relation ship in Equation 2.17. The waveform as seen in Figure 2.12 is designed such that the the integrals of the positive and negative regions are equal.

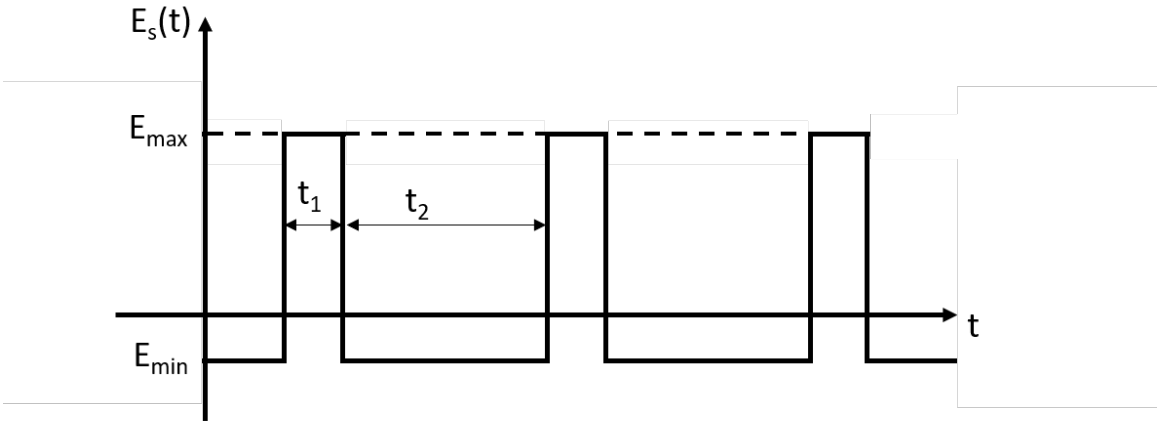

Figure 2.12: An ideal FAIMS waveform.

The positive and negative regions or the waveform induces a zigzag motion in the ions and only ions with mobility coefficients that are independent of the electric fields (where $\alpha = 0$) will pass through the drift tube.

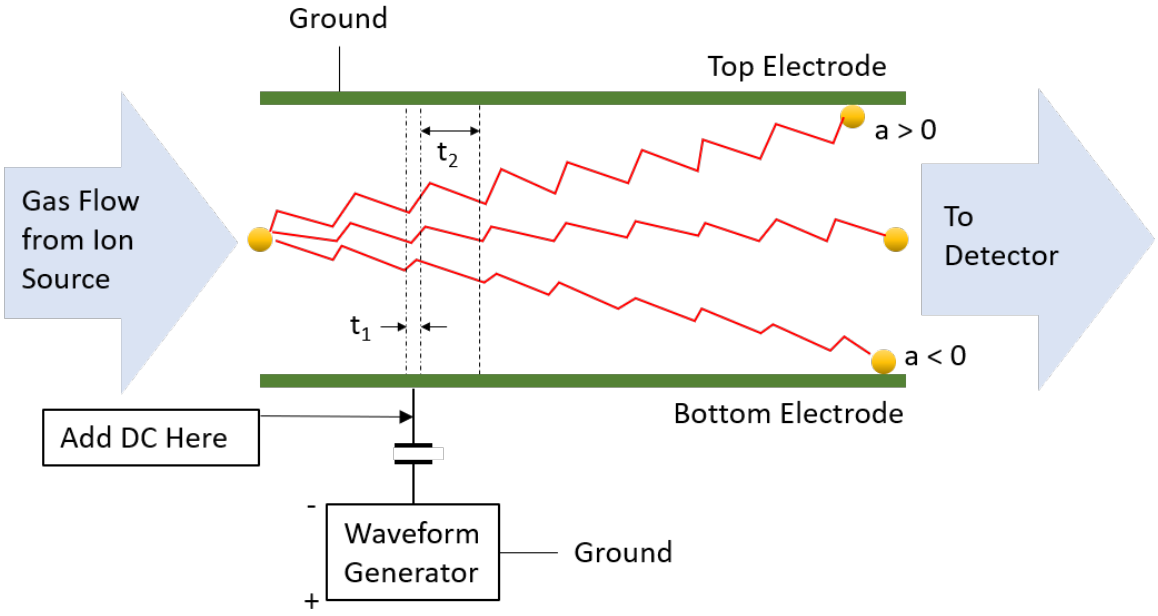

Figure 2.13: Effect of high asymmetric waveform on ions.

The asymmetric waveform results in filtering of ion species. Some ions are deflected in the drift tube and collide with the drift tube walls. These ions do not reach therefore are not detected by the detector. A small Direct Current (DC) referred to as the compensation voltage could be superimposed on the waveform to control the deflection of ions towards the side walls of the drift tube. As shown in Figure 2.14, ion species reaching the detector could be varied by varying the magnitude of the compensation voltage (U_C).

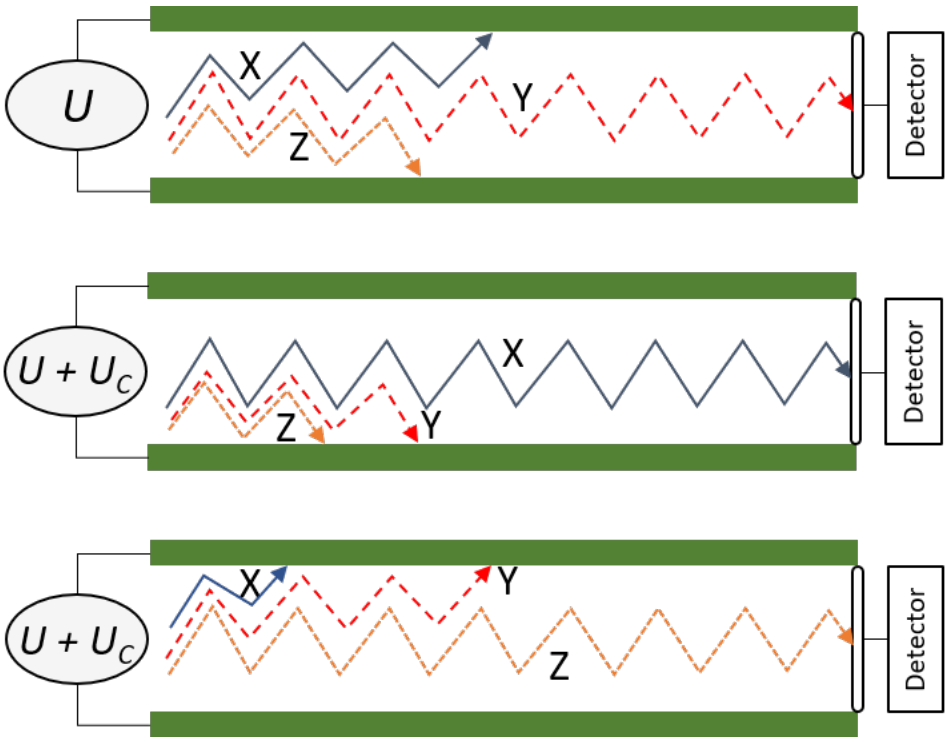

Figure 2.14: Effect of compensation voltage U_C on ion species.

A balance between the plate gap and the waveform properties is necessary to achieve deflection of ions. With smaller gaps measuring 35 μm asymmetric waveforms with 22.2 MHz have been used [67]. For larger gap sizes such as the 0.5 mm design by Miller *et al*, a 1700 V 2 MHz waveform with a duty cycle of 30% was used [69]. The effective gap between the electrodes g, which is the gap required for the ions to oscillate without colliding with the walls is given by:

$$g = d - \frac{SK}{2F}\langle|f|\rangle \tag{2.18}$$

Where d,S,K,F is the gap between the plates, amplitude of the waveform, ion mobility, and frequency [68]. $\langle|f|\rangle$ relates to the separation field waveform. Designing power supplies and generation circuits for the ideal waveform in Figure 2.12 is

hampered by engineering constraints. Hence, approximations of this waveform has been implemented in FAIMS drift tube designs[54] and these are shown in Figure 2.15. It includes the bisinusoidal and clipped sinusoid waveforms.

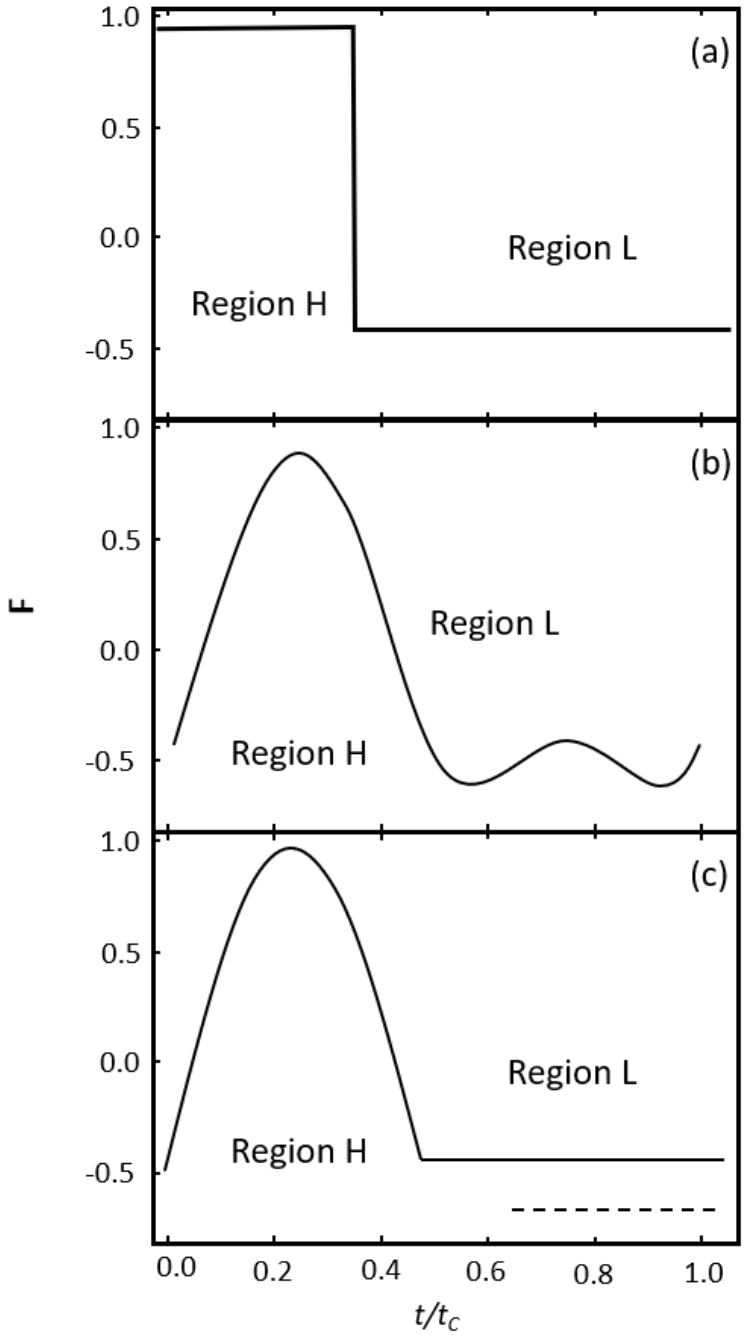

Figure 2.15: Waveforms used in FAIMS drift tube (a) ideal (b) bisinusoidal (c) clipped waveform.

The bisinusoidal [68] waveform is most used in FAIMS designed. This sinusoidal

waveform $F(t)$ is obtained by adding a sinusoid to its second overtone shifted by 90°:

$$F(t) = [f \sin \omega t + \sin(2\omega t - \pi/2)]/(f + 1) \tag{2.19}$$

The effect of the three waveforms on ion species are compared using the separation coefficients which are computed from Equation 2.20.

$$\langle f^n \rangle = \frac{1}{T} \int_0^T f^n(t) dt \tag{2.20}$$

Separation coefficients for rectangular or ideal, bisinusoidal and clipped waveforms are compared in Table 2.4. Best separation is obtained using the rectangular waveform, however, due to the difficulty in practical implementation of this waveform, the bisinusoidal waveform is commonly used in literature and commercial FAIMS devices.

Table 2.4: FAIMS waveform separation coefficients [68]

Waveform	f^2	f^3	f^4
Rectangular(ideal)	0.512	0.269	0.330
Bisinusoidal	0.310	0.110	0.120
Clipped	0.236	0.111	0.103

Two major advantages of FAIMS over ADT IMS drift tube designs are its high speed and an ion focusing effect that often improves sensitivity [70]. The ion focussing effect of FAIMS has led to increased used as a precursor to other analytical systems such as MS.

2.3.4 IMS applications

Over 5000 stand-alone IMS instruments are currently used throughout the world in the detection of chemical-warfare agents, drugs and explosives [71–75]. As result of the sensitivity, selectivity and rapid response times offered by IMS instruments, growing number of these instruments have also been applied in clinical analysis, pharmaceuticals, food and drink, environmental monitoring and process monitoring [29, 76, 77]. This section discusses literary works describing the application of IMS technology in three areas - food and drink, pharmaceuticals and clinical analysis.

Food and drink

Several reports have been published on analysis to determine the state of food and drink using IMS technology. IMS has also been applied in assessing the quality of a wide variety of food and drink [33, 78–82]. Alonso *et al* reported discriminating between meats from free range pigs fed in pasture and confined pigs by analysing VOC in fats using a photoionisation IMS [42]. Vestergaard *et al* investigated the quality of pork meat toppings on consumer pizza samples using a multi drift tube IMS instrument[83]. A a portable IMS produced by Gesellschaft für Analytische Sensorsysteme (G.A.S. mbH, Dortmund, Germany) with Tritium ionization source was used by Márquez-Sillero *et al* to investigate the presence of 2,4,6-Trichloroanisole which is one of the musty odours of wines [38].

Pharmaceuticals

The sensitivity and response speed of IMS systems makes them suitable for quality control and quality assurance tests in the pharmaceutical industry. IMS has been

applied in the rapid qualitative and quantitative of active ingredients in drugs for quality assurance tests [84]. Strege *et al* showed a TIMS instrument for cleaning verification of manufacturing equipments to avoid contamination between batches of pharmaceutical products [61]. In their quality assurance tests, Qin *et al* analysed 30 samples from pharmaceutical machinery in 2 hours offering a mode of quality assurance that reduces machine downtime [85].

Clinical analysis

IMS technology has also been applied to the diagnosis of diseases and metabolic profiling using human exhaled breath, urine, vaginal and blood samples [28, 30–32, 86, 87]. In diagnostic analysis, analytic results obtained from patients with a specific disease is compared to healthy control. Statistical methods were used to generate models for identifying disease groups from healthy control. Vera *et al* analysed VOCs in breath using an IMS with a ^{63}Ni radioactive source coupled to a Multi Capillary Column (MCC) [29]. The study had 40 subjects with 18 healthy controls and 22 pulmonary lung infection patients. Different spectra were obtained for patients and control groups. In a similar study, Baumbach analysed exhaled breath from 32 patients with lung cancer and 54 healthy control patients using an IMS instrument coupled with a MCC [88]. Using linear discriminant analysis, Baumbach's results showed separation between lung cancer groups and control patient groups (Figure 2.16).

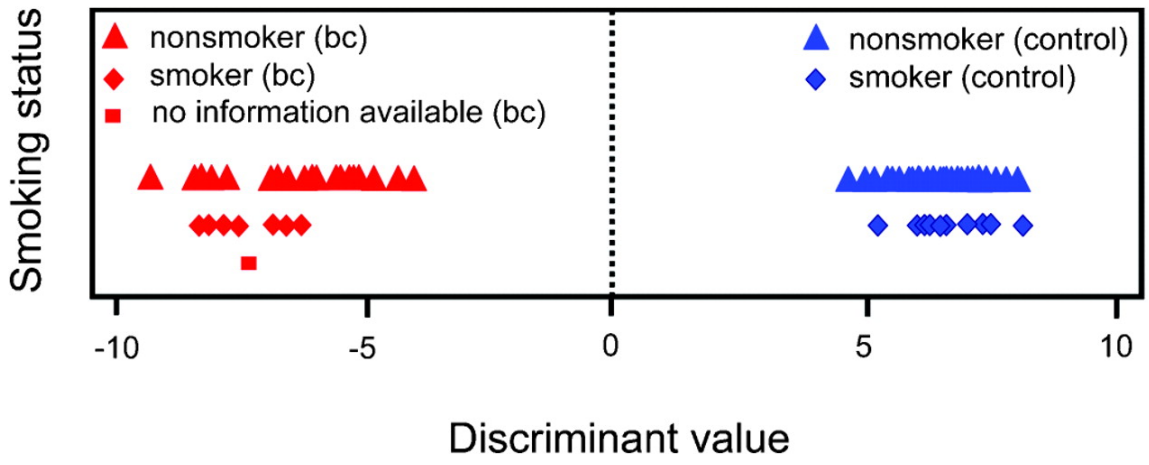

Figure 2.16: Linear discriminate analysis of IMS samples from lung cancer and control groups [88].

Some of the application of IMS technology in diagnosis are summarised in Table 2.5. The table shows the technologies, diseases and associated compounds that have been used in medical diagnosis

Table 2.5: IMS in diagnosis.

Technology	**Disease**	**Medium**	**Ref.**
IMS	Sarcoidosis	Breath	[86, 87, 89]
FAIMS	*Clostridium difficile*	Stool	[90]
IMS	Lung cancer	Breath	[30]
IMS	Fat metabolism related diseases	Urine	[31]
IMS	Bacterial vaginosis	Vaginal fluid	[32]
IMS	COPD	Breath	[91]
IMS	Lung carcinoma	Breath	[92]
IMS	Polychondritis	Breath	[93]
IMS	Alzheimer's\Parkinson's disease	Breath	[94]
IMS	Neutropenia	Breath	[95]
CD-IMS	Renal failure	Breath	[96]
FAIMS	Inflammatory Bowel Disease (IBD)	Urine	[97]
FAIMS	IBD	Breath	[90]

IMSs has been used in investigating drugs and drug metabolites in the human body using various biological mediums. This includes the detection of thiocyanate in the saliva of smokers [98], cocaine [99], Verapamil [48], and ephedrine [100] in urine.

2.4 References

[1] Laurent Spinelle, Michel Gerboles, Gertjan Kok, Stefan Persijn, and Tilman Sauerwald. Review of portable and low-cost sensors for the ambient air monitoring of benzene and other volatile organic compounds. *Sensors*, 17(7):1520, 2017.

[2] https://www.raesystems.com/sites/default/files/content/resources/pid_handbook_1002-02.pdf, November, 2018.

[3] https://www.raesystems.com/sites/default/files/content/resources/pid_handbook_1002-02.pdf, November, 2018.

[4] John GW Price, David C Fenimore, Peter G Simmonds, and Albert Zlatkis. Design and operation of a photoionization detector for gas chromatography. *Analytical Chemistry*, 40(3):541–547, 1968.

[5] http://www.intlsensor.com/pdf/photoionization.pdf, 2019.

[6] Gary Alan Eiceman, Zeev Karpas, and Herbert H Hill Jr. *Ion mobility spectrometry*. CRC press, 2013.

[7] FM Peng, PH Xie, YG Shi, JD Wang, WQ Liu, and HY Li. Photoionization detector for portable rapid gc. *Chromatographia*, 65(5-6):331–336, 2007.

[8] https://graywolfsensing.com/directsense-tvoc-volatile-organic-compound-meter/, November, 2018.

[9] http://www.alphasense.com/web1213/wp-content/uploads/2016/09/pid-ah2.pdf, November, 2018.

[10] http://www.alphasense.com/web1213/wp-content/uploads/2016/09/pid-a12.pdf, November,2018.

[11] https://www.draeger.com/en_aunz/applications/products/mobile-gas-detection/multi-gas-detection-devices/multi-pid-2, November , 2028.

[12] https://www.draeger.com/en_uk/applications/products/mobile-gas-detection/draegersensors/pid-sensors, November, 2018.

[13] http://www.hnu.com/pdf/portableanalyzertechnology_specs514.pdf, November, 2018.

[14] https://www.ionscience.com/product-range/pid-sensors/, November, 2018.

[15] http://www.geotechenv.com/pdf/air_quality/ion_science_cub.pdf, November, 2018.

[16] https://www.ionscience.com/wp-content/uploads/2016/07/tiger-voc-detector-brochure-v1.9.pdf, November, 2018.

[17] http://products.baseline-mocon.com/viewitems/oem-sensors-detectors/rs-detectors-pid-tech-evx-photoionization-detector, November 2018.

[18] https://www.raesystems.com/products/minirae-3000-wireless-handheld-voc-monitor, November, 2018.

[19] https://www.raesystems.com/products/ppbrae-3000, November, 2018.

[20] http://www.ereinc.com/uploads/pdf/tiger

[21] http://www.ereinc.com/uploads/pdf/tiger

[22] Di Li and Hajime Haneda. Photocatalysis of sprayed nitrogen-containing fe2o3–zno and wo3–zno composite powders in gas-phase acetaldehyde decomposition. *Journal of Photochemistry and Photobiology A: Chemistry*, 160(3):203–212, 2003.

[23] John N Driscoll. Evaluation of a new photoionization detector for organic compounds. *Journal of Chromatography A*, 134(1):49–55, 1977.

[24] Mozhgan Ahmadi, Claes Brage, Krister Sjöström, Klas Engvall, Harrie Knoef, and Bert Van de Beld. Development of an on-line tar measurement method based on photo ionization technique. *Catalysis today*, 176(1):250–252, 2011.

[25] https://www.ionscience.com/wp-content/uploads/2017/03/pr-76-provectus-chooses-ion-science-tiger-pid-for-humidity-resistant-and-anti-contamination-design-1-2.pdf, November, 2018.

[26] https://www.ionscience.com/wp-content/uploads/2016/11/pr-46-national-oceanography-centre-waves-goodbye-to-potential-exposure-to-volatile-organic-compounds-uni-lab.pdf, November,2108.

[27] IA Buryakov, EV Krylov, EG Nazarov, and U Kh Rasulev. A new method of separation of multi-atomic ions by mobility at atmospheric pressure using a high-frequency amplitude-asymmetric strong electric field. *International Journal of Mass Spectrometry and Ion Processes*, 128(3):143–148, 1993.

[28] M Westhoff, P Litterst, L Freitag, and Ji Baumnach. Ion mobility spectrometry in the diagnosis of sarcoidosis: Results of a feasibility study 1 lung hospital

hemer, hemer, germany; 2 isas-institute for analytical sciences, department of metabolomics, dortmund, germany.

[29] Vera Ruzsanyi, Jörg Ingo Baumbach, Stefanie Sielemann, P Litterst, M Westhoff, and Lutz Freitag. Detection of human metabolites using multi-capillary columns coupled to ion mobility spectrometers. *Journal of Chromatography A*, 1084(1-2):145–151, 2005.

[30] Michael Westhoff, Patric Litterst, Lutz Freitag, Wolfgang Urfer, Sabine Bader, and Joerg Ingo Baumbach. Ion mobility spectrometry for the detection of volatile organic compounds in exhaled breath of lung cancer patients. *Thorax*, 2009.

[31] R Garrido-Delgado, L Arce, CC Pérez-Marín, and M Valcárcel. Use of ion mobility spectroscopy with an ultraviolet ionization source as a vanguard screening system for the detection and determination of acetone in urine as a biomarker for cow and human diseases. *Talanta*, 78(3):863–868, 2009.

[32] Zeev Karpas, Walter Chaim, Rachel Gdalevsky, Boris Tilman, and Avi Lorber. Novel application for ion mobility spectrometry: diagnosing vaginal infections through measurement of biogenic amines. *Analytica Chimica Acta*, 474(1-2):115–123, 2002.

[33] Malick Camara, Nasser Gharbi, Emmanuelle Cocco, Cedric Guignard, Marc Behr, Daniele Evers, and Pierre Orlewski. Fast screening for presence of muddy/earthy odorants in wine and in wine must using a hyphenated gas chromatography-differential ion mobility spectrometry (gc/dms). *International Journal for Ion Mobility Spectrometry*, 14(1):39–47, 2011.

[34] Helko Borsdorf and Gary A Eiceman. Ion mobility spectrometry: principles and applications. *Applied Spectroscopy Reviews*, 41(4):323–375, 2006.

[35] GA Eiceman, EG Nazarov, JE Rodriguez, and JF Bergloff. Positive reactant ion chemistry for analytical, high temperature ion mobility spectrometry (ims): Effects of electric field of the drift tube and moisture, temperature, and flow of the drift gas. *Int J Ion Mobility Spectrom*, 1:28–37, 1998.

[36] Chi-Mun Yun, Yoshio Otani, and Hitoshi Emi. Development of unipolar ion generator—separation of ions in axial direction of flow. *Aerosol science and technology*, 26(5):389–397, 1997.

[37] JW Leonhardt. A new ppb-gas analyzer by means of gc-ion mobility spectrometry (gc-ims). *Journal of Radioanalytical and Nuclear Chemistry*, 257(1):133–139, 2003.

[38] Isabel Márquez-Sillero, Eva Aguilera-Herrador, Soledad Cárdenas, and Miguel Valcárcel. Determination of 2, 4, 6-tricholoroanisole in water and wine samples by ionic liquid-based single-drop microextraction and ion mobility spectrometry. *Analytica chimica acta*, 702(2):199–204, 2011.

[39] Mahmoud Tabrizchi and Azra Abedi. A novel electron source for negative ion mobility spectrometry. *International Journal of Mass Spectrometry*, 218(1):75–85, 2002.

[40] CA Hill and CLP Thomas. A pulsed corona discharge switchable high resolution ion mobility spectrometer-mass spectrometer. *Analyst*, 128(1):55–60, 2003.

[41] Mahmoud Tabrizchi and Vahideh ILbeigi. Detection of explosives by positive

corona discharge ion mobility spectrometry. *Journal of hazardous materials*, 176(1-3):692–696, 2010.

[42] Ruth Alonso, Vicente Rodríguez-Estévez, Ana Domínguez-Vidal, Maria José Ayora-Cañada, Lourdes Arce, and Miguel Valcárcel. Ion mobility spectrometry of volatile compounds from iberian pig fat for fast feeding regime authentication. *Talanta*, 76(3):591–596, 2008.

[43] Herbert H Hill Jr, William F Siems, and Robert H St. Louis. Ion mobility spectrometry. *Analytical Chemistry*, 62(23):1201A–1209A, 1990.

[44] Fang Li, Z Xie, H Schmidt, S Sielemann, and JI Baumbach. Ion mobility spectrometer for online monitoring of trace compounds. *Spectrochimica Acta Part B: Atomic Spectroscopy*, 57(10):1563–1574, 2002.

[45] Wolfgang Vautz, Jürgen Nolte, Rita Fobbe, and Jörg Ingo Baumbach. Breath analysis—performance and potential of ion mobility spectrometry. *Journal of breath research*, 3(3):036004, 2009.

[46] Michael A Baim and Herbert H Hill. Tunable selective detection for capillary gas chromatography by ion mobility monitoring. *Analytical Chemistry*, 54(1):38–43, 1982.

[47] Eric J Davis, Kristopher F Grows, William F Siems, and Herbert H Hill Jr. Improved ion mobility resolving power with increased buffer gas pressure. *Analytical chemistry*, 84(11):4858–4865, 2012.

[48] Yan Wang, Sabatino Nacson, and Janusz Pawliszyn. The coupling of solid-phase microextraction/surface enhanced laser desorption/ionization to ion mo-

bility spectrometry for drug analysis. *Analytica chimica acta*, 582(1):50–54, 2007.

[49] Raid-m 100, June 2018.

[50] Gc-ims-odor, June 2018.

[51] Quantum sniffer qs-h150, June 2018.

[52] Gda-fr, June 2018.

[53] E5000 series trace detectors, June 2018.

[54] Alexandre A Shvartsburg. *Differential ion mobility spectrometry: nonlinear ion transport and fundamentals of FAIMS*. CRC Press, 2008.

[55] Synapt g2-si high definition mass spectrometry, June 2018.

[56] http://www.waters.com/waters/en_us/synapt-g2-si-high-definition-mass-spectrometry/nav.htm?cid=134740622&locale=en_us/, November, 2018.

[57] Abby S Gelb, Rebecca E Jarratt, Yuting Huang, and Eric D Dodds. A study of calibrant selection in measurement of carbohydrate and peptide ion-neutral collision cross sections by traveling wave ion mobility spectrometry. *Analytical chemistry*, 86(22):11396–11402, 2014.

[58] Raquel Cumeras, Eduard Figueras, CE Davis, Jörg Ingo Baumbach, and Isabel Gracia. Review on ion mobility spectrometry. part 1: current instrumentation. *Analyst*, 140(5):1376–1390, 2015.

[59] Francisco Fernandez-Lima, Desmond A Kaplan, J Suetering, and Melvin A Park. Gas-phase separation using a trapped ion mobility spectrometer. *International Journal for Ion Mobility Spectrometry*, 14(2-3):93–98, 2011.

[60] Itemiser dx, June 2018.

[61] Mark A Strege, Jessica Kozerski, Nieves Juarbe, and Patrick Mahoney. At-line quantitative ion mobility spectrometry for direct analysis of swabs for pharmaceutical manufacturing equipment cleaning verification. *Analytical chemistry*, 80(8):3040–3044, 2008.

[62] Emilio Sacristán and Andro A Solis. A swept-field aspiration condenser as an ion-mobility spectrometer. *IEEE Transactions on Instrumentation and Measurement*, 47(3):769–775, 1998.

[63] Stefan Zimmermann, Sebastian Barth, Wolfgang KM Baether, and Joachim Ringer. Miniaturized low-cost ion mobility spectrometer for fast detection of chemical warfare agents. *Analytical chemistry*, 80(17):6671–6676, 2008.

[64] https://www.environics.fi/wp-content/uploads/2018/02/chempro100i_handheld_chemical_dete November, 2018.

[65] https://www.environics.fi/product/chempro100i/, November, 2018.

[66] Roger Guevremont and Randy W Purves. High field asymmetric waveform ion mobility spectrometry-mass spectrometry: an investigation of leucine enkephalin ions produced by electrospray ionization. *Journal of the American Society for Mass Spectrometry*, 10(6):492–501, 1999.

[67] Lauren J Brown, Danielle E Toutoungi, Neil A Devenport, James C Reynolds, G Kaur-Atwal, P Boyle, and Colin S Creaser. Miniaturized ultra high field asymmetric waveform ion mobility spectrometry combined with mass spectrometry for peptide analysis. *Analytical chemistry*, 82(23):9827–9834, 2010.

[68] EV Krylov, EG Nazarov, and RA Miller. Differential mobility spectrometer: Model of operation. *International Journal of Mass Spectrometry*, 266(1-3):76–85, 2007.

[69] Raanan A Miller, Erkinjon G Nazarov, Gary A Eiceman, and A Thomas King. A mems radio-frequency ion mobility spectrometer for chemical vapor detection. *Sensors and Actuators A: Physical*, 91(3):301–312, 2001.

[70] Alexandre A Shvartsburg, Keqi Tang, and Richard D Smith. Modeling the resolution and sensitivity of faims analyses. *Journal of the American Society for Mass Spectrometry*, 15(10):1487–1498, 2004.

[71] Abu B Kanu, Prabha Dwivedi, Maggie Tam, Laura Matz, and Herbert H Hill. Ion mobility–mass spectrometry. *Journal of mass spectrometry*, 43(1):1–22, 2008.

[72] Zeev Karpas. Ion mobility spectrometry: A tool in the war against terror,". *Bulletin of the Israel Chemical Society*, (24), 2009.

[73] Marko A Makinen, Osmo A Anttalainen, and Mika ET Sillanpaa. Ion mobility spectrometry and its applications in detection of chemical warfare agents, 2010.

[74] GA Eiceman, EV Krylov, NS Krylova, EG Nazarov, and RA Miller. Separation of ions from explosives in differential mobility spectrometry by vapor-modified drift gas. *Analytical chemistry*, 76(17):4937–4944, 2004.

[75] Jie ZHANG, LI Ling-Feng, GUO Da-Peng, Yuan ZHANG, WANG Qi, LI Peng, and WANG Xiao-Zhi. Determination of hazardous chemicals by

microchip-based field asymmetric ion mobility spectrometric technique. *Chinese Journal of Analytical Chemistry*, 41(7):986–992, 2013.

[76] Helko Borsdorf, Thomas Mayer, Mashaalah Zarejousheghani, and Gary A Eiceman. Recent developments in ion mobility spectrometry. *Applied spectroscopy reviews*, 46(6):472–521, 2011.

[77] Sergio Armenta, Manel Alcala, and Marcelo Blanco. A review of recent, unconventional applications of ion mobility spectrometry (ims). *Analytica chimica acta*, 703(2):114–123, 2011.

[78] Zeev Karpas, Boris Tilman, Rachel Gdalevsky, and Avraham Lorber. Determination of volatile biogenic amines in muscle food products by ion mobility spectrometry. *Analytica Chimica Acta*, 463(2):155–163, 2002.

[79] A Peter Snyder, Charles S Harden, Dennis M Davis, Donald B Shoff, and Waleed M Maswadeh. Hand-portable gas chromatography-ion mobility spectrometer for the determination of the freshness of fish. 1995.

[80] Olavi Raatikainen, Ville Reinikainen, Pentti Minkkinen, Tiina Ritvanen, Petri Muje, Juha Pursiainen, Teri Hiltunen, Paula Hyvönen, Atte von Wright, and Satu-Pia Reinikainen. Multivariate modelling of fish freshness index based on ion mobility spectrometry measurements. *Analytica Chimica Acta*, 544(1-2):128–134, 2005.

[81] M Ali Awan, I Fleet, and CL Paul Thomas. Optimising cell temperature and dispersion field strength for the screening for putrescine and cadaverine with thermal desorption-gas chromatography–differential mobility spectrometry. *analytica chimica acta*, 611(2):226–232, 2008.

[82] Wolfgang Vautz, Jörg Ingo Baumbach, and Johannes Jung. Beer fermentation control using ion mobility spectrometry—results of a pilot study. *Journal of the Institute of Brewing*, 112(2):157–164, 2006.

[83] Jannie S Vestergaard, Magni Martens, and Pekka Turkki. Application of an electronic nose system for prediction of sensory quality changes of a meat product (pizza topping) during storage. *LWT-Food Science and Technology*, 40(6):1095–1101, 2007.

[84] Roberto Fernández-Maestre and Herbert H Hill. Ion mobility spectrometry for the rapid analysis of over-the-counter drugs and beverages. *International Journal for Ion Mobility Spectrometry*, 12(3):91–102, 2009.

[85] C Qin, A Granger, V Papov, J McCaffrey, and DL Norwood. Quantitative determination of residual active pharmaceutical ingredients and intermediates on equipment surfaces by ion mobility spectrometry. *Journal of pharmaceutical and biomedical analysis*, 51(1):107–113, 2010.

[86] A Bunkowski, B Bödeker, S Bader, M Westhoff, P Litterst, and JI Baumbach. Signals in human breath related to sarcoidosis.—results of a feasibility study using mcc/ims. *International Journal for Ion Mobility Spectrometry*, 12(2):73–79, 2009.

[87] Alexander Bunkowski, Bertram Bödeker, Stefan Bader, Michael Westhoff, Patric Litterst, and Jörg Ingo Baumbach. Mcc/ims signals in human breath related to sarcoidosis—results of a feasibility study using an automated peak finding procedure. *Journal of breath research*, 3(4):046001, 2009.

[88] Jörg Ingo Baumbach. Ion mobility spectrometry coupled with multi-capillary

columns for metabolic profiling of human breath. *Journal of breath research*, 3(3):034001, 2009.

[89] Alexander Bunkowski, Bertram Bödeker, Stefan Bader, Michael Westhoff, Patric Litterst, and Jörg Ingo Baumbach. Mcc/ims signals in human breath related to sarcoidosis—results of a feasibility study using an automated peak finding procedure. *Journal of breath research*, 3(4):046001, 2009.

[90] JA Covington, MP van der Schee, ASL Edge, B Boyle, RS Savage, and RP Arasaradnam. The application of faims gas analysis in medical diagnostics. *Analyst*, 140(20):6775–6781, 2015.

[91] Jorge Pereira, Priscilla Porto-Figueira, Carina Cavaco, Khushman Taunk, Srikanth Rapole, Rahul Dhakne, Hampapathalu Nagarajaram, and José Câmara. Breath analysis as a potential and non-invasive frontier in disease diagnosis: an overview. *Metabolites*, 5(1):3–55, 2015.

[92] JI Baumbach, S Maddula, U Sommerwerck, V Besa, I Kurth, B Bödeker, H Teschler, L Freitag, and K Darwiche. Significant different volatile biomarker during bronchoscopic ion mobility spectrometry investigation of patients suffering lung carcinoma. *International Journal for Ion Mobility Spectrometry*, 14(4):159–166, 2011.

[93] Ayano Usuba, Hiroshi Handa, Teppei Inoue, Shinya Azagami, Yoshihisa Yamano, Masamichi Mineshita, Teruomi Miyazawa, and Jörg Ingo Baumbach. Breath analysis for relapsing polychondritis assessed by ion mobility spectrometry. *International Journal for Ion Mobility Spectrometry*, 18(3-4):177–183, 2015.

[94] Jan-Philipp Bach, Maike Gold, David Mengel, Akira Hattesohl, Dirk Lubbe, Severin Schmid, Björn Tackenberg, Jürgen Rieke, Sasidhar Maddula, Jörg Ingo Baumbach, et al. Measuring compounds in exhaled air to detect alzheimer's disease and parkinson's disease. *PLoS One*, 10(7):e0132227, 2015.

[95] Rhoikos Furtwängler, A-C Hauschild, Julia Hübel, Hande Rakicioglou, Bertram Bödeker, Sasidhar Maddula, Arne Simon, and Jörg Ingo Baumbach. Signals of neutropenia in human breath? *International Journal for Ion Mobility Spectrometry*, 17(1):19–23, 2014.

[96] Elham Jazan and Hadi Mirzaei. Direct analysis of human breath ammonia using corona discharge ion mobility spectrometry. *Journal of pharmaceutical and biomedical analysis*, 88:315–320, 2014.

[97] Ramesh P Arasaradnam, Nathalie Ouaret, Matthew G Thomas, Nabil Quraishi, Evelyn Heatherington, Chuka U Nwokolo, Karna D Bardhan, and James A Covington. A novel tool for noninvasive diagnosis and tracking of patients with inflammatory bowel disease. *Inflammatory bowel diseases*, 19(5):999–1003, 2013.

[98] MT Jafari and M Javaheri. Selective method based on negative electrospray ionization ion mobility spectrometry for direct analysis of salivary thiocyanate. *Analytical chemistry*, 82(15):6721–6725, 2010.

[99] Yao Lu, Ryan M O'Donnell, and Peter B Harrington. Detection of cocaine and its metabolites in urine using solid phase extraction-ion mobility spectrometry with alternating least squares. *Forensic science international*, 189(1-3):54–59, 2009.

[100] John K Lokhnauth and Nicholas H Snow. Solid phase micro-extraction coupled with ion mobility spectrometry for the analysis of ephedrine in urine. *Journal of separation science*, 28(7):612–618, 2005.

Chapter 3

Development of a Gas Sensor Calibration Rig

3.1 Introduction

Currently gas sensors and gas based analytic instruments implement several techniques to both identify and quantify compounds. The difference in design approach from several manufacturers results in different sensitivity and selectivity of gas sensor products [1]. Manufacturers therefore, test their sensors in controlled environments to calibrate the sensors. There are other advantages to be gained from rigorously undertaking sensor calibration tests. For example, these tests ensure a predictable response to test samples under defined test conditions. This information is paramount to the end used as it helps them to ascertain the capabilities and limitations of the sensor devices and ensure they are operated within an optimum window. Additionally, the response of any gas sensing system is affected by several factors including the composition, humidity, temperature and pressure of the test gas. These factors

are often varied during sensor calibration tests and the behaviour of the sensor to changes in these parameters is recorded. For instances where results of these tests are not satisfactory when compared with the manufacturer's design goals, the results could inform further developments necessary to improve the sensor. Analysis of these results could also infer adjustments needed in one parameter, for example flow rate, to improve overall sensor performance. A gas calibration rig is required to carry out these tests and to this end, such a unit has been manufactured in-house. This chapter presents the design and manufacture of the gas calibration test rig.

The goal of calibration tests is to define the capabilities and limitations of the sensor in a given environment and for a particular test gas. To achieve this goal the calibration rig is expected to produce a repeatable test environment for these tests. The test rig needs to provide gas mixtures at defined flow rates, pressure, temperature and humidity. The unit was divided into four distinct sections namely: the Gas Mixer, Dilutor, Permeation Source, Humidity Generator, Gas Analyser. The design of these components are discussed in Section 3.2 - 3.6. Section 3.6.2 and 3.7 highlights the integration and control of the devices as a single unit.

3.2 The Gas Mixer

Calibration tests require compounds in many concentrations and compositions. Gasses for laboratory use are usually purchased in gas bottles with a single compound or a mixture of compounds at known concentrations. However, it is expensive to acquire gas bottles for every concentration and mixture required. The solution to this challenge is Gas Mixer device that takes several gas inputs and provides a gas output at the required concentration and composition. During operation, the user

inserts gasses with known concentration into the input. Using a software designed in-house, the user can regulate the flow rates of the input gasses to obtain an output with desired composition from the input gasses.

3.2.1 Mechanical design

The Gas Mixer system was designed to provide a single airflow from two input gas/vapour streams in a consistent and safe manner. The major mechanical components used in this design and its layout are illustrated in Figure 3.1.

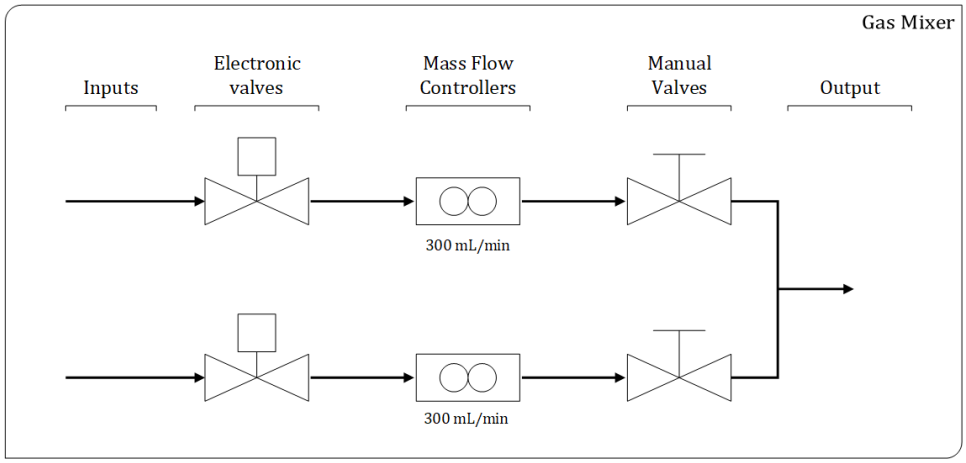

Figure 3.1: Schematic of the Gas Mixer pneumatic system

Mass flow controllers

Flow through the system was controlled using electronic flow meters to ensure precise flow rates that were repeatable. Two UFC-1100A MFC manufacture by Unit Instruments Inc., USA were used to control flow rates through the system. Both UFC-1100A MFCs were rated for a maximum pressure of 500 psi at 300 ml/min. The inlets and outlets were fitted with 1/8 inch Swagelok compression fittings which allows a leak proof integration with other components upstream and downstream.

The Mass Flow Controller (MFC) is powered by providing ± 15 V to its input pins. The user inputs a signal between 0 - 5 V to specify a required flow rate, which is linearly related to applied voltage. The input voltage 0 and 5 V corresponds to no-flow and maximum flow respectively. A 0 - 5 V signal voltage output from the MFC gives the user and indication of the current flow rate over the MFC flow rate range.

Electronic valves

Electronic valves were added to the flow path to ensure safety and avoid leakage. Several ETO-2-12 in-line electronic valves from Clippard, USA were used. These valves offer fast response times taking between 5 to 10 milliseconds to switch states. The valves operate on a 12 V supply. These are normally closed valves therefore a voltage signal must be supplied to open the valves. The valve supply lines are threaded with a 10 - 32 UNF thread therefore a Swagelok adapter was fitted to adapt this thread to a 1/8 inch Swagelok compression fitting ensuring consistency across the system. This also avoids leak throughout the system. An additional manual Swagelok 2-way valve was placed in-line with the output to allow a safe manual override of the system's output.

3.2.2 Electronics design

Several voltage levels are required to power the components in the Gas Mixer consequently a power supply and distribution circuit board was designed. Additionally, a communication interface circuit board was manufactured and this is discussed below.

Electronics power supply

The main power requirements for the Gas Mixer were - supply regulated ± 15 V(for both MFCs) and 12 V (for both electronic valves). An electronic circuit to provide these voltages was designed using Autodesk EAGLE electronic design application. Support for connecting to a National Instrument Data Acquisition board (NI-DAQ) board was also added. This provision allows easy integration of the power supply and communication circuits leading to a more compact design.

Communication interface

Precise flow control was achieved using a custom computer program via the NI-DAQ USB-6001 OEM Data Acquisition Board. This NI-DAQ board is a full-speed USB device that provides 8 single-ended analogue inputs which were used to measure the analogue flow rate signals from the MFCs. It also includes 2 analogue output channels and these were used to set the flow rate on both MFCs by providing voltage signals between 0 and 5. There are 13 digital input/output channels on the data acquisition board. Two of these digital channels were connected to the electronic valves to open or stop fluid flow.

3.2.3 System assembly

A physical model of the device was designed before construction to ensure there was enough physical space within the inside the 19-inch rackmount enclosure for all internal components. The model also informs appropriate placing of structural supports and fasteners for the internal components. SolidWorks (2016, France), a modelling computer-aided design application by Dassault Systèmes was used to

model the system assembly. Each of the major components in the unit were modelled and placed in the enclosure. Accurate models of structural supports were designed and the fasteners required to hold these in place were added. The CAD assembly is shown in Figure 3.2.

Figure 3.2: CAD modelling of Gas Mixer assembly

After modelling, the panels of the enclosure were machined for mounting components. On the front panel, a slot was added for a power switch which turns on the power supply to the device. An LCD display was also mounted at the top of the front plate. This display shows mixture states giving the user an indication of the flow rates of both MFCs. Two LEDs were also added to indicate when power is supplied or cut-off from the MFCs. To ensure safety during power down, two manual mechanical valves were installed in the front panel in-line with the outlet from the MFCs. The valves are connected to two 1/8 inch Swagelok buckheads mounted on the front panel and serving as outlet. A similar configuration of two 1/8 inch Swagelok is mounted on the back panel and this serves as gas inlet to the device. A socket is also mounted on the back plate for power supply connections. Internally,

the electronic circuits and the NI-DAQ were mounted on a support below the MFCs to save space. Both electronic valves were mounted on the inlet pipe. The system assembly is shown in Figure 3.3.

Figure 3.3: The assembled Gas Mixer Unit

3.3 The Dilutor

The Gas Mixer was sufficient for tests requiring flow rates below 300 ml/min and dilution of a single compound. It was also applicable for tests requiring mixture of a maximum of two compounds. However, some gas analytic techniques like IMS and the VOC sensor designed in this project sometimes require flow rates in excess of 1 L/min [2]. Additionally some sensor characterisation and chemical selectivity tests require mixtures of more than two compounds. For this reason, a high flow rate multi channel gas mixer was developed. The unit consists of a portable gas mixer developed in-house coupled with a Model 700 Mass Flow Calibrator T-API.

At high flow rates, gas bottles do not provide a cost effective solution since they are consumed quickly. An alternative to using gas bottles is to obtain VOC vapour from compounds in the liquid state and use the volatiles that evaporate from it. This process is tedious but offers a low-cost and flexible alternative to purchasing gas bottles. A method of obtaining VOC at known concentrations from liquids is discussed briefly in the next section before presenting the mechanical and electronic design of the Dilutor.

3.3.1 VOC vapour generator

As mentioned in the preceding section, a more cost effective alternative to purchasing analytes in gas bottles is obtaining vapours from liquids of pure substances. There are several formulae for evaluating the vapour pressure of a system at vapour-liquid equilibrium when the temperature is known[3]. Antoine's equation widely used to correlate vapour pressure, P_{vp} to temperature and is given in Equation 3.1 [4] where t is temperature in degree Celsius.

$$log_{10}P_{vp} = A - \frac{B}{t + C} \tag{3.1}$$

Constants A, B and C are tabulated for a number of substances. These tables can be found in [4–7]. The vapour pressure term P_{vp} obtained is with the units mmHg. In use, an aliquot of the liquid compound is poured into a bottle that is kept in a chiller bath to control the vapour temperature. In this project, a Neslab RTE-300 chiller bath was used as shown in Figure 3.4.

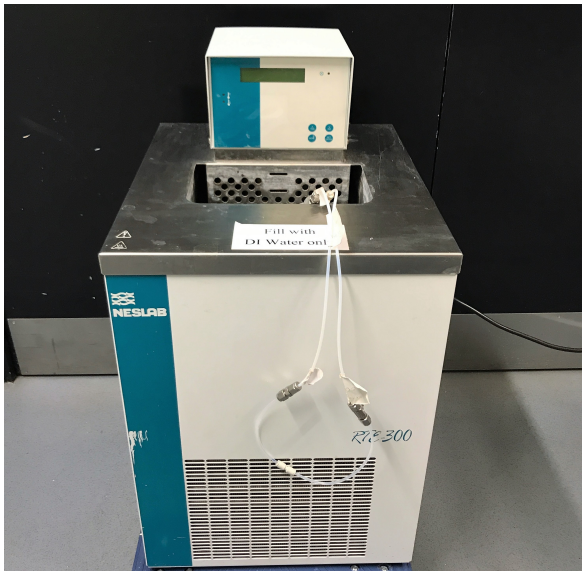

Figure 3.4: Neslab RTE-300 chiller bath and with bubblers

The bottles used have two bores on the cap serving as an inlet and outlet. The inlet is connected to a bubbler in the bottle and externally to a clean air source. The outlet from the bottle is connected to gas mixer where the bubbled VOC is mixed or diluted with other gasses. The concentration of vapour C_{vp} (ppm) is given by Equation 3.2 where P was previously measured as 760.0021 $mmHg$ and P_{vp} is the vapour pressure obtained from Equation 3.1.

$$C_{vp} = \frac{P_{vp}}{P} * 10^6 \tag{3.2}$$

The flow rate of carrier clean air through the bubbler F_{vp} is used to obtain a desired output concentration C (in ppm) of vapour and is obtained using Equation 3.3 where F_{total} is the sum of the flow rates of the vapour and the diluting gas through the mixer.

$$F_{vb} = \frac{C * F_{total}}{C_{vp}} \tag{3.3}$$

Using the setup and the equations described in the section above, vapours at known concentrations can be obtained. For most compounds, C_{vp} from Equation 3.2 are in excess of 1000 parts per million (ppm) hence a Dilutor is required to dilute the concentration to desired levels using Equation 3.3. The mechanical and electronic design of the Dilutor is shown in the following section.

3.3.2 Mechanical design

Here, a Dilutor was developed in-house and then coupled with a Model 700 Mass Flow Calibrator T-API. The schematic showing the gas flow paths for both units is shown in Figure 3.5.

Similar to the Gas Mixer, the Dilutor has two MFCs for precise flow rate control. Two UFC-1100A MFC manufacture by Unit Instruments Inc., USA were used. One of the UFC-1100A MFCs was rated for a maximum flow rate of 2000 mL/min and the other UFC-1100A MFC was rated for a maximum flow rate of 2000 mL/min. The larger flow ratio between the flow controllers increases the mixing ratio capacity of the system. Additionally, the portable gas mixer adds two mixing channels when used in combination with the Gas Mixer. Both MFCs were powered by providing ± 15 V to its supply pins. The user inputs a signal within 0 - 5 V to specify a required flow rate with 0 and 5 V corresponding to no-flow and maximum flow respectively. A 0 - 5 V signal output gives the user an indication of the current flow rate over through MFC. The inlets and outlets were fitted with 1/8 inch push-fit fitting. A schematic diagram of the portable gas mixer is shown in Figure 3.6.

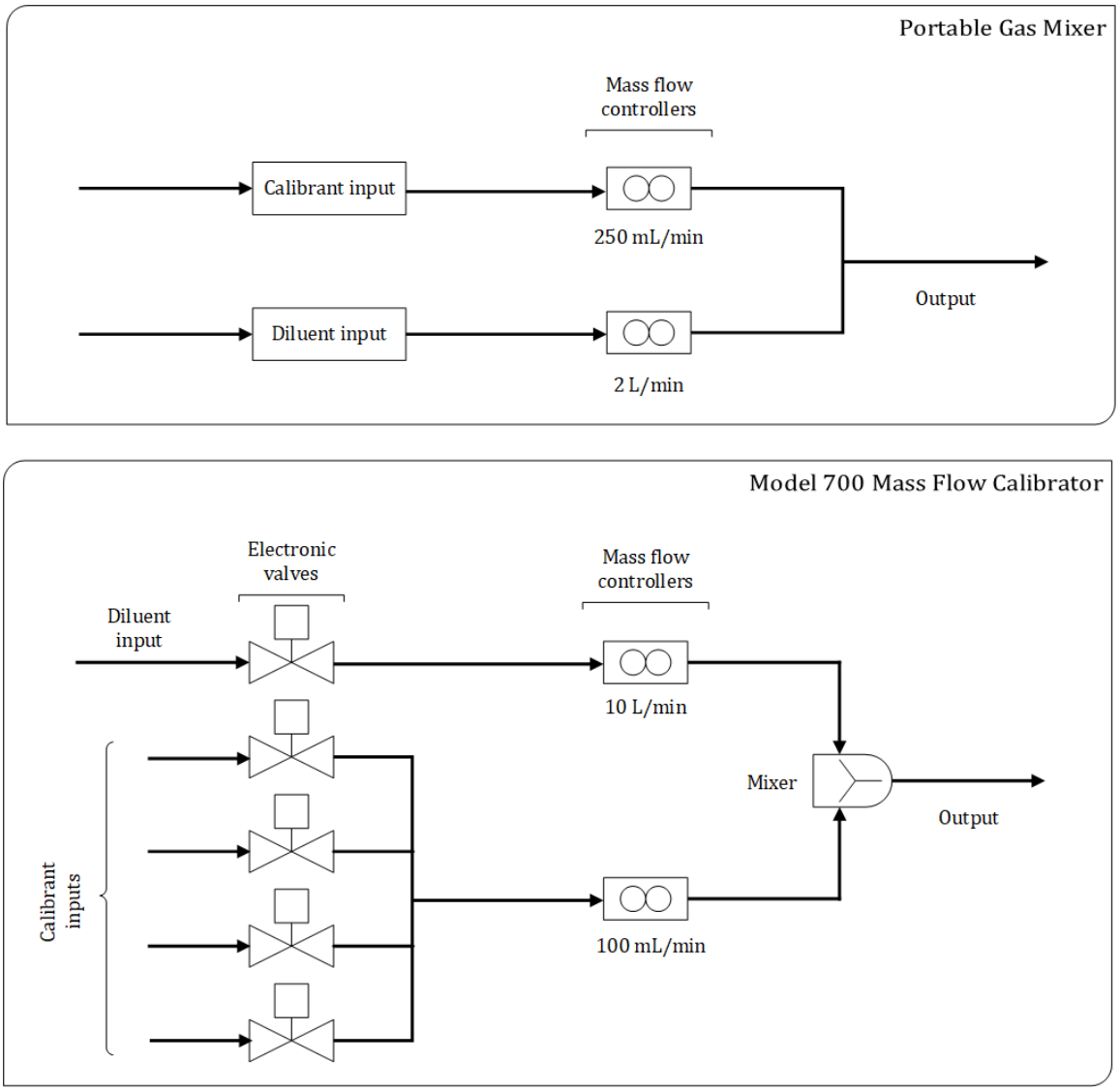

Figure 3.5: Schematic of the Portable Gas Mixer and Model 700 Calibrator

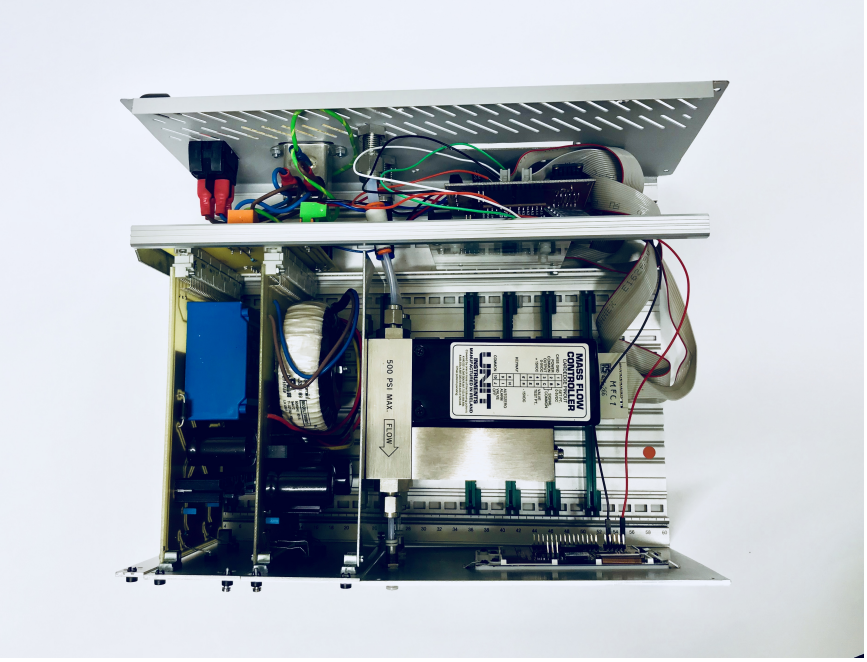

Figure 3.6: Mechanical and electronic components of the Dilutor.

The Model 700 Mass Flow Calibrator T-API (Figure 3.7)is equipped with two MFCs rated at 100 mL/min and 10000 mL/min. The higher flow rate ratios between the MFCs increases the mixing ratio capacity of the system. This instrument has four channel input and a single output. However, only two of these inputs can be used simultaneously. Four electronic valves, a pressure and flow sensor are used to select flow input into device. A combination of the Model 700 calibrator, Dilutor and Gas Mixer allows mixture of up to six different gasses/vapours over a wide range of concentrations.

Figure 3.7: Model 700 Mass Flow Calibrator T-API

3.3.3 Electronics design

Similar to the Gas Mixer, the main power requirements for the Dilutor unit were to supply regulated ± 15 V to both MFCs. A custom electronic circuit steps down 240 VAC to regulated ± 15 V which is supplied to the MFCs. Flow control and communication were managed by an ATmega328P microcontoller. This microcontroller features six analogue inputs. Two of these analogue pins were used to read flow rate from the MFCs. The voltage signal to control flow was generated using an MCP4725 12-Bit Digital to Analog Converter (DAC). Using this high resolution DAC enables precise flow control. The Graphical User Interface (GUI) was designed on the Universal Windows Platform (UWP) using Microsoft Visual Studio 2017 and C♯ programming language. Communication between a computer running the software and both units was achieved via Bluetooth LE 4.1 interface using the Nordic nRF51822 chipset. A 4D system touch screen was added to front panel to display system information to the user. The assembled unit is shown in Figure 3.8.

Figure 3.8: The Dilutor

The Model 700 Mass Flow Calibrator multitasking operating system allows it to do instrument control, monitor test points, provide an analogue test output, interface with dataloggers or analysers, and provide a user interface via the display on the front panel. It can be interfaced with external devices via an RS-232 port on the back panel. Although the Model 700 Calibrator includes buttons and a display for setting process parameters, using this function was cumbersome for processes with more than one steps. Additionally, the system often shuts down when there are unexpected changes to system parameters such as input gas pressure. To resolve this issue an interface to manage the Model 700 Calibrator was added to the Universal Windows Platform (UWP) app used to control the Dilutor. This app communicates with the Model 700 Calibrator via the RS232 port. An added advantage with this approach was a seamless control of both mixers via a single software allowing the user to set timing and test gas sequences for both devices from a single application. A setup of the portable gas mixer and Model 700 Calibrator is shown in Figure 3.9. This setup in isolation can be used to deliver gas mixtures to test sensors in

situations were only concentration is to be investigated.

Figure 3.9: The Dilutor and Model 700 Calibrator

3.4 Permeation Source (OVG 4)

Low concentration gasses/vapour can be achieved using the Gas Mixer and VOC vapour generating technique presented earlier. However, generating low (ppb) concentrations is challenging owing to the fluctuations of the MFC at very low flow rates. An Owlstone Calibration Gas Generator (OVG-4) unit was purchased as a solution to this challenge. The OVG-4 (Figure 3.10) is a calibration gas system that can generate NIST traceable, precise, repeatable, and accurate concentrations of chemicals and calibration gas standards [8] at low ppb.

Figure 3.10: Owlstone Calibration Gas Generator (OVG-4) unit [8]

During use, a small quantity of the target compound is sealed in the permeation tube and placed in a heating chamber within the unit. As the analyte permeates from the surface of the tube, a stream of carrier gas flows over the surface of the tube carrying the permeated analytes through the outlet at a fixed flow rate.This device requires the user to make and calibrate tubes similar to the one shown in Figure 3.11 for each compound they wish to analyse.

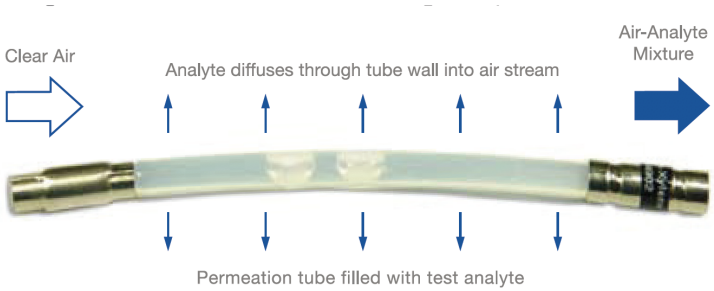

Figure 3.11: Owlstone permeation tube [9].

Equation 3.4 is used to compute the concentration from the properties of the

permeation tube and the flow rate through the chamber [10].

$$C = \frac{q_d * 22.4}{F * M_w} \tag{3.4}$$

In this Equation, the output concentration C (ppm) is related to the flow rate F (mL/min) and the molecular weight M_w (g/mol) of the analyte. The permeation rate (ng/min), q_d is obtained during calibration of the tube at a fixed temperature.

3.5 Humidity Generator

As mentioned previously, humidity is factor that affects the performance of sensors hence tests are carried out to evaluate sensor performance at various humidity levels. A humidity generator (Figure 3.12) was designed in the School of Engineering to facilitate humidity calibration of gas sensors. The Humidity Generator provides gas flow at specified humidity. This is achieved by flowing clean laboratory air through a series of water bubblers to humidify it before using this air to dilute analytes from the Gas Mixer, Dilutor and Model 700 Calibrator. The device houses two MFCs which are programmed to channel air through a 'dry line' or through the 'wet line' (water bubbled) to produce the desired humidity. A Sensiron SHT75 and an NXP MPXM2053GS sensor were installed in the gas flow path to provide temperature, humidity and pressure measurements. A custom software was also designed to provide precise humidity control via a NI-DAQ 6008 OEM Data Acquisition module.

Figure 3.12: Humidity generator device and water bubbler

3.6 Gas analyser

The previous sections describe the development of equipment needed to generate gases/vapours with known humidity, concentration, and flow rate. To check the output of the gas rig is as desired by the user, a "gas analyser" was created to measure the gas output. The Gas Analyser was designed to examine the composition and quantity of gas from sensor undergoing calibration. As illustrated in the system schematic in Figure 3.13, the Gas Analyser uses several sensors to produce information on the temperature, pressure, flow rate and chemical composition of the effluent from the calibration process. This section presents the design of the Gas Analyser.

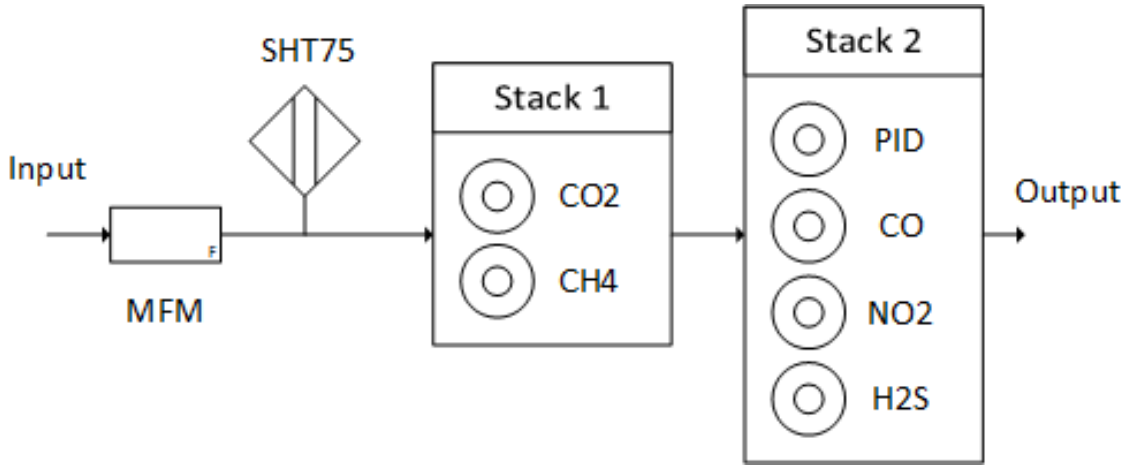

Figure 3.13: Schematic of the Gas Analyser

3.6.1 Sensors

An array of commercial sensors were used in this design to analyse gas composition of calibration process. These sensors are:

Methane gas sensor

The Prime 1 high resolution methane sensor, acquired from Clairair LTD, was used to sense a wide range of hydrocarbons. This sensor integrates an infrared radiation source, custom infrared detector and an internal ARM7 core microprocessor into a compact 20 × 8 mm package. The Prime 1 is temperature compensated and was selected for its high resolution (0-100% LEL methane) [11]. This sensor provides measurement signals on the hydrocarbon content of gasses after going through gas test rig and calibration sensor. A Cirius X transmitter board from Clairair LTD was added to the design to manage sensor power supply and provide communication interface with the sensor [12].

CO_2 sensor

This sensor was added to the Gas Analyser to measure CO_2. The Alphasense IRC-AT CO_2 sensor was selected because it covers a wide range of concentrations (0 - 5000 ppm[13]) . Additionally, the sensor only requires up to 60 mA and has a transmitter board (Alphasense IRC-TX NDIR CO_2 [14]) which enables easy integration of the sensor with the other electronics in the device.

Temperature and Humidity

The SHT75 is, a high end sensor by Sensiron, was used to measure gas temperature and humidity. Desirable features of the sensor for this project includes a 12-bit resolution measurement of relative humidity to an accuracy to $\pm 1.0\%$ $r.h.$ and a low average power consumption of 90 μW [15] . Temperature is measured to $\pm$ 0.3 °C accuracy at a resolution of 0.01 °C .

PID sensor

The PID sensor measures VOCs to very low concentrations and is considered the gold standard for VOC measurement. The sensor uses UV light to ionise target compounds which are later detected and measured. A voltage signal of this measurement is given by the sensor's onboard electronics and is an indication of the concentration of the gas tested. Available commercial sensors covers concentration in a range of 1 ppb to 6000 ppm. The Alphasense PID-A12 with a range of 50 ppb to 6000 ppm was used to provide information on the VOC composition of gasses from the sensor undergoing calibration [16].

CO, NO_2 and H_2S sensors

Sensors for common test gasses such as CO, NO_2 and H_2S were added for concentration measurement of these compounds. An Alphasense CO-A4 electrochemical sensor was used to measure CO levels. This sensor covers a 0 - 500 ppm range and a sensitivity of $\approx 0.3\ mA$/ppm in 2 ppm CO [17]. NO_2 and H_2S electrochemical sensors were also purchased from Alphasense. All three sensors output analogue current corresponding to the concentration of the test gas. An Analogue Front End (AFE) circuit was also purchased from Alphasense which provides low noise electronics to drive the sensors and optimise their performance. The PID, CO, NO_2 and H_2S and the AFE housed in a gas hood, as shown in Figure 3.14.

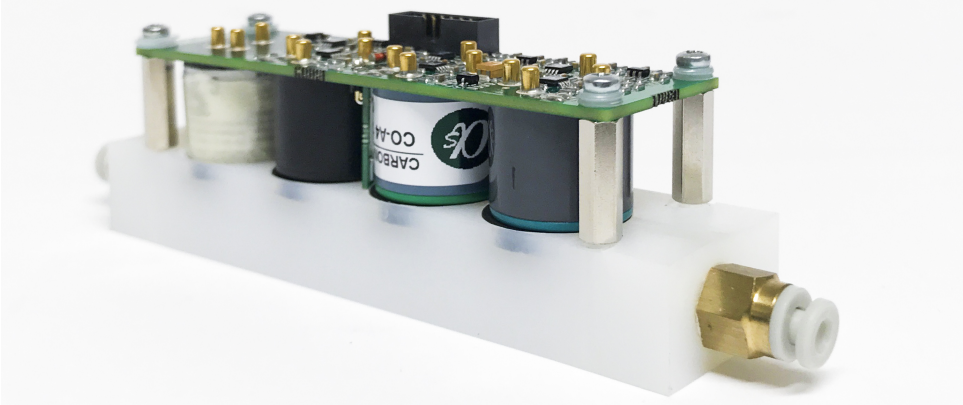

Figure 3.14: PID, CO, NO_2 and H_2S and the AFE housed in a gas hood.

Mass Flow Meter (MFM)

The MFM is similar to MFC described previously. Unlike the MFC the MFM does not control flow, it only measures flow rate. Hence, a control signal is not required to drive the MFM. It is powered by supplying ± 15 V to its power supply pins. During use, the MFM outputs a linear signal within 0 - 5 V with 0 indicating no flow and 5 V indicating maximum flow. The inlets and outlets of the MFM were

fitted with 1/4 inch Swagelok compression fittings.

3.6.2 Electronics and communication

The electronic components discussed in Section 3.6.1 require various voltages for their operation. It is also important that these supply voltages are free from interference which could affect the measurement obtained from the sensors. A summary of these requirements is shown in Table 3.1.

Table 3.1: Summary of voltage requirements for Gas Analyser components

Component	**Manufacturer**	**Voltage(s)**	**Current/Power**
Prime 1 (via Ciriux X)	Clairair	8.0 - 36.0 V	1.5 W
IRC-AT (via IRC-TX)	Alphasense	12 - 40 V	$\approx$ 60 mA
SHT75	Sensiron	2.4 - 5.5 V	80 μW
PID-A12	Alphasense	3.6 - 10.0 V	85 mW
CO, NO_2 and H_2S	Alphasense	3.6 - 6.4 V	-
MFM	Units Instruments Model	$\pm$ 15 V	150 mA
Pump	-	6v	-

An electronic circuit was designed to provide regulated voltages at the levels shown in Table 3.1 from a single 24 V power supply. Most of the components have low power requirements, however ,the MFM requires a significant amount of power to function. Therefore, a Traco TEN 5-2423 DC-DC converter was used to supply regulated $\pm$ 15 V at 200 mA to the MFM. An electronic circuit board was designed using Autodesk EAGLE electronic design application and is shown in Figure 3.15.

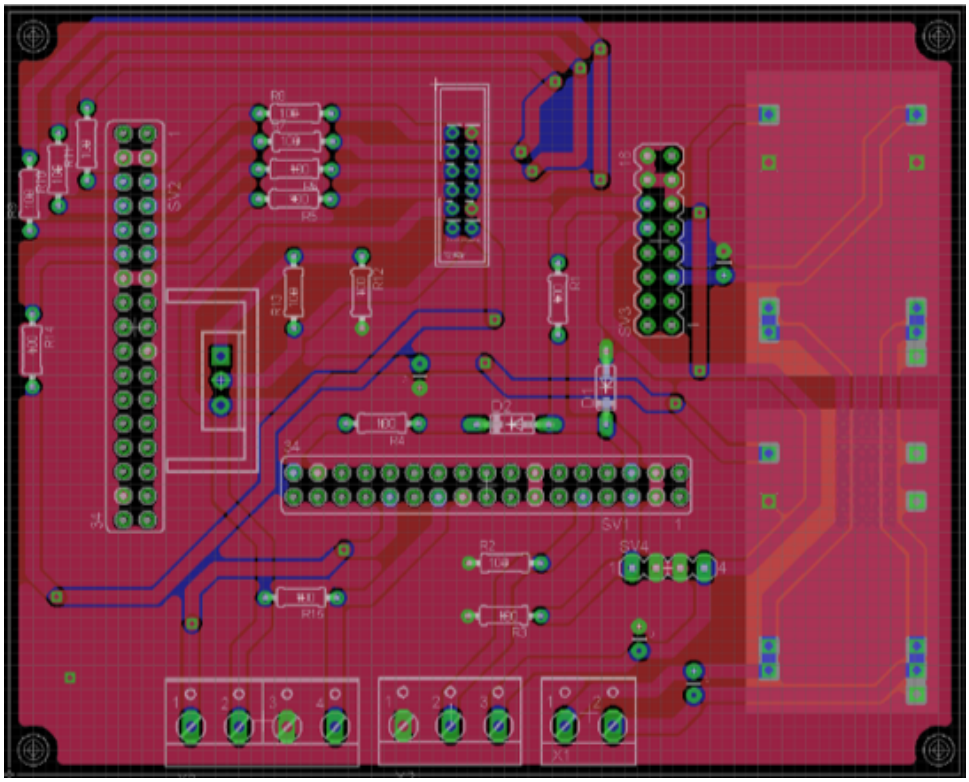

Figure 3.15: Gas Analyser power distribution circuit.

Two 34-way sockets were added to the board to interface with the NI-DAQ 6001 OEM Data Acquisition Boards. The NI-DAQ is connected to the electronic components listed in Table 3.1 and has a USB interface to transfer these measurements to a computer and control signals from the computer to the Gas Analyser. A control software was designed using National Instruments LabVIEW to provide a GUI for users to interact with the Gas Analyser. Using the LabView software, users get a visual feedback of the components in the Gas Analyser such flow rate, concentrations, temperature etc. The software also allows users to log these parameters for further investigation.

3.6.3 System assembly

A major consideration in the assembly of the Gas Analyser was the PID. Most commercial PID sensors are designed to allow gas travel to through the sensor and do not provide a leak-proof inlet and outlet. Consequently, an enclosure is required for the PID when testing hazardous compounds. Without this enclosure test compounds will leak into the environment. To prevent this, it was decided to use IP68 certified enclosure for the Gas Analyser. The Ingress Protection marking, IP, rates the degree of protection against dust, dirt, intrusion, water, air etc. IP68 certification is applied when a test unit has complete protection against particles entering or leaving the unit in a vacuum and can be immersed in 1m or more of water without leaking. After modelling the internal components to ascertain the space requirements for the Gas Analyser, a 330 $\times$ 230 $\times$ 110 mm IP68 certified Euronord enclosure was selected. This enclosure also includes an O-ring seal compressed around the lid to provide adequate seal. As shown in Figure 3.16, the internal components were mounted to perspex sheets compressed to the internal walls with a middle structure added to provide support for the horizontal supports.

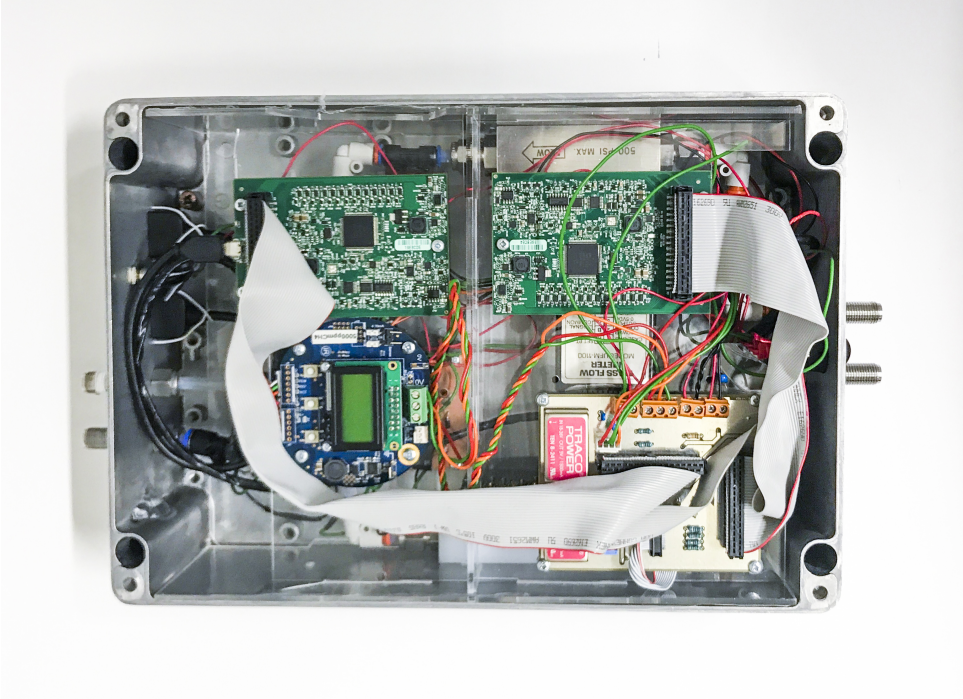

Figure 3.16: Assembly of the Gas Analyser.

This technique was employed to ensure the components were not screwed to the enclosure side walls and could lead to leaks. A mini vacuum pump was mounted inside the unit to pump air within the enclosure through an outlet on the back on the back panel. Two female USB sockets were also mounted on the back plate. These USB mounts were connected to the NI-DAQ boards and provided a connection port to the computer running the control software. On the front panel, two 1/4 inch Swagelok buckheads were mounted. One of these buckheads was used as inlet and this was connected to the MFM. The other buckhead is the unit's outlet and connected to the outlet of the sensors stacked on the AFE. The completed Gas Analysers is shown in Figure 3.17.

Figure 3.17: The Gas Analyser

3.7 System Integration and Software

The entire Gas Test Rig is shown in Figure 3.18. The unit comprises the Gas Mixer, OVG 4 Permeation Unit, Humidity Generator, Model 700 Calibrator, Dilutor, Gas Analyser and computer running the control LabVIEW software.

Figure 3.18: The Gas Test Rig

The Gas Mixer, OVG 4 Permeation Unit, Humidity Generator and Gas analyser are enclosed in an acrylic sealable enclosure. This setup allows calibration tests using hazardous compounds as these are trapped in the acrylic and released through the exhaust system. A Crowcon Gas-Pro sensor with 4 gas sensors (CH_4, H_2S, CO and O_2) was mounted in the enclosure for safety. This sensor provides information on the composition of air in the enclosure and sounds an alarm when a certain limit is exceeded informing the user if it is safe to open the enclosure. Space is also provided within the enclosure for users to place their test sensors for calibration.

The computer on the Gas Test Rig enclosure runs the control LabView software. A screenshot of the software's interface is shown in Figure 3.19. This software is used to set, measure and record the Test Rig parameters such as flow rates and humidity

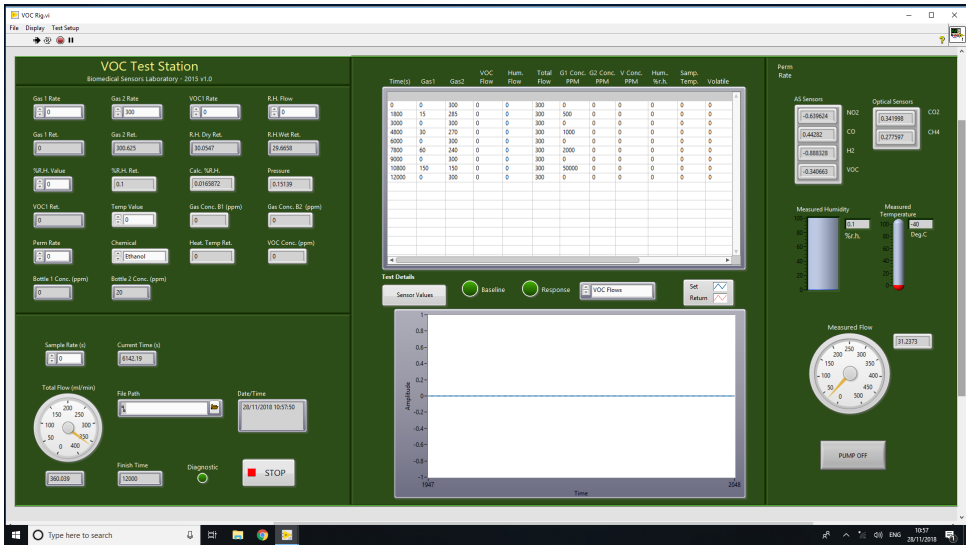

Figure 3.19: The Gas Test Rig

3.8 Conclusion

This chapter presented the development and construction of Gas Test Rig for sensor calibration tests. The Test Gas Rig includes a Gas Mixer, OVG 4 Permeation Unit, Humidity Generator, Model 700 Calibrator, Dilutor, Gas Analyser. A combination of these devices enables users to generate test gas at specified flow rates, concentrations, humidity and composition. Custom software was designed to control the unit was also shown.

3.9 References

[1] Xiao Liu, Sitian Cheng, Hong Liu, Sha Hu, Daqiang Zhang, and Huansheng Ning. A survey on gas sensing technology. *Sensors*, 12(7):9635–9665, 2012.

[2] Raanan A Miller, Erkinjon G Nazarov, Gary A Eiceman, and A Thomas King.

A mems radio-frequency ion mobility spectrometer for chemical vapor detection. *Sensors and Actuators A: Physical*, 91(3):301–312, 2001.

[3] Quan Yang. *Automatic development of global phase diagrams for binary systems in pressure-temperature space*. PhD thesis, 2006.

[4] Norbert Adolph Lange and John A. Dean. *Lange's handbook of chemistry*. McGraw-Hill, New York, 1985.

[5] Tomáš Boublík, Vojtěch Fried, and Eduard Hála. The vapour pressures of pure substances. 1984.

[6] Carl L Yaws. *Thermodynamic and physical property data*. Gulf Publishing, 1992.

[7] Bruce E Poling, John M Prausnitz, John P O'connell, et al. *The properties of gases and liquids*, volume 5. Mcgraw-hill New York, 2001.

[8] https://www.owlstoneinc.com/products/ovg-4/, October, 2018.

[9] https://www.owlstoneinc.com/media/uploads/files/ovg-4_technical_specification.pdf, October, 2018.

[10] https://www.gasdetection.com/wp-content/uploads/whitepaper_-_generating_calibration_gas_standards_with_ovg-4_and_permeation_tubes.pdf, October, 2018.

[11] https://www.clairair.co.uk/wp-content/uploads/2014/05/prime1datasheetdes12iss1.pdf, October, 2018.

[12] https://www.clairair.co.uk/wp-content/uploads/2014/05/ciriusx-datasheet-iss2.pdf, October,2018.

[13] http://www.alphasense.com/web1213/wp-content/uploads/2016/11/irc-at.pdf, October, 2018.

[14] http://www.alphasense.com/web1213/wp-content/uploads/2017/09/ndir-transmitter.pdf, October-2018.

[15] https://www.sensirion.com/en/download-center/humidity-sensors/pintype-digital-humidity-sensors/, October, 2018.

[16] http://www.alphasense.com/index.php/products/pid-air/, O.

[17] http://www.alphasense.com/index.php/products/carbon-monoxide-air/, October, 2018.

Chapter 4

Design of a Pre-concentrator and Gas Chromatograph

4.1 Introduction

Over the years several technologies have been developed for Volatile Organic Compound (VOC) detection. This includes mass spectrometer, Ion Mobility Spectrometry (IMS), Photoionization Detector (PID), Metal Oxide Sensor (MOS) and optical sensors to name a few. Although all of these technologies are able to detect VOCs in the ppm range, trace analysis of vapours with theses technologies can be challenging. MOS and optical sensors, for example, struggle with analysis of compounds below 1ppm [1]. PID, mass spectrometers and IMS can offer detection limits in the ppb region [1] [2]. However, they offer limited selectivity when used in isolation [3]. To improve the sensitivity and selectivity of these sensing technologies they are usually coupled with a Pre-concentrator (PC) and/or Gas Chromatograpy (GC).

PCs are integrated in the frontend of analytical instruments to improve overall performance of the system. PCs improve concentration and purify a chemical sample before introduction to an analytical system [4] thereby increasing the limit of detection of the overall system. Advantages from using PCs includes selective sampling of target compounds and operation at high flow rates. GCs provides analytical systems with a mixture of good accuracy and precision, very high selectivity and resolution, wide dynamic concentration range and high sensitivity [5]. It is used to separate complex mixtures before analysis by detectors such as IMS and PID [6]. When integrated with gas detection technologies, both PC and GC increase the limit of detection, selectivity, sensitivity of the sensor device. The development of at PC and GC will be presented in this chapter.

4.2 Pre-concentrator design

In practical gas analysis situations, the concentration of test samples may be lower than the limit of detection for a specific detector. PC resolves this issue by allowing the collection of enough sample mass to obtain detectable signals from the detector. Additionally, PC can provide some degree of humidity compensation [7]. Conventional PCs are made up of a stainless-steel tube or glass-capillary tube coated with an absorbent material [8–12]. In use, the sample is flowed over adsorbent material and the target compound is trapped in the pores of the adsorbent. After this capture process, the trapped concentrated samples are released or desorbed by heating the adsorbent material [4]. The adsorbent material is the most important component of the PC and selecting a suitable adsorbent material is important to ensure proper pre-concentrating of the target sample. Adsorbent material selection for this

research is discussed in the next section.

4.2.1 Adsorbent material

A major design requirement for PC is high affinity for target compounds and large surface area for increased adsorption. Adsorbent materials such as amorphous silicon dioxide powder [13], carbowax x [14][15], mesoporous silica, zeolite [16], Tenax TA [13, 17] meet this requirement and have been used in many PC designs. In this design however, Activated Carbon Cloth (ACC) which is both easily available and capable of adsorbing VOCs was used. Woven ACC has been utilised extensively as a filter to trap VOCs and has been shown to have a high affinity for VOCs [18], however it has not been fully investigated as a PC material. ACC is usually processed to increase its porosity, surface area and selectivity. One major advantage in the use of ACC is its high porosity and large surface area (1000-2000 m^2/g [19]) compared with standard commercial adsorbents such as Tenax (35 m^2/g [20]). Another advantage is the lower regenerative temperature of ACC (150°C [21]) compared with Tenax (300°C) leading to more power efficient and safer designs. Additionally, the lower price point of ACC compared to the other adsorbent materials mentioned allows it to be implemented in disposable designs where cross contamination is crucial.

ACC are usually manufactured by weaving or knitting activated carbon. An SEM image comparing the microstructure of a knitted and woven ACC is shown in 4.1.

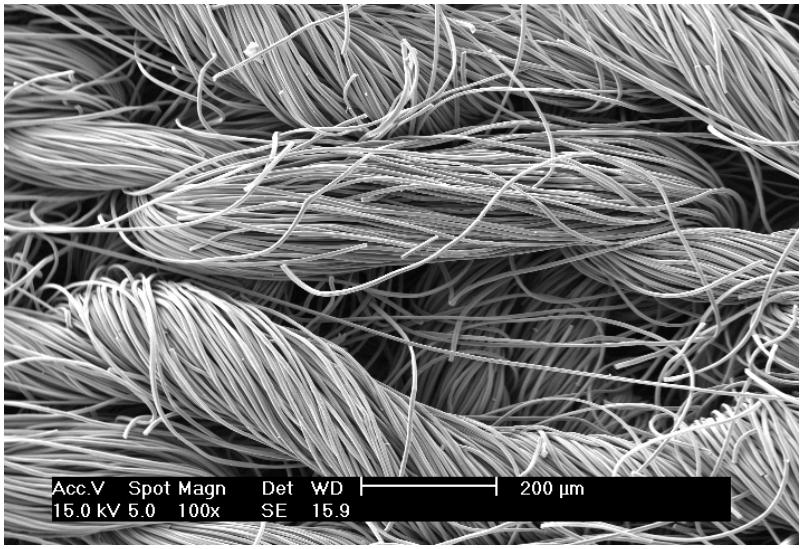

(a) Knitted

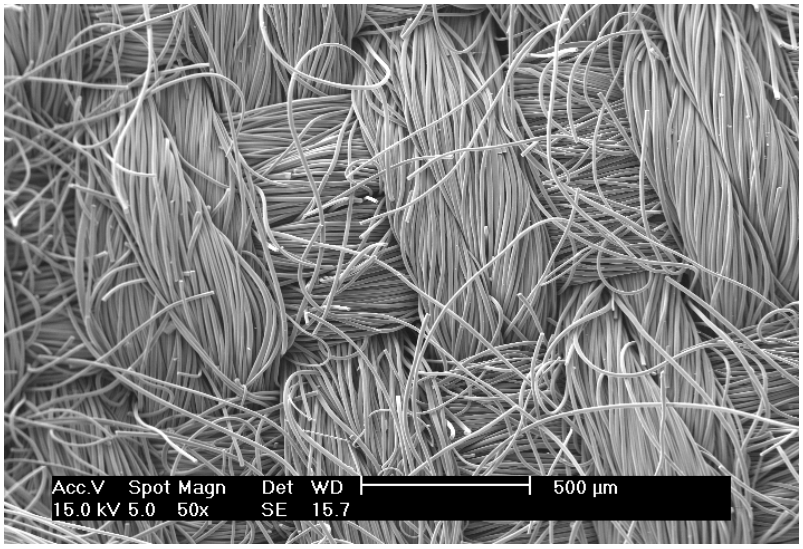

(b) Woven

Figure 4.1: Microstructure of ACC

Several proprietary ACC are commercially available and some of these are shown in Table 4.1. These clothes were compared using adsorption and desorption tests. In these tests, VOCs were sampled from several chemicals and desorbed into different analytical instruments. To aid the adsorption and desorption process several sampling and desorbing instruments were developed.

Table 4.1: ACC materials and manufacturers

Commercial name	Manufacturer
IAC Cloth	Mast Carbon
C-Tex	Mast Carbon
DL laminated	-
FM 30 K	Chemviron
FM 40 k	Chemviron
FM 70	Chemviron
FM 120	Chemviron

4.2.2 Adsorber and thermal desorber development

The pre-concentrating process involves passing a stream of the low concentration sample over the surface of the adsorbent material. Target compounds to be pre-concentrated are trapped in the pores of the adsorbent material or adhere to its surface. This process is referred to as adsorption. To extract the concentrated sample from the adsorbent material, the temperature of the adsorbent material is increased until all trapped molecules are released into a stream of flowing gas. This process is known as thermal desorption. The pre-concentration is achieved by releasing the adsorbed compounds into a smaller volume of gas. Several devices were developed to aid adsorption and desorption of the ACC materials shown in 4.1. This includes a headspace sampler, several adsorbers and thermal desorbers.

Headspace sampler

Many biomedical test samples exist in the liquid phase, therefore, analysis of such samples requires extracting VOC from the liquid phase. To facilitate this process, a headspace sample 'stool' was designed to suspend the ACC in the headspace above a target liquid in a vial. A CAD of the headspace suspender is shown in Figure 4.2. The headspace suspender carries the ACC at a height 30 mm above the base

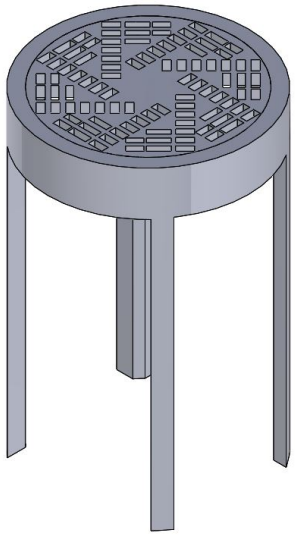

Figure 4.2: CAD of the ACC headspace suspender

of the vial. For a 20 mL vial, this height allows 10 mL of liquid sample to be stored below the ACC. The suspender is manufactured from stainless steel for improved inertness and to avoid corrosion. During adsorption, an aliquot of the test liquid is pipetted into a 20 mL vial. The suspender is inserted into the vial and several 15 mm diameter ACCs were stacked on the suspender. After this, the vial is sealed with the cap. The rate and amount of adsorption can be increased by releasing more VOC from the liquid into vapour. This is achieved by inserting the vial into a hotplate (Stuarts CB162) and increasing the temperature to 40°C. VOCs released from the liquid are trapped in the ACC suspended above. Vials containing the suspender and ACC during a sampling process is shown in Figure 4.3.

After sampling is completed the ACC is removed from the vial and inserted into a Thermal Desorber (TD) to extract the concentrated VOC for analysis in a gas based analytical instrument. Several TDs were designed to heat the ACC in an enclosed space and channel the concentrated VOC released into a test instrument. These thermal desorbers are presented in the next section.

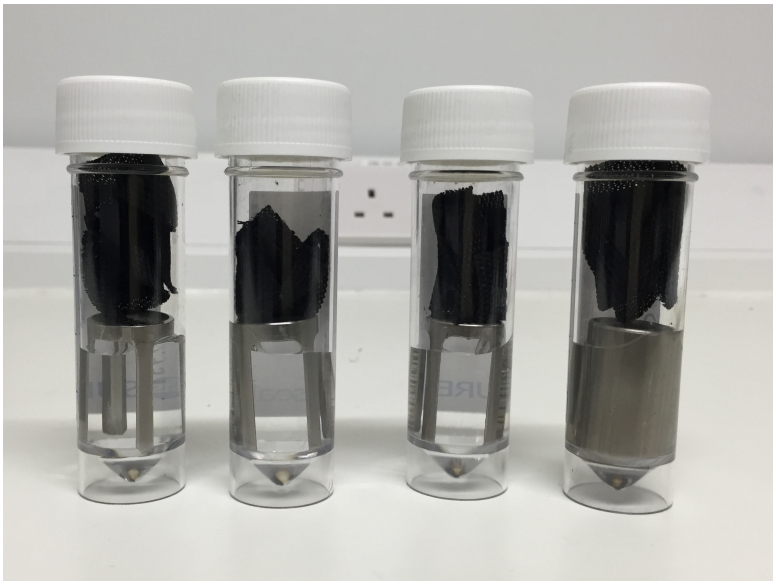

Figure 4.3: Headspace suspender with ACC during sampling

Thermal desorbers

After capturing VOC with the ACC, the VOC is extracted for analysis using a TD by heating the cloth to its regenerative temperature of 150°C resulting in the release of trapped VOC. Three concepts of TD were developed and manufactured. The design approach for each concept was to manufacture a stand-alone TD that could be integrated with various gas analytic instruments. The first concept allows quick desorption of the ACCs previously charged with VOC using the headspace sampler. The 15 *mm* diameter ACC can be heated in a confined heating chamber in Concept-1 therefore the released VOC is carried from the chamber with a carrier gas flow. A CAD representation of this concept is shown in Figure 4.4.

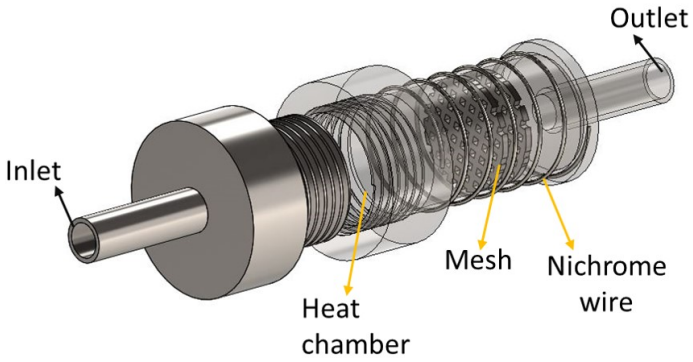

Figure 4.4: Concept-1 thermal desorber for ACC

The TD is manufactured from stainless steel for increased inertness to desorbed compounds. The inlet is a 6.35 mm stainless tube attached to 20 mm base plate. This baseplate screws into a 20 × 30 mm cylinder which acts as the heating chamber. The cylinder is shown in Figure 4.4 and has been made transparent to show the filter mesh. These stainless steel mesh plates are used to position the ACC perpendicular to the direction of flow, increasing the surface that is exposed to the carrier gas. The mesh also improves heat transfer by transporting heat from the cylinder surface to the ACC. Another 20 mm stainless steel plate is used to the seal base end of the cylinder. This back plate is attached to a 6.35 mm outer diameter stainless tube which serves as outlets.

The heating system comprises a 25 gauge nichrome wire wrapped around the heating chamber. The wall of the heating chamber is 1 mm thick to improve heat transfer. For electrical insulation, the nichrome wire was sleeved with a Pro-Power GSX-S24-1100-NAT fibreglass sleeve. Temperature control was achieved using a K-type thermocouple wound around the cylinder between the nichrome wire to measure the cylinder surface temperature. The thermocouple is interfaced with an AT-

SAMD21 microcontroller using the MAX31855 thermocouple-to-digital chip which allows 14-Bit temperature measurements over SPI. The ATSAMD21 is programmed to read the current chamber temperature from the thermocouple and adjust the temperature of the nichrome as required. A Proportional Integral Derivative controller software was designed in C++ language to provide precise temperature control. This software controls the PWM output pins on the ATSAMD21 microcontroller. This PWM signal is used to control the voltage input on a Crydom CMX60D10 relay with the load voltage pins of the relay connected in series with the nichrome coil and a 24 V power supply. The heating system was improved by enclosing the heating coils and chamber in a Spacetherm thermal insulating blanket of 1 cm thickness. The insulating blanket ensures heat generated is transferred to the chamber only and not lost to the environment. The assembled Concept-1 TD with the input end unscrewed is shown in Figure 4.5.

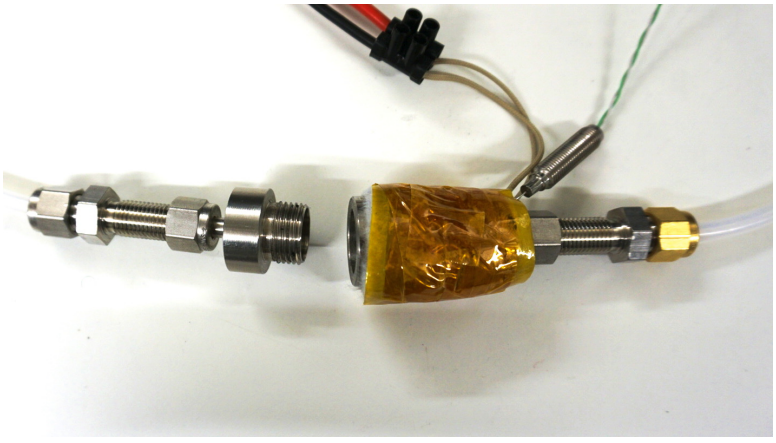

Figure 4.5: Assembled Concept-1 thermal desorber for ACC

Using this TD the adsorption and desorption capabilities of several ACC were tested. The unit was also explored as a simultaneous sampler and TD. In the sampling configuration, new ACC were first inserted in the TD before sampling. The inlet cap was screwed in place and a 1/4" tube was connected from the outlet

of the vial carrying the sample liquid. While heating the liquid a purified air carrier gas is used to flush the headspace from the vial into the TD. The ACC in the TD adsorb the VOC in the flow stream. Once sampling is complete, the adsorbed VOC is extracted using the desorption method described previously.

During tests it was observed that temperatures beyond the 150°C regenerative temperature was required to fully extract VOC from the ACCs. This was due to less heat transferred to the surface of the cloths. To improve heat transfer and reduce power consumption while increasing sampling capacity Concept-1 was revised. A CAD of Concept-2 is shown in Figure 4.6.

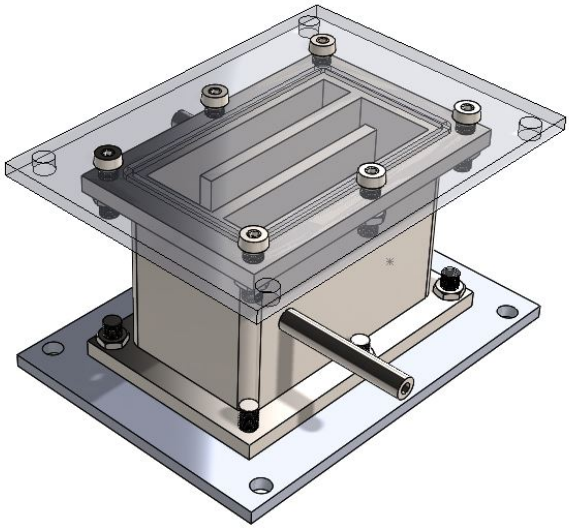

Figure 4.6: CAD of Concept-2 thermal desorber for ACC

In Concept-2 the ACC are placed in cells separated by heating fins in a heating chamber. The fins were added to transfer heat from the TD surface to the ACC. This designs ensures a the entire surface area of the cloth and heating fins are in contact improving heat transfer to the ACC. Additionally, adsorption and desorption was improved in Concept-2 as the sample travels in a serpentine flow path along the

plane longitudinal of the ACC cloth. The chamber and fins in Concept-2 TD were manufactured from a single block of stainless steel (31 × 47 mm). Two stainless steel plates (45 × 61 mm) with 10 mounting holes were used to cap both ends of the chamber. Similar to Concept-1, nichrome wire and a K-type thermocouple was wrapped around the chamber. The heating circuit is also driven with a PWM signal from a programmed ATSAMD21 microcontroller. The assembled unit with the cover plates removed to show the internal fins is shown in Figure 4.7. Less power consumption was recorded when using Concept-2 compared with Concept-1. Additional, trapped VOCs were completed released without increasing the surface temperature above 150°C.

Figure 4.7: Assembled Concept-2 thermal desorber for ACC

With both concepts presented, changing the ACCs after desorption of toxic compounds may lead to hazardous exposure. Additionally, sampling with disposable ACC to avoid cross contamination was challenging since it was difficult to reach the heating chamber. Concept-3 was developed to eliminate these issues. Here, the ACC are enclosed in disposable tubes. A CAD illustration of this design is shown

in Figure 4.8.

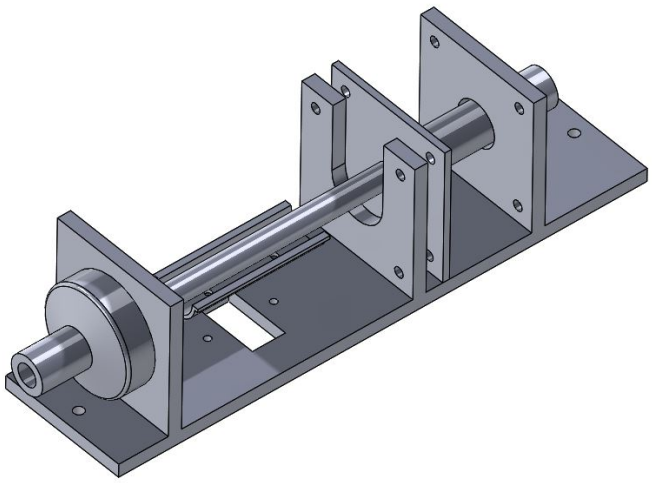

Figure 4.8: CAD of Concept-3 thermal desorber for ACC

In this design, the ACC is wound into a cylinder and inserted into metal tubes. The tubes had an internal diameter of 6.35 and were 80 mm in length. The tubes carrying the ACC is inserted into Concept-3 TD. The user is shielded from the cloth and its contents during sampling and analysis. This design also allows adsorption to be performed without the TD by mounting the tubes on a vial containing the sample as seen in Figure 4.9.

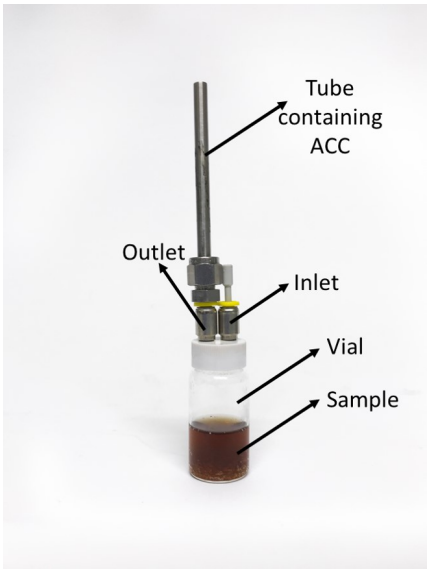

Figure 4.9: Adsorption using stainless steel sample tube

After sampling, the tubes are transported to the TD for desorption. Another improvement with Concept-3 was that it has a faster desorption cycle as the tubes can be changed immediately to run another test without waiting for the unit to cool down before running another adsorption/desorption test. The adsorption tube slots into a PTFE recess on one end of the TD and a spring loaded 3.50 mm tube with a 30 mm flange plugs into the tube from the other end. A semicircular stainless steel section stretching 40 mm is mounted between both end plates of the TD. This section is wrapped with nichrome and is used to heat the tube sitting above it in a similar manner to Concept-1 and Concept-2. The assembled Concept-3 TD is show in Figure 4.10.

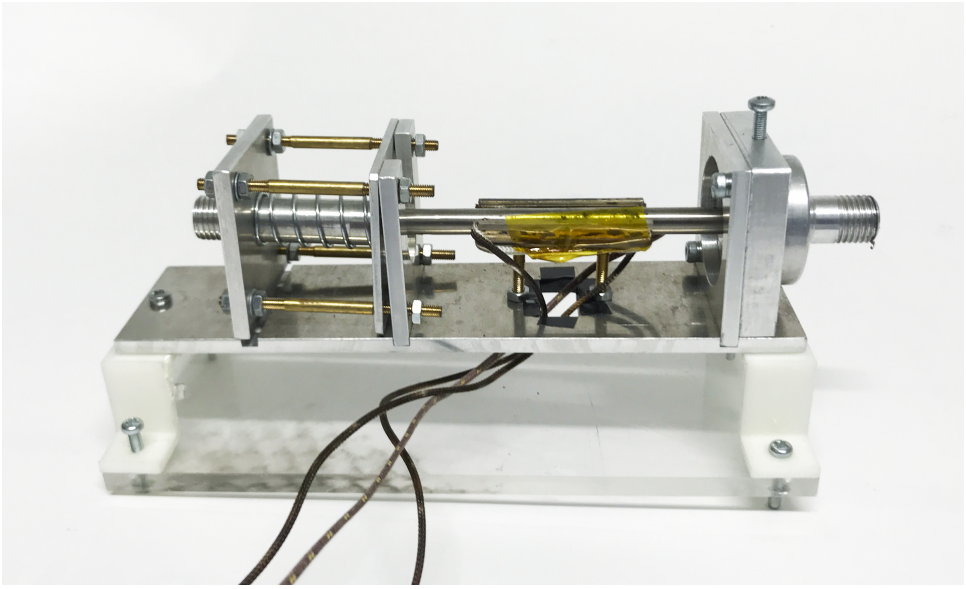

Figure 4.10: Concept-3 TD

Some of the ACCs shown in Table 4.1 and the TD concepts presented were used for adsorption and desorption tests. The test setup and results are shown in the next section.

4.3 Tests, results and discussion

Initial tests were performed to ensure compounds of interest were adsorbed by the ACC and no artefacts were introduced as a result of dissociation of the ACC material during the adsorption and desorption process. In this test, 0.1% solution of acetone and propanol and 0.05% solution were adsorbed onto a FM30K ACC and desorbed into the Owlstone Lonstar Field Asymmetric Ion Mobility Spectrometry (FAIMS) instrument. The test method involved adsorbing the samples for 10 minutes. This was achieved by mounting a tube containing the ACC in a flow path of the sample to be tested. After sampling is completed, the tube was inserted in Concept-3 TD

and the desorbed into the FAIMS. The desorption procedure included heating the tube to 100°C for 5 minutes. Next the desorbed compounds were flushed from the tube using a flow of laboratory clean air. The test was repeated six times for each test compound. The compounds were also directly analysed on the FAIMS without using the PC. The direct tests were carried out for comparison with ACC adsorption and desorption test results. Scaled PCA plots of the direct control tests shown in Figure 4.11.

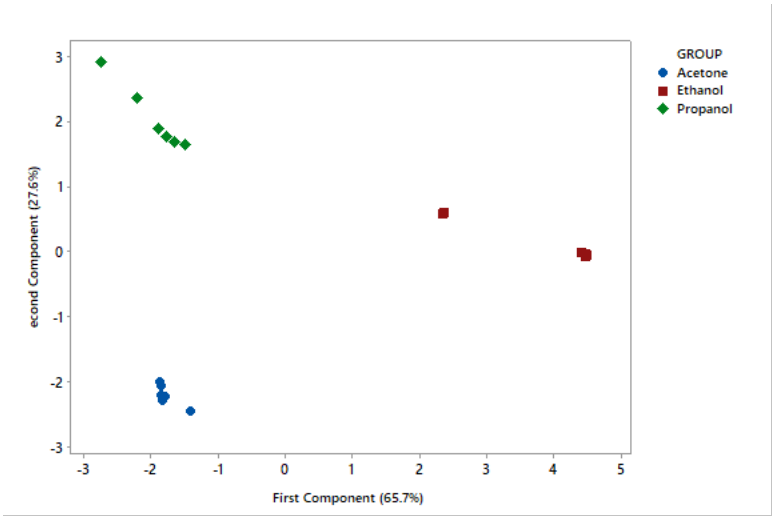

Figure 4.11: FAIMS analysis of acetone, isopropanol and propanol.

As expected, the FAIMS instrument showed good separation between acetone, isopropanol and propanol groups. Scaled PCA plot of the adsorption and desorption tests with ACC is shown in Figure 4.12 below.

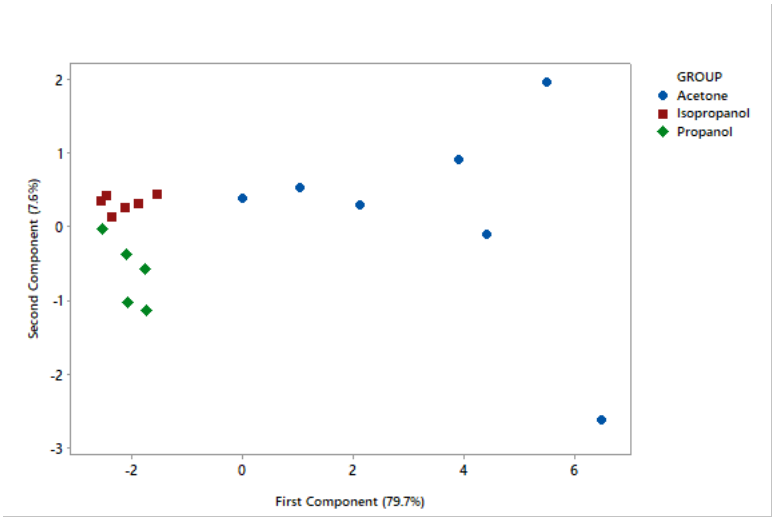

Figure 4.12: FAIMS analysis of desorbed acetone, isopropanol and propanol.

The desorption tests results in Figure 4.12 shows clustering of analysed acetone, ethanol and propanol. This results shows that ACC adsorbs and desorbs VOC effectively without introducing artefacts which would have been present in all test resulting in poor separation of the test compounds. Further tests were carried out to compare the ACCs mentioned in Table 4.1. In this series of tests, each adsorption sampling was carried out by suspending a 15mm strip of ACC in the headspace of a solution using the suspenders shown in Figure 4.3. Solutions containing 0.1% acetone, 0.1% propanol and 0.05% isopropanol in water were used. The vial containing the solutions and ACC was placed in a Techne DB200/2 Dri-Block heater and heated to 45°C for 10 mins. For adsorption using the ACC tubes, an outlet slot was added to the vial cap and the tubes were mounted over the slot. After adsorption, the samples were desorbed into several instruments including the Cyranose 320 electronic nose. This procedure was repeated 10 times for each compound.

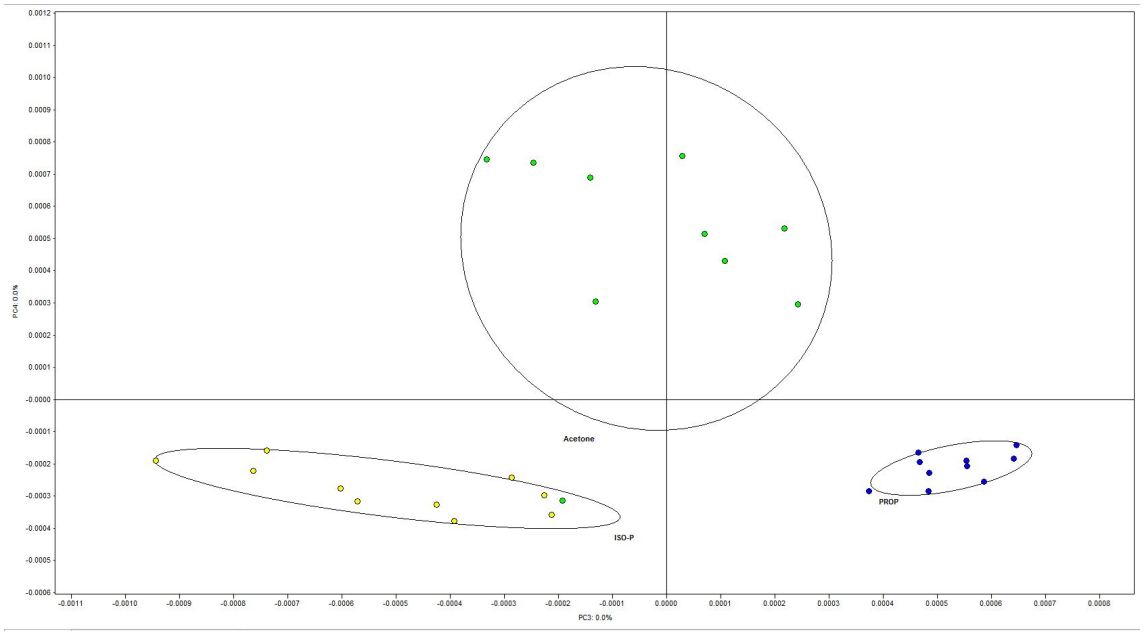

Figure 4.13: Scaled PCA plots of desorbed acetone, propanol and isopropanol using AC

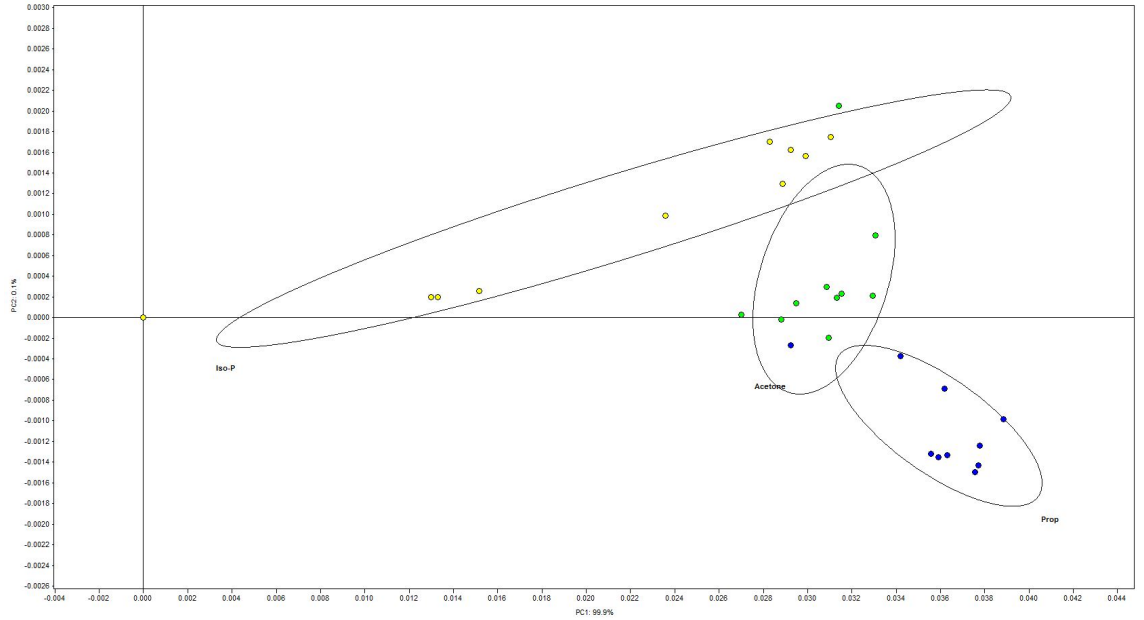

Figure 4.14: Scaled PCA plots of desorbed acetone, propanol and isopropanol using DL cloth

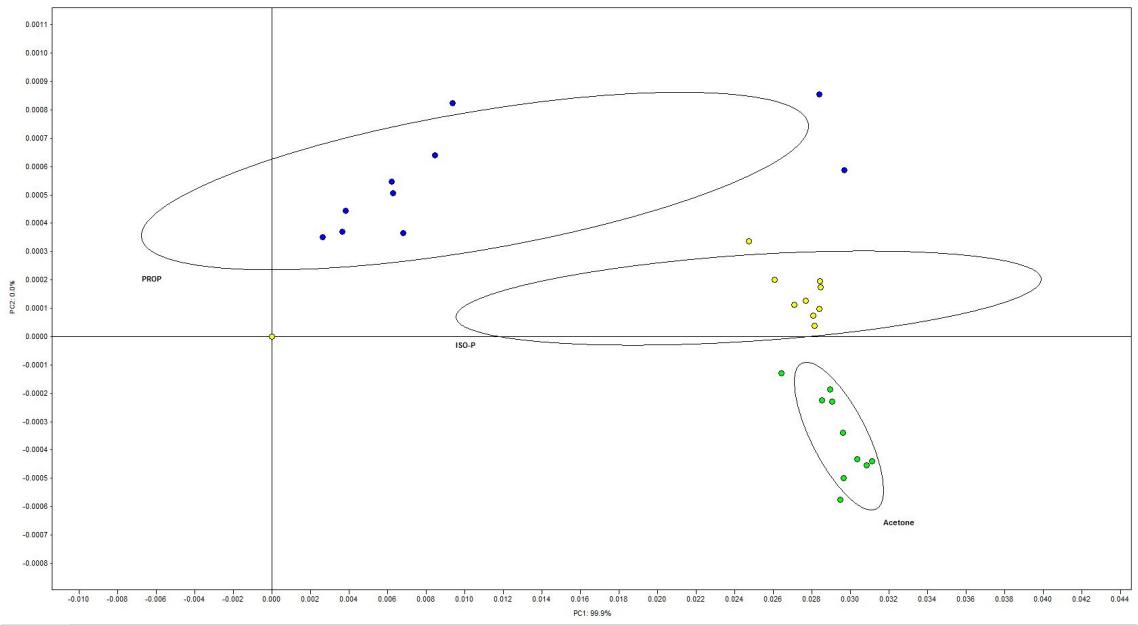

Figure 4.15: Scaled PCA plots of desorbed acetone, propanol and isopropanol using C-Tex cloth

Figures 4.13, 4.14 and 4.15 shows the sensor response obtained from the Cyranose 320 after desorbing AC, C-Tex and DL ACC with the thermal desorber. All three cloths exhibit good VOC adsorption properties with observable clustering for the compound groups tested. It was also observed that desorption results from the AC and C-Tex cloths showed better separation than those obtained from DL cloths.

Pre-concentration properties of the cloths were tested to show the capabilities of the assembled ACC and TD to function as a PC unit. In these sequence of tests 55 ppb isbutylene and acetone were adsorbed onto C-Tex cloths. They were desorbed at 150°C into a Tiger VOC Detector from Ion Science. Additional control tests were performed by testing the compounds directly on the Tiger instrument without using the PC unit. Figure 4.16 is a plot of the responses obtained from the Tiger instrument showing a 110 times increase in concentration for the compounds tested.

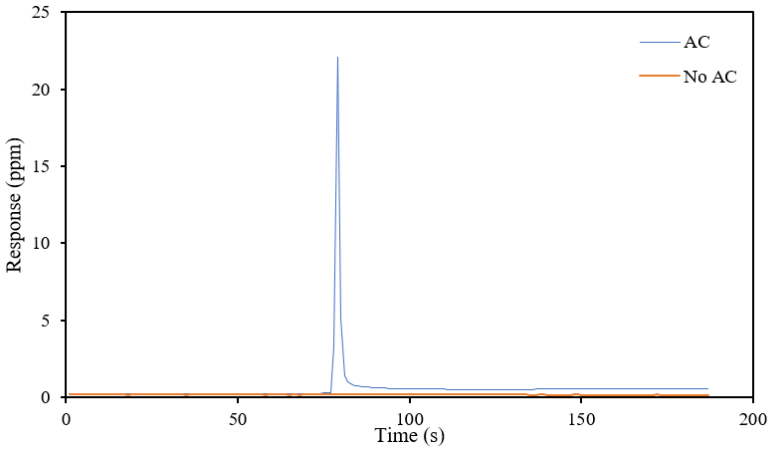

(a) Isobutylene

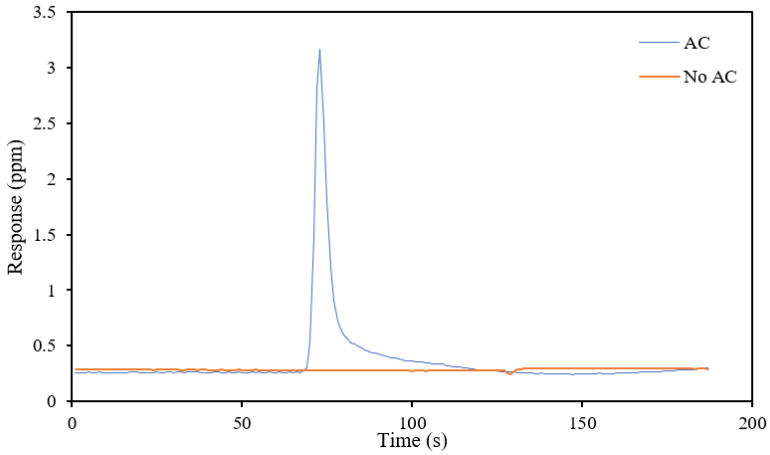

(b) Acetone

Figure 4.16: Tiger PID sensor response with and without PC

More tests were carried out to determine the concentration factor of the ACC. Adsorption tests were performed with a 15 *mm* strip of ACC in the headspace of a solution using the suspenders shown in Figure 4.3. Solutions containing 0.1% acetone were used. The vials containing the solutions and ACC was placed in a Techne DB200/2 Dri-Block heater and heated to 45°C for 10 mins. The ACC was extracted from the vial and inserted in the TD with the outlet connected to a 1^{st} Detect MMS1000® mass spectrometer. The test was repeated without using the

PC therefore the vial was connected directly to the 1^{st} Detect MMS1000® mass spectrometer.

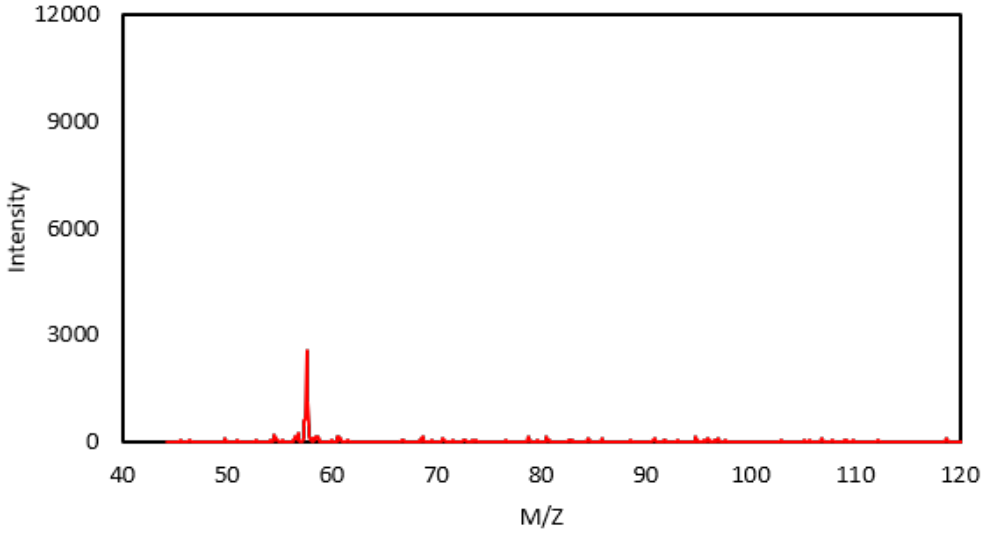

(a) Without ACC

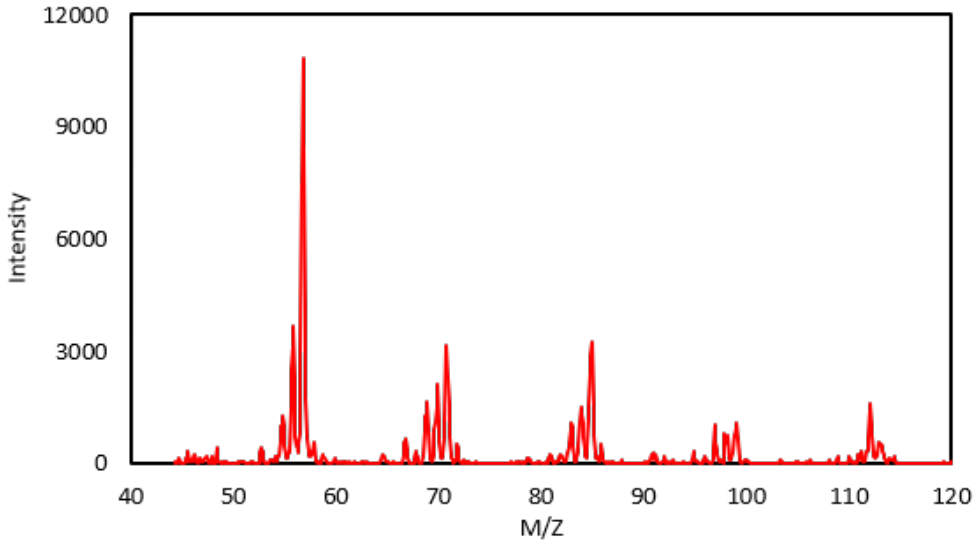

(b) With ACC

Figure 4.17: Mass spectra of acetone from MMS1000 mass spectrometer with and without ACC

Figure 4.17 shows the mass spectra obtained from the 1^{st} Detect MMS1000® after desorption. A peak for acetone is observed at peak at 57.5 m/z showing

that acetone was successfully captured and desorbed. There was an 830% increase in response intensity from a maximum peak of 1175 without ACC to 10878 when ACC.

The tests and results obtained shows the suitability of the PC presented for sampling and concentrating VOC. There are several advantages in using PC in gas-based analytical systems detection systems. The concentrated target compound can be released in a single pulse providing a narrow time width of high concentration signal, thereby improving the overall effectiveness of the analytical instrument. As demonstrated in the tests, another advantage of the PC is that it can be interfaced with different types of chemical instruments serving as a convenient channel between sample and instrument. Apart from PCs, many analytical instruments incorporate a GC to provide further compositional information. The next section presents work carried out to design the GC.

4.4 Gas Chromatograph development

A GC separates compounds in a mixture based on their boiling points, polarity and relative affinity for a stationary phase lining the GC column [22]. The solvent travels through the column and the retention time in the column is used for qualitative analysis. It suggests the identity of the solute when it is compared to a predefined standard. The height of the resulting response peak or area determines the concentration of the solutes when again compared with known standards. When separation is completed, it is expected that the results have non-overlapping curves with their respective narrow peaks. The main objective of the GC in this scenario is to ensure that a compounds going through the column is delayed before being

reaching the analytical instrument of choice. This delay will vary for different compounds depending on their interaction with the stationary phase lining the walls of the GC. The aim here is not to obtain a complete separation of the compounds, as in commercial GC systems but to introduce a temporal delay that will improve compound discrimination.

4.4.1 GC design

Current trend in GC design utilises micromachining techniques to manufacture miniature GC columns. Various silicon micromachining methods, such as LIGA[23] and DRIE[24], can be used to construct high aspect ratio micro-channels and microstructures and have been applied in micro channel GC manufacture. However, fabricating structures using silicon machining is time consuming and costly. Additionally these techniques do not produce true 3D structures. For this design, Micro Stereo Lithography (MSL) and CNC has been selected over silicon micromachining as it enables manufacture of full 3D structures. One advantages of using MSL is the rapid development of high-resolution three dimensional objects during design. Utilising MSL and CNC, GC systems with serpentine column topologies were designed and manufactured. In the School of Engineering, at Warwick University, we have access to MSL machines including the Form2 Desktop 3D printer and Envisiontec Perfactory Mini. GC concepts were first designed using the SolidWorks CAD software before being transferred to the MSL machines for manufacture.

The preliminary concept consist of a block with interconnected rectangular passages acting as the GC column. A CAD illustration of this concept is shown in Figure 4.18. Externally, this design measures 20.5 $\times$ 20.75 $\times$ 12 mm. The columns have a cross sectional dimension of 0.5 $\times$ 0.5 mm. In total, the 179 columns stretch

$\approx$ 2.5 m. Columns were connected by a recess on the face of the block. The inlet and outlet were designed to fit standard 3.175 mm push-fit fittings.

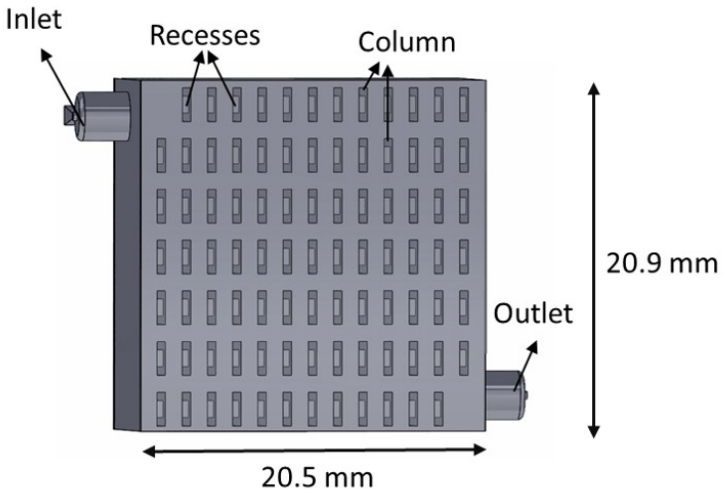

Figure 4.18: CAD of Concept-1 GC

Sealing this GC design was achieved by mounting two acrylic places on both exposed sides of the GC. Before attaching the plates, a thin layer of the R11 resin used by the Envisiontec Perfactory Mini for additive manufacturing was spun on the surfaces of the plates. Both plates were aligned on the exposed surfaces of the GC. The plates were secured using 8 M3 screws and nuts (Figure 4.19). After the assembly process, the R11 was cured by exposure to Ultraviolet (UV) light.

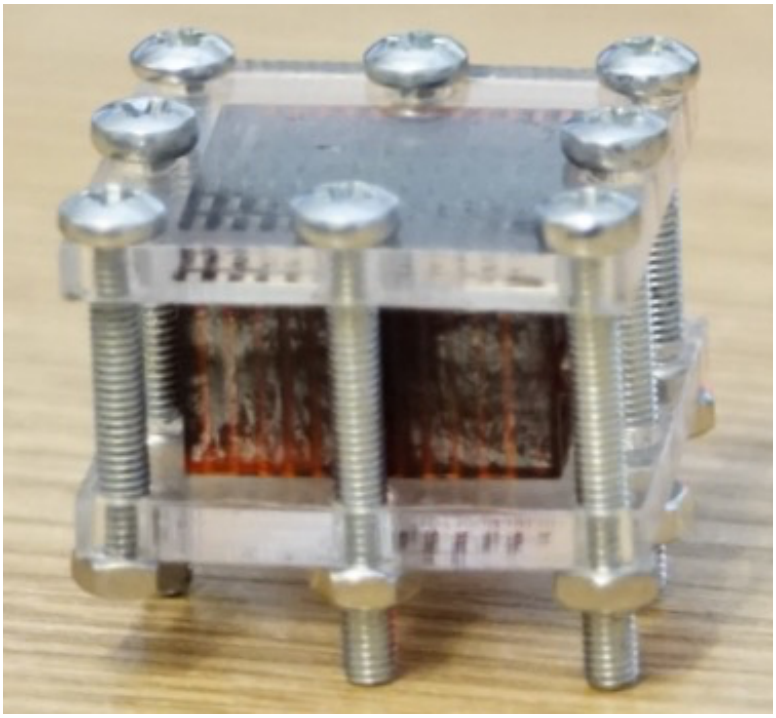

Figure 4.19: Assembled Concept-1 GC

Although the part was successfully built, removing excess material from the structure before curing was challenging. Since the columns were narrow and relatively long, ejecting stuck material before curing introduced imperfections to the column walls which resulted in uneven coating of the column wall with the stationary phase. This could lead to peak broadening and overlapping effluents. This situation was eliminated with Concept-2 design where all of the build was held in a single plane. The column in this design consist of a semi-circular channel which runs as a spiral on both faces of a 20 $\times$ 20 $\times$ 5 mm block (Figure 4.20(a)). The cross sectional geometry of the column was a 0.5 $\times$ 0.9 mm rectangle with rounded corners of 0.1 mm. The corners were rounded to stop manufacturing material or stationary phase coating from getting stuck at the right angle corners. The column is terminated with a 3 mm recess at both ends. One end of the spiral has a 3 mm hole leading to

another 3 mm recess on the opposite face. This bore is used to transport samples from one spiral to the spiral on the opposite side of the GC. Using this method, two separate spirals could function as one GC. This also opens the opportunity for multi-dimensional analysis by using different coatings on different sides of a single GC.

(a) Single GC (b) Stacked GC

Figure 4.20: CAD representation of Concept-2 GC

The second pot serves as inlet or outlet to the spiral column depending on the configuration. When a single GC is used, a 10-32 UNF threaded hole on an acrylic cover is aligned with this pot. The acrylic also has two other holes for mounting to the GC using two M2 screws. When multiple GCs are stacked as shown in Figure 4.20(b), this pot aligns with inlet pot on the subsequent GC. An acrylic plate is inserted between stacked GCs to separate samples and ensure transport to the next GC stage is via the recess. Sealing the GC was performed similarly to Concept-1. An acrylic plate measuring 20×20 mm with two M2 mounting holes and a a 10-32 UNF threaded hole for the inlet. The acrylic plate was coated with a thin layer of the R11 on one surface. The coated surface was mated with one face of the GC.

This procedure was repeated for the second face and the two M2 screws and nuts were used to secure the acrylic covers to the GC. Next the resin serving as adhesive was cured by exposing the assembly to UV light source.

In GC, separation can be improved by increasing the length of the column. Longer columns increase interaction between the sample and the stationary phase coating the column wall. This leads to further delay between effluents from the GC. A single block of Concept-2 GC measures 0.5 m. It would require a stack of 5 to achieve similar length to Concept-1 column albeit with a larger cross sectional area. Additionally, it was observed the stacking process made the unit susceptible to leaks. It was decided that the length of the column will be increased to increase the efficiency of the column.

Concept-2 was altered to increased separation by increasing length. The external dimensions were increased to 100 × 100 × 4 mm. Similar to the original geometry with a a 0.5 × 0.8 mm rectangle with rounded corners of 0.1 mm. With the larger face estate, the column was extended to measure 8.75 m on a single block. This design was larger than the base plates of the available rapid prototyping instruments. At this stage, CNC manufacturing technique was employed. The column was manufactured from a 4 mm aluminium plate. The new design features a single inlet recess on either face (Figure 4.21). A 1 mm bore at the centre of the plate transports analysed samples from the column on one face to the other. A 3.2mm hole was bored in the middle of the plate to allow securing a cover from the middle of the GC and 16 additional 3.2 mm holes were bored around the spiral column to ensure the covering plates mates completely with the GC.

Figure 4.21: CAD of Concept-3 GC

The plates used to seal the GC were manufactured from a single piece of 4 mm acrylic plate measuring 100 × 100 mm. Holes aligning with the 17 holes located in the GC were bored on the cover . A 10-32 UNF thread was machined to align with the inlet\outlet ports which allows a 10-32 UNF to Swagelok 1/8 fitting to be connected to the GC. The acrylic and aluminium block were sealed by coating a single face with a thin layer of the R11. The coated surface was mated with one face of the aluminium GC block. This procedure was repeated for the second face and 17 M3 screws and nuts were used to secure the acrylic covers to the GC. Next the R11 was cured to form a solid bond between the components of the GC by exposing the assembly to UV light. The assembled GC showing the inlet with a 10-32 UNF to Swagelok 1/8 fitting is shown in Figure 4.22.

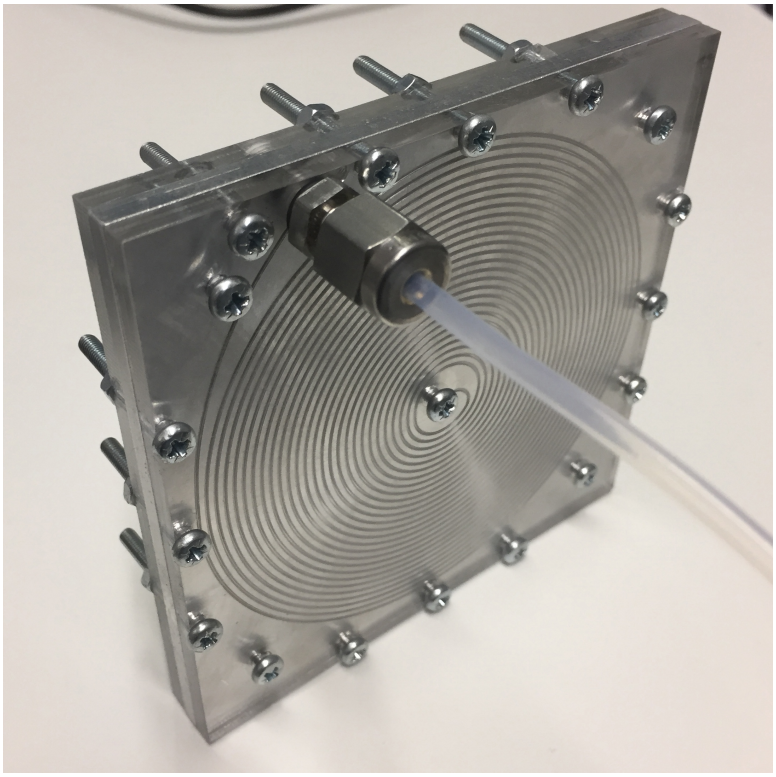

Figure 4.22: Concept-3 GC

The heating system comprises a 25 gauge nichrome wire wrapped around the aluminium wall of the GC. For electrical insulation, the nichrome wire was sleeved with a Pro-Power GSX-S24-1100-NAT fibreglass sleeve. Temperature control was achieved using a K-type thermocouple wound around the GC wall between the nichrome wire. The thermocouple is used to measure the GC surface temperature. The thermocouple is interfaced with an ATSAMD21 microcontroller using the MAX31855 thermocouple-to-digital chip which allows 14-bit temperature measurements over SPI. A Proportional Integral Derivative controller software similar to the controller used for the TDs was designed in C++ language to provide precise temperature control. This software controls a separate PWM output pin on the ATSAMD21 microcontroller. This PWM signal is used to control the voltage input

on a Crydom CMX60D10 relay with the load voltage pins of the relay connected in series with the nichrome coil and a 12 V power supply. The heating system was improved by enclosing the heating coils and chamber in a Spacetherm thermal insulating blanket of 0.5 cm thickness. The GC with the heater and insulation is shown in Figure 4.23.

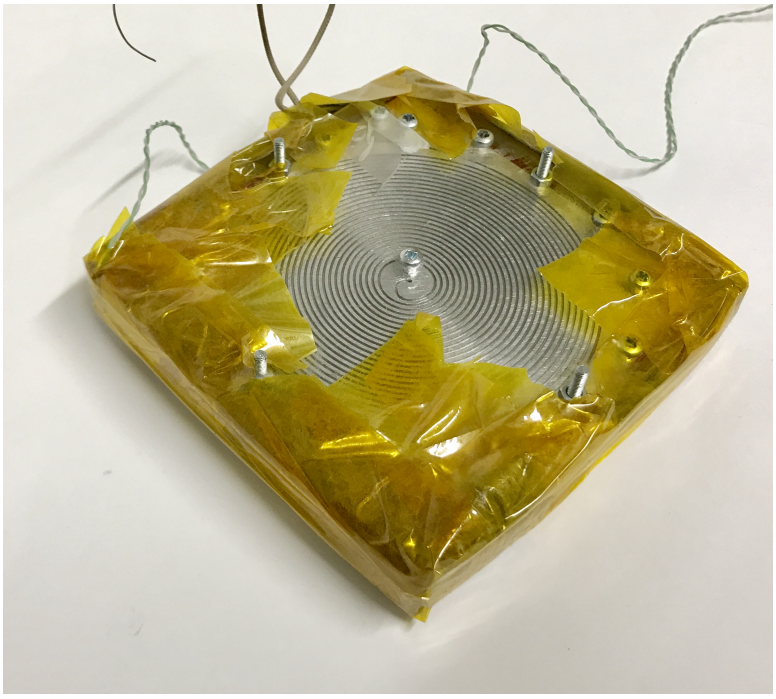

Figure 4.23: Assembly of Concept-3 GC

4.4.2 Stationary phase coating

Separation of compounds in mixture is achieved by interactions between the stationary phase lining the column and the compounds travelling in the column. This makes the stationary phase one of the most important components in GC systems. Over 200 stationary phases were analysed by McReynolds[25] and of these Delley [26] suggested four phases: Carbowax 20M, OV-225, OV-17 and OV-101 as suitable for about 80% of GC analysis. GC stationary phases are generally categorised into

ionic, polar and non-polar phases depending on their interaction with compounds in those categories. Stationary phases are selected to match the compounds that will be analysed, hence, a polar compound will interact more with a polar phase leading to better separation. Non-polar phases are usually preferred in systems where one column is to be targeted at a broad range of compounds because of its better resistance to hydrolysis and oxidation. Poly(organosiloxane) phases are the most commonly used phases owing to their increased chemical inertness, thermal stability, low column bleeding, solubilizing power, selectivity and wide range of polarities [6, 23]. For this design, OV-1(100% Polydymethilsiloxane) was selected as the stationary phase.

There are several methods of coating the stationary phase to the inner walls of the GC column. These methods fall into two groups: static and dynamic coating techniques[27]. Dynamic coating technique involves preparing a solution of the stationary phase and filling the column with it. Next, a plug is used to drive the solution through the column [28, 29]. Figure 4.24 illustrates this procedure showing the red stopper driven along a cutaway section of a column. Lambertus *et al* reported using pressurised helium to drive the stationary phase through the column [30]. Once the coating is complete, the GC is left to dry overnight. This method produces a thin film of the stationary phase on the column wall.

Figure 4.24: Dynamic coating procedure plug driven through the column

Static coating is commonly used commercially as it produces a highly uniform film on the column wall [6, 31]. In this technique, the column is filled with a solution

of the stationary phase and some low boiling point solvent such as pentane. A cross sectional view of a column using technique is illustrated in the Figure 4.25. One end of the column is sealed and a vacuum pump is connected to the other end causing a controlled evaporation of the solvent[29]. This leaves behind a uniform deposition of the stationary phase on the column. Given the geometry of the designed columns and the longer time required to execute the dynamic coating technique, the static coating technique was used.

Figure 4.25: Static coating procedure with plug at column end

The static coating procedure was initially performed as described by Liu *et al* [32] who reported successfully coating OV-1 stationary phase onto a micro-fabricated GC column to produce a 200 nm coating. A solution of the stationary phase was prepared by dissolving 22.3 mg of OV-1 in 6 ml dichloromethane. This mixture was placed on a flash shaker for 45 $mins$ to ensure complete mixing of solute and solvent. Next the column was filled with the solution and one end of the column was sealed. A vacuum pump was connected to the other end to evaporate the solution from the column. The GC was inserted in a vacuum pumped oven (Figure 4.26) for 5 hours at 50°C to evaporate any remaining solvent.

Figure 4.26: Croydon vacuum oven

After coating it was observed that the parts of the channel were blocked by dried stationary phase solution (Figure 4.27). Further examination showed that this was because the dichloromethane in the stationary phase dissolved the acrylic before it was completely evaporated.

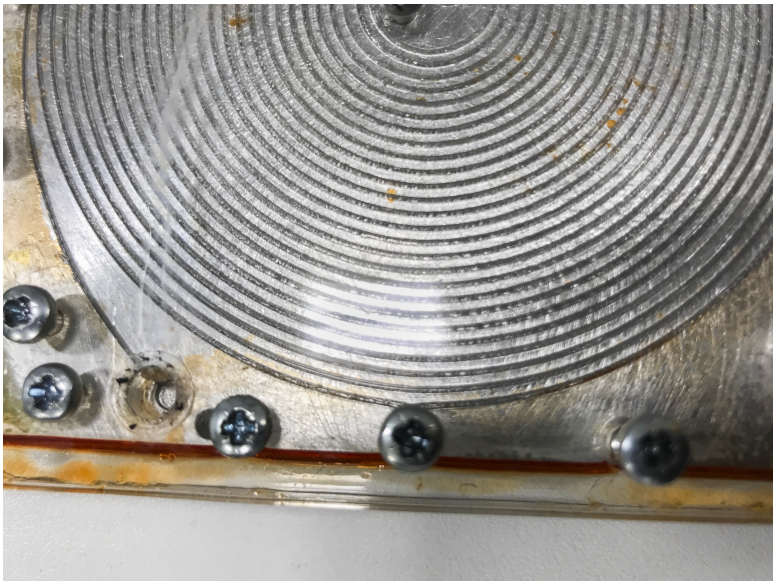

Figure 4.27: GC with blocked column

The coating process was adjusted to resolve this issue. The stationary phase solution was prepared by dissolving 22.3 mg of OV-1 in 6 ml dichloromethane as was mentioned earlier. This mixture was placed on a flash shaker for 45 $mins$ to ensure complete mixing of solute and solvent. Next the exposed column without the acrylic was filled with the solution and allowed to stand for 10 mins. The aluminium spiral column was inserted in a vacuum oven for 1 hour. This procedure was repeated for the other side of the spiral column. Finally, the acrylic cover and aluminium block were sealed by coating a single face with a thin layer of the R11. The coated surface was mated with one face of the aluminium GC block. This was repeated for the second face and 17 M3 screws and nuts were used to secure the acrylic covers to the GC. Next the R11 was cured to form a solid bond between the components of the GC by exposing the assembly to UV light. This procedure produced a coated GC without any blockages. Tests using the PC, GC and VOC detector are presented in Chapter 7.

4.5 Conclusion

This chapter discussed the design process for a PC and GC. ACC was introduced as a PC adsorbent material. Several iterations of TD were designed to improved desorption and efficiency. These designs were tested with the ACC. The steps taken to manufacture the GC was also discussed.

4.6 References

[1] Bartosz Szulczynski and Jacek Gebicki. Currently commercially available chemical sensors employed for detection of volatile organic compounds in outdoor and indoor air. *Environments*, 4(1):21, 2017.

[2] Wei-qi Zhang, Hong Li, Yu-jie Zhang, Fang Bi, Ling-shuo Meng, Xin-min Zhang, Jing-ying Mao, Nian-liang Cheng, Bin Fang, Yuan Yang, et al. Fast determination of monocyclic aromatic hydrocarbons in ambient air using a portable gas chromatography–photoionization detector. *Chromatographia*, 80(8):1233–1247, 2017.

[3] Paweł Mochalski, Helmut Wiesenhofer, Maria Allers, Stefan Zimmermann, Andreas T Güntner, Nicolay J Pineau, Wolfgang Lederer, Agapios Agapiou, Christopher A Mayhew, and Veronika Ruzsanyi. Monitoring of selected skin- and breath-borne volatile organic compounds emitted from the human body using gas chromatography ion mobility spectrometry (gc-ims). *Journal of Chromatography B*, 1076:29–34, 2018.

[4] Ioana Voiculescu, Mona Zaghloul, and Nachchinarkkinian Narasimhan. Microfabricated chemical preconcentrators for gas-phase microanalytical detection systems. *TrAC Trends in Analytical Chemistry*, 27(4):327 – 343, 2008.

[5] F.J Santos and M.T Galceran. The application of gas chromatography to environmental analysis. *TrAC Trends in Analytical Chemistry*, 21(9):672 – 685, 2002.

[6] Katja Dettmer-Wilde and Werner Engewald. *Practical Gas Chromatography*. Springer, 2016.

[7] Chia-Jung Lu and Edward T Zellers. A dual-adsorbent preconcentrator for a portable indoor-voc microsensor system. *Analytical chemistry*, 73(14):3449–3457, 2001.

[8] William A Groves, Edward T Zellers, and Gregory C Frye. Analyzing organic vapors in exhaled breath using a surface acoustic wave sensor array with preconcentration: Selection and characterization of the preconcentrator adsorbent. *Analytica Chimica Acta*, 371(2-3):131–143, 1998.

[9] Jay W Grate, Norman C Anheier, and David L Baldwin. Progressive thermal desorption of vapor mixtures from a preconcentrator with a porous metal foam internal architecture and variable thermal ramp rates. *Analytical chemistry*, 77(6):1867–1875, 2005.

[10] Chongdee Thammakhet, Panote Thavarungkul, Roman Brukh, Somenath Mitra, and Proespichaya Kanatharana. Microtrap modulated flame ionization detector for on-line monitoring of methane. *Journal of Chromatography A*, 1072(2):243–248, 2005.

[11] Naihong Zhu, Zixian Li, and Somenath Mitra. Application of on-line membrane extraction microtrap gas chromatography (olmem-gc) for continuous monitoring of voc emission. *Journal of Microcolumn Separations*, 10(5):393–399, 1998.

[12] Qing-Yun Cai, Jeongim Park, Dylan Heldsinger, Meng-Da Hsieh, and Edward T Zellers. Vapor recognition with an integrated array of polymer-coated flexural plate wave sensors. *Sensors and Actuators B: Chemical*, 62(2):121–130, 2000.

[13] Yuko Ueno, Tsutomu Horiuchi, Takashi Morimoto, and Osamu Niwa. Microfluidic device for airborne btex detection. *Analytical chemistry*, 73(19):4688–4693, 2001.

[14] I Gràcia, P Ivanov, F Blanco, N Sabate, X Vilanova, X Correig, L Fonseca, E Figueras, J Santander, and C Cané. Influence of the internal gas flow distribution on the efficiency of a μ-preconcentrator. *Sensors and Actuators B: Chemical*, 135(1):52–56, 2008.

[15] F Blanco, X Vilanova, V Fierro, A Celzard, P Ivanov, E Llobet, N Cañellas, JL Ramírez, and X Correig. Fabrication and characterisation of microporous activated carbon-based pre-concentrators for benzene vapours. *Sensors and Actuators B: Chemical*, 132(1):90–98, 2008.

[16] S Camou, A Shimizu, T Horiuchi, and T Haga. Ppt-level aqueous benzene detection with an uv-spectroscopy based portable sensor. In *Sensors, 2009 IEEE*, pages 2021–2024. IEEE, 2009.

[17] Bassam Alfeeli. *Chemical micro preconcentrators development for micro gas chromatography systems*. PhD thesis, Virginia Tech, 2010.

[18] S Giraudet and P Le Cloirec. Activated carbon filters for filtration–adsorption. In *Activated Carbon Fiber and Textiles*, pages 211–243. Elsevier, 2017.

[19] Zorflex acc, October 2018.

[20] Tenax surface area, October 2018.

[21] A Subrenat, P Le Cloirec, and E Subrenat. Voc adsorption-desorption cycle with activated carbon cloth: regeneration by joule effect.

[22] Abhinav Bhushan, Dawit Yemane, Edward B Overton, Jost Goettert, and Michael C Murphy. Fabrication and preliminary results for liga fabricated nickel micro gas chromatograph columns. *Journal of microelectromechanical systems*, 16(2):383–393, 2007.

[23] Abhinav Bhushan, Dawit Yemane, Dan Trudell, Edward B Overton, and Jost Goettert. Fabrication of micro-gas chromatograph columns for fast chromatography. *Microsystem Technologies*, 13(3-4):361–368, 2007.

[24] Satish G Kandlikar and William J Grande. Evolution of microchannel flow passages: thermohydraulic performance and fabrication technology. In *ASME 2002 International Mechanical Engineering Congress and Exposition*, pages 59–72. American Society of Mechanical Engineers, 2002.

[25] Eugene F Barry and Robert L Grob. *Columns for gas chromatography: performance and selection*. John Wiley & Sons, 2007.

[26] R Delley and K Friedrich. System cg 72 von bevorzugten trennflüssigkeiten für die gas-chromatographie. *Chromatographia*, 10(10):593–600, 1977.

[27] Milton L Lee. *Open Tubular Column Gas Chromatography: Theory and Practice*. Wiley-Interscience, 1984.

[28] ES Kolesar and RR Reston. Silicon-micromachined gas chromatography system used to separate and detect ammonia and nitrogen dioxide. ii. evaluation, analysis, and theoretical modeling of the gas chromatography system. *Journal of microelectromechanical systems*, 3(4):147–154, 1994.

[29] Shaelah Reidy, Gordon Lambertus, Jennifer Reece, and Richard Sacks. High-performance, static-coated silicon microfabricated columns for gas chromatography. *Analytical Chemistry*, 78(8):2623–2630, 2006.

[30] Gordon Lambertus, Andrea Elstro, Kathryn Sensenig, Joseph Potkay, Masoud Agah, Susan Scheuering, Kensall Wise, Frank Dorman, and Richard Sacks.

Design, fabrication, and evaluation of microfabricated columns for gas chromatography. *Analytical chemistry*, 76(9):2629–2637, 2004.

[31] Kurt Grob. *Making and manipulating capillary columns for gas chromatography*. Hüthig, 1986.

[32] Jing Liu, Jung Hwan Seo, Yubo Li, Di Chen, Katsuo Kurabayashi, and Xudong Fan. Smart multi-channel two-dimensional micro-gas chromatography for rapid workplace hazardous volatile organic compounds measurement. *Lab on a Chip*, 13(5):818–825, 2013.

Chapter 5

Design And Development of VOC Ionisation Detector

5.1 Introduction

There has been an increase in the application of Volatile Organic Compound (VOC) detectors in various fields due to increasing regulatory requirements for VOCs which are considered harmful at even low concentrations. Detection of VOCs have been applied to the diagnosis of various diseases [1–5]. It has also been widely used in monitoring agricultural produce [6–9], pharmaceuticals [10], air quality [11], food and beverages [10, 12, 13].

Several technologies have been employed in VOC detection. Currently, instruments used for VOC analysis include Gas Chromatography Mass Spectrometry (GC-MS), Gas Chromatography Ion Mobility Spectrometry (GC-IMS), Photoionization Detector (PID), Metal Oxide Sensor (MOS) and optical sensors to name a few.

GC-MS is often stated as the gold standard for VOC analysis because of its high sensitivity, accuracy, reproducibility and overall robustness. However, wider adoption of this technologies outside the lab environment is limited by several factors including cost of purchase, complexity of operation and long analysis time. Its size and weight reduce their portability and restrict their use. MOS and PID instruments are smaller in size, significantly cheaper and more portable in comparison. Some commercial PIDs offer analysis times within a second [14]. MOS sensors are the cheapest but tend to suffer from cross sensitivity to inorganic gases. They also have poor humidity tolerance and can drift over time with low accuracy outputs. PID sensors are still relatively low cost and are highly sensitive and so used extensively for the detection of a broad range of VOCs. They can provide a linear output to a single chemical or mixture of chemicals, in real-time, and have a sensitivity in the parts per billion (ppb) range [15, 16]. Furthermore, as they are undertaking a physical measurement, they are less likely to drift over time. PIDs have also been used to detect effluent from Gas Chromatograpy (GC), Liquid Chromatography (LC) and coupled with Ion Mobility Spectrometry (IMS) and Mass Spectrometry (MS) [16]. Several PID sensors are commercially available from manufacturers including Alphasense and Mocon and cost under $500. Although these attributes make the PID a suitable sensor for many VOC analysis, PID sensors only provides a concentration value of the sample being tested, without any additional information of the chemical composition. In this chapter, a novel VOC ionisation detector that offers additional compositional information about the sample under test is presented.

5.2 Theory

As explained in Chapter 2, the operation of a commercial PID can be divided into three steps: gas supply, ionisation and detection. In use, gas phase samples flow through an ionisation chamber within the PID sensor. Some commercial PIDs include pumps to enhance gas flow through the chamber. Once in the chamber, the gas is ionised by absorbing the energy released from an ionisation source. The ionisation reaction mechanism leading to the formation of photoions is given by Equation 5.1.

$$hv + M \rightarrow M^{+} + e^{-} \tag{5.1}$$

Photons (hv) from the ionisation source are absorbed by an analyte molecule (M) leading to the formation of an excited molecule (M^{*}). When hv is greater than the ionisation energy (IE) of the molecule, the molecule releases an electron leading to the formation of a cation.

In the detection step an electric field applied to drive the cations to an electrode. The resulting current is measured and it is an indication of the quantity of M^{+} present hence providing information on the concentration of the analytes. In use, PIDs sensors do not provide any compositional information, giving only an indication of the concentration value of the sample under tested. Additionally these sensors cannot be used for the analysis of toxic samples, without additional equipment as they are not leak proof. The following sections presents the mechanical and electronic work undertaken to design a leak proof PID sensor that provides some compositional information.

5.3 Mechanical Design

The ionisation detector was separated into three regions namely:

Ionisation region where samples are trapped in a cavity and ionised.

Electric field/filtration region where ionised samples are filtered/separated.

Detection region where surviving ion species from the previous steps are measured.

These regions are shown in the PID device depicted in Figure 5.1

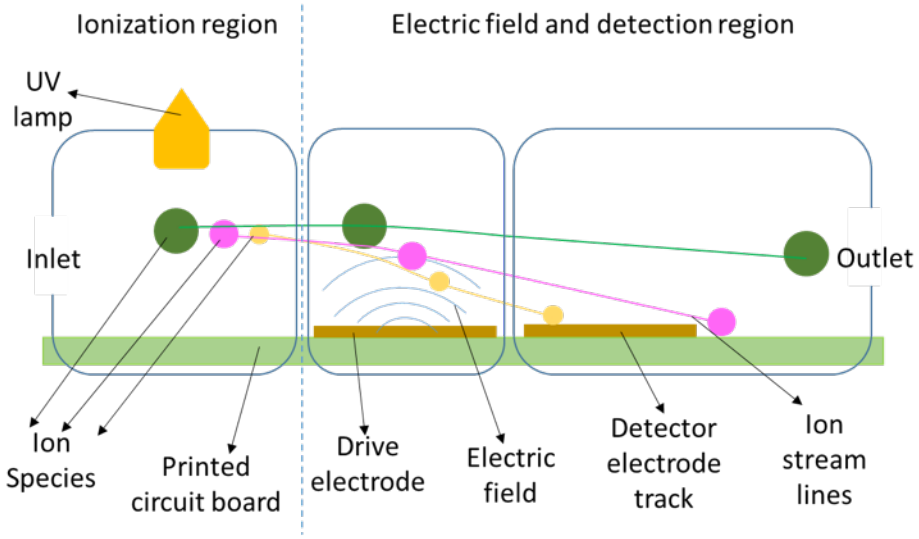

Figure 5.1: Active sections in a PID sensor

5.3.1 Ionisation source

To improve ionisation in comparison to commercial PID sensors, several ionisation sources were considered including the following:

1. Electrospary
2. Corona discharge
3. Radioactive sources (Americium - 241, Nickel – 63 etc.)
4. Photoionisation

The cost and complexity of designing an electrospray and corona discharge ionization source made these options unsuitable for a simple, low-cost instrument. Additionally, the large size of these sources and their associated power supply would reduce portability. Since these options are contrary to the design objective of a simple, low-cost device, they were discarded. Radioactive and photoionisation sources are compared Table 5.1.

Table 5.1: Comparison of Photoionization and Radioactive Sources

Characteristics	**Photoionization**	**Radioactive Sources**
Ionising energy	9 – 11 eV	5.48 MeV
Ionisation range	VOCs with ionization energy less than 11eV	All VOCs
Ionisation distance	Few centimetres	Few centimetres
Safety	Relatively safe when kept in ideal case	Requires specialized casing
Human exposure effect	Damaging to eyes and skin when exposed to Ultraviolet (UV) light	Toxic and radioactive. Fatal radiation sickness when in direct contact or within a few centimetres from source
Power source	RF or high voltage	None
Procurability	Easy	Difficult

Radioactive ionisation offers higher ionisation potential. However, the hazard associated with radioactive sources makes them difficult to procure, use, transport and dispose. These factors also increase the cost of devices using radioactive ionisation as special ionisation chambers, instrument enclosures and transportation cases are required to meet legal requirements for using radioactive sources. Photoionisation sources are relatively straightforward to implement in industrial designs and is the cheapest of the four ionisation sources presented. The electric potential of the UV sources cover most of the target VOCs and the risk associated with their use is low when compared with radioactive sources.

Several photoionization sources were considered from various manufacturers in-

cluding Hamamtsu and Alphasense. Photoionisation light sources from Hamamtsu measured about 240 × 110 mm and required an additional cooling fan and a mains powered power supply measuring 298 × 123 mm and cost about £ 1300. These units were too large and expensive for the intended application. UV light bulbs from Alphasense measure 6 × 11 mm. They can be powered using RF power or high voltages (>1000 V) and these circuits could be integrated with the PID power supply circuit. Their small size enhances the design of a smaller ionisation chamber and reduces the power required for ionisation. Additionally, it improves portability of the overall instrument. UV bulbs with 9.6 eV, 10.6 eV and 11.7 eV are available from Alphasense. The 9.6 eV bulbs have ionisation energy too low for some of the target VOCs. While the 11.7 eV bulb covers the ionisation energy range of interest, it has a very short lifetime. The 10.6 eV UV bulbs have a 2000-hour lifetime and can ionise most of the VOCs to be analysed hence it was decided that 10.6 eV bulbs would be utilised for ionisation in this system. One of the bulbs sourced from Alphasense is shown in Figure 5.2.

5.3.2 Ionisation chamber

The ionisation chamber traps the analytes in a defined space ensuring it is ionised by high energy photons from a UV bulb. The leak proof chamber was designed to enhance ionisation by allowing maximum exposure of the analytes to the ionisation source. The design of the ionisation chamber was improved over several iterations. This design process discussed in the following section.

A CAD model and fluid simulation of the first prototype ionization chamber is shown in Figure 5.3. It shows the mounting hole for the UV bulb, inlet and outlet into the filtration/separation region. This approach was to ensure exposure of

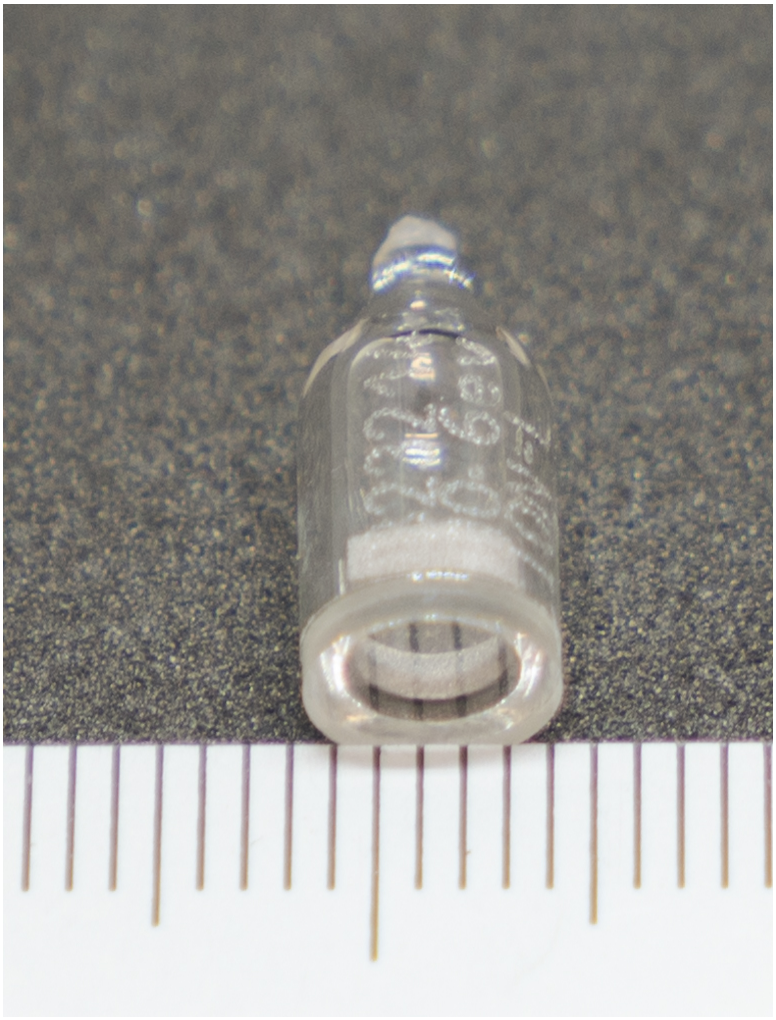

Figure 5.2: UV ionisation bulb

analytes to photons from the UV source and to create a good seal. Manufacturing this prototype was expensive and complex, as it required the assembly of four different components - the top cover with UV bulb mount, inlet male connector, base cover and outlet to separation/filtration connector. Additionally, this design makes it difficult to integrate electronic connections that will be required for the filtration and detection signals downstream, while ensuring the integrity of inner chamber surfaces.

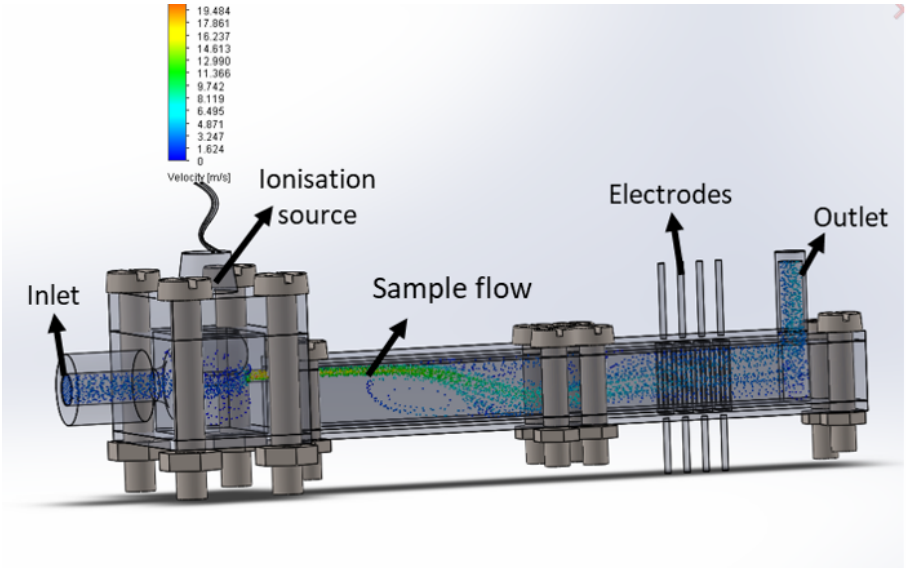

Figure 5.3: Design-1 Ionisation chamber and detection region

Design-1 was simplified by redesigning the ionisation chamber. The new design requires fewer components and improved integration with the required electronics. This novel design incorporates all electronic components onto a single PCB with the electrodes exposed on the PCB surface. The chamber is designed to enclose the electrode and provide a sealed cavity for sample flow perpendicular to the UV rays. In design-2, the ionisation chamber was machined from a single block of aluminium measuring 70 × 35 × 5 mm. Two holes were machined on the top of the chamber to serve as sample inlet and outlet. Both holes were threaded to 10 - 32 UNF size. Two 10 - 32 UNF to 1/8" push-fit connector adapters were connected to the top of the ionisation chamber. These adapters made it easier to connect the inlet to 1/8" tubing for sample injection and ejection. A 6 mm bore was machined between the inlet and outlet to mount the UV bulb and allowed the UV rays into the stream of molecules travelling in the chamber. A channel with 0.2 mm depth was machined to link the inlet to the outlet beneath the UV bulb mounting hole. This channel guided the samples from the inlet to the outlet through the exposed bore for the UV bulb.

The chamber was fastened to the PCB already containing the filtering/detection electrodes and electronics using 14 M3 screws and nuts. Design-2 chamber is shown in Figure 5.4.

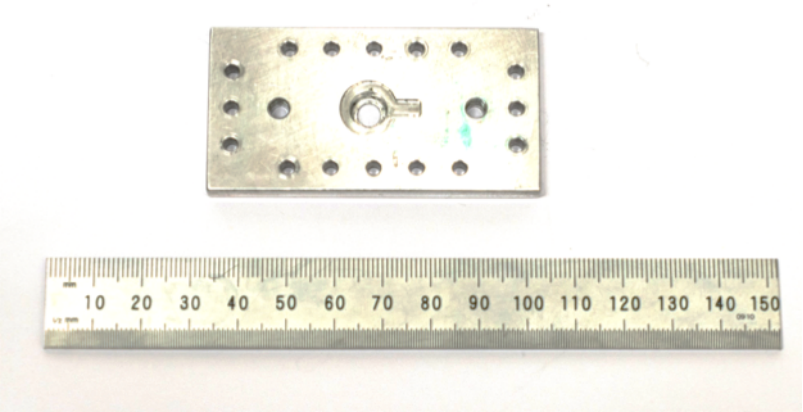

Figure 5.4: Design-2 ionisation chamber

A 0.6mm groove was machined around the channel, inlet and outlet and a 1 mm O-ring was inserted into the groove. When fastened to the PCB, the O-ring was compressed between the bottom of the ionisation chamber and the PCB to improve the sealing of the chamber. This is shown in Figure 5.5.

Figure 5.5: Design-2 ionisation chamber with groove and O-ring

It was observed that the tubing connection to both the inlet and the outlet via the 10-32 UNF fittings resulted in mechanical stresses which were transferred from the chamber to the PCB. With prolonged use, the PCB began to flex leading leaks from the mating surface between the PCB and chamber surfaces. This situation originated from the location of the tubing and fittings transverse to the length of the chamber, hence the forces of both upright fittings were increased by the moment at the chamber surface.

In Design-3, the inlet, outlet and sample path were redesigned to lie parallel to the length of the chamber, which significantly reduced the forces transferred from the tubing to the chamber. Additionally, the size of the chamber was reduced to be 45mm $\times$ 18mm $\times$ 10 mm. This reduction in size reduces the moments acting on the chamber, and reduced the overall footprint of the sensor. A CAD design of Design-3 with both inlet and outlet fittings attached is shown in Figure 5.6. The chamber

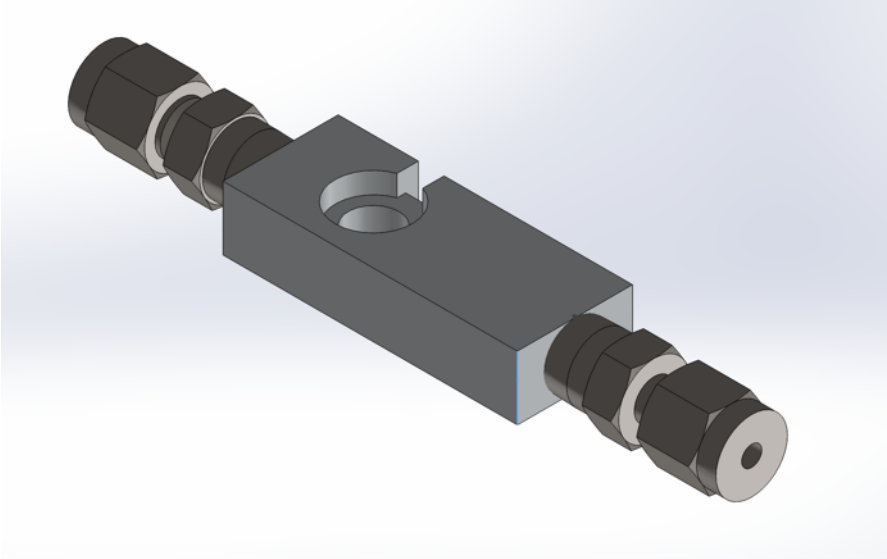

Figure 5.6: Design-3 showing UV bulb bore and 10-32 UNF inlet and outlet fittings

volume and distance of travel between inlet and ionisation source were also reduced in to improve ionisation and detection. Additionally, a channel was machined to

guide analytes from the inlet through the ionisation, filtration and detection regions to the outlet. The channel path just below the UV bulb was constricted to the diameter of the UV bulb window (6 mm) to ensure all analytes were sufficiently exposed to the high energy photons from the bulb. The path after the ionisation region was split in two to allow simultaneous analysis of the same ion species using different electric fields. Both sides of this split were separated using a 0.6 mm O-ring. A 0.6 mm groove was machined around the sample path and a 1 mm O-ring was inserted into the groove to seal the chamber. The channel in Design-3 and split sample path is shown in Figure 5.7.

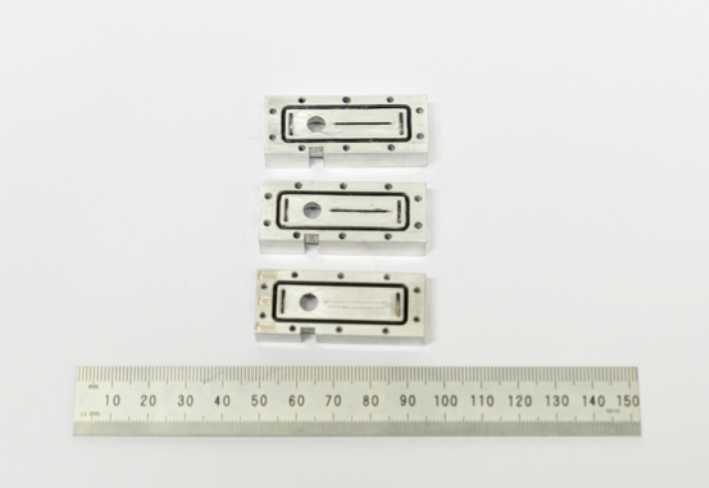

Figure 5.7: Design-3 ionisation chamber with 0.3, 0.1, 0.05 mm channel depth and split sample path

Design-3 had several advantages including ease of manufacture, requiring fewer components, smaller footprint and relatively easy integration with the PID electronics. Tests carried out using Desing-3 showed low concentration ionised samples were easily ionised and detected. However, applying high voltage electric field in the filtration region resulted in interference at the detection electrode. A contributing factor was the small gap between the PCB and the chamber which allows electromagnetic interference to be transmitted through the chamber. The interfering signal

travels along the chamber to the detection region where it affects sensitive detection circuit.

Design-4 was developed to reduce the interference between the filtration and the detection regions. The chamber was split into two halves with the split located at 17 mm from the outlet. A 3 x 2 mm thick flange were machined into the mating faces of the outlet and inlet halves respectively. The CAD assembly of this design is shown in 5.8.

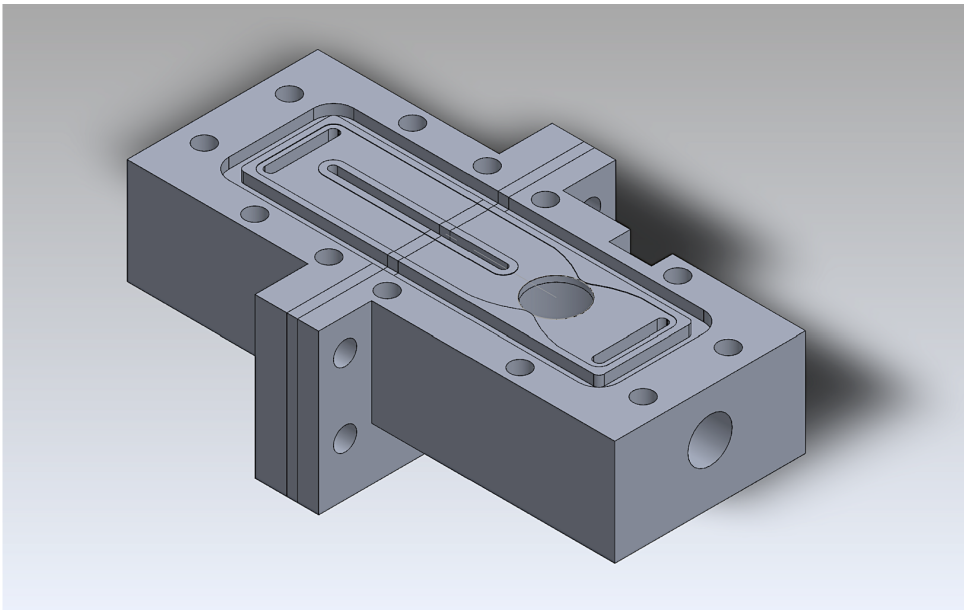

Figure 5.8: Design-4 CAD assembly

It was a challenge to machine features under the chamber including O-ring grooves, sample channel pathway and slots. This was because the PTFE flexed during machining resulting in misalignment between both halves of the chamber. A custom metal case was manufactured to improve the rigidity of the chamber during machining (Figure 5.9).

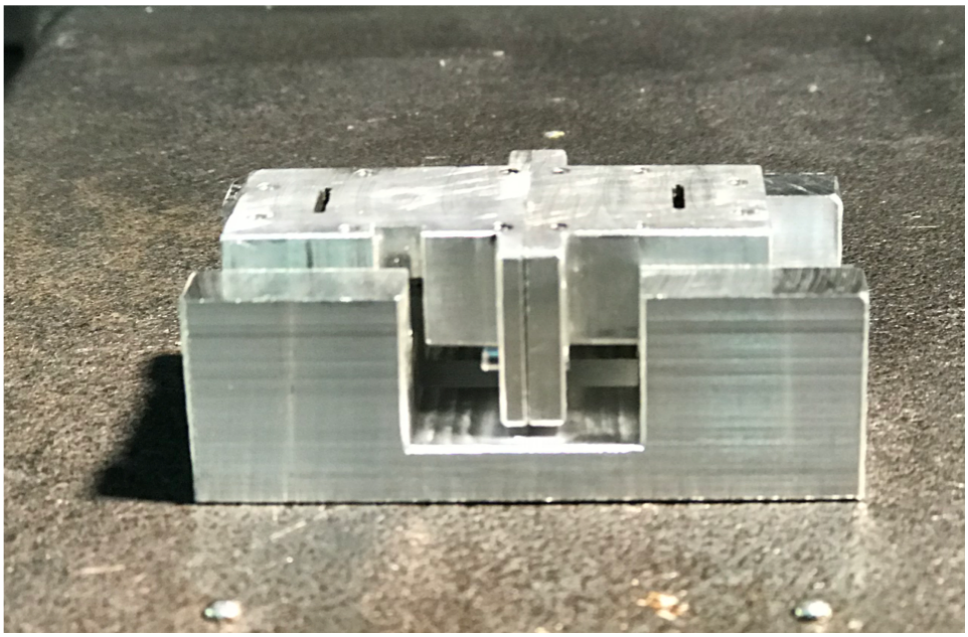

Figure 5.9: Design-4 CAD assembly

Five 2 mm holes were drilled through the flanges to mate to the chamber parts. For electrical isolation between the different regions of the chamber, a 1 mm PTFE section was inserted between both halves and the assembly. The PTFE isolator was held in place by five PTFE M2 screws and nuts. PTFE screws and nuts were used to ensure electrical insulation between the filtration and detection regions. The final assembly of the chamber with the PTFE isolator is shown in Figure 5.10.

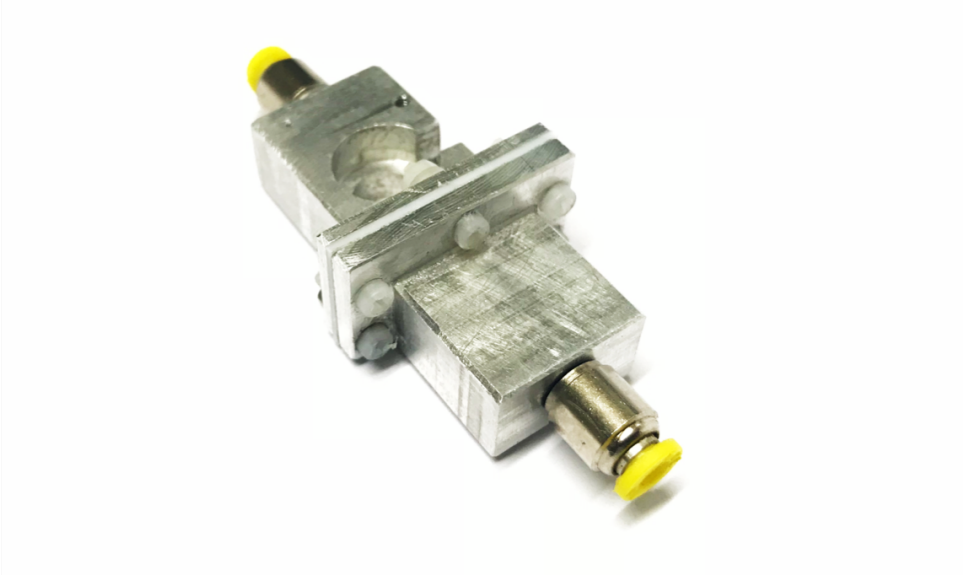

Figure 5.10: Design-4 ionisation chamber.

Electromagnetic/radio frequency interference was significantly reduced with the split chamber in Design-4. However, the metal chamber acts as an antenna when high voltages are supplied, which resulted in some interference when the high voltage filtering signal is in use. To solve this challenge, electrically insulated chambers manufactured from "Clear Photoreactive Resin" (FormLabs) were explored. Clear Photoreactive Resin is a rapid prototyping material consisting of methacrylic acid esters and photoinitiator. Using 3D printing technology, chambers were built from ensuring complete electrical insulation between different regions in the chamber. These chambers were manufactured using 3D printing technology. The Form 2 Desktop 3D printer manufactured by FormLabs was used to manufacture the chamber models. The printer is capable of achieving resolutions down to 200 microns. A CAD design of this approach is shown in Figure 5.11.

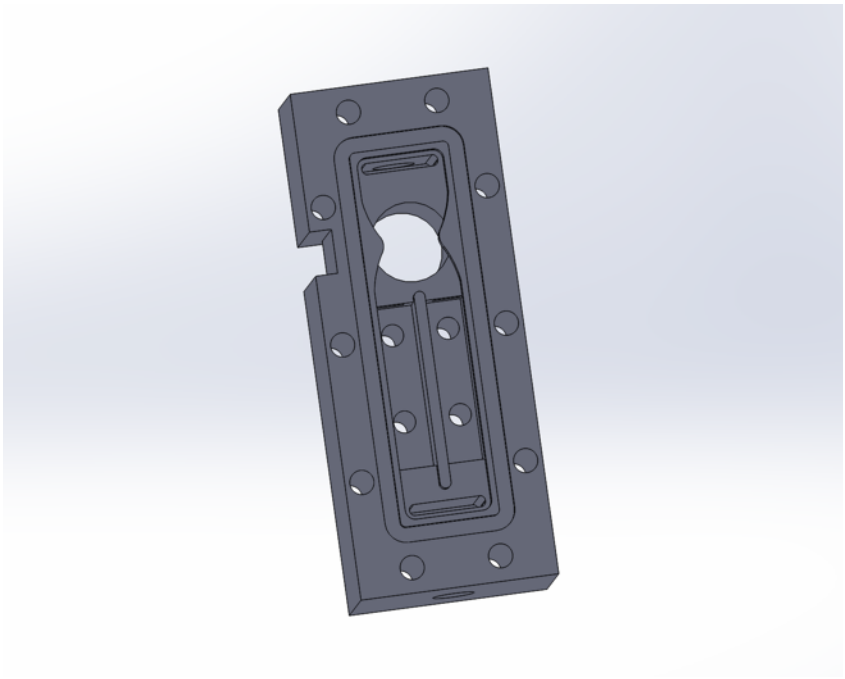

Figure 5.11: CAD representation of Design-5 ionisation chamber showing bores for deflection pads.

The chamber measures 46 × 18 mm. However, the depth was increased to 15 mm. This was necessary to allow further machining and polishing of the mating surface since the flatness/smoothness of the 3D printed surface is not assured during manufacture. Two 15 × 3.5 × 3 mm slots were built into the chamber to house electrode pads that will be used as opposing electrodes above the PCB. Connections to the pads are serviced by four 2 mm bores. A 1 mm O-ring is inserted into a 0.6 mm groove to provide a seal around the sample path. The threaded plastic material does not provide enough strength to fasten the chamber to the PCB. For this reason, the 12 M2 threads used to fasten the chamber to the PCB were replaced with 10 2.2 mm bores running through the depth of the chamber. In this configuration, 10 × 22 mm length M2 screws and nuts were used to affix the chamber to the PCB.

Figure 5.12: 3D manufactured ionisation chamber with exposed slots for electrode pads

The upper electrodes were designed from a single PCB with two pads on one side. A 0.8 mm via was drilled in the middle of the pads and a 20 mm copper pin was soldered to the via. This assembly was inserted into the slot in the 3D printed chamber with the copper pins emerging from the top of the chamber. Filtration and detection signals were transmitted to the chamber via cables soldered to the electrode pins. The assembly was held in place with Loctite glue. This approach produced the least interference at the detection circuit.

5.4 Electronics Design

Traditional PID sensors provide concentration information by measuring the total current generated from the ionisation in the previous stage. In this work a novel

filtration/separation stage was introduced to affect the ions generated and provide some form of compositional information on the sample tested. The generated ions are propelled over an array of electrodes for filtering and detection. This array consists of electrodes supplying a high electric field to deflect the stream of ions resulting in some ions striking the chamber walls. Some of the ions reach the other electrodes serving as detectors. Two of this array configuration was implemented in the design. In one array, the electric field was held constant and the output from this configuration is an indication of the total sample concentration (similar to commercial PID sensor). This configuration comprises a concentration electrode generating a fixed electric field for deflection ions and a detection electrode measuring the concentration of the sample. In the second array, the electric field is varied resulting in changes to the deflection of ions. This electric field acts as a filter by eliminating some ion specie before the detection stage. The output from this configuration provides some composition information on the analytes. The arrays are separated by a grounded plane to ensure there is no interference between the electrode configurations. Additionally, each configuration sample path is isolated, therefore, ions from one configuration cannot reach the detectors of the other.

5.4.1 Filtration electronics

Cations from the ionisation chamber carry a net positive charge. By varying the electric field in the filtration region the trajectory of ions could be changed to affect ions reaching the detection. Three approaches were developed to alternate the electric field in the filtration region. These are sweep, integral and field asymmetric waveform concepts.

Sweep electric field

Here the electric field is generated by applying a triangular waveform to the filtration region. This waveform was swept between a fixed positive and negative voltage at 2Hz. As the magnitude and charge of the electric field changes its effect on the ionised samples changes depending on the charge and mass of the ions. A LabVIEW software was designed to generate the triangular waveform. The software drives a Ni-DAQ USB 6008 which generates a triangular waveform from + 10V to - 10V. This output is connected to the sweep electrodes. The array of electrodes is shown in Figure 5.13. The concentration electrode is held at a ground potential which allows all ions generated at the ionisation stage to reach the concentration detector. The measurement obtained from the concentration detector corresponds to the total detectable molecules in the sample. The electric field was further increased by

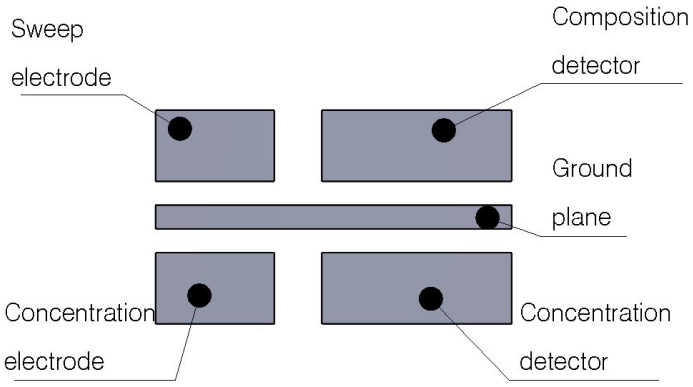

Figure 5.13: Sweep electric field sensor electrode layout

increasing the voltage peak to 22 V resulting in increased filtering of ions. The Ni-DAQ USB 6008 was replaced with an ATSAMD21G18 M0 microcontroller offering 12-bit analogue to digital converter, smaller form factor and easier customisation of electronics and software. An MCP4725 digital to analogue converter was connected

to one of the I^2C ports exposed on the ATSAMD21G18. A C/C++ software was written for the ATSAMD21G18 to control the MCP4725 and generate a 5Vpp triangular waveform output from the MCP4725. This waveform was fed into a voltage

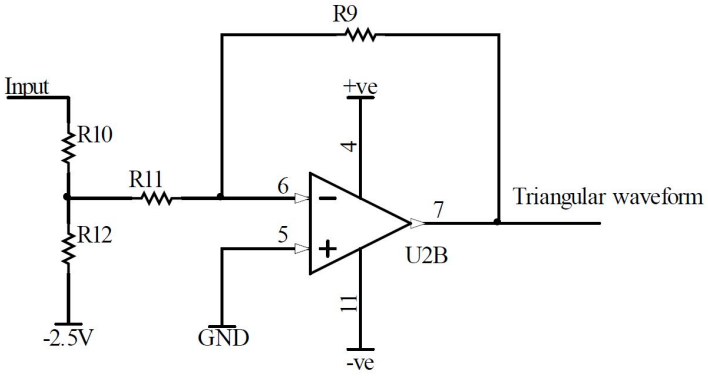

Figure 5.14: Sweep electric field generator

divider circuit shown as R11 and R12 in Figure 5.14. The voltage divider is used to convert the 0 to 5V waveform from the MCP4725 to a -1.25V to +1.25V triangular waveform at the inverting input of the op-amp. The triangular waveform output from the opamp could be swept from +6 kV/cm to - 6 kV/cm. The output from this op-amp is connected to the sweep electrode in Figure 5.13.

Integral electric field

By scanning through a range of voltages the sweep electric field generates a varying electric field that is non dependent on the molecules tested. The integral electric field was developed to introduce a relationship between the samples tested in the concentration electrode and the electric field generated in the integral electrode. The electrode configuration in this setup is shown in Figure 5.15.

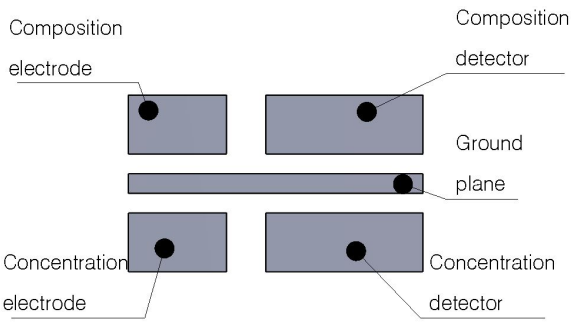

Figure 5.15: Integral electric field sensor electrode layout

The measured current from the concentration detector is fed back into the composition electrode after passing through a trainsimpedance amplifier. The electronic circuit for the integral electric field generator is shown in Figure 5.16. The concentration detector is connected to U1D, which converts and amplifies the current to be a voltage. This voltage is supplied to U1B inverting input through R4. The inverting input is connected to the voltage obtained from the composition detector. The op-amp U1B serves as an integrator, it generates a voltage that corresponds to the magnitude and duration of the peak voltage measured from the concentration detector in U1D.

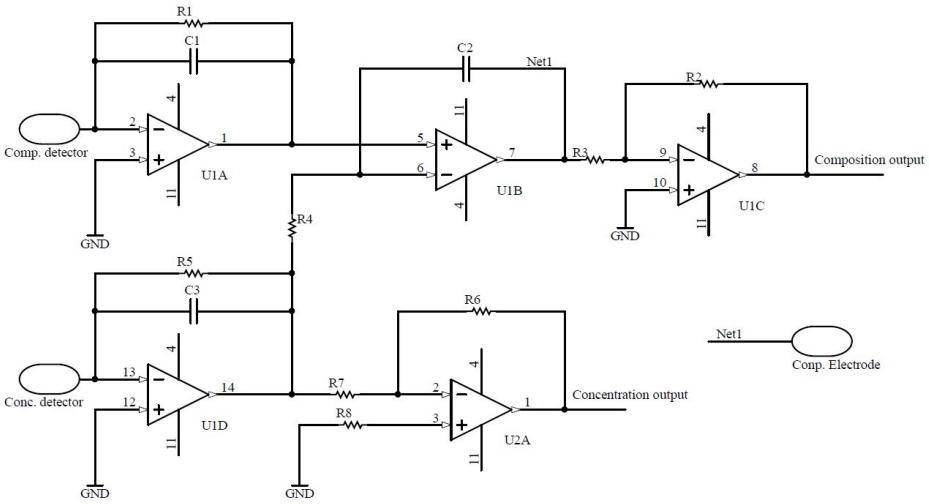

Figure 5.16: Integral electric field sensor electrode layout

For a constant concentration voltage the output of U1B is ramped and fed to the composition electrode. The ramp in the composition electric field results in an increase or decrease in ions detected at the composition electrode. Current measured at the composition electrode is fed into the non-inverting input of U1B after the transimpedance amplifier U1A. This makes U1B produce an output that equates to the difference between the magnitude and duration of a particular molecules concentration and the measured composition voltage. This setup changes the composition electric field to find an electric field that corresponds to the molecules under test.

Field asymmetric waveform

The approach applied here was to design a waveform similar to the filtration waveform used in Field Asymmetric Ion Mobility Spectrometry (FAIMS). In FAIMS, the mobility of most ions in the filtration region is described by Equation 5.2 where α represents the dependence of mobility on the ratio of the electric field E and the

neutral density N.

$$K\left(\frac{E}{N}\right) = K_0\left(1 + \alpha\left(\frac{E}{N}\right)\right) \tag{5.2}$$

The mobility of ions depends on an asymmetric waveform applied to the ion stream with E greater than 20,000 V/cm and -1000 V/cm. The waveform changes the trajectory of the ion species depending on their individual mobility and the electric field. Some ions pass through the electric field to the detector, while others are deflected towards the chamber boundaries. A low DC voltage can be superimposed on the waveform to direct a narrow band of ions through the channel towards the detector. This voltage is referred to as the compensation voltage.

The FAIMS waveform was generated by amplifying a 5 V square wave signal using a 555 chip running in astable mode is shown in Figure 5.17.

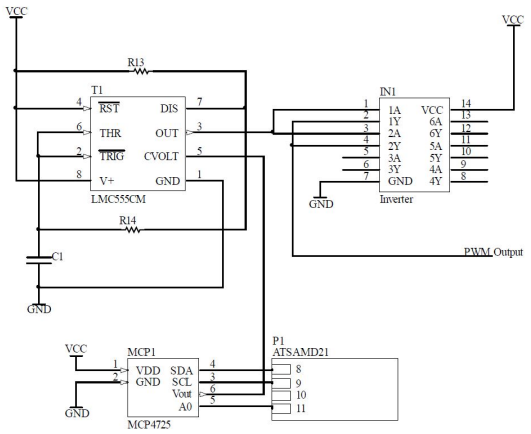

Figure 5.17: 555 PWM signal generator

Resistors R13, R14 and capacitor C1 can be varied to produce the desired PWM frequency. To create an asymmetric waveform, the voltage at pin 5 of the 555 timer is varied to change the pulse width. The ATSAMD21 microcontroller is programmed to change the voltage at pin 5 using MCP4725 Digital to Analog Converter (DAC).

This allows evaluation of the FAIMS against several pulse widths for ion filtration optimisation. The PWM output from the 555 chip was fed into a hex inverter which helps to reduce distortion in the waveform at high frequencies.

Several waveform amplification techniques were investigated to step up the PWM signal to generate electric fields in excess of 20,000 V/cm. The monostable multivibrator was also explored however this suffered from distortion at frequencies above 300 kHz. A custom MOSFET driver was designed with the aim of amplifying PWM peak voltage to 600 V with frequency above 1 MHz. An illustration of the components of this circuit is shown in Figure 5.18.

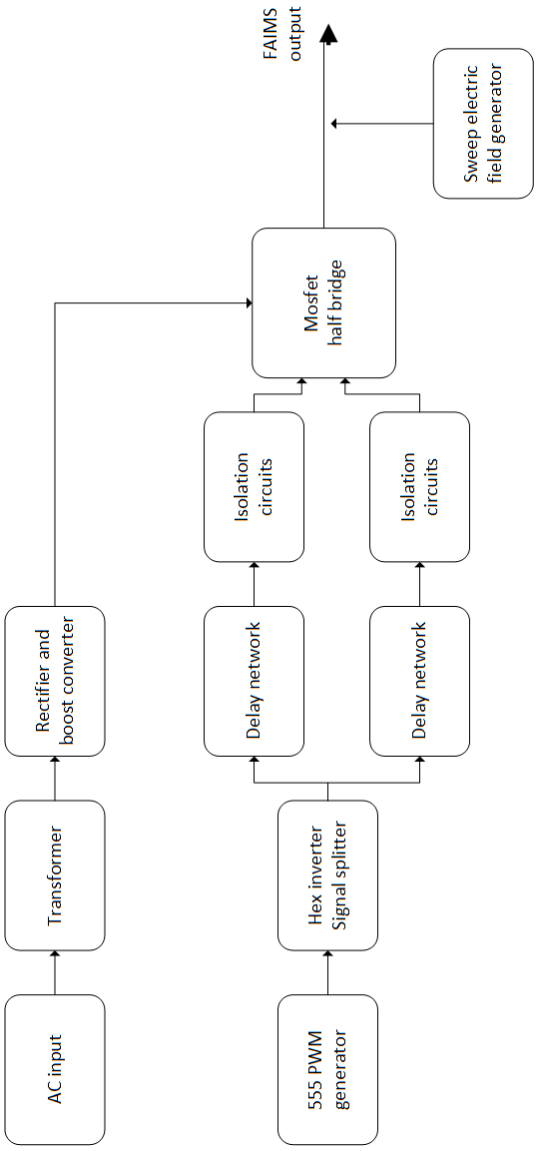

Figure 5.18: Custom FAIMS amplifier design

The PWM signal from the 555 PWM generator is fed into the hex inverter which is used to split the waveform into two square wave with opposing polarities. The hex inverter also ensured both waveforms were in phase. Both waveforms were fed into delay circuits to ensure the MOSFETs were not powered on at the same time. An isolator stage was used to isolate the high voltage MOSFET stage from the low

voltage PWM generator circuit. Finally the waveforms was used to switch two n-channel MOSFETs in a half-bridge configuration. A high voltage power supply was designed to convert 240 VAC to 900 VDC which was fed to the half-bridge MOSFET network. The compensation electric field was generated with a similar circuit design described in Section 5.4.1. Both waveforms are added using a custom mixer and fed into the FAIMS electrode shown in Figure 5.19.

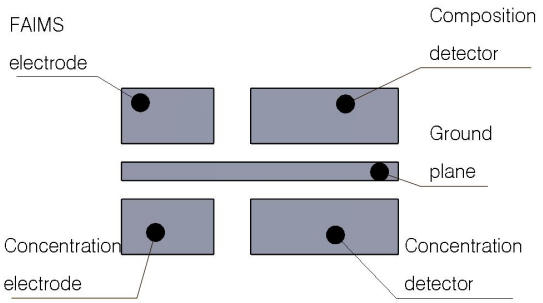

Figure 5.19: FAIMS electrode layout

As mentioned earlier, a FAIMS waveform must be without distortion to achieve molecular filtration. A distortion free square wave was obtained from the FAIMS circuit when 260 V was supplied and the PWM was set to 600 kHz at 50% duty circle. This waveform is shown in Figure 5.20 .

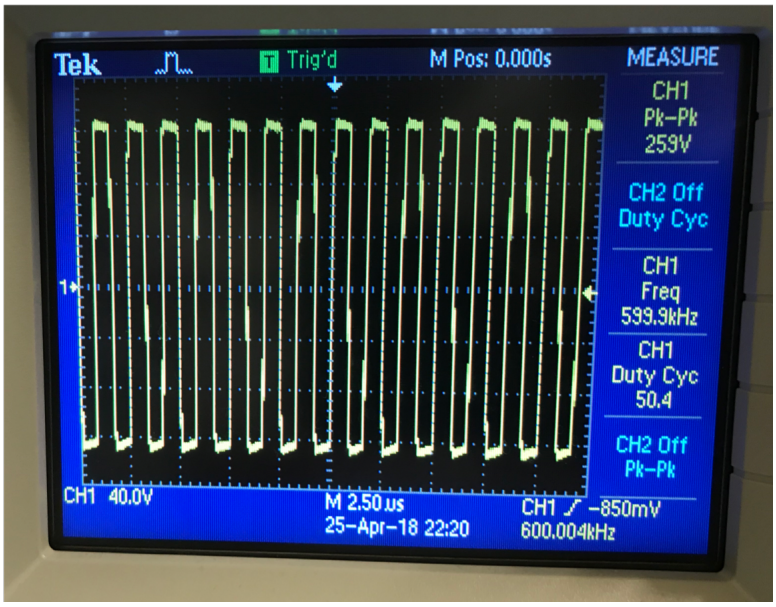

Figure 5.20: Integral electric field sensor electrode layout

However, FAIMS requires and asymmetric waveform so the duty cycle was reduced to 33%. The frequency was also increased by 100 kHz. This resulted in curves in the leading edges of the waveform as seen in Figure 5.21.

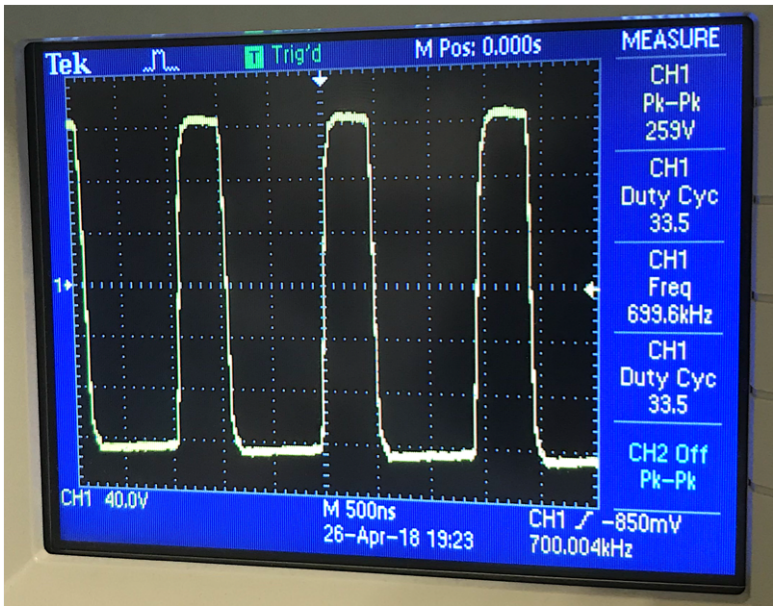

Figure 5.21: Integral electric field sensor electrode layout

Increasing the high voltage supply to 400 V and the frequency to 1 MHz resulted in some distortion to the waveform as seen in Figure 5.22. It was initially suspected that this may have been due to the delay in switching the MOSFETS introduced by the delay network. However, further tuning of the delay network did not improve the waveform.

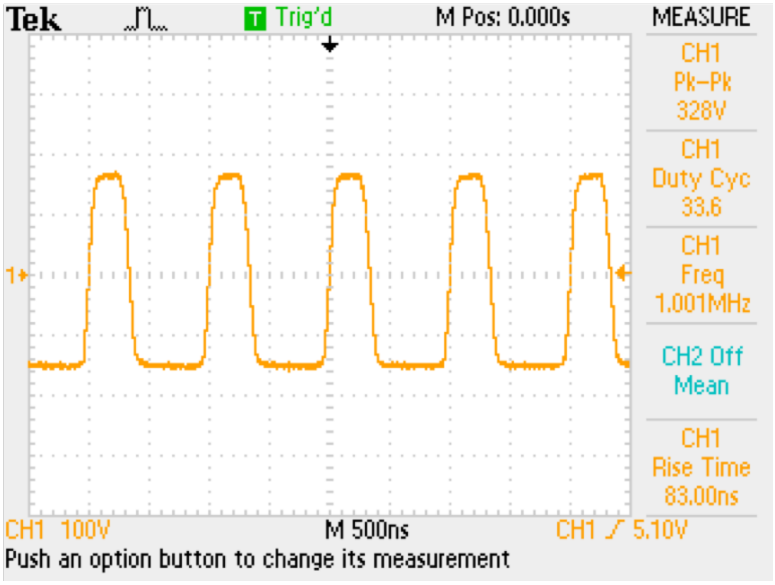

Figure 5.22: Integral electric field sensor electrode layout

At 1.1 MHz the peak-to-peak voltage output from the circuit dropped to 316 V (Figure 5.23). Several power switching MOSFETS with low gate charge were tested to improve the FAIMS output. This includes IXTH16P60P manufactured by IXYS, C3M0065090D by Cree. These made little improvements to the output waveform distortion or peak voltage. It was concluded that the current circuit design will be used at 260 V and 700 kHz for optimum waveform output.

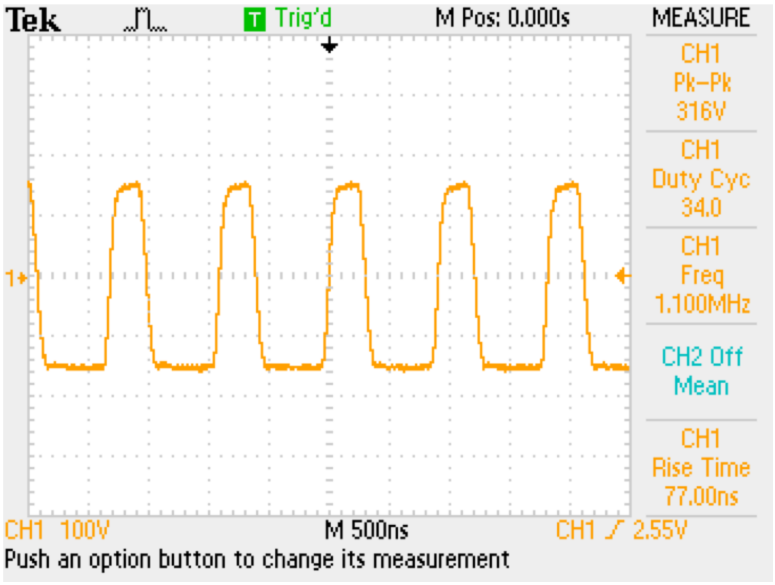

Figure 5.23: Integral electric field sensor electrode layout

5.4.2 Detector electronics

Ionised molecules surviving the filtration region lose their charge when they reach the detector electrodes. This process generates current, usually in the picoamp range. An amplification circuit (Figure 5.24) was designed to measure and amplify this current.

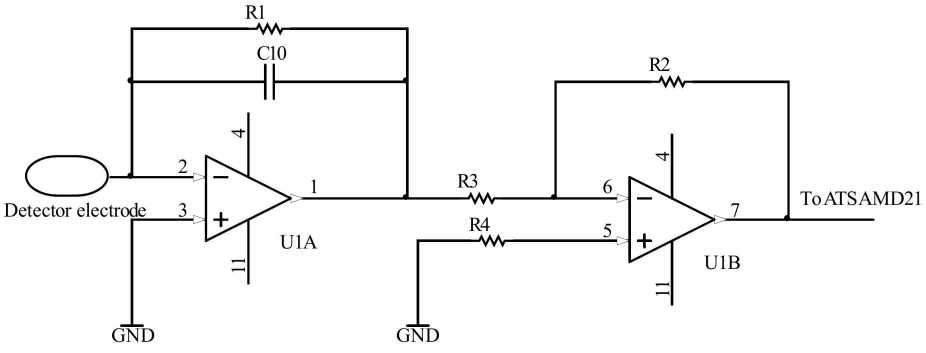

Figure 5.24: Schematic showing detector amplification circuit.

The opamp U1A is used as first stage transimpeadance amplify which converts current to voltage. The opamp U1B serves as a differential amplifier which ampifies the difference between the non-inverting input voltage and the output voltage from U1A. The amplified voltage is fed to the ADC on the ATSAMD21 microcontroller.

The chamber and electronics where assembled into a single unit. A modular configuration of this unit is shown in Figure 5.25.

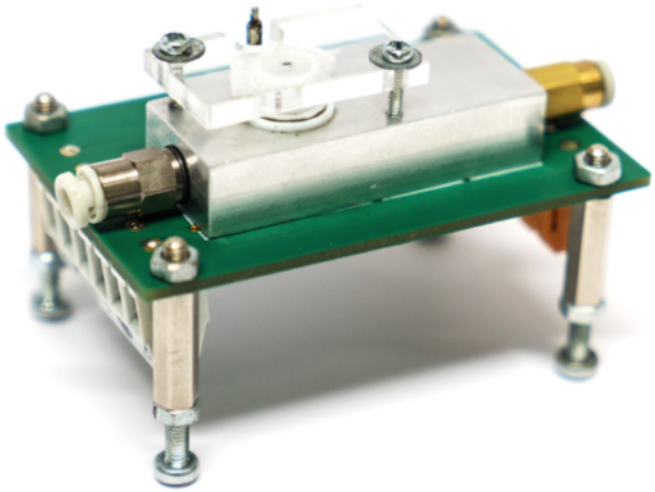

Figure 5.25: Modular IMS amplification circuit with ionisation chamber and UV bulb

5.5 Tests and results

5.5.1 Chemical concentration information

Performance of the VOC sensors was characterised using isobutylene. This is a common test gas for characterising gas sensors and is used extensively by industry. The

standard test procedure involves supplying a known concentration of isobutylene gas into the sensor and measuring the current generated at the detection electrode. This output is related to the concentration of isobutylene gas. An isobutylene gas bottle was purchased (BOC, UK) at 100 parts per million (ppm) concentration in air. It was diluted with zero air gas using an API Model T700 Dynamic Calibrator to generate low concentration isobutylene gas at 9 mL/min. The diluted gas was supplied into the sensor and the current generated at the detector electrode was measured using a custom windows application (this application is discussed in Chapter 6). To characterise the dynamic response time and repeatability of the sensor, 10 ppm isobutylene was supplied into the sensor inlet for 10 s followed by a supply of zero air for 10 s. This sequence was repeated 4 times. Figure 5.26 shows the amplified signal response. Once the system has stabilised in clean air. The VOC detector shows a fast response time of less than 2 seconds (defined as time to achieve 90% of final value). This response time can be adjusted in software by increasing/reducing the cycle time and noise reducing algorithm effect but is ultimately limited by the characteristics of our test station. However, better stability was observed between pulses using 100 ms cycling time. The result also shows repeatability of the sensor to a fixed concentration. The voltage output was similar across all four tests shown.

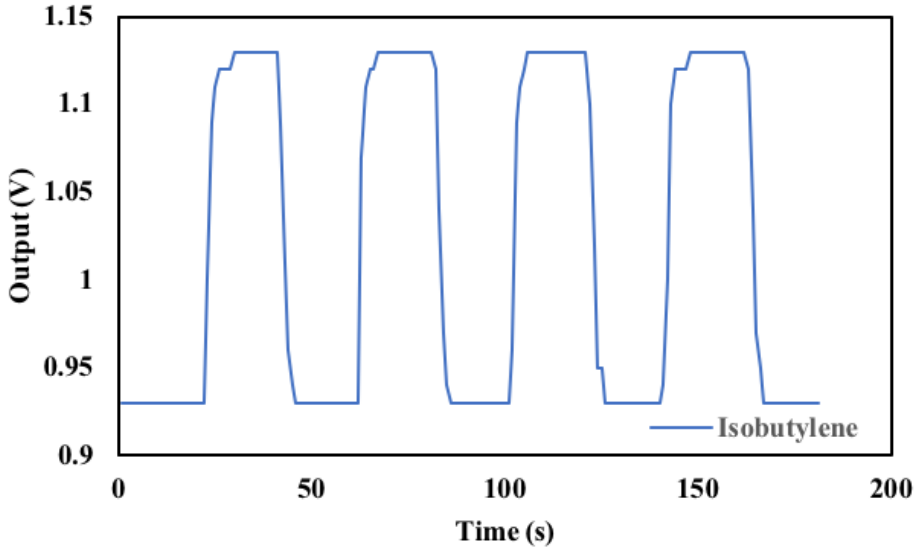

Figure 5.26: Dynamic concentration response for isobutylene.

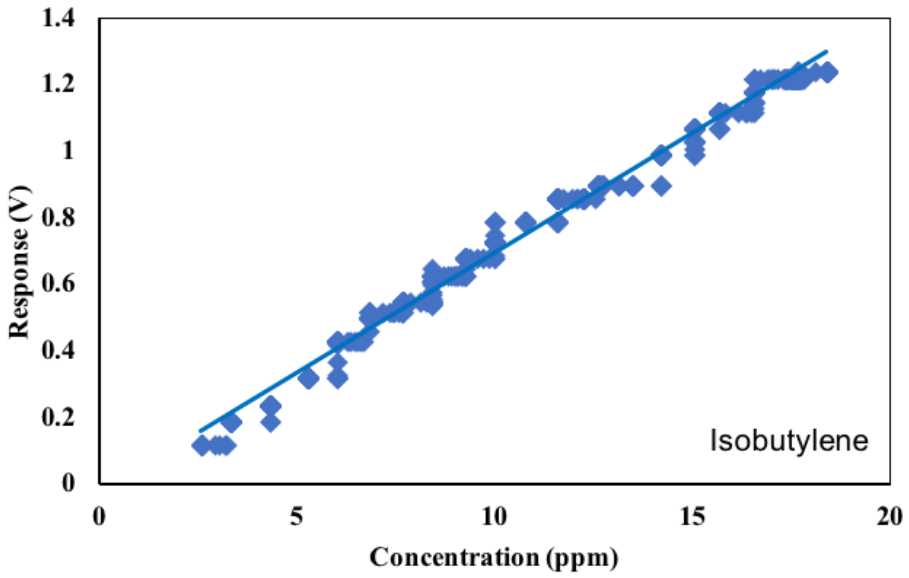

Figure 5.27: Dynamic response for 0-18ppm isobutylene at 10 seconds intervals

One of the advantages of commercial PID sensors is fast response to varying concentration. This property of the VOC detector was tested by delivering increasing concentrations of isobutylene gas into the sensor. Isobutylene was delivered into the sensor with concentration increasing from 0 to 18 ppm in steps of 2 ppm. The sensor

concentration output shown in Figure 5.27 shows that the limit of detection is likely to be in the ppb region for isobutylene.

5.5.2 Chemical composition information

The VOC detector provides a second output with information on the chemical composition of the analytes, a feature not available in commercial PID sensors. This feature was investigated by analysing various VOCs using the VOC detector and comparing the sensor response. During analysis, a supply of test VOC with a fixed concentration was delivered to the sensor. The electric field, which results in a deflection of cations, was varied from -7 kV/m to +7 kV/m in steps of 500 V/cm. At zero electric field strength there is no deflection of the flow of ions and all of the ions contact the detector plate and giving the maximum response. Sweeping the electric field in the positive or negative direction results in reduced current (and thus signal) due to loss in charge when ions hit the walls of the chamber and thus do not reach the detection electrode. The deflection observed could be due to the interaction between the charge and/or weight of the ions in the stream and the intensity of the electric field. Between each step change in electric field, the gas supply was turned off and resumed after changing the electric field. Signal response due to the varying amount of ions reaching the compositional electrode is measured over the period of test. This analysis was repeated for 10 ppm isobutylene and 2-pentanone. To remove any bias associated with concentration, the compositional sensor response was normalised. This is shown in Figure 5.28 and 5.29.

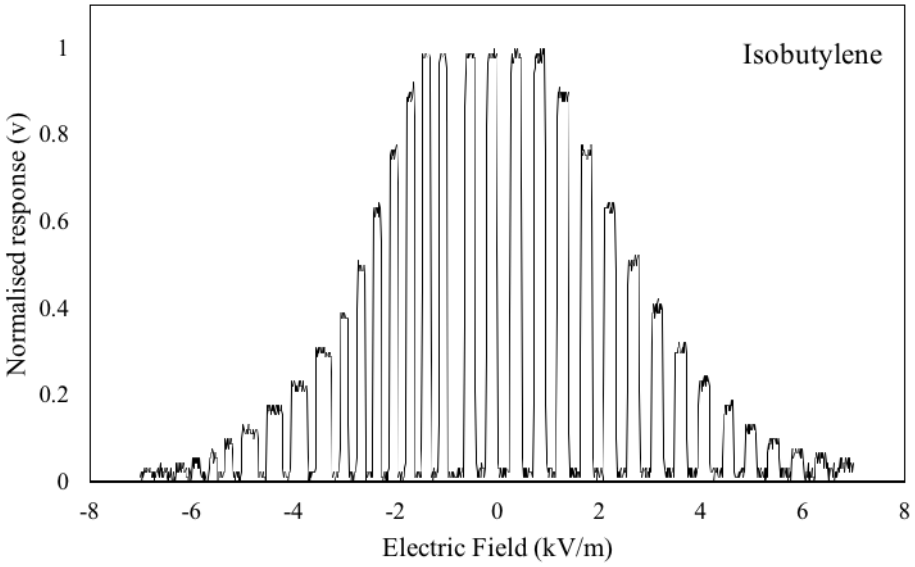

Figure 5.28: Normalised chemical compositional signal response for 10 ppm isobutylene

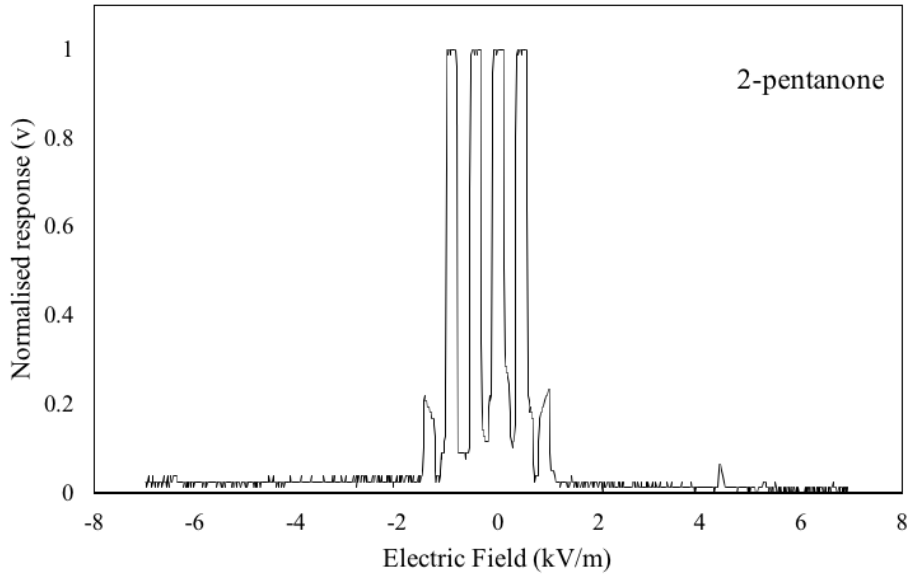

Figure 5.29: Normalised chemical compositional signal response for 2-pentanone.

The results show significant difference in sensor output for isobutylene and 2-pentanone over the range of applied electric fields. An electric field of 1 kV/m

on the composition electrode results in a 0.67 V separation between the signal obtained for both compounds. This information can be used to train the sensor to target the identification of certain compounds. To achieve this, the electric field could be set to a value associated with a known response for the target compound. The response from the concentration electrode array could also be added providing increased dimensionality for statistical methods such as linear discriminate analysis.

In another test, 2 ppm of 2-hexanone was fed into the sensor at 7 mL/min. In this test, the supply of analytes remained constant for the duration of the analysis. The electric field voltage was varied from -3 kV/cm to 3 kV/cm in steps of 200 V/cm. This procedure was repeated for 10 ppm propanol. Testing compounds of different concentration was carried out to represent real life test scenarios where test compounds will not always have a similar concentration, but the instrument is expected to provide responses not biased towards concentration. A comparison of the normalised compositional signal response for both compounds sensor is shown in Figure 5.30.

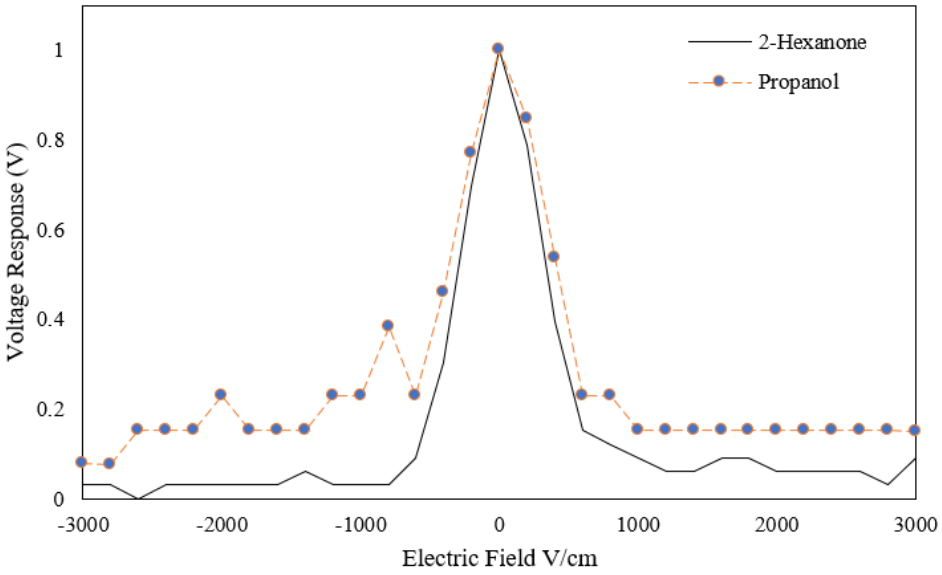

Figure 5.30: Comparison of chemical compositional signal response for 2-hexanone and propanol

A 0.063 V separation in signal response when the electric field is set to 1000 V/cm, which was repeatable over 5 different experiments. This shows that by sweeping through a range of electric field, the VOC detector can distinguish between VOCs . Although the compositional output at a fixed electric field is different, the shape of the curve and area under the curve for the period of analysis provides more information for pattern recognition analysis.

The repeatability of results obtained during analysis of VOCs and the detector's potential to distinguish between VOC compounds were further verified using 10 ppm 2-hexanone, 2-octanone, propanol and 2-heptanone, in dry zero air. In this analysis, a fixed concentration of VOC was supplied in to the sensor inlet. The electric field was varied from -7 kV/m to +7 kV/m while the voltage response from the sensor was measured and recorded. After sweeping through the voltages, the supply of VOC was shut off. This procedure was repeated 20 times for 2-hexanone, 2-octanone

and propanol. Principal Component Analysis (PCA) was utilized to reduce the dimensionality of the recorded data. The first and second principal component accounted for 96 % of data variance in the original dataset and a scaled plot of these components is shown in Figure 5.31. The results from the VOC detector shows discrimination between responses obtained for 2-hexanone, 2-octanone and propanol.

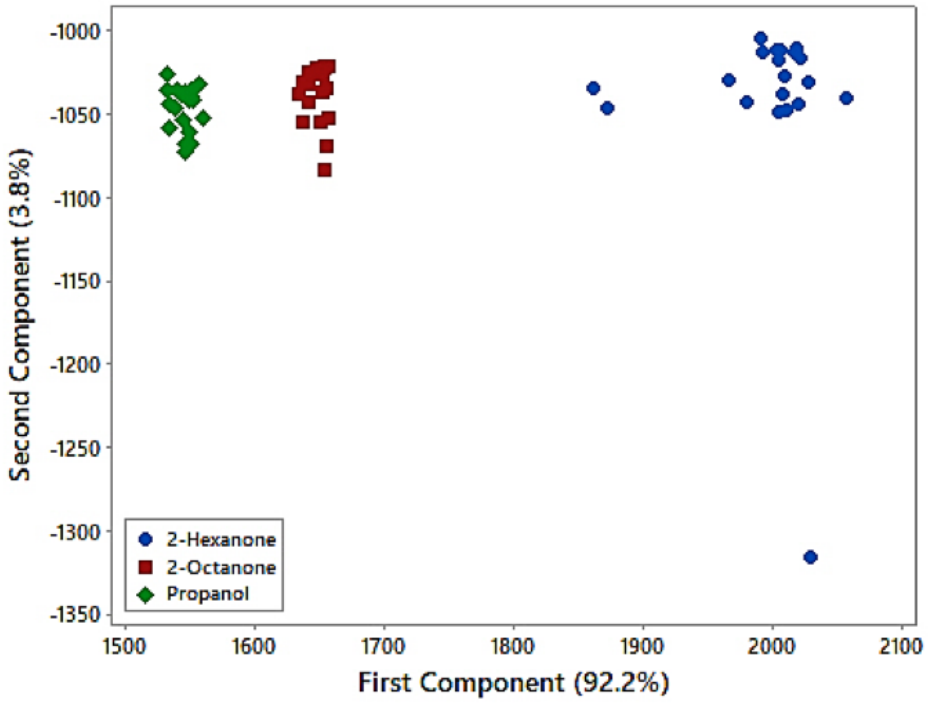

Figure 5.31: Scaled PCA plot of the VOC detector response for 2-hexanone, 2-octanone and propanol

Further tests were carried out using 10 ppm 2-heptanone and 2-octanone as test VOC samples. Fixed concentration of VOC was flowed into the sensor during the analysis. The electric field was varied from -7 kV/m to +7 kV/m. This procedure was repeated 20 times for both VOCs . The compositional responses measured during the tests were recorded and analysed using PCA. Figure 5.32 shows a scaled

plot of the first and second principal components. The first and second components accounted for 97.8 % variance in the original data set. As depicted in Figure 5.32, there is also clear discrimination between compositional information obtained for 2-heptanone and 2-octanone.

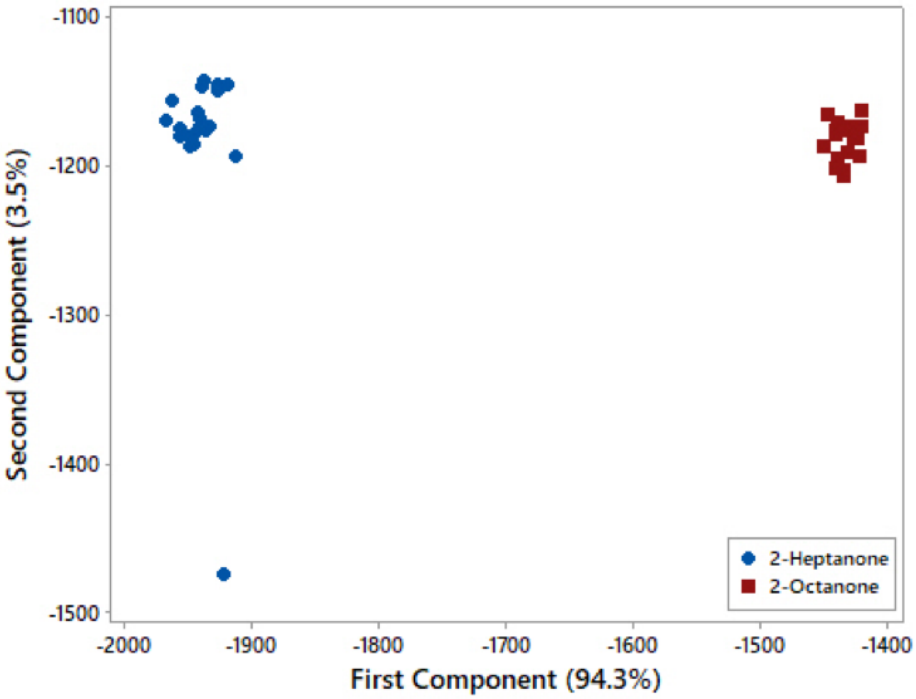

Figure 5.32: Scaled PCA plot of the VOC detector response for 2-heptanone and 2-octanone

These results demonstrate that the sensors can be used to detect low concentration VOCs. They also show that the VOC detector can distinguish between VOCs. In the current sensor design, the high voltage electric field required for VOC identification results in considerable interference and signal loss at lower concentration. Future efforts will focus on improving the electric field generator to reduce interference and improve signal response when testing low concentration VOCs . Additionally, further investigate into the VOC detector electric field potential to separate complex mixtures of VOCs during analysis will be required.

5.6 Conclusion

This chapter reports on the design of a novel VOC detector sensor with added sample composition output that has been designed, manufactured and tested. The sensor provides two voltage outputs proportional to the concentration and composition of the test sample. Concentration tests were carried out with low concentration isobutylene and the concentration response was found to increase linearly with concentration. An increase in concentration in from 0 – 18 ppm resulted in an increase in output voltage of 2.3V, with an estimated sensitivity of below 1 ppm. The composition response shows a significant distinction between 2-pentanone and isobutylene when 1kV/m was applied in the chamber. A 0.063 V difference was observed between 2-heptanone and propanol when 1000 V/cm electric field was applied. the VOC detector compositional response also discriminated between 10 ppm 2-hexanone, 2-octanone and propanol when the electric field was varied from -7 kV/m to +7 kV/m. This chapter also showed discrimination between 2-heptanone and 2-octanone over the same electric field range. The added composition information, leak proof feature and low cost makes this unit potentially provide more information at a lower price point when compared with existing commercial sensors.

5.7 References

[1] Xing Chen, Mingfu Cao, Yi Li, Weijun Hu, Ping Wang, Kejing Ying, and Hongming Pan. A study of an electronic nose for detection of lung cancer based on a virtual saw gas sensors array and imaging recognition method. *Measurement Science and Technology*, 16(8):1535, 2005.

[2] Nuria Queralto, Anders N Berliner, Brett Goldsmith, Raymond Martino, Paul

Rhodes, and Sung H Lim. Detecting cancer by breath volatile organic compound analysis: a review of array-based sensors. *Journal of breath research*, 8(2):027112, 2014.

[3] Gang Peng, Ulrike Tisch, Orna Adams, Meggie Hakim, Nisrean Shehada, Yoav Y Broza, Salem Billan, Roxolyana Abdah-Bortnyak, Abraham Kuten, and Hossam Haick. Diagnosing lung cancer in exhaled breath using gold nanoparticles. *Nature nanotechnology*, 4(10):669, 2009.

[4] Gang Peng, Meggie Hakim, Yoav Y Broza, Salem Billan, Roxolyana Abdah-Bortnyak, Abraham Kuten, Ulrike Tisch, and Hossam Haick. Detection of lung, breast, colorectal, and prostate cancers from exhaled breath using a single array of nanosensors. *British journal of cancer*, 103(4):542, 2010.

[5] Michael Phillips, Nasser Altorki, John HM Austin, Robert B Cameron, Renee N Cataneo, Robert Kloss, Roger A Maxfield, Muhammad I Munawar, Harvey I Pass, Asif Rashid, et al. Detection of lung cancer using weighted digital analysis of breath biomarkers. *Clinica chimica acta*, 393(2):76–84, 2008.

[6] Phillip Evans, Krishna C Persaud, Alexander S McNeish, Robert W Sneath, Norris Hobson, and Naresh Magan. Evaluation of a radial basis function neural network for the determination of wheat quality from electronic nose data. *Sensors and Actuators B: Chemical*, 69(3):348–358, 2000.

[7] J Brezmes, E Llobet, X Vilanova, G Saiz, and X Correig. Fruit ripeness monitoring using an electronic nose. *Sensors and Actuators B: Chemical*, 69(3):223–229, 2000.

[8] S Capone, P Siciliano, F Quaranta, R Rella, M Epifani, and L Vasanelli. Analysis of vapours and foods by means of an electronic nose based on a sol–gel

metal oxide sensors array. *Sensors and Actuators B: Chemical*, 69(3):230–235, 2000.

[9] Sindhuja Sankaran, Ashish Mishra, Reza Ehsani, and Cristina Davis. A review of advanced techniques for detecting plant diseases. *Computers and Electronics in Agriculture*, 72(1):1–13, 2010.

[10] Roberto Fernández-Maestre and Herbert H Hill. Ion mobility spectrometry for the rapid analysis of over-the-counter drugs and beverages. *International Journal for Ion Mobility Spectrometry*, 12(3):91–102, 2009.

[11] RE Baby, M Cabezas, and EN Walsöe De Reca. Electronic nose: a useful tool for monitoring environmental contamination. *Sensors and Actuators B: Chemical*, 69(3):214–218, 2000.

[12] W Vautz and JI Baumbach. Analysis of bio-processes using ion mobility spectrometry. *Engineering in Life Sciences*, 8(1):19–25, 2008.

[13] Zeev Karpas, Boris Tilman, Rachel Gdalevsky, and Avraham Lorber. Determination of volatile biogenic amines in muscle food products by ion mobility spectrometry. *Analytica Chimica Acta*, 463(2):155–163, 2002.

[14] Hnu portable analyzer, July 2018.

[15] Wei-qi Zhang, Hong Li, Yu-jie Zhang, Fang Bi, Ling-shuo Meng, Xin-min Zhang, Jing-ying Mao, Nian-liang Cheng, Bin Fang, Yuan Yang, et al. Fast determination of monocyclic aromatic hydrocarbons in ambient air using a portable gas chromatography–photoionization detector. *Chromatographia*, 80(8):1233–1247, 2017.

[16] Ivano Marchi, Serge Rudaz, and Jean-Luc Veuthey. Atmospheric pressure photoionization for coupling liquid-chromatography to mass spectrometry: a review. *Talanta*, 78(1):1–18, 2009.

Chapter 6

System Assembly and Software

6.1 Introduction

In Chapter 4 the design and assembly of the Pre-concentrator (PC) and Gas Chromatograpy (GC) were discussed. Chapter 5 covered the design and testing of a novel advanced Photoionization Detector (PID) sensor. In this chapter, the assembly of these components into a single analytical instrument is presented. This chapter will also cover the software designed to manage various aspects of the instrument including power supply, pneumatics, and logging test data.

The mechanical assembly of the components and system pneumatics will be covered in the next section. Section 6.3 will discuss the power and communication electronics and Section 6.4 covers the control software.

6.2 Mechanical assembly

This section presents the integration of the 3 major components - PC, GC and VOC detector, into a single analytical device. It is essential that the sample flow through the instrument is consistent and repeatable across several tests as change in sample flow could lead to difference in system performance. The pneumatic system was designed to ensure repeatable sample flow through the instrument, using a process of flow control instrumentation and control software. The components have been designed using a modular approach which allows various components to be used individually or together in a range of combinations. A schematic of the mechanical assembly showing the pneumatic connection is shown in Figure 6.1.

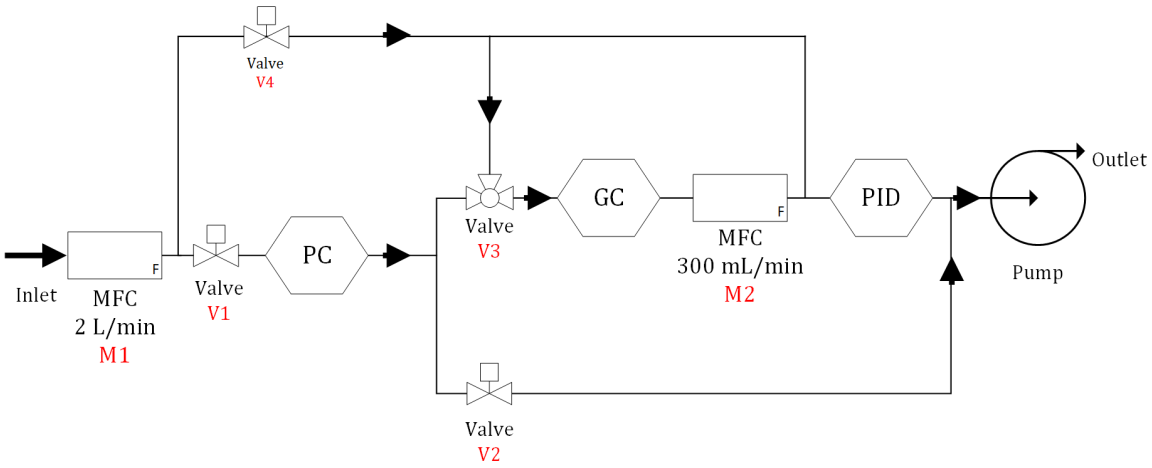

Figure 6.1: Schematic of the Gas Mixer pneumatic system

The sample travels from the inlet through the Mass Flow Controller (MFC) M1 which is used to regulate fluid flow into the instrument. Next the valve V1 is used to direct flow through the PC or towards the GC and PID. Elute from the PC can either go through valve V2 to the outlet or valve V3 to the GC or through both V3 and V2 depending on the selected operated mode. The operating modes will be

covered in Section 6.2.2. Flow through the GC is controlled using MFC M2. The ratio of flow through M1 and M2 is used to set the GC split flow. Finally the sample exits the GC and enters the VOC detector, mixed with carrier gas flowing through M1. Pumps were installed after the PID to pull sample through the unit and send sample through the outlet after analysis. A brief description of these components is given below.

Mass flow controllers

Two UFC-1100A MFCs (M1 and M2) manufactured by Unit Instruments Inc., USA were used for precise flow through the instrument. One of the UFC-1100A MFCs M1 was rated for a maximum flow rate of 2000 mL/min and the other (UFC-1100A) MFC, M2 was rated for a maximum flow rate of 300 mL/min. Both MFCs were powered by providing $\pm$ 15 v to its input pins. The user inputs a signal within 0 - 5 v to specify a required flow rate with 0 and 5 v corresponding to no-flow and maximum flow respectively. A 0 - 5 v voltage signal output gives the user an indication of the current flow rate through the MFC flow rate range. The inlets and outlets were fitted with 1/8 inch push-fit fitting. M1 is used to set the total flow rate through the instrument. M2 is used to set the flow rate through the GC only. During use GCs operate at low flow rates for increased separation of analytes. However, the PID operates at flows in excess of 1 L/min. As shown in Figure 6.1 M1 and M2 were installed in a configuration that allows the flow through the GC to be set independent from the flow through PID.

Valves

An ETO-3-12 3-way valve (V3) and three ET-2-12 2-way valves (V1, V2, V4) manufactured by Clippard (US) were used to control flow direction through the instrument. Both valves were operated on a 12 V signal. The ET-2-12 is set to be normally closed and requires a 12 V signal to open. The ETO-3-12 has two inlet ports and a single outlet port. Flow is normally open through one of the inlet ports and a 12 V signal applied to the valve switches flow to the second inlet. Valve V1 was installed to direct flow to the PC or to the other components in the unit via V4. V2 is used to control flow from the PC to the pumps. Valve V3 is used to select input into the GC. Depending on the operation mode, flow from either the PC or M1 could be allowed into the GC.

6.2.1 Sensors

Several sensors were integrated to measure system temperatures and humidity. Two MAX6675 chips from Maxim Integrated were used to convert K-type thermocouple readings into a digital output. The thermocouples were wrapped around the PC and GC to measure their temperatures. The HTU21D from sharp was originally used to measure humidity. A chamber was designed channel gas over the sensor. The sensor and the chamber assembly is shown in Figure 6.2.

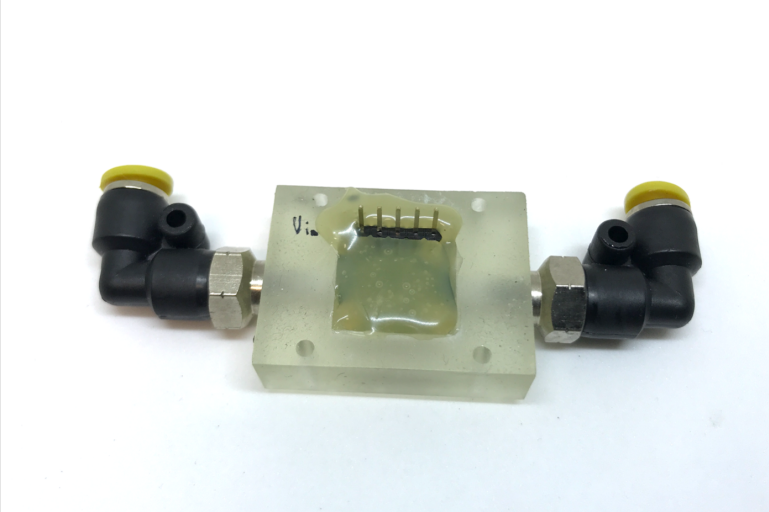

Figure 6.2: HTU21D sensor and chamber assembly

During humidity calibration tests with the EL-USB-2 Data Logger from Lascar Electronics, it was observed that the HTU21D was not as accurate as stated in the datasheet and an additional sensor was tested, specifically the SHT75 which showed better humidity response. Therefore, the SHT75 sensor was used. A housing was designed for the sensor as shown in Figure 6.3. Therefore, the SHT75 sensor was held in place and sealed using a transparent EVA glue from SilverlineTools.

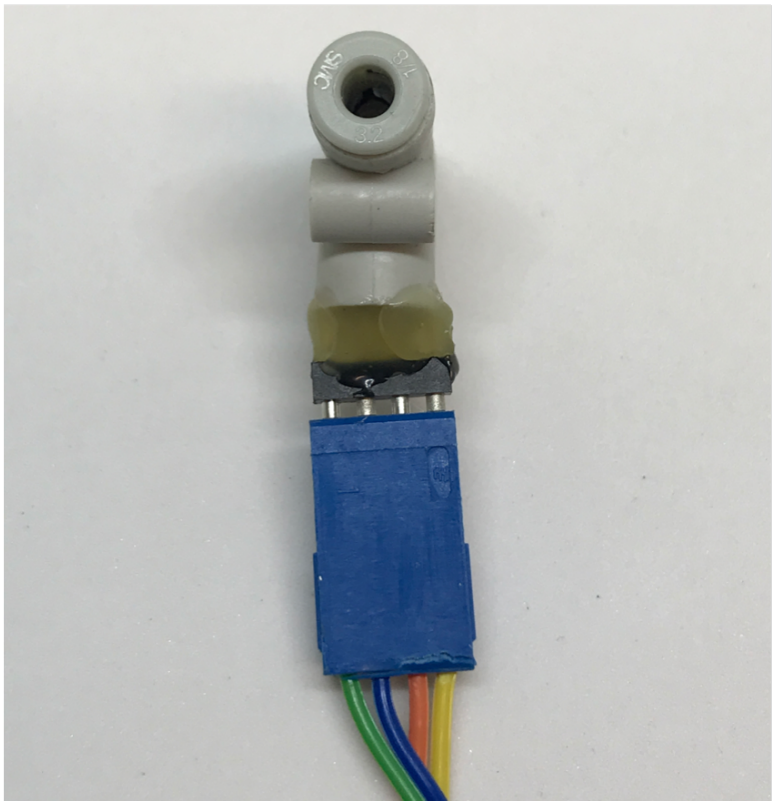

Figure 6.3: SHT75 sensor and chamber assembly

6.2.2 Operating modes and flow paths

As mentioned earlier, the unit was designed with a modular approach to allow operation in various configurations depending on the intended procedure. Complete gas analysis with the instrument involves sampling analytes, pre-concentrating, desorption, injection, analysis and cleaning of the PC. These procedures will be referred to as operating modes for clarity. The sample flow path and activated components vary depending on the operating mode and this is expanded on below.

Sampling

During sampling, the aim is to capture the gaseous analyte from the external sample into the instrument. A schematic of the flow path and activated component is shown in Figure 6.4. The activate flow path is highlighted in red.

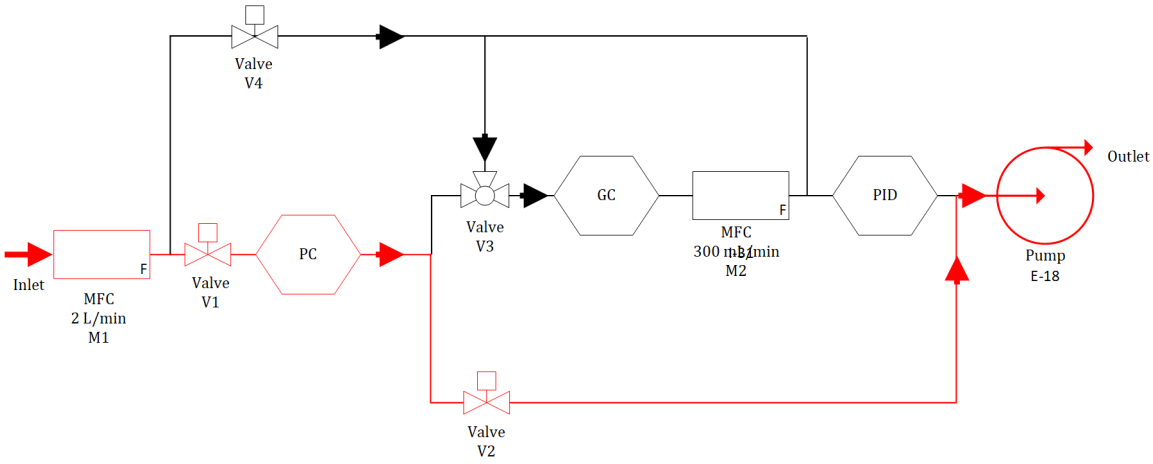

Figure 6.4: Schematic of the VOC detector's pneumatic system.

In this operating mode the pump is powered on to provide suction. Gaseous sample flows through M1 at a sampling flow rate prescribed in software. Valve V4 is closed to stop flow to the rest of the system. V3 is also closed to stop flow into the GC. Valve V1 is opened allowing samples into the PC where VOC are adsorbed by the carbon cloth housed in the PC. The flow continues through valve V2 which is also opened to the outlet through the pumps. The duration of the sampling procedure is also set in software.

Desorption

After sampling, the M1 is set to 0 mL/min and valve V1 is closed before switching of the pump. The delay in switching off the pump allows the system to create a vacuum

downstream. This vacuum is needed to assist with fast elution of samples from the PC during the injection procedure. The active flow path during the desorption stage is represented in Figure 6.5.

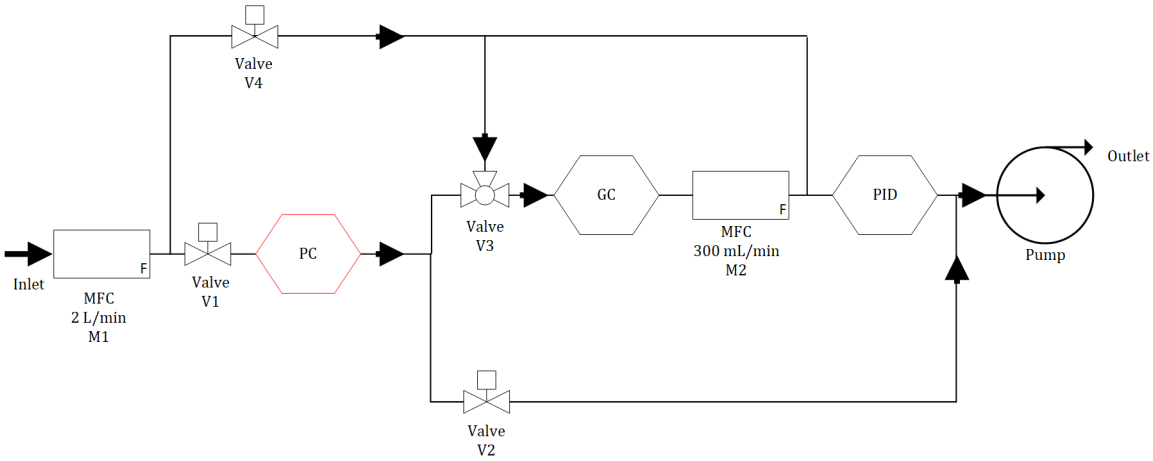

Figure 6.5: Schematic of the VOC detector's pneumatic system.

During this procedure the temperature of the PC is set to the desorption temperature defined in software. The duration of the procedure is also set in software. All the sample eluted during desorption is trapped in the PC since valves V1,V2 and V3 are closed.

Injection

The aim during injection is to get the samples into the GC in a narrow band to ensure efficient desorption. Hence the desorbed samples in the PC is quickly swept into the GC during injection. For concentrated samples it is possible to overload the GC, to avoid this valve V2 could be opened during injection. Figure 6.6 shows the flow path during this procedure. The temperature of the GC is now increased to the desired temperature set in software if an isothermal GC analysis is desired. If

the GC temperature will be ramped, the temperature is set to the first temperature in the ramp sequence.

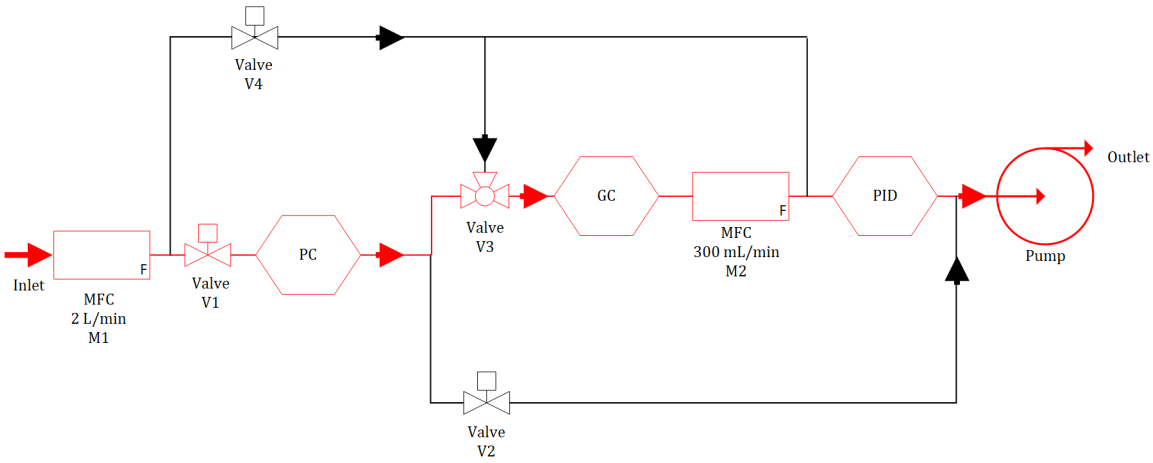

Figure 6.6: Schematic of the VOC detector's pneumatic system.

The injection procedure begins with switching on the pumps and setting M2 to the desired flow rate using the software. Next M1 is set to the desired total flow rate and valves V1 and V3 are opened. The duration of injection can be set to values as low as from 500 ms.

Analysis

After injection is complete, V1 and V3 are switched off to stop sample flow from the PC into the GC and allow carrier gas from M1 to flow through the GC (Figure 6.7). Valve V4 is opened to allow carrier gas flow through the GC at the flow rate of M1. The temperature of the GC remains unchanged if an isothermal GC analysis is desired. If the GC temperature will be ramped, the temperature begins to ramp as prescribed by the user in the software.

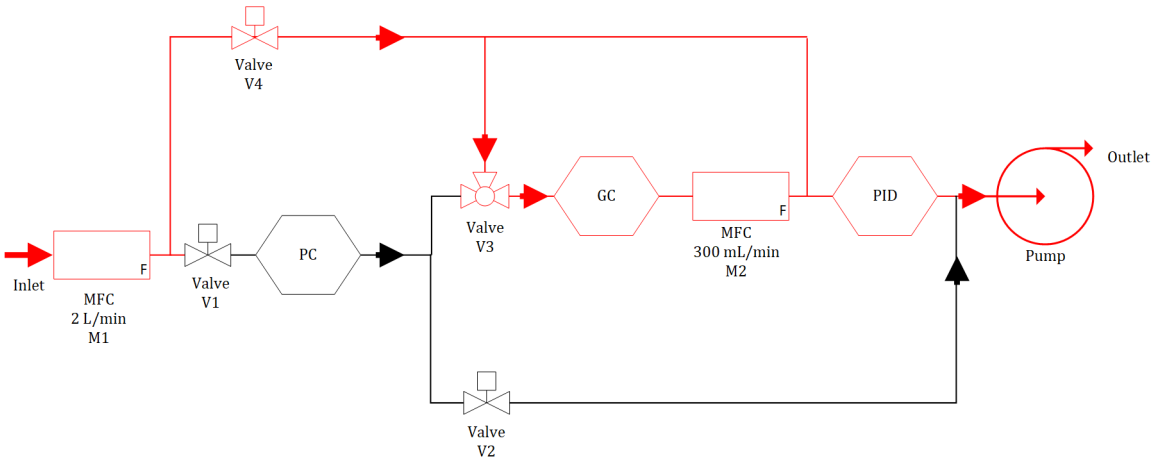

Figure 6.7: Schematic of the VOC detector's pneumatic system.

Elute from the GC is mixed with carrier gas as it enters the PID chamber. This configuration allows both PID and GC to operate at their optimum flow rates albeit dilution of the sample entering the PID. The dilution ratio is given in Equation 6.1.

$$\text{GC} : \text{PID} = \frac{M2 flowrate}{M1 flowrate} \tag{6.1}$$

Cleaning

During cleaning, the PC temperature is set to the regenerative temperature for the carbon cloth. Flow is channelled through the PC, V2 and out through the pump as shown in Figure 6.8.

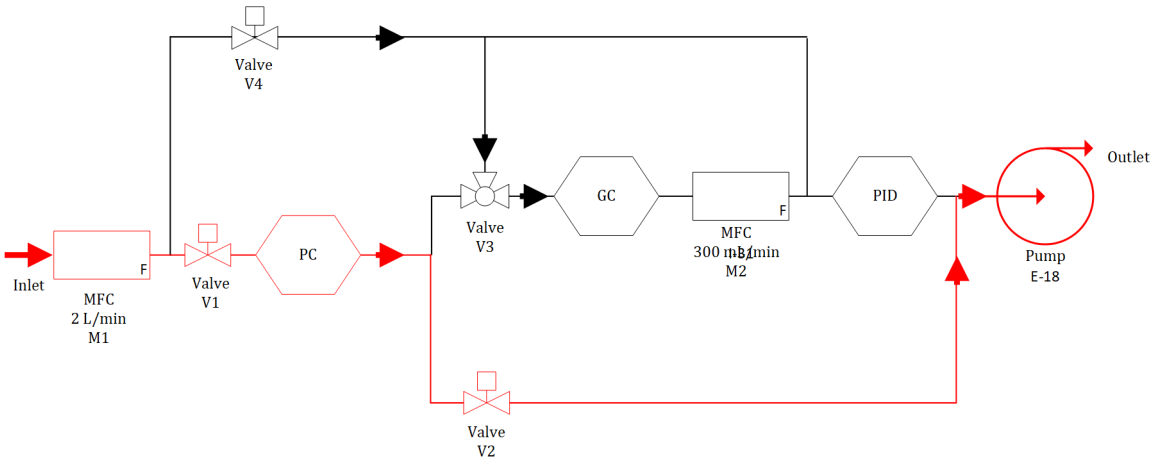

Figure 6.8: Schematic of the Gas Mixer pneumatic system

The flow rate is set to 2 L/min to force the remaining desorbed samples from the PC.

6.3 Power supply and digital electronics

6.3.1 Power electronics

The components in the system have varying power requirements. It is important that the power is supplied to these components is free from interference as it could affect the functioning of the actuators, measurement signals from sensors or damage the instrument altogether. High power components such as the PC heater and GC heater require high current to reach the desired temperatures in a short period of time. For example the PC requires 12 V at 2 A to increase desorption temperature from room temperature to 150 °C in 20 s. Intermittent power components such as the valve and pump require power supply for a short time period. However their switching action introduces noise in the power lines. This is more the case with the fast

switching high voltage generator for the detector unit. The Field Asymmetric Ion Mobility Spectrometry (FAIMS) waveform generator outputs up to 260 V at 700 kHz introducing Radio Frequency Interference (RFI) and Electromagnetic Interference (EMI) into the system. Measurements from highly sensitive components such as the Volatile Organic Compound (VOC) detector circuit and other sensors integrated in the system could easily be adversely affected by these interference if powered on the same power supply lines. Therefore, the power system was developed with two power lines to isolate sensitive components from high power components. This is shown in Figure 6.9.

Alternating Current (AC) at 240 V was supplied from mains into the system via a Qualtek 880-06/006 EMI panel mount filter citequaltek. Its function is to reduce high frequency electronic noise in the mains voltage that may cause interference with other devices in the system. This EMI filter consists of passive components, including capacitors and inductors, to form a filtering LC circuit. The inductor blocks the harmful unwanted high frequency currents and allows low frequency currents or Direct Current (DC) or to pass through. The capacitors divert the high frequency noise away from the filter network by providing a low impedance path to the ground connection or back into the power supply. The X and Y capacitors used in this filter meet EMI regulations safety standards. The X class capacitors are connected between the AC lines to eliminate the potential for shock in the event of failure. The Y capacitors are connected between the AC lines and ground [1].

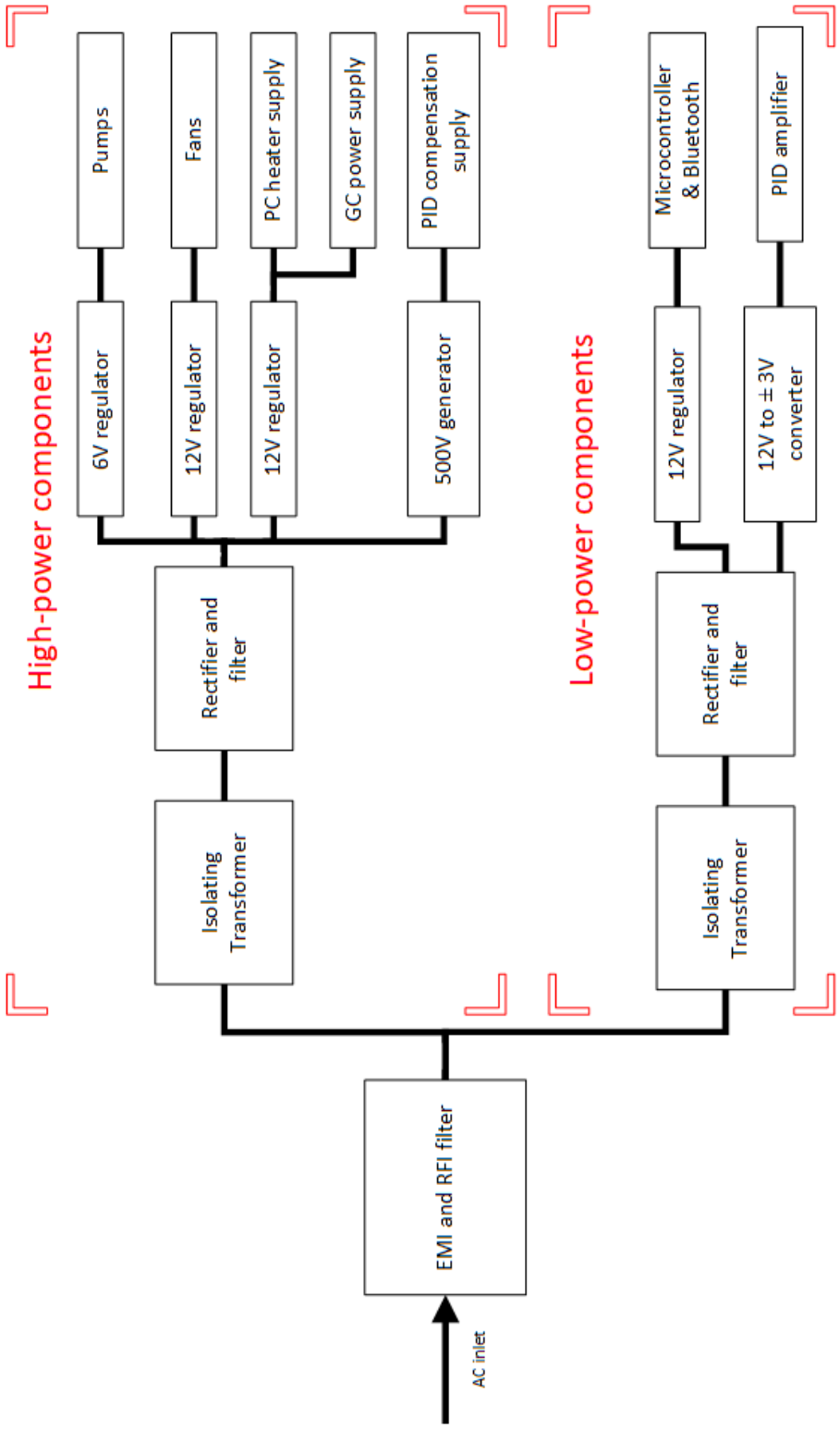

Figure 6.9: Power supply layout

The filtered AC supply is split at this point to separate lines feeding components categorised as either high power or sensitive components. This fed into a transformer to isolate the system from mains power supply and step down the voltage. A rectifier and filtering network converts the AC to DC. This DC is supplied to various components through regulators that ensure the correct voltage is supplied to the component. The power requirements of major components in summarised in Table 6.1.

Table 6.1: Summary of system component power requirements

Component	**Category**	**Quantity**	**Voltage**	**Current/power**
Pumps	High power	3	12 V	
Fans	High power	2	12 V	100 mA
PC heater	High power	1	12 V	2 A
GC heater	High power	1	12 V	2 A
Detector filter	High power	1	12 V	≈200 mA
Microcontroller	Low power	1	12 V	≈300 mA
Bluetooth	Low power	1	5 V	50 mA [2]
Detector amplifier	Low power	1	± 3 V	≈10 mA
SHT75	Low power	1	5 V	1 mA [3]

6.3.2 Digital electronics

The digital electronic system was designed to manage functions relating to the flow of samples to the VOC sensor, measuring the sensor response, control temperatures and communicating all of this information to and from the control software. An Arduino Micro microcontroller unit was selected to manage this task. It interfaces

with the many transducers, actuators and sensors in the system. The Micro [4] is based on the ATmega32U4 microcontroller. It has 20 digital input/output pins (7 can be used as Pulse Width Modulation (PWM) outputs and 12 as analogue inputs,) which is sufficient to control the components used in this project. Another reason why the Micro was selected is because it has a 5 V operating voltage [5] which eliminates the need to for level shifters when interfacing with peripherals like the Bluetooth LE to UART module.

Control signals from the Micro were used to actuate 4 valves, 2 MFCs and 3 pumps. It was also used to supply power for heating to the PC and GC. The Micro also controls the filtering circuit, powering it off when not in use to save power. The 5 V signal from the Micro is interfaced with those components via the Ningbo Songle Relay SRD-05VDC-SL-C non latching relays [6]. This relay is rated to supply 10 A 30 V load using a 5 V signal. Digital pins from the Micro were connected to the relay inputs. The relay load pins was used to control power supply to other components.

The response signals from the VOC detector were fed to the analogue pins on the Micro. The Micro also receives gas humidity and temperature measurements from the SHT75 using I^2C communication protocol. GC and PC temperatures are tracked by the Micro using the MAX31855 thermocouple-to-digital chips, which sends this information to the Micro via a SPI communication protocol. All this information are processed into a data stream that is then sent through Bluetooth LE 4.0 to a controlling software running on a computer. The computer receives this information and sends instructions to the Micro using the same Bluetooth channel.

Bluetooth communication module is based on the CC2540 2.4-GHz Bluetooth low energy System-on-Chip [7] from Texas Instruments. This module is compliant with worldwide Radio Frequency (RF) configurable resolution regulations (ETSI

EN 300 328 and EN 300). It includes a Generic Attributes Profile (GATT) that exposes several services and characteristics. Information to be streamed form the Micro is loaded into one of these characteristics through Universal Asynchronous Receiver/Transmitter (UART). This information can be read from this characteristic by another Bluetooth LE device. Information from an external device is received into one of the characteristic on the CC2540 chip. The chip sends this information to the Micro via UART.

The mechanical components discussed in Section 6.2 and Section 6.3 were assembled in two-tier configuration. The lower stage houses the electronics. This includes the transformers, power supply and distribution circuits. It also contains the FAIMS voltage generator and relay network banks to digital control.

The upper tier houses the gas flow network including pumps and valves. It also carries the VOC detector sensor, Micro and Bluetooth communication module. The assembly was enclosed in a CiT F3 Micro-ATX Case from CiT. This enclosure measures 37 $\times$ 21 $\times$ 42 cm and is shown in Figure 6.10.

Figure 6.10: System assembly enclosed in the CiT F3 enclosure

6.4 Software design

Control algorithms for gas sensing instruments tend to mimic smelling in animals. For humans the smelling process involves uptake of air into the nose where odorants bind to localised receptors on olfactory neurons. This activate cells in the olfactory receptor cells sending signals to the glomeruli. The signals are then transmitted to higher regions of the brain where the signal is processed. The human brain is

able to process smells based on the receptors that trigger the signal [8] and we have approximately 393 olfactory receptor genes [9]. This amazing ability to smell is not so amazing when compared with animals in nature. Guinea pigs, for example, have 796 olfactory receptor genes, rats have 1207. Elephants have 1948 which helps them detect water 12 miles away. The animal believed to have the best sense of smell is the Bear with a sense of smell 2100 times better than that of a human. Bears use this keen sense of smell to keep track of their cubs, find mates and food, avoid danger and detect an animal's carcass 20 miles away. [10–13]. In recognition its sense of smell, it was decided that the overarching control software for this detector will be called Bear!

Bear was designed to manage the gas testing operations for the instruments covered in Chapter 3 - 6. The aim was design a single port of operations to allow these instruments function together during analysis. Bear also provides a layer of abstraction to the user by managing gas flows, timing, humidity, concentration, heating and several other parameters. It is essential that these parameters are consistent across gas analysis ensuring repeatable and reproducible results. Additionally Bear records test measurements to a *.csv* file for further statistical analysis. Bear was written in C♯ for the Universal Windows Platform (UWP) and targeted at the 64 bit Windows 10 version 1803.

This section will discusses the design of Bear for humidity, concentration, PID and manual analysis using the Model 700 Calibrator, Dilutor and the AC,PC,VOC detector assembly described earlier.

6.4.1 Software overview

Bear is designed to provide the user with at automated control interface for analysis using the Model 700 Calibrator, Dilutor, AC,PC and VOC detector. It allows the user to use all of these instruments for robust sensor calibration or select a few components for simple sample analysis. A chart of the software layout is shown in Figure 6.11.

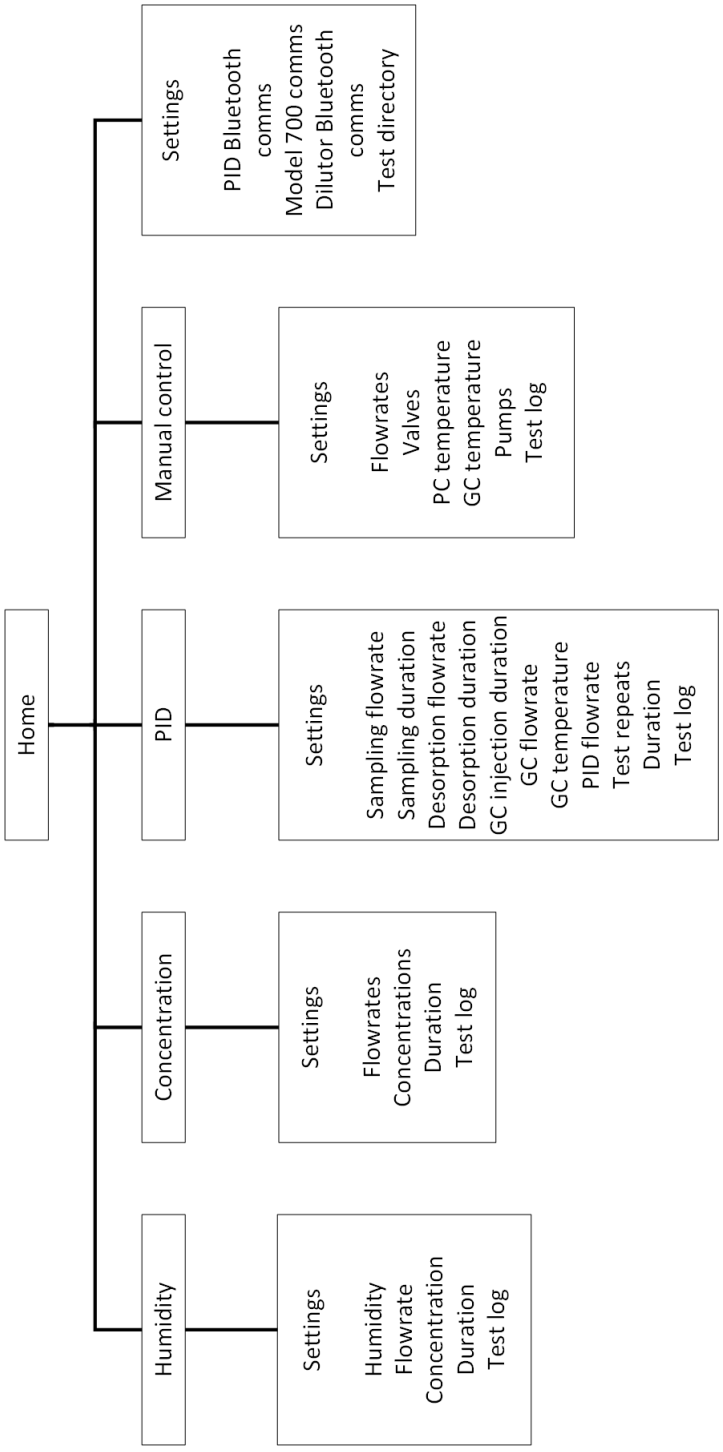

Figure 6.11: Bear software layout.

Bear provides four test scenarios namely Humidity, Concentration, PID and

Manual control. Each test scenario has an associated Settings page allowing the user to set specify test parameters for the sensor. Bears Graphical User Interface (GUI) is designed in a Master-Detail style. The Master pane on the left lists analysis scenarios and the general Settings button at the bottom of the pane. The Detail view covers majority of the screen and provides controls for the user to interact with the instrument. The controls available to the user as will be explained depends on the selected scenario. These test scenarios are discussed next.

6.4.2 General settings

The General Settings page is where housekeeping for Bear is managed. Here the user specifies a directory to be used as the working directory. This is where test sequences, measurements and sensor responses are stored. On this page (Figure 6.12) Bear enumerates surrounding Bluetooth LE devices and allows the user to establish a Bluetooth connection between Bear and the VOC detector and Dilutor. Bear also connects to the Model 700 Calibrator via a USB to RS232 converter.

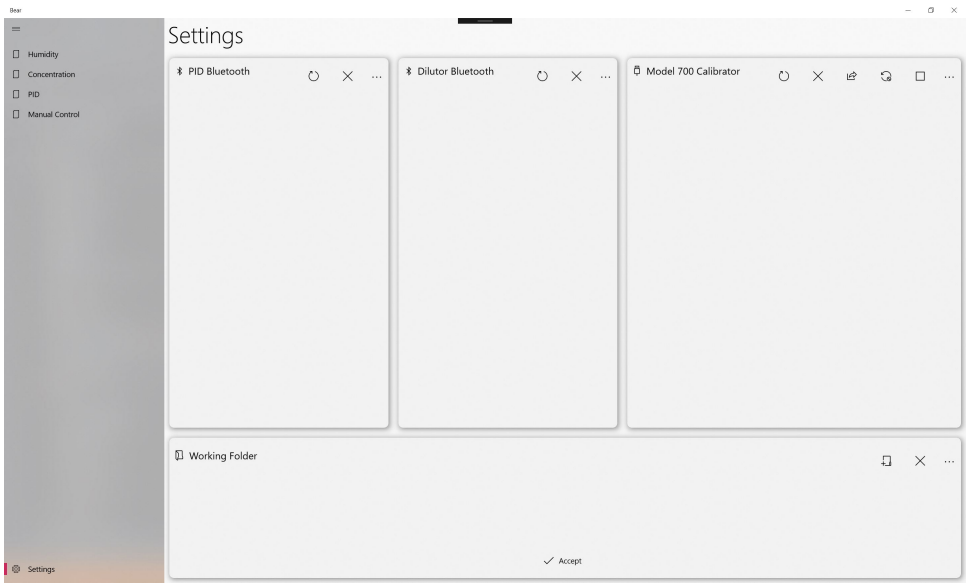

Figure 6.12: General Settings page

6.4.3 Humidity

The Humidity test page is designed to aid humidity calibration tests on the instrument. The gas flow for this sequence is illustrated in Figure 6.13.

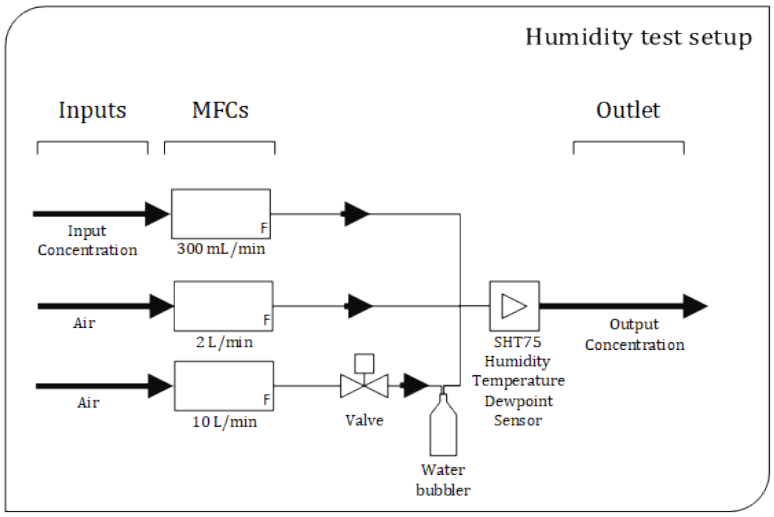

Figure 6.13: Humidity test gas flow

Calibration analyte of a known concentration is fed into the 300 mL/min MFC in the Dilutor. Zero air is fed supplied into the 2 L/min and 10 L/min MFCs in the Dilutor and Model 700 Calibrator. The output from the Model 700 Calibrator is bubbled in a water bubbler to humidify the air before being mixed with the output from the other MFCs. The mixture is passed through a chamber containing the SHT75 sensor before being fed into the VOC detector. The relative humidity measurement from the SHT75 is sent to Bear. Using this information Bear adjusts the dry air flow through either the 2 L/min or the wet air flow through the 10 L/min MFC. A proportional derivative controller class was designed to aid with precise humidity control. This controller is simplified in Equation 6.2.

$$Flowrate_w = K_p e(t) + K_i \int_0^t e(t') + K_d \frac{de(t)}{dt} \tag{6.2}$$

This equation determines the wet flow rate, $Flowrate_w$, through the 10 L/min MFC. $e(t)$ is the error or difference between the humidity set-point and the current humidity. K_p, K_i and K_d are the proportional, integral and derivative gains which are specified by the user. The proportional term adjusts the flow rate proportionally to the current error, the integral term accounts for both the magnitude and duration of the error while the derivative term accounts for the rate of change of the error. By varying K_p, K_i and K_d, the controller response can be tuned to adjust humidity as desired by the user. Bear computes the dry flow rate $Flowrate_d$ using Equation 6.3 by subtracting the wet flow rate $Flowrate_w$ and the input gas flow rate GF (obtained using Equation 6.4) from the total flow rate specified by the user.

$$Flowrate_d = Total flowrate - Flowrate_w - GF \tag{6.3}$$

For Humidity analysis, the user specifies calibration settings on the Humidity settings page (Figure 6.14). Here, the user specifies if the responses obtained from the VOC detector and test measurements should be logged and provides a file name. They also provide the input concentration of the analyte to be tested, the desired output concentration to be fed into the VOC detector and the fixed flow rate from the test. The user now goes on to build a humidity test sequence in the test sequence table by specifying humidity and duration. Bear ensures that the calibration gas supplied to the instrument is at fixed flow rate and concentration and that only humidity is varied and prescribed by the test sequence. This approach allows sensor calibration based on humidity alone eliminating the effects of changing concentration and flow rates on the sensor.

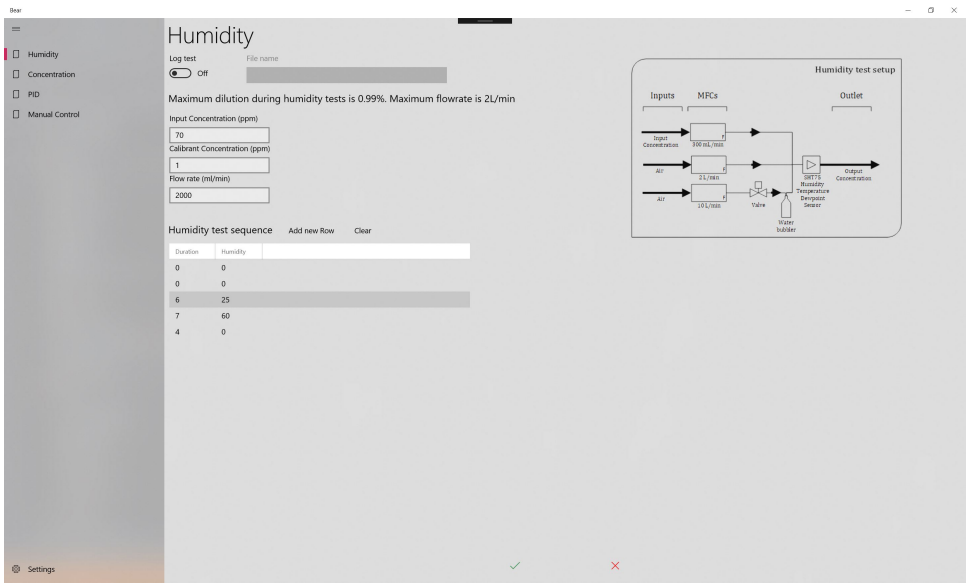

Figure 6.14: Humidity Settings page.

Bear computes the gas flow rate GF through the 300 mL/min to achieve the

desired test concentration or calibration concentration CC using Equation 6.4.

$$GF = \frac{Total flowrate * CC}{IC} \tag{6.4}$$

The $Total flowarate$ and input concentration IC are provided by the user in the Humidity settings page. Clicking the Accept button at the bottom of this page navigates the user to the Humidity main page (Figure 6.15). Here the user can click the Start button at the bottom of the page to start the Humidity test.

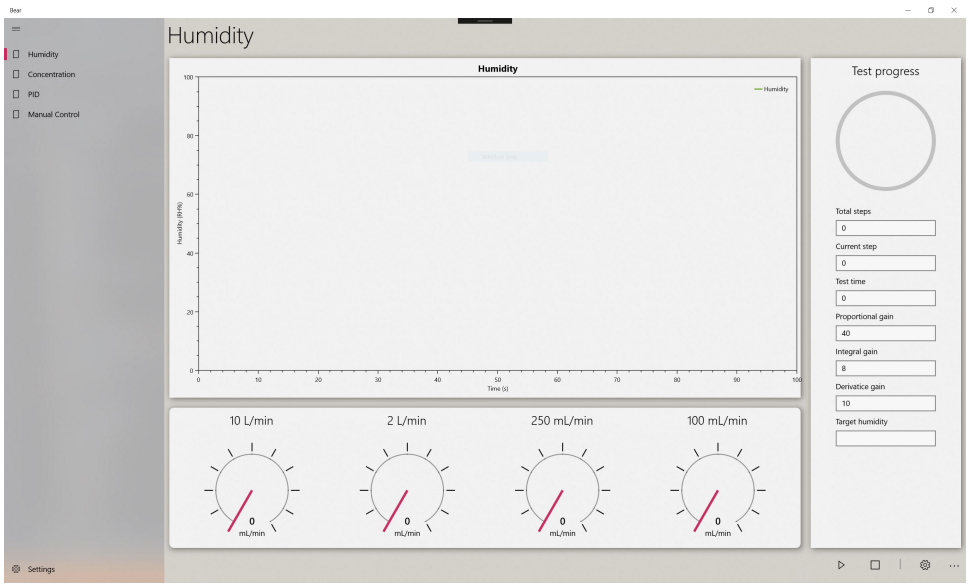

Figure 6.15: Humidity Test page.

During tests Bear creates a timer on a separate processor thread. This ensures accurate repeatable test timing since the test timer in not impeded by any other computing processes. The timer raises an event at predefined intervals and the event handler checks if the duration for a particular sequence has expired. Once the duration for a sequence is complete Bear iterates to the next step in the test sequence until the test is complete. Three input controls are provided for the user

to adjust the proportional, integral and derivative gain during a analysis ensuring that the desired humidity is always achieved.

6.4.4 Concentration

The Concentration test page is designed to aid concentration calibration tests. It allows the user to mix gasses and perform analysis such as Limit of Detection (LOD) tests on the VOC detector. The gas flow path for this test setting is shown in Figure 6.16.

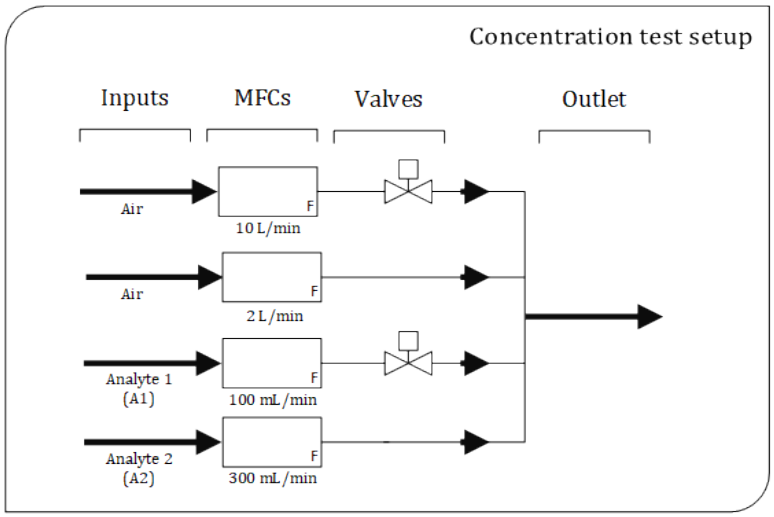

Figure 6.16: Concentration Settings page.

Two analytes, A1 and A2, can be supplied into the 100 mL/min and 300 mL/min MFCs respectively. Diluent air is supplied into the 10 L/min and 2 L/min MFCs allowing a maximum of 0.99% gas dilution. For calibration analysis the user specifies if the test will involve mixing of two gasses or a single gas test. After supplying the analyte concentration A_{conc} and total flow rate F_T Bear computes the maximum concentration Max_{conc} and minimum Min_{conc} that is achievable for analyte A1

using Equation 6.5 and 6.6.

$$Max_{conc} = \frac{100}{F_T + 100} * A1_{conc} \tag{6.5}$$

$$Min_{conc} = \frac{20}{F_T + 20} * A1_{conc} \tag{6.6}$$

Using this information the user builds a concentration test sequence within the concentration range by specifying duration and concentrations in the sequence table (Figure 6.17). Bear ensures that the total flow rate reaching the sensor is fixed during analysis so that sensor responses obtained are only due to changes in concentration of analyte and not flow rate.

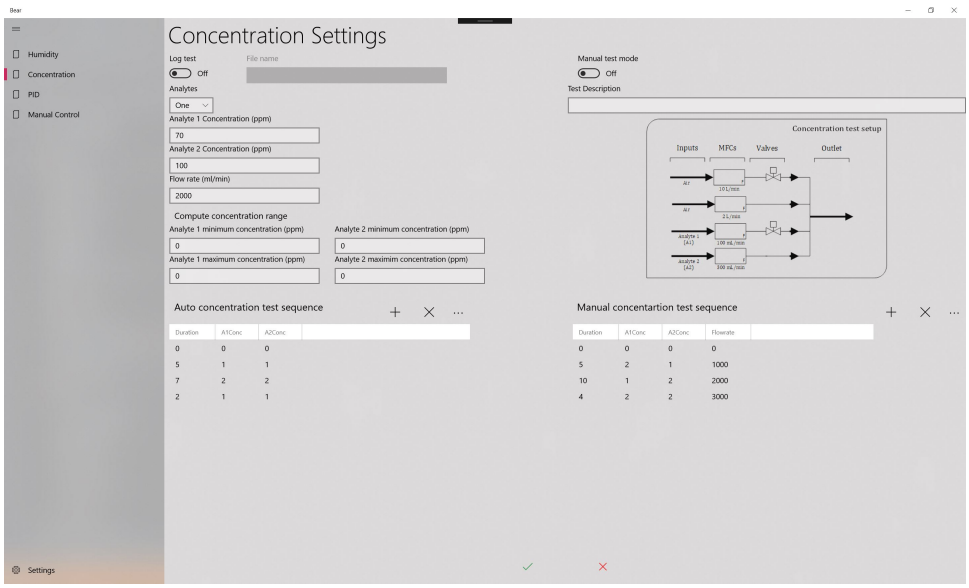

Figure 6.17: Concentration Settings page.

A second test sequence table is provided for tests where the effect of changes to flow rate is also investigated. This table allows the user to change flow rates for each sequence in the test. This is for tests where the effect of flow rates on the sensor is to

be analysed. Clicking on the accept button navigates the user to the Concentration test page (Figure 6.18). Here the user starts the analysis by clicking start at the bottom of the page. Similar to the Humidity page, Bear creates are timer and iterates through the user prescribed concentrations. A graphical representation of the sensor responses are displayed for user as well as flow rates from the MFCs.

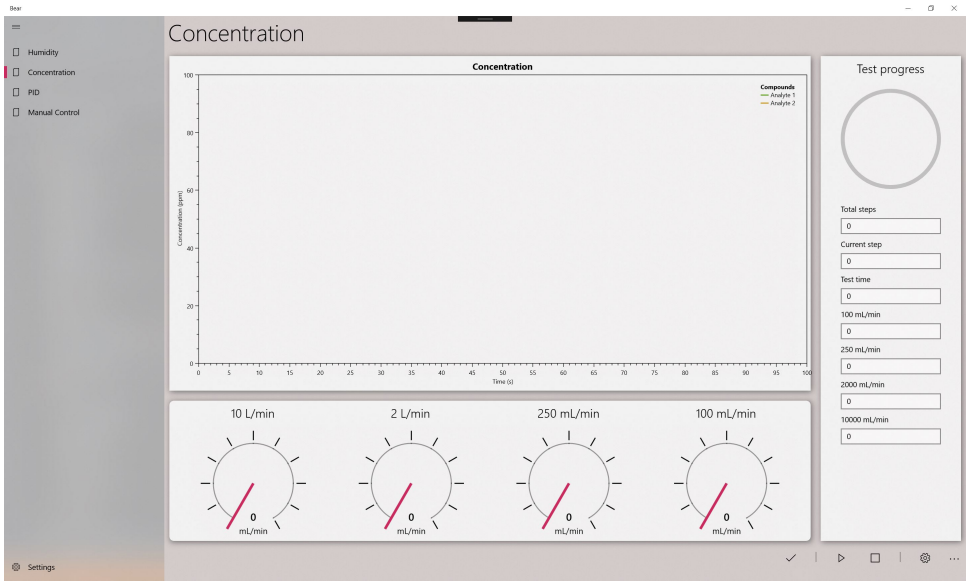

Figure 6.18: Concentration Test page.

6.4.5 PID

This page was designed aid operating the instrument as a gas analytical instrument. On the PID Settings page (Figure 6.19) the operating modes described in Section 6.2.2 are presented to be customised by the user. Various operating modes can be enabled or disabled. The duration, flow rates and temperature controls allows the user to define complete tests sequences for the GC, PC, and VOC detector.

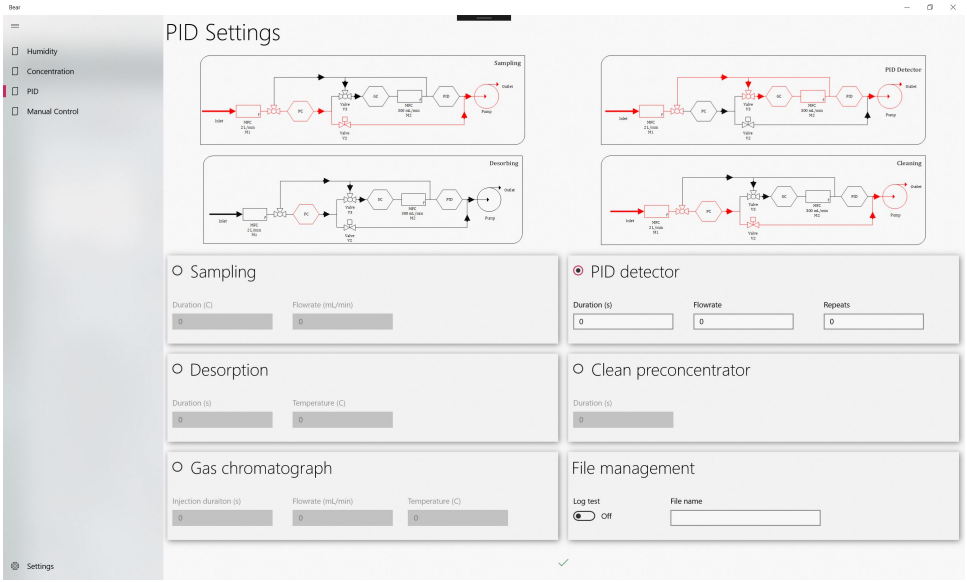

Figure 6.19: Detector Settings page.

After entering the analytic settings, the user navigates to the PID test page (Figure 6.20) to begin the test. Clicking start at the bottom of the page creates a timer for each operating mode enabled. This allows Bear to independently manage the function of each mode. For example, during the desorption process, Bear runs a parallel timed background tasks that prepares the GC and pumps for sample injection. Using this technique, Bear ensures all three components are in the required state before the sample reaches each component. The interface displays a plot of the detector responses, flow rates from the MFCs and temperature measurements from the AC and GC. All system measurements are also saved to a *.csv* for future statistical analysis.

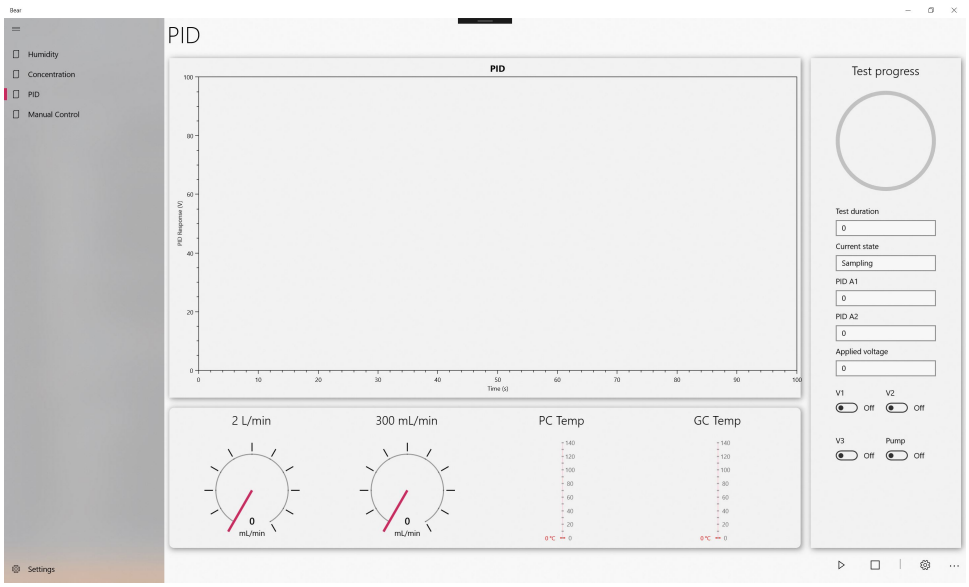

Figure 6.20: Detector Test page.

6.4.6 Manual control

The final test scenario on the Bear software is the Manual Control. This mode allows the user to build a manual test sequence specifying duration, valve and pump states, PC and GC temperatures, MFCs flow rates etc. All of these settings are collected on a central data grid in the Manual Control Settings page.

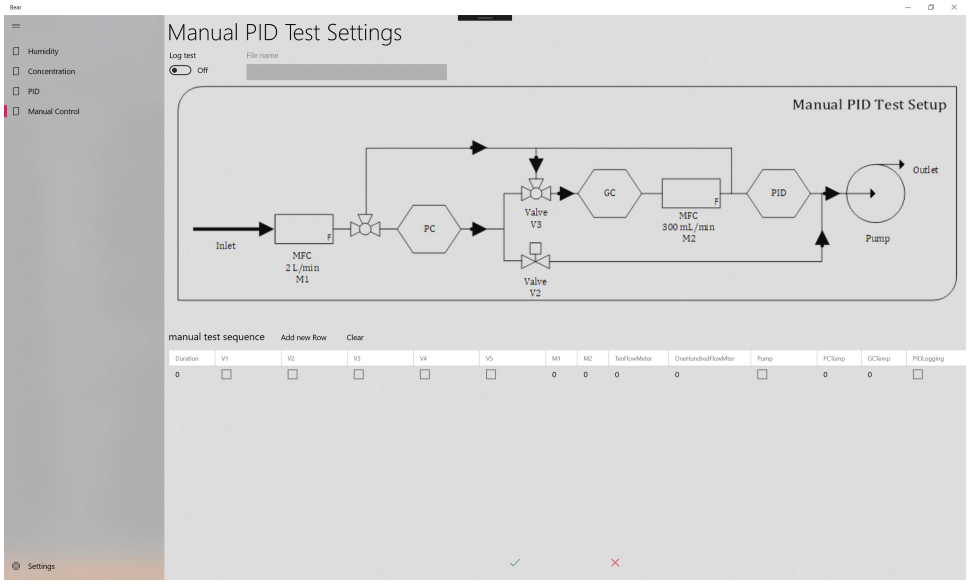

Figure 6.21: Manual Settings page.

On the Manual Control test page (Figure 6.22), the user begins the test by clicking Start button at the bottom of the page. Toggle controls and textboxes are added to this settings page to allow manual override of the test sequence during analysis.

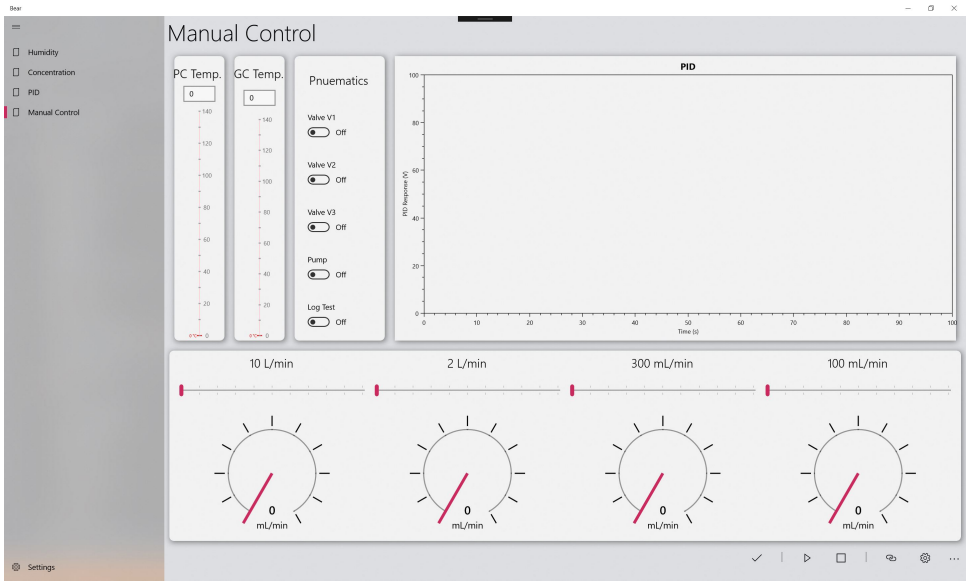

Figure 6.22: Manual Test page.

6.5 Conclusion

In this chapter the assembly of the PC, GC and PID VOC detector have been presented. The power supply design approach to ensure various components in the system function without EMI and RFI were also discussed. An analytic software was also developed to manage the operation of the assembled system. The next chapter discusses gas analysis tests and results carried using this instrument.

6.6 References

[1] https://www.illinoiscapacitor.com/pdf/papers/emi_rfi_suppression_capacitors.pdf, November, 2018.

[2] http://www.martyncurrey.com/hm-10-bluetooth-4ble-modules/, November, 2108.

[3] http://www.mouser.com/ds/2/682/sensirion_humidity_sht7x_datasheet_v5-469726.pdf, November, 2018.

[4] https://store.arduino.cc/arduino-micro, November, 2018.

[5] http://ww1.microchip.com/downloads/en/devicedoc/atmel-7766-8-bit-avr-atmega16u4-32u4_datasheet.pdf, November, 2018.

[6] http://www.circuitbasics.com/wp-content/uploads/2015/11/srd-05vdc-sl-c-datasheet.pdf, November, 2018.

[7] http://www.ti.com/lit/ds/symlink/cc2540.pdf, November, 2018.

[8] Andrea Rinaldi. The scent of life: The exquisite complexity of the sense of smell in animals and humans. *EMBO reports*, 8(7):629–633, 2007.

[9] https://www.seeker.com/10-best-sniffers-in-the-animal-kingdom-1768828254.html, November, 2018.

[10] https://www.worldatlas.com/articles/which-animals-have-the-strongest-sense-of-smell.html, November, 2018.

[11] G Law and A Reid. Enriching the lives of bears in zoos. *International Zoo Yearbook*, 44(1):65–74, 2010.

[12] William R Boone, Becky B Keck, Jeffery C Catlin, Kevin J Casey, Edna T Boone, Penny S Dye, Randy J Schuett, Toshio Tsubota, and Janice C Bahr. Evidence that bears are induced ovulators. *Theriogenology*, 61(6):1163–1169, 2004.

[13] Steve Wolverton. Caves, ursids, and artifacts: a natural-trap hypothesis. *Journal of Ethnobiology*, 21(2):55–76, 2001.

Chapter 7

Biomedical Tests and Results

7.1 Introduction

Chapters 4 to 6 presented the work carried out to design a new Volatile Organic Compound (VOC) detection instrument for biomedical diagnosis. Various tests were presented in those chapters showing the ability of the instrument to detect VOCs at very low concentrations. To be used as a diagnostic tool, a significant amount of biomedical testing and trials must be done with this instrument. This chapter presents the biomedical tests carried out using this instrument. Before discussing the tests, the next section introduces the biomedical premise for the test.

7.2 Biomedical premise

In the United States, sepsis is becoming increasingly prevalent affecting 240 per 100,000 per year [1]. Sepsis is often lethal with a survival rate of 55 to 65 percent in

affected patients [2]. Antimicrobial drugs are necessary for the treatment of sepsis to prevent septic shock from bacterial infection. Mortality rate increased by 10 to 15 percent for patients who do not receive prompt appropriate antibiotic therapy[2]. In a study of 3929 patients where 984 progressed to septic shock, Whiles *et al.* reported that for each hour that passed between triage of these patients at the emergency department and antibacterial administration, the risk of progression to septic shock increased by 8% [3]. In their findings, the timing of antibiotics is an important factor in determining progression to sepsis shock.

Although the prompt delivery of appropriate antibacterial limits the progression of sepsis, antibacterials should not be administered until bacterial infection is diagnosed[4]. This is due to the prevalence of antibacterial resistance which in part, has resulted from medical abuse of antibiotics and the proliferation of drug resistant bacteria strains [5, 6]. Resistance to multiple drugs was first reported in the 1950s and has been detected in several bacteria including *Escherichia coli, Shigella and Salmonella* [5–8]. Therefore there is a need for swift detection of causative pathogens before the onset of antimicrobial therapy [9].

Current diagnostic methods incudes developing cultures for pathogen strains. However this may take days before the test results are available [9]. Additionally cultures may have limited sensitivity for patients already receiving antibiotics for a different infection [4]. Several studies have shown that bacteria have distinct metabolic pathway leading to the formation of certain VOCs. These VOCs are detected using gas analytic instruments such as electronic noses, Selected Ion Flow Tube Mass Spectroscopy (SIFT-MS), Gas Chromatography Mass Spectrometry (GC-MS) [10–12]. The presence of these compounds indicates the presence of the causative bacteria hence an infection is diagnosed.

Several bacteria have been detected in patients with sepsis. The six most abundant are *Klebsiella pneumoniae, Staphylococcus aureus, Enterococcus faecalis, Streptococcus pneumoniae, Pseudomonas aeruginosa*, and *Escherichia coli* [9]. All of these bacteria produce isopentanol, formaldehyde, methyl mercaptan, and trimethylamine which are not produced by humans. Table 7.1 shows the volatile biomarkers released in from the metabolic activities of some of these bacteria.

Table 7.1: Bacteria and volatile biomarkers given off during metabolism [9, 13, 14]

Bacteria	**Volatile biomarkers**
Staphylococcus aureus	Isovaleric acid, 2-methyl-butanal, acetone
Pseudomonas aeruginosa	1-undecene, 2,4-dimethyl-1-heptane, 2-butanone, 4-methyl-quinazoline, hydrogen cyanide, and methyl thiocyanide, acetone, indole
Escherichia coli	Methanol, pentanol, ethyl, acetate, acetone, and indole

For strains of *Escherichia coli* bacteria, indole (C_8H_7N) is the major VOC released [10, 12, 15–18]. Indole consists of six-membered benzene ring fused to a five-membered pyrrole ring (Figure 7.1) and could be detected in faeces, saliva and urine of infected humans [19].

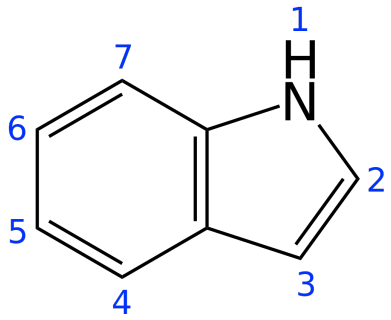

Figure 7.1: Indole.

Indole is biosynthesized in the Shikimate pathway from the amino acid Tryptophan by the enzyme tryptophanase as shown in Equation 7.1[20].

$$\mathrm{L{-}Tryptophan} + \mathrm{H_2O} \xrightarrow[PLP,NH_4+]{Tryptophanase} \mathrm{Indole} + \mathrm{Pyruvate} + \mathrm{NH_3} \tag{7.1}$$

Although the concentration of indole in faeces is documented and is available in the Human Metabolome Database [19], literature on the concentration of indole in urine is not readily available. Thorn *et al.* reported a concentration of 551.21 ppb of indole after incubating *Escherichia coli* for 24 hours and 147 ppb after incubating for 5 hours in some strains. They also reported a 210 parts per billion (ppb) concentration of acetone after 5h incubation of *Escherichia coli* [12].

The tests reported here were carried out to characterise the performance of this VOC analytic instrument as a diagnostic tool for detecting *Escherichia coli*, *Staphylococcus aureus* and *Pseudomonas aeruginosa* in urine medium. The test and statistical analysis where aimed at:

- detecting indole and acetone biomarkers in urine
- discovering limit of detection for indole and acetone

- identifying statistical methods best suited for diagnosis with this instrument

7.3 Materials and methodology

Experiments were designed to access the performance of the instrument in diagnosing bacterial infection in urine by detecting the presence of indole and acetone in urine. Therefore three tests were carried out to characterise the instruments performance as a diagnostic tool. The tests and aims are listed in Table 7.2:

Table 7.2: Diagnostic test sequence

Test	**Aim**
Detection of indole biomarker in urine	Demonstrate the instruments ability to detect *Escherichia coli*, *Staphylococcus aureus*, and *Pseudomonas aeruginosa*. Test for Limit of Detection (LOD) for indole and acetone to ascertain the minimum concentration of biomarker detectable by the instrument
Detection of random indole concentration	Eliminate the effect of biomarker concentration in diagnosis
Detection of indole and acetone in urine	General diagnosis of bacteria in urine

For each test in the sequence, a set of urine was analysed and compared with the urine containing the biomarker. To ensure consistency across urine samples used for the tests, synthetic urine was used. Surine Neg Urine Control was purchased from Sigma-Aldrich. The indole biomarker used was the Indole 99% (50 g) which

was obtained from VWR. Liquid acetone was also purchased from Sigma-Aldrich to be used as biomarker for the tests. Section 7.3.1 - 7.3.3 describes the sample preparation and test methodology for the different sample groups.

7.3.1 Urine

The preparation process involves pipetting 10 mL of urine sample into a 20 mL glass vial. The vial was covered with a vial cap. Since the urine samples are stored in a fridge, the vial was allowed to sit for 3 hours to attain 25°C room temperature. Next the vial cap was replaced with a sampling cap with two 1/8 inch push-fit adaptors to allow 1/8 inch tubing to be connected to the vial. One of the adaptor was connected to the inlet of the instrument and the other end was blocked to trap VOCs in the headspace of the vial. The vial was placed in a Dri-Block (Techne) heater and heated to a temperature of 40°C for five minutes. This step releases the volatiles in the solution in the headspace in the vial. Next, the analytic process with the instrument is started using Bear and the block on the other vial inlet is removed. Bear's settings for analysis are presented in Table 7.3. The sample was supplied into the instrument with at a flow rate of 300 mL/min with 1200 mL/min clean air make-up flow.

Table 7.3: Instrument analytic sequence using Bear

Procedure	**Duration (s)**
Sampling	10
Desorbtion	30
GC and PID analysis	40

7.3.2 Indole

Urine containing indole were analysed on the VOC detector instrument to simulate diagnostic tests for bacteria infection. As mention earlier, *Escherichia coli* and *Pseudomonas aeruginosa* have been shown to produce indole in urine, breath and saliva. Preparation of the indole sample begins with dissolving the solid indole in urine solution. However to obtain a lower concentration sample, indole was first dissolved in water and the dissolved solution was added to urine. The masses of indole were measured using the GR-202 Semi-Micro Analytic Balance from A&D Company LTD. The analytic balance offers a 0.01 mg resolution allowing precise indole mass measurement. In this procedure, the concentration of indole in water C_{iw} is given by Equation 7.2

$$C_{iw} = \frac{m_i}{V_w} * 1000 \tag{7.2}$$

Using 7.2 a solution with a known concentration of indole in parts per million (ppm) can be obtained from a given mass of indole (m_i) and volume of water V_w. The solid indole in water was dissolved in water by stirring with magnetic stirrer for 45 minutes. Next 0.1 mL of this solution is pipetted into a 10 mL solution of urine. The concentration of indole in urine C_{iu} was obtained using Equation 7.3.

$$C_{iu} = \frac{V_{iw}}{V_{iw} + V_u} * C_{iw} \tag{7.3}$$

Using 7.3, a urine solution with a known concentration of indole in ppm can be obtained from a fixed volume of aqueous indole V_{iw} containing a known concentration of indole C_{iw} and volume of urine V_u. Using equation 7.2 and 7.3, several urine and

indole solutions were generated.

The test procedure is similar to tests with urine alone. Again, 10 mL of indole and urine mixture were pipetted into a 20 mL glass vial and allowed to sit for 3 hours to attain room temperature. Next the vial cap was replaced with a sampling cap with two 1/8 inch push-fit adaptors to allow 1/8 inch tubing to be connected to the vial. One of the adaptor was connected to the inlet of the instrument and the other end was blocked to trap VOCs in the headspace of the vial. The vial was placed in a Dri-Block (Techne) heater and heated to a temperature of 40°C for five minutes to release the volatiles in the solution. Next, the analytic process process with the instrument is started using Bear and the block on the other vial inlet is removed. Bear's settings for analysis are the same with the urine tests as presented in Table 7.3. The sample flow was set to 300 mL/min with a clean air flow of 1200 mL/min. This dilution enables the instrument to test lower concentration of indole C_{id} using the Gas Test Rig presented in Chapter 3.

The mixtures and concentrations of indole tested are summarised in Table 7.4.

Higher concentrations of indole were obtained by dissolving indole directly in urine. Dissolving a given mass of indole m_i in a volume of urine V_u gives a urine solution with an indole concentrations C_{iu} in ppm given by Equation 7.4.

$$C_{iu} = \frac{m_i}{V_w} * 1000 \tag{7.4}$$

The indole solutions obtained by directly dissolving indole in urine are shown in Table 7.5.

Table 7.4: Low concentration indole and urine mixtures

m_i (mg)	V_w (mL)	C_{iw} (ppm)	V_{iw} (mL)	V_u (mL)	C_{iu} (ppm)	C_{id} (ppb)	$\approx C_{id}$
1	1000	1	0.1	10	0.01	1.98	2 ppb
10	1000	10	0.1	10	0.10	19.80	20 ppb
10	100	100	0.1	10	0.99	198.02	200 ppb
51	100	510	0.1	10	5.05	1009.90	1 ppm
10	10	1000	0.1	10	9.90	1980.20	2 ppm
21	10	2000	0.1	10	19.80	3960.39	4 ppm

Table 7.5: High concentration indole and urine mixtures

m_i (mg)	V_u (mL)	C_{iu} (ppm)	C_{id} (ppm)
0.5	10	50	10
1	10	100	20

7.3.3 Acetone

Urine containing acetone was tested on the VOC detector instrument to simulate diagnostic tests for bacteria infection from *Pseudomonas aeruginosa* and *Staphylococcus aureus*. Preparation of the acetone and urine samples begins with mixing small quantity of acetone in urine solution. Similar to the preparation of indole samples, low concentration acetone samples were obtained by mixing in two stages. First, a fixed volume of acetone V_a is mixed with a known volume of water V_w. The concentration of acetone C_{aw} (ppm) in the acetone water solution is given by Equation 7.5

$$C_{aw} = \frac{V_a}{V_a + V_w} * 1000000 \tag{7.5}$$

Next 0.1 mL of the acetone water mixture V_{aw} is pipetted into a fixed volume of the urine sample. The concentration of acetone in urine C_{au} (ppm)was obtained using Equation 7.6.

$$C_{au} = \frac{V_{aw}}{V_{aw} + V_u} * C_{aw} \tag{7.6}$$

The test procedure is similar to tests with indole. Again, 10 mL of acetone and urine sample were pipetted into a 20 mL glass vial and allowed to sit for 3 hours to attain room temperature. Next the vial cap was replaced with a sampling cap

with two 1/8 inch push-fit adaptors to allow 1/8 inch tubing to be connected to the vial. One of the adaptor was connected to the inlet of the instrument and the other end was blocked to trap VOCs in the headspace of the vial. The vial was placed in a Dri-Block (Techne) heater and heated to a temperature of 40°C for five minutes to release the volatiles in the solution. Next, the analytic process process with the instrument is started using Bear and the block on the other vial inlet is removed. Bear's settings for analysis are the same with the urine tests as presented in Table 7.3. The sample flow was set to 300 mL/min with a clean air flow of 1200 mL/min. This dilution enables the instrument to test lower concentration of acetone C_{iad} using the Gas Test Rig presented in Chapter 3. The mixtures and concentrations of acetone tested are summarised in Table 7.6.

The acetone, indole and urine solutions described in this section were used for the diagnostic test sequences listed in Table 7.2. Before discussing the results, the next section introduces the statistical approach used in the analysis of the test measurements.

7.4 Statistical analysis

The signals produced by gas based diagnostic instruments are translated to meaningful results using statistical analytic methods. The statistical analysis carried out in this section was not exhaustive and was aimed at identifying statistical methods that best demonstrate the instrument's performance as a diagnostic tool. Several statistical methods are often used in medical diagnosis including Logistic Regression (LR)[21], Random Forest (R-F)[22], Support Vector Machine (SVM) [22–24], Linear Discriminant Analysis (LDA) [25], Hierarchical clustering (HC) [23], k-means clustering (KMC) [22], K-nearest neighbour (KNN) [26], Naive Bayes (NB) [27]. These methods could be group into supervised and unsupervised learning methods. With supervised learning methods, the sample groups ($i.e$ infected, control) groups are known. For unsupervised learning methods, the groups are not known and the selected statistical method is expected to find clustering of these groups within the dataset. With a view to identifying the best statistical analytic method for this diagnostic instrument, all the methods mentioned were evaluated. In the end an analytic pipeline based on the best models were designed for both supervised and unsupervised diagnostic scenarios. For supervised learning methods, classes of indole, acetone and urine test results were used to train the model and later tested on a separate test set. For unsupervised models, it is assumed that classes of indole,

Table 7.6: Low concentration acetone and urine mixtures

v_a (mL)	V_w (mL)	C_{aw} (ppm)	V_{aw} (mL)	V_u (mL)	C_{au} (ppm)	C_{id} (ppm)	$\approx C_{id}$
0.052	500	99.99	0.1	10	0.099	0.198	200 ppb
0.05	100	499.75	0.1	10	4.95	0.989	1 ppm
0.1	90	1109.88	0.1	10	0.99	2.19	2 ppm
0.5	100	4975.12	0.1	10	5.05	9.85	10 ppm
1	99	10000.00	0.1	10	9.90	19.80	20 ppm

acetone and urine test results were unknown. The result of this analysis demonstrates the instruments ability to separate within these groups. A summary of the statistical methods used for the various tests are shown in Table 7.7.

Table 7.7: Statistical methods

Test	**Learning type**	**Statistical methods**
Detection of biomarker	Supervised	LR, NB, SVM, R-F, KNN
Detection of random biomarker conc.	Unsupervised	HC, KMC
Detection of indole and acetone	Supervised & unsupervised	LDA,HC, KMC

All statistical pipelines where written in the Python programming language (Python 3.7.2) using the `sklearn` package for data analysis and the `matplotlib` package for visualisation. Microsoft's Visual Studio Code (version 1.30.1) was used as the integrated development environment. The major processing steps for the supervised and unsupervised learning pipelines are summarised in Tables 7.8 and 7.9.

Table 7.8: Steps in unsupervised learning pipeline

Step	**Processes**
Data preprocessing	Obtain data
	Binary encode labels
	Standardize dataset
Data analysis	Split data into training set (60%) and test (40%) sets
	Feature extraction using Principal Component Analysis (PCA) (not applicable for LDA)
	Select and fit models using training set
	Predict outcome using test set
Model validation	Tune hyper-parameters using `GridSearch` cross-validation
	Re-run model fitting and prediction using optimum hyper-parameters
	Validate model using 10-fold cross-validation
	Compute Confusion Matrix (CM), f1-score, accuracies of model
	Visualise diagnostic results

Table 7.9: Steps in supervised learning pipeline

Step	**Processes**
Data preprocessing	Obtain data
	Remove labels
	Standardize dataset
Data analysis	Plot dendograms (HC) to deduce number of clusters
	Use elbow method to deduce number of clusters (KMC)
	Fit model to dataset
	Visualise diagnostic results

After each statistical method was fitted to the test results, the CM, f1-score and accuracies for the models were computed to ascertain the appropriate statistical model for such tests using this instrument.

7.5 Results and discussion

7.5.1 Detection of biomarkers in urine

The aim of this test is to demonstrate the instrument's performance in diagnosing the presence of *Escherichia coli*, *Pseudomonas aeruginosa* and *Staphylococcus aureus* by indole and acetone in urine. The test procedure included testing 20 sets of urine controls. For the indole infected group, sets of indole in urine samples were tested various indole concentrations. The concentration of indole was reduced between tests to discover the LOD for the instrument. The sample groups are summarized in Table 7.10

Table 7.10: Indole detection samples

Simulated Group	**Sample**	Concentration (ppm)	Quantity
Control	Urine	N/A	10
Infected	Urine and indole	20	20
Infected	Urine and indole	10	10
Infected	Urine and indole	4	10
Infected	Urine and indole	2	10
Infected	Urine and indole	1	10
Infected	Urine and indole	0.2	10
Infected	Urine and indole	0.02	10
Infected	Urine and indole	0.002	20

For the acetone group, various concentration of acetone in urine samples were tested. The concentration of acetone was reduced between tests to discover the LOD for the instrument. The sample groups are summarized in Table 7.11

Table 7.11: Acetone detection samples

Simulated Group	**Sample**	Concentration (ppm)	Quantity
Control	Urine	N/A	10
Infected	Urine and acetone	20	20
Infected	Urine and acetone	10	10
Infected	Urine and acetone	2	10
Infected	Urine and acetone	1	10
Infected	Urine and acetone	0.2	20

The sensor response for urine and 2pp indole after 20 repeats are shown in Figure 7.2.

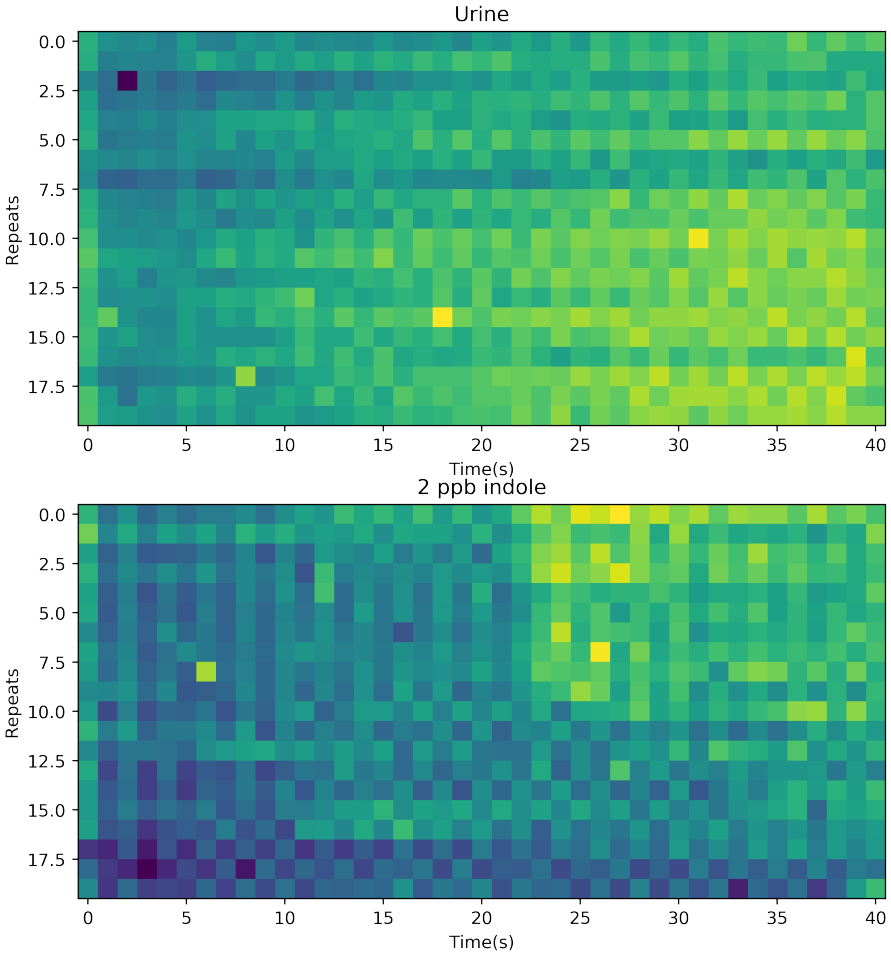

Figure 7.2: Sensor response for urine and 2pp indole after 20 repeats.

Classification of urine versus the infected groups were obtained using LR, NB, SVM, R-F, KNN. The best accuracy and f1-score was obtained using the R-F classification method with an f1-score of 1 and an accuracy of 100% for indole tests. An f1-score of 0.94 and an accuracy of 93% was obtained using R-F on the acetone test samples. The decision boundary obtained using this classifier for the training and test sets of the 2 ppb indole samples are show in Figure 7.3 and 7.4.

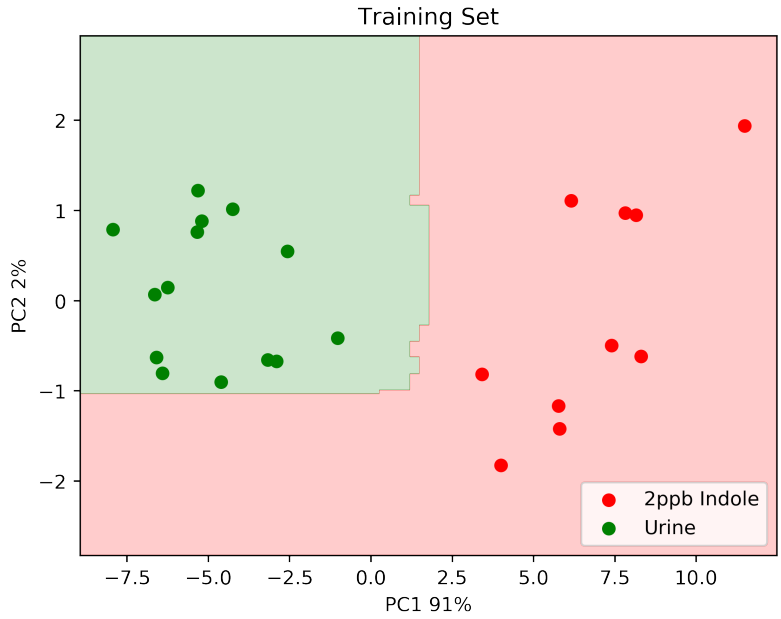

Figure 7.3: Plot showing decision boundary classifying 2 ppb indole and urine training set using R-F

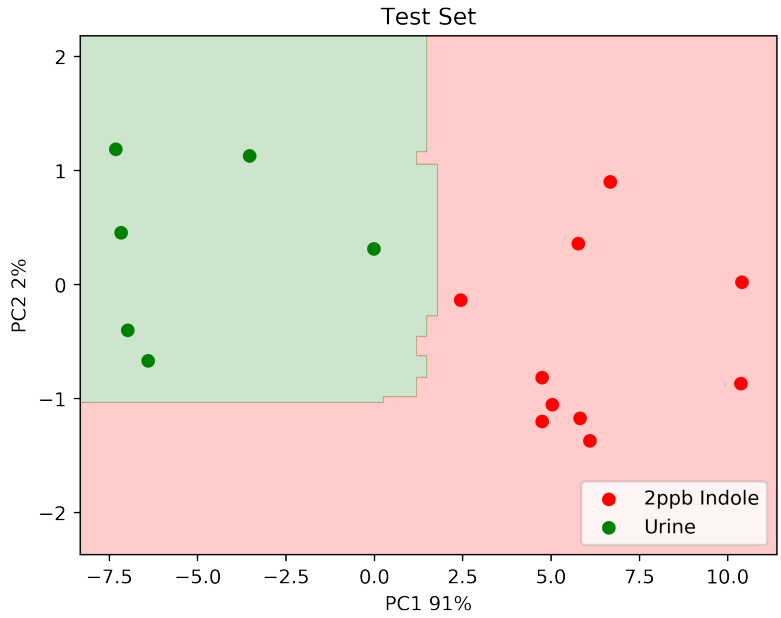

Figure 7.4: Plot showing decision boundary classifying 2 ppb indole and urine test set using R-F

The results demonstrate that the instrument differentiates between low concentration indole, acetone and urine samples and urine samples. As mentioned earlier, Thorn *et al.* reported a concentration of 551.21 ppb of indole after incubating *Escherichia coli* for 24 hours and 147 ppb after incubating for 5 hours in some strains. They also reported a 200 ppb concentration of acetone after incubating *Escherichia coli* for 5 hours. Lower concentrations of acetone in urine could not be tested due to limitations of the liquid measuring instrument. However, the classification results presented for 2 ppb indole suggests the instruments would be suitable to test the presence of indole in urine without the need for incubation.

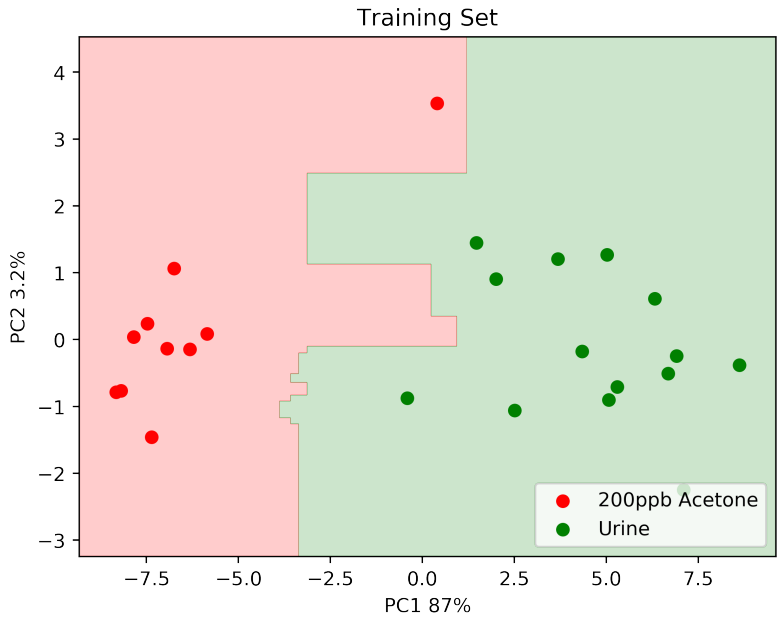

Figure 7.5: Plot showing decision boundary classifying 200 ppb acetone and urine train set using R-F

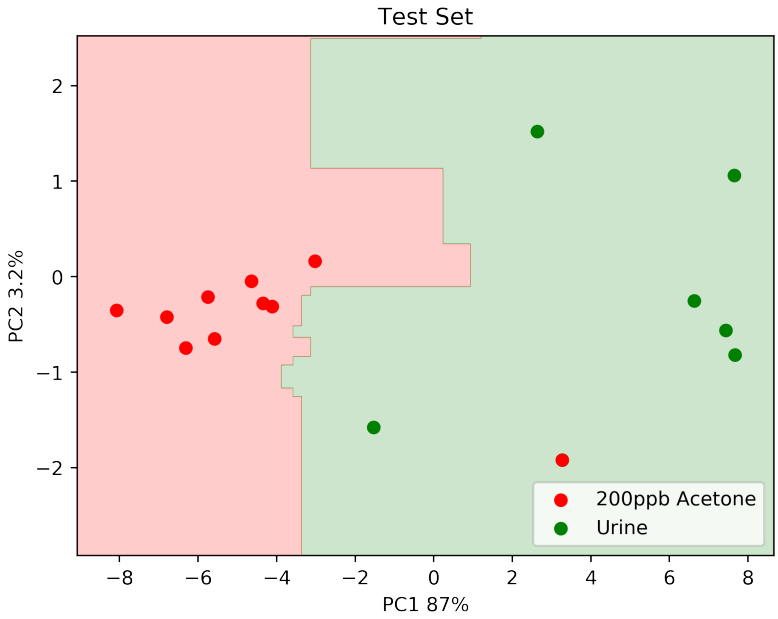

Figure 7.6: Plot showing decision boundary classifying 200 ppb acetone and urine test set using R-F

Results from classification of urine versus 2 ppb indole infected groups analysed using LR, NB, SVM, and KNN are presented in Appendix 9.1. Results from classification of urine versus 200 ppb indole infected groups analysed using LR, NB, SVM, and KNN are presented in Appendix 9.2.

7.5.2 Detection of random biomarker concentrations

This test was performed to demonstrate the effect of biomarker concentration on the clustering of the sample groups. Unsupervised statistical learning methods were used for this analysis. This was done to simulate test scenarios where the identity of the of the sample group is not available.

Two sets of tests were carried out. One set involved testing 20 urine samples and 80 indole samples. The indole samples had concentrations ranging from 2 ppb

to 20 ppm. The other set involved testing 20 urine samples and 50 acetone samples with concentrations ranging from 200 ppb to 20 ppm. The KMC method was used to find clusters within the results. To find the number of clusters within the test results, the Elbow method was used. The within-cluster sums of squares (WCSS) and number of clusters are plotted in Figure 7.7 for indole and for acetone 7.8.

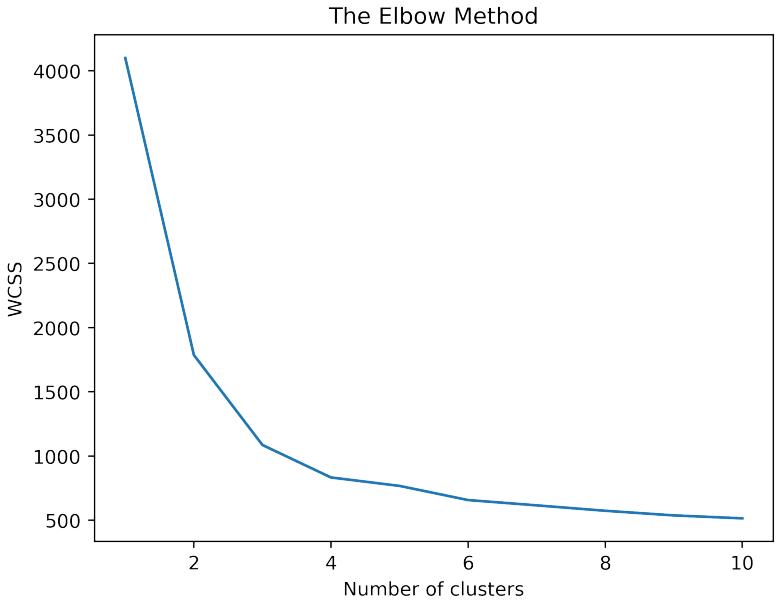

Figure 7.7: Elbow method plot for urine and indole tests

Both plots suggests there are three classes in the group. Analysis using a k value of 2 and 3 produces similar clustering plots as shown in Figure 7.9 and 7.10 for indole.

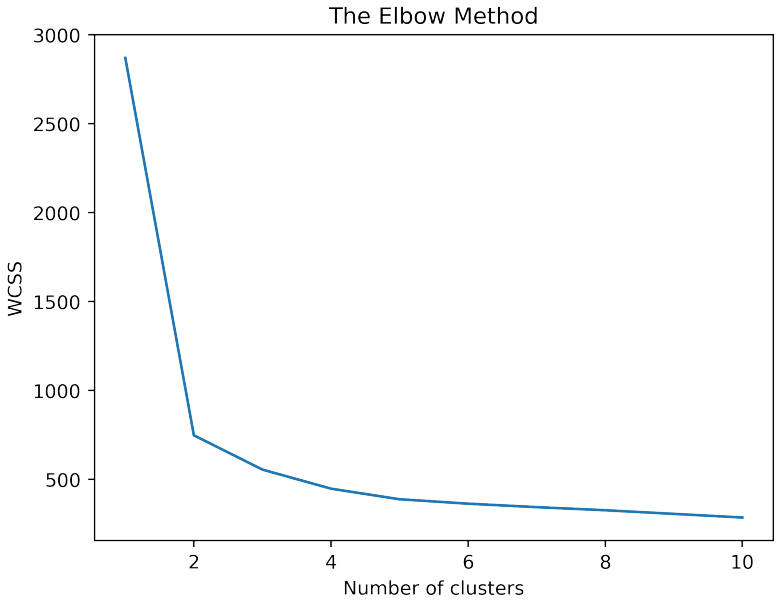

Figure 7.8: Elbow method plot for urine and acetone tests

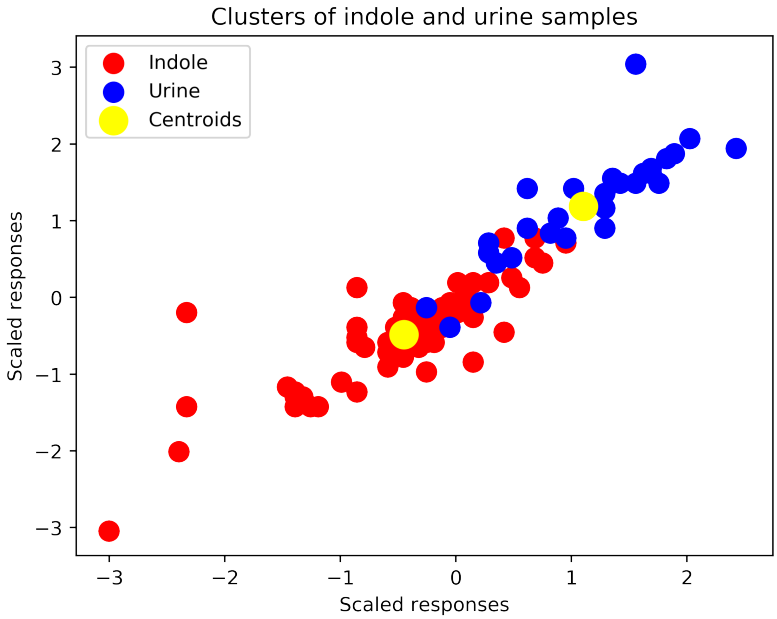

Figure 7.9: Clustering of urine and indole test samples using KMC ($k = 2$)

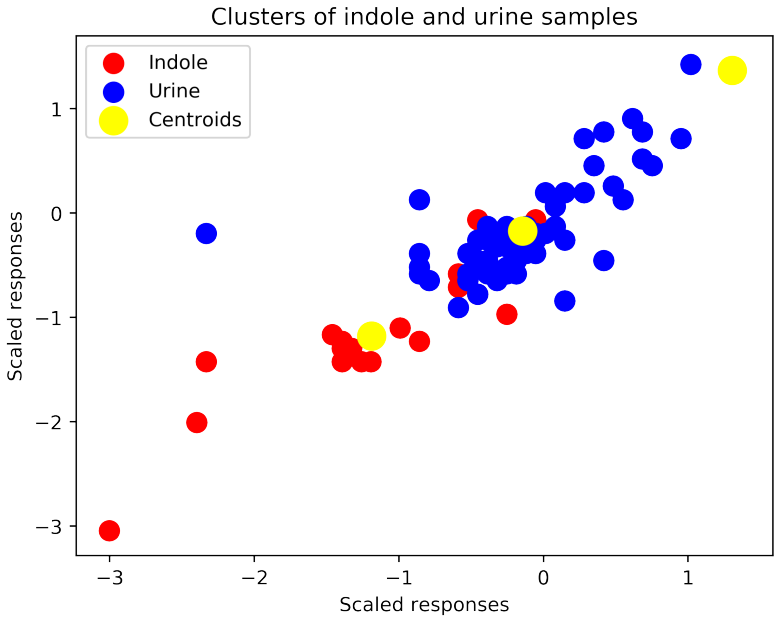

Figure 7.10: Clustering of urine and indole test samples using KMC ($k = 3$)

The third centroid when $k = 3$ appears to be an outlier and a better clustering of the test groups is observed when $k = 2$. Using a cluster number of 2 produces better clustering using the HC method. A plot of the indole and urine clusters using HC is shown in Figure 7.11.

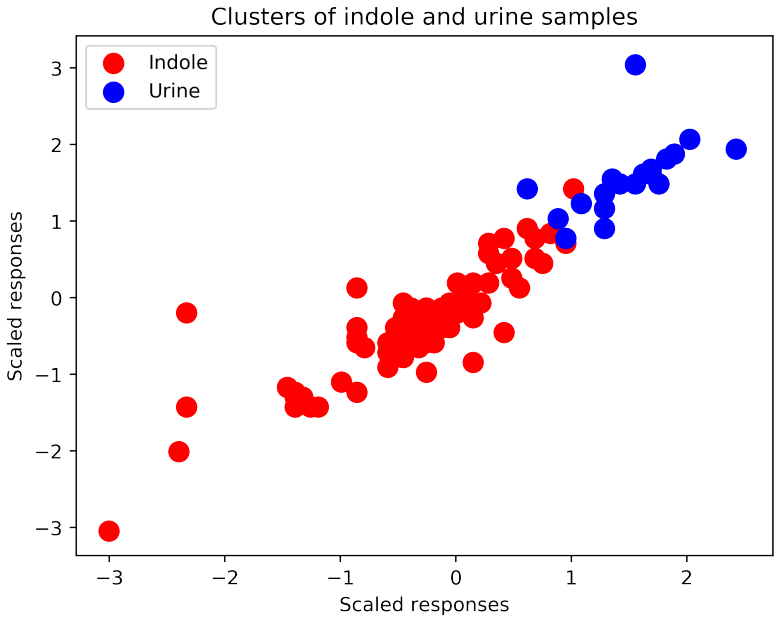

Figure 7.11: Clustering of urine and indole test samples using HC (`n_components` = 2)

The results are more interesting for acetone samples. Analysis using a k value of 2 and 3 produces distinct clustering plots as shown in Figure 7.12 and 7.13.

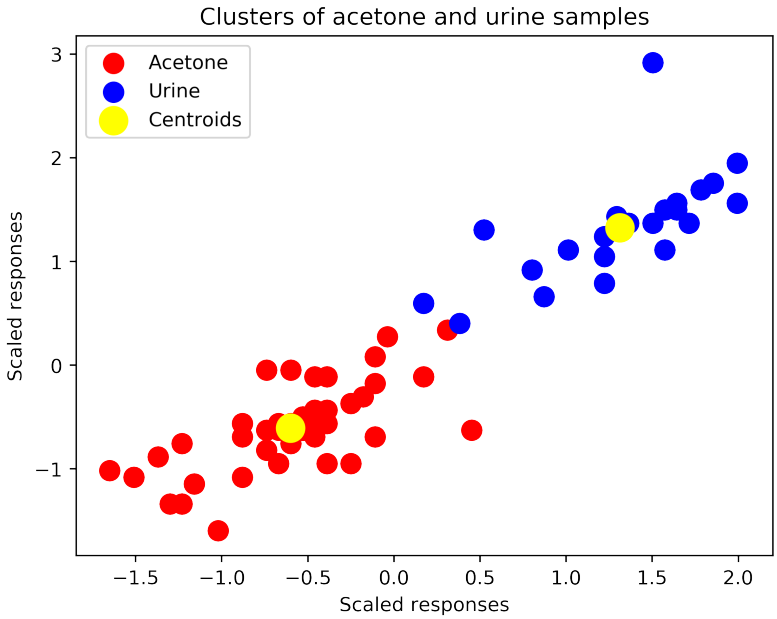

Figure 7.12: Clustering of urine and acetone test samples using KMC ($k = 2$)

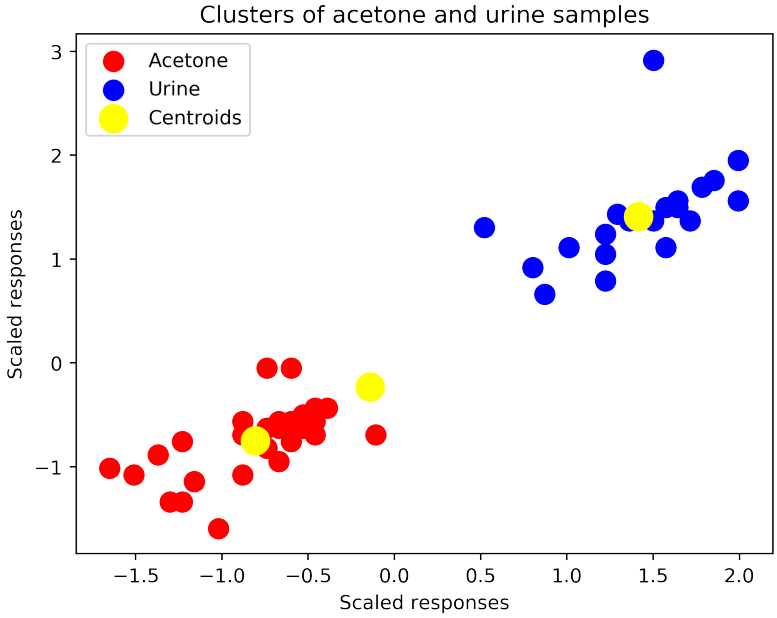

Figure 7.13: Clustering of urine and acetone test samples using KMC ($k = 3$)

Distinct clusters of acetone and urine samples are shown for k values of 2 and 3. The third centroid appears to be closer to the acetone clusterindicating separate

clusters within the acetone cluster. This could be as a result of the varying concentration in the sample set. However, both centroids are further from the urine centroid indicating a separation between the sample groups. Similar distinction between clusters is observed using HC with `n_components` set to 2.

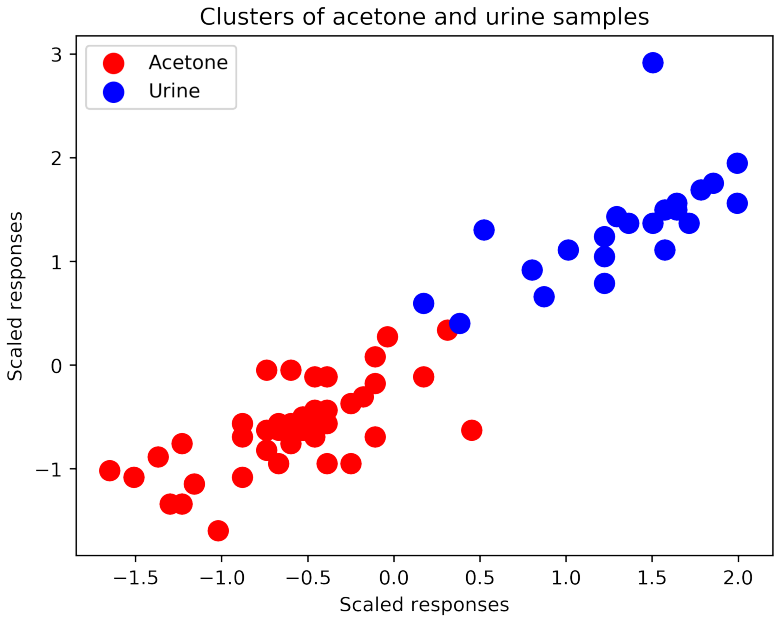

Figure 7.14: Clustering of urine and acetone test samples using HC (`n_components` = 2)

The results presented shows that the instrument could be used to analyse urine samples with varying concentration of acetone or indole. However, there was significant overlap between these clusters using the KMC method for analysis of indole tests. This could be due to the lower concentration levels of indole in the dataset. However, the results improved, showing significant clustering between urine and indole when the HC method is used. This demonstrates that mixed samples of urine control and infection could be analysed using this instrument without prior knowledge of the sample groups.

7.5.3 Detection of acetone and indole in urine

Patients are likely to be infected with either *Staphylococcus aureus*, *Pseudomonas aeruginosa* or *Escherichia coli* or a combination of these. It is expected that this diagnostic tool should diagnose the causative pathogen from the amount of acetone or indole in urine. This test was designed to ascertain the instruments performance in this aspect. The test samples consisted sets of 20 urine, 20 indole and 20 acetone. The results were analysed using LDA. This is because LDA models the difference between the classes of data. The decision boundary obtained from the analysis are plotted in Figure 7.15.

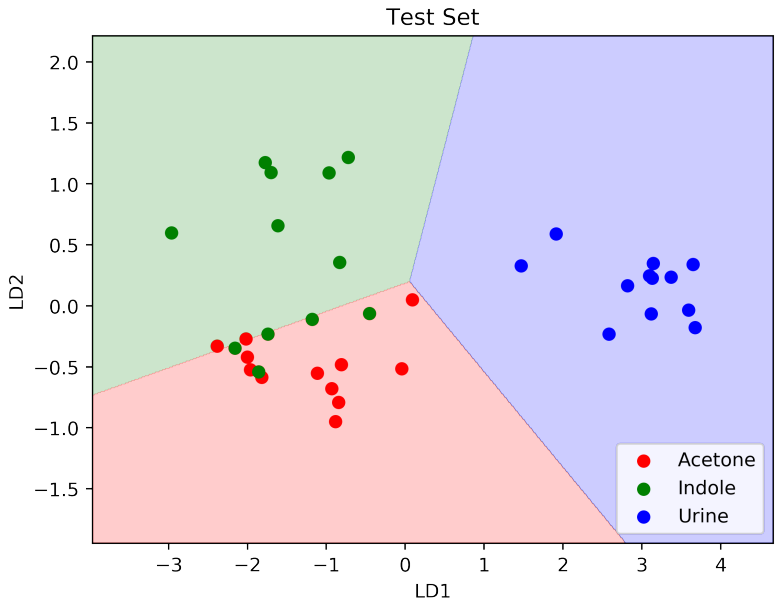

Figure 7.15

The instrument clearly differentiated between the infected samples (acetone and indole) and the urine samples. However, the model did not completely separate between indole and acetone samples. This shows the instrument is better suited to diagnosing infection than separating between the infections using the biomarkers

tested.

7.6 Conclusion

This chapter presented the practicality of using this instrument as a non-invasive diagnostic tool for bacterial infection. The initial results indicate that the instrument is capable of detecting VOCs released by causative pathogens such as *Staphylococcus aureus*, *Pseudomonas aeruginosa* or*Escherichia coli.* Indole and acetone, known biomarkers for these pathogens were tested. From the results, the instrument is capable of detecting the presence of the biomarkers in urine, down to 2 ppb indole and 200 ppb acetone. These results indicate that the instrument diagnosed the simulated infected groups from control with the possible benefit of eliminating the need for culture before testing for bacterial infection. The time saved by faster diagnosis of bacterial infection could improve the treatment and mortality rate of sepsis patients.

7.7 References

[1] Greg S. Martin, David M. Mannino, Stephanie Eaton, and Marc Moss. The epidemiology of sepsis in the united states from 1979 through 2000. *New England Journal of Medicine*, 348(16):1546–1554, 2003. PMID: 12700374.

[2] Arthur P. Wheeler and Gordon R. Bernard. Treating patients with severe sepsis. *New England Journal of Medicine*, 340(3):207–214, 1999. PMID: 9895401.

[3] Bristol B Whiles, Amanda S Deis, and Steven Q Simpson. Increased time

to initial antimicrobial administration is associated with progression to septic shock in severe sepsis patients. *Critical care medicine*, 45:623–629, April 2017.

[4] C J Grace, J Lieberman, K Pierce, and B Littenberg. Usefulness of blood culture for hospitalized patients who are receiving antibiotic therapy. *Clinical infectious diseases : an official publication of the Infectious Diseases Society of America*, 32:1651–1655, June 2001.

[5] Carlos Amábile-Cuevas. Antibiotic resistance in mexico: a brief overview of the current status and its causes. *Journal of infection in developing countries*, 4:126–131, March 2010.

[6] S B Levy. Antibiotic resistance: consequences of inaction. *Clinical infectious diseases : an official publication of the Infectious Diseases Society of America*, 33 Suppl 3:S124–S129, September 2001.

[7] Stuart B Levy and Bonnie Marshall. Antibacterial resistance worldwide: causes, challenges and responses. *Nature medicine*, 10:S122–S129, December 2004.

[8] T WATANABE. Infective heredity of multiple drug resistance in bacteria. *Bacteriological reviews*, 27:87–115, March 1963.

[9] Lieuwe DJ Bos, Peter J Sterk, and Marcus J Schultz. Volatile metabolites of pathogens: a systematic review. *PLoS pathogens*, 9(5):e1003311, 2013.

[10] Stefan Schulz and Jeroen S Dickschat. Bacterial volatiles: the smell of small organisms. *Natural product reports*, 24:814–842, August 2007.

[11] Alphus D Wilson and Manuela Baietto. Advances in electronic-nose technologies developed for biomedical applications. *Sensors (Basel, Switzerland)*, 11:1105–1176, 2011.

[12] Robin Michael Statham Thorn, Darren Michael Reynolds, and John Greenman. Multivariate analysis of bacterial volatile compound profiles for discrimination between selected species and strains in vitro. *Journal of microbiological methods*, 84:258–264, February 2011.

[13] Mohsen Sohrabi, Li Zhang, Kai Zhang, Adnan Ahmetagic, and Ming Q Wei. Volatile organic compounds as novel markers for the detection of bacterial infections, May 2014.

[14] Mohammed Ashrafi, Matt Bates, Mohamed Baguneid, Teresa Alonso-Rasgado, Riina Rautemaa-Richardson, and Ardeshir Bayat. Volatile organic compound detection as a potential means of diagnosing cutaneous wound infections. *Wound Repair and Regeneration*, 25(4):574–590, 2017.

[15] Andre G. Senecal, Joshua Magnone, Walter Yeomans, and Edmund M. Powers. Rapid detection of pathogenic bacteria by volatile organic compound (voc) analysis. In *Environmental and Industrial Sensing*, volume 4575, page 11. SPIE, 2002.

[16] Hesham Elgaali, T. R. Hamilton-Kemp, M. C. Newman, R. W. Collins, Keshun Yu, and D. D. Archbold. Comparison of long-chain alcohols and other volatile compounds emitted from food-borne and related gram positive and gram negative bacteria. *Journal of Basic Microbiology*, 42(6):373–380, 2002.

[17] Keshun Yu, Thomas R. Hamilton-Kemp, Douglas D. Archbold, Randall W. Collins, and Melissa C. Newman. Volatile compounds from escherichia coli o157:h7 and their absorption by strawberry fruit. *J. Agric. Food Chem.*, 48(2):413–417, February 2000.

[18] Hidetada Hirakawa, Yoshihiko Inazumi, Takeshi Masaki, Takahiro Hirata, and Akihito Yamaguchi. Indole induces the expression of multidrug exporter genes in escherichia coli. *Molecular microbiology*, 55:1113–1126, February 2005.

[19] http://www.hmdb.ca/metabolites/hmdb0000738, November, 2018.

[20] Esmond E. Snell. *Tryptophanase: structure, catalytic activities, and mechanism of action.* Advances in Enzymology - and Related Areas of Molecular Biology, 1975.

[21] Atsushi Ishibe, Mitsuyoshi Ota, Akemi Takeshita, Hiroshi Tsuboi, Satoko Kizuka, Hidenori Oka, Yusuke Suwa, Shinsuke Suzuki, Kazuya Nakagawa, Hirokazu Suwa, et al. Detection of gas components as a novel diagnostic method for colorectal cancer. *Annals of gastroenterological surgery*, 2(2):147–153, 2018.

[22] Giorgia Purcaro, Christiaan A Rees, Wendy F Wieland-Alter, Mark J Schneider, Xi Wang, Pierre-Hugues Stefanuto, Peter F Wright, Richard I Enelow, and Jane E Hill. Volatile fingerprinting of human respiratory viruses from cell culture. *Journal of breath research*, 12(2):026015, 2018.

[23] Tarik Saidi, Omar Zaim, Mohammed Moufid, Nezha El Bari, Radu Ionescu, and Benachir Bouchikhi. Exhaled breath analysis using electronic nose and gas chromatography–mass spectrometry for non-invasive diagnosis of chronic kidney disease, diabetes mellitus and healthy subjects. *Sensors and Actuators B: Chemical*, 257:178–188, 2018.

[24] Raphael BM Aggio, Ben de Lacy Costello, Paul White, Tanzeela Khalid, Norman M Ratcliffe, Raj Persad, and Chris SJ Probert. The use of a gas chromatography-sensor system combined with advanced statistical methods,

towards the diagnosis of urological malignancies. *Journal of breath research*, 10(1):017106, 2016.

[25] Riikka J Niemi, Antti N Roine, Emmi Eräviita, Pekka S Kumpulainen, Johanna U Mäenpää, and Niku Oksala. Faims analysis of urine gaseous headspace is capable of differentiating ovarian cancer. *Gynecologic oncology*, 151(3):519–524, 2018.

[26] Dongmin Guo, David Zhang, Naimin Li, Lei Zhang, and Jianhua Yang. A novel breath analysis system based on electronic olfaction. *IEEE transactions on biomedical engineering*, 57(11):2753–2763, 2010.

[27] Jan Baumbach, Alexander Bunkowski, Sita Lange, Timm Oberwahrenbrock, Nils Kleinbölting, Sven Rahmann, and Jörg Ingo Baumbach. Ims2–an integrated medical software system for early lung cancer detection using ion mobility spectrometry data of human breath. *Journal of Integrative Bioinformatics*, 4(3):186–197, 2007.

Chapter 8

Conclusion and Further Work

The aim of this project is to develop a prototype point of care tool that has the potential to be developed into a future commercial product for the detection of bacteria in patients. The need for this product stems from the limitations associated with current gas based diagnostic tools such as Gas Chromatography Mass Spectrometry (GC-MS), Ion Mobility Spectrometry (IMS) and electronic noses. Factors limiting the widespread adoption of these techniques includes cost of purchase, complexity of operation and long analysis time. The size and weight of these instruments reduce their portability and restrict their use to mostly laboratory analysis. Therefore, limits their use in point of care in hospital wards, GP surgeries. Electronic noses and Photoionization Detectors (PIDs) are further limited to analysis where compositional information of the compound under test is not required, as they generally do not offer information on the identity of Volatile Organic Compound (VOC). They are sensitive to a wide range of compounds hence have poor selectivity. Therefore, in this project a portable, low-cost diagnostic tool was designed to enable faster diagnosis of bacterial infection.

As mentioned in Chapter 1, the objectives to achieve this aim included designing a low-cost novel VOC detector. The design approach combines the merits of commercial IMS systems and PID sensors. Unlike commercial PID devices, the detector developed in this study provides compositional information on the compound being tested. With the design approach taken, the instrument could be made available to consumers at a lower price point than IMS systems with a market potential to sit somewhere between the lower end PID and the higher end IMS systems. Peripheral Pre-concentrator (PC) and Gas Chromatograpy (GC) were also developed to boost the sensitivity and specificity of the detector, for particularly complex chemical compositions. An end user software was designed to enable non-technical personnel to use the instrument in diagnosis. Several chemical analyses were carried out on the components to benchmark the instruments performance in undertaking VOC detection. Initial diagnostic tests were also carried out using urine and some key biomarkers for bacterial infections. Finally, statistical methods applied in the area of gas based diagnostic medicine were also investigated. This was done to develop an understanding of statistical approaches that were best suited for this instrument. The conclusions from carrying out these objectives are discussed in more detail in the next section.

8.1 Conclusions

In the first part of the work a literature review on PID and IMS technology was carried out. The review presented some existing PID and IMS designs and their applications. It also discussed some of the merits and disadvantages of these technologies. From the review it was stated that depending on the choice of Ultraviolet (UV)

lamp used for ionisation, PIDs could be targeted at compounds below the ionisation potential of the UV lamp. However, the system will still detect all molecules below the ionisation potential and so specificity would be limited. This was one of the reason PID technology was used in this project as it enables analysis in air since the components of air have higher Ionisation Energy (IE) than most UV lamps. A second advantage in using PID sensors is their ability to function in ambient pressure requiring less auxiliary equipment to operate. This facilitates portability of PID sensors and makes them suitable for testing in a range of environments and has resulted in their increased use for *in situ* analysis. While these advantages are desirable, application of PIDs sensors in analysis requiring compositional information is limited because PIDs sensors only provides a concentration value of the sample being tested. The IMS technology was also reviewed and two major advantages of Field Asymmetric Ion Mobility Spectrometry (FAIMS) over Aspirator Drift Tube (ADT) IMS drift tube designs were presented. This includes the high speed and an ion focusing effect that often improves sensitivity of FAIMS over ADT and IMS. This review informed the design decision to develop a novel advanced VOC detector based on the PID and FAIMS technologies.

The design of a Gas Sensor Calibration Rig was also presented. The Gas Sensor Calibration Rig comprises of a Gas Mixer, Permeation Source, Humidity Generator, Dilutor, and Gas Analyser. This instrument enables users to test their sensors in controlled environments to calibrate the sensors. The test rig provides gas mixtures at defined flow rates, pressure, temperature and humidity.

Several PCs and GCs were also developed to improve the analytical performance of the system. PCs are used with gas based analytical equipment to enable selective sampling of target compounds, reduce Limit of Detection (LOD), and allow

operation at high flow rates. GCs provides analytical systems with a mixture of good accuracy and precision, very high selectivity and resolution, wide dynamic concentration range and high sensitivity. GCs are used to separate complex mixtures before analysis by detectors such as IMS and PID. When integrated with gas detection technologies, both PC and GC increase the limit of detection, selectivity, and sensitivity of the sensor device. This project presents a novel use of Activated Carbon Cloth (ACC) as an adsorption material. The results presented shows a 830% increase in response intensity when ACC was used. As demonstrated in the tests, the PC serves as interface for different types of chemical instruments serving as a convenient channel between sample and instrument.

The design of a novel advanced VOC ionisation sensor that offers additional compositional information about the sample under test was presented. The sensor provides two voltage outputs proportional to the concentration and composition of the test sample. Tests were carried out with low concentration isobutylene and the response was found to increase linearly with concentration. An increase in concentration from 0 – 18 ppm resulted in an increase in output voltage of 2.3V, with an estimated sensitivity of below 1 ppm. The composition response shows a significant distinction between 2-pentanone and isobutylene when 1kV/m was applied in the chamber. A 0.063 V difference was observed between 2-heptanone and propanol when 1000 V/cm electric field was applied. The VOC detector compositional response also discriminated between 10 ppm 2-hexanone, 2-octanone and propanol when the electric field was varied from -7 kV/m to +7 kV/m. Similar discrimination was also observed for 2-heptanone and 2-octanone over the same electric field range.

The PC, GC, and VOC detector were assembled into a single analytical in-

strument. A new software - Bear, was designed to manage various aspects of the instrument including power supply, pneumatics, and data. Bear was designed to function as a single port of operations to allow these instruments function together during analysis. The software also provides a layer of abstraction to the user by managing gas flows, timing, humidity, concentration, heating and several other parameters. It is essential that these parameters are consistent across gas analysis ensuring repeatable and reproducible results. Additionally Bear records test measurements to a *.csv* file for further statistical analysis. Bear was written in C♯ for the Universal Windows Platform (UWP) and targeted at the 64 bit Windows 10 version 1803.

Biomedical testing and trial were carried out to demonstrate the practicality of using the designed instrument as a non-invasive diagnostic tool for bacterial infection. Several statistical models used in medical diagnosis were also investigated. The initial results indicated that the instrument is capable of detecting VOCs released by causative pathogens such as *Staphylococcus aureus*, *Pseudomonas aeruginosa* or*Escherichia coli*. Indole and acetone, as known biomarkers for these pathogens were tested. From the results, the instrument is capable of detecting the presence of these biomarkers in urine, down to 2 parts per billion (ppb) indole and 200 ppb acetone. These results indicated that the instrument diagnosed the simulated infected groups from control with the possible benefit of eliminating the need for culture before testing for bacterial infection. It also demonstrated the feasibility of using this instrument as point-of-care diagnostic tool in a primary healthcare environment. Further trials with urine samples from patients with these bacterial infection would be required. Therefore, the next section discusses recommendation for further work.

8.2 Recommendations for further work

The recommendations are separated into three major sections:

8.2.1 GC

The design of a spiral GC was presented in this work. However, extensive tests are required to characterise the performance of the GC. These tests will demonstrate the GCs as a stand-alone precursor for gas based analytical instruments.

8.2.2 VOC detector

The FAIMS based VOC detector requires high voltage waveform to achieve filtration of ions. Designing a low voltage filtration circuit will reduce space, costs and power requirements. This approach will lead to more compact, battery powered detector instruments for mobile point-of-care applications. Additionally, the reduction in waveform power will reduce the Electromagnetic Interference (EMI) and Radio Frequency Interference (RFI) in the system. Therefore, a more sensitive detection circuit could be used without interference from the filtration circuit.

8.2.3 Biomedical trials and statistical analysis

The biomedical tests in this work were carried out using Surine Neg Urine Control to simulate urine. Indole and acetone were used as biomarkers for *Escherichia coli*, *Staphylococcus aureus*, and *Pseudomonas aeruginosa*. Further tests with urine samples from patients will be required to validate the results obtained in this projects.

From the statistical investigation it was observed that Logistic Regression (LR), Hierarchical clustering (HC), Linear Discriminant Analysis (LDA) were the best statistical methods for supervised, unsupervised and non-binary supervised biomedical diagnosis respectively. It is recommended that these analytical methods are built into Bear. This enables faster diagnosis at the point of care eliminating the delay associated with exporting test results to a statistician for analysis.

Chapter 9

Appendix

9.1 Classification of indole infected groups

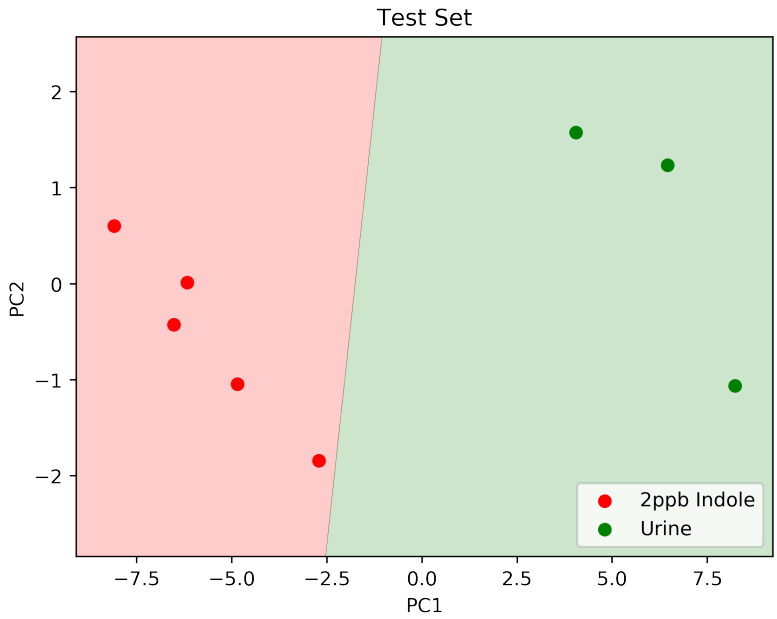

Figure 9.1: Plot showing decision boundary classifying 2 ppb indole and urine test set using LR

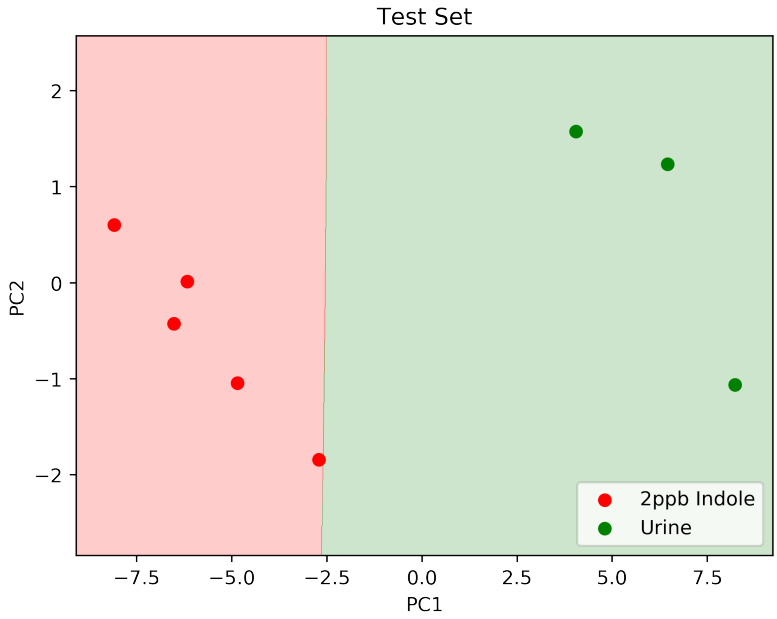

Figure 9.2: Plot showing decision boundary classifying 2 ppb indole and urine test set using Naive Bayes (NB)

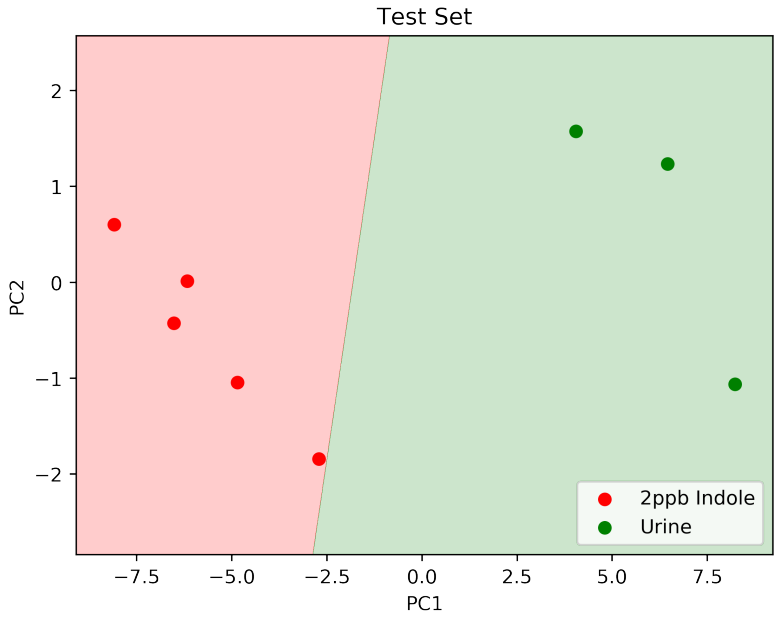

Figure 9.3: Plot showing decision boundary classifying 2 ppb indole and urine test set using Support Vector Machine (SVM)

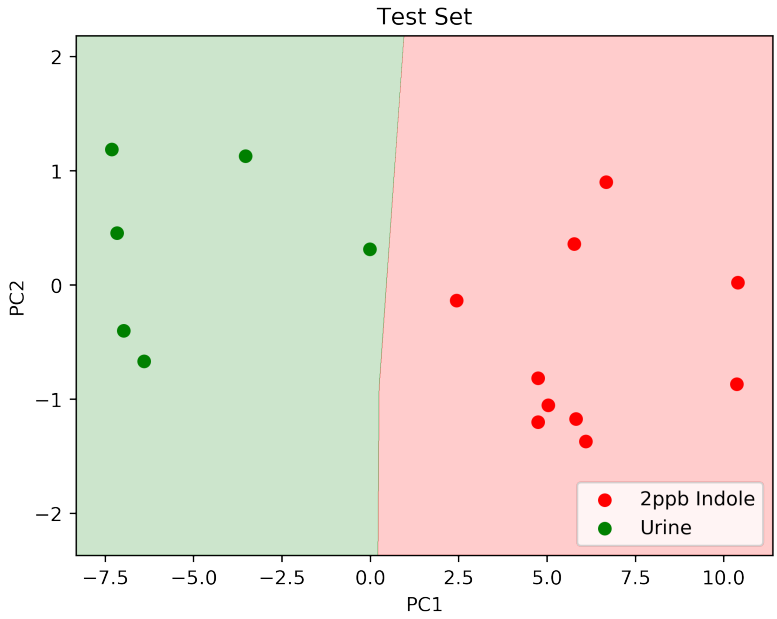

Figure 9.4: Plot showing decision boundary classifying 2 ppb indole and urine test set using K-nearest neighbour (KNN)

9.2 Classification of acetone infected groups

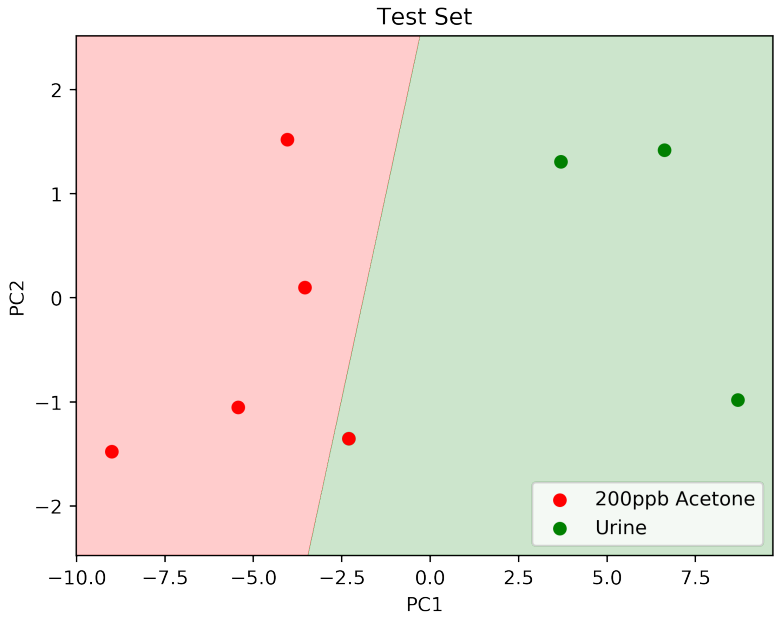

Figure 9.5: Plot showing decision boundary classifying 200 ppb acetone and urine test set using LR

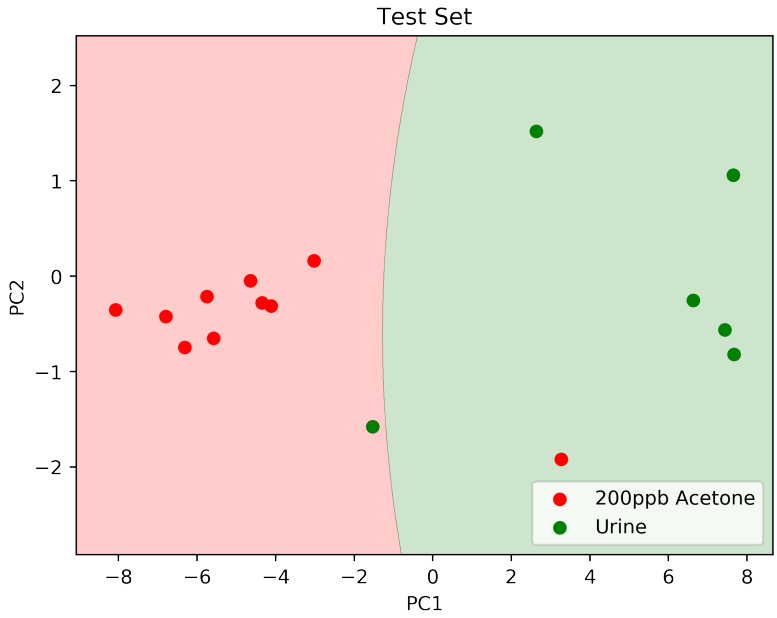

Figure 9.6: Plot showing decision boundary classifying 200 ppb acetone and urine test set using NB

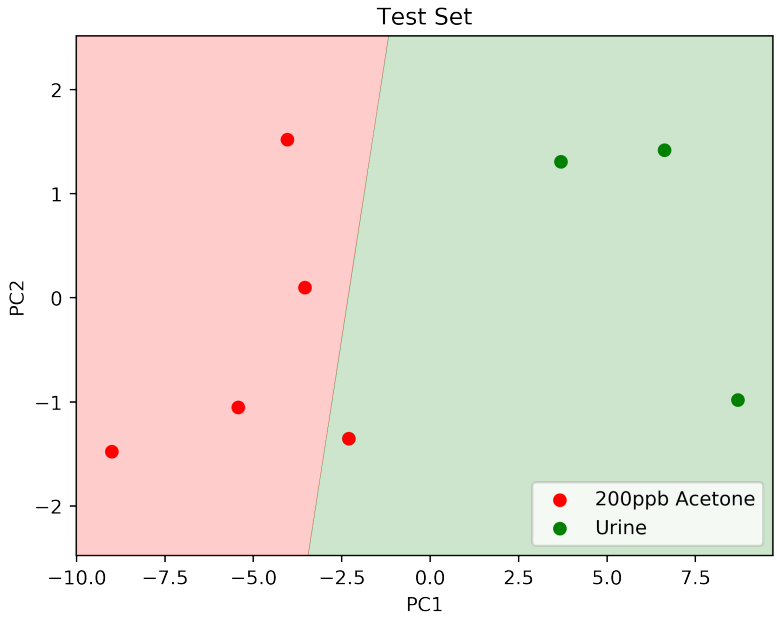

Figure 9.7: Plot showing decision boundary classifying 200 ppb acetone and urine test set using SVM

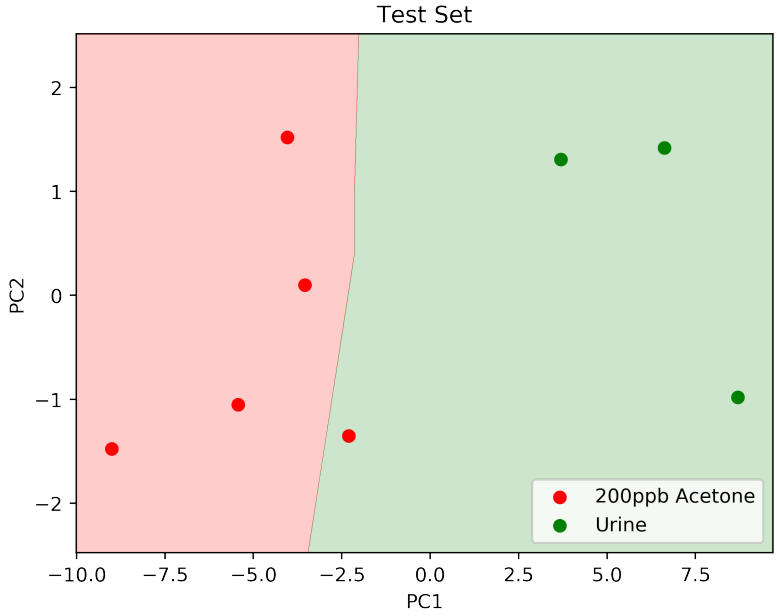

Figure 9.8: Plot showing decision boundary classifying 200 ppb acetone and urine test set using KNN